

PROCEEDINGS

OF 7TH INTERNATIONAL CONFERENCE ON
COMMUNICATIONS, ELECTROMAGNETICS AND MEDICAL
APPLICATIONS (CEMA'12)

Organized by:



FACULTY OF TELECOMMUNICATIONS
TECHNICAL UNIVERSITY OF SOFIA, BULGARIA



NATIONAL TECHNICAL UNIVERSITY OF ATHENS, GREECE,
SCHOOL OF ELECTRICAL AND COMPUTER ENGINEERING

NATIONAL TECHNICAL
UNIVERSITY OF ATHENS,
GREECE



SCHOOL OF ELECTRICAL
AND COMPUTER
ENGINEERING

Athens, Greece
08th - 10th November, 2012

KING

Edited by Prof. Dr. Eng. **Dimiter Tz. Dimitrov**

All rights reserved. This book, or parts there of, may not be reproduced in any form or by any means, electronic or mechanical, including photocopying or any information storage and the retrieval system now known or to be invented without written permission from the Publisher.

ISSN: 1314-2100

Printed in Bulgaria
KING 2001, Sofia



P. Frangos



D. Dimitrov

Dear Colleagues,

It is our privilege to thank all of you for your contributions submitted at 7th regular International Conference on 'Communication, Electromagnetic and Medical Applications' CEMA'12. This is a conference which should help future collaboration in the area of engineering, especially in the area of communication technologies and medical applications. This is an important scientific event not only in Balkan region, but in Europe, also. The International Conference on Communication, Electromagnetism and Medical Applications CEMA'12 is dedicated to all essential aspects of the development of global information and communication technologies, and their impact in medicine, as well. The objective of Conference is to bring together lecturers, researchers and practitioners from different countries, working on the field of communication, electromagnetism, medical applications and computer simulation of electromagnetic field, in order to exchange information and bring new contribution to this important field of engineering design and application in medicine. The Conference will bring you the latest ideas and development of the tools for the above mentioned scientific areas directly from their inventors. The objective of the Conference is also to bring together the academic community, researchers and practitioners working in the field of Communication, Electromagnetic and Medical Applications, not only from all over Europe, but also from America and Asia, in order to exchange information and present new scientific and technical contributions. Many well known scientists took part in conference preparation as members of International Scientific Committee or/and as reviewers of submitted papers. I would like to thank all of them for their efforts, for their suggestions and advices.

On behalf of the International Scientific Committee, we would like to wish you successful presentations of your papers, successful discussions and new collaborations for your future scientific investigations. Engineering and medicine should provide high level of living for all people.

P. Frangos
Conference Chairman

D. Dimitrov
Conference Vice Chairman

INTERNATIONAL SCIENTIFIC COMMITTEE

Honorary Chairman:

Prof. N. UZUNOGLU, National Technical University of Athens, Greece

Chairman:

P. FRANGOS, National Technical University of Athens, Greece

Vice Chairman:

D. TZ. DIMITROV, Technical University of Sofia, Bulgaria

Members:

AMPILOVA, N.	University of Perersburg, Russia
BEHARI, J.	Jawaharlal Nehru University, New Delhi, India
BEKJARSKY, A.	Technical University of Sofia, Bulgaria
DEKERIS, B.	Kaunas University of Technology, Lithuania
DEMIREV, V.	Technical University of Sofia, Bulgaria
DUMBRAVA, V.	Kaunas University of Technology, Lithuania
EIDUKAS, D.	Kaunas University of Technology, Lithuania
ESCUDEIRO, N.	Inst. Sup. de Engenharia do Porto, Portugal
GAGO-RIBAS, E.	University of Oviedo, Spain
GOUSSETIS, G.	Heriot - Watt University, United Kingdom
GRIGORIEV, A.	St. Petersburg University, Russia.
HOFMANN, M.	University of Ulm, Germany
HRISTOV, H.	UTFSM, Valparaíso, Chile
HRISTOV, V.	University of Blagoevgrad, Bulgaria
ILIEV, I.	Technical University of Sofia, Bulgaria
JORDANOVA, L.	Technical University of Sofia, Bulgaria
KLIROS, G.	Hellenic Air-Force Academy, Greece
KRIVICKAS, R.	Kaunas University of Technology, Lithuania
MALHEIRO, B.	Inst. Sup. de Engenharia do Porto, Portugal
MALLET, G.	University "Sophia Antipolis", Nice, France
MATSOPOULOS, G.	National Technical University of Athens, Greece
MARTINS, M.	Instituto Superior Técnico, Lisboa, Portugal
MORALES-GONZALES, M.	University of Valladolid, Spain
NARBUTAITE, L.	University of Technology, Kaunas, Lithuania
NIKITA, K.	National Technical University of Athens, Greece
M. NIKOLOVA, M.	High Naval School, Varna, Bulgaria
PETROVSKA, J.	Medical University of Sofia, Bulgaria
PRATO, F.	University of Western Ontario, Canada
ROTH, H.	University of Siegen, Germany
SAUTBEKOV, S.	Euroasian University, Astana, Kazakhstan
SAVOV, A.	Medical University of Sofia, Bulgaria
SAVOV, S.	Technical University of Varna, Bulgaria
SCHADE, H-P.	Technical University of Ilmenau, Germany
SEBASTIAN, J.	Universidad Complutense de Madrid, Spain
SONG, L.	Technical University of Harbin, China
SVILAINIS, I.	University of Technology, Kaunas, Lithuania
USHEVA, A.	University of Boston, USA

REVIEWERS

BALZANO, Q.	University of Maryland, USA
BEHARI, J.	Jawaharlal Nehru University, New Delhi, India
BOEMO, E.	Technical University of Madrid, Spain
DIMITROV, D.	Technical University of Sofia, Bulgaria
DONTSHEWA, M.	University of Applied Sciences, Dornbirn, Austria
GOUSSETIS, G.	Heriot - Watt University, United Kingdom
JORDANOVA, L.	Technical University of Sofia, Bulgaria
HRISTOV, H.	UTFSM, Valparaíso, Chile
HOEYE, S.	University of Oviedo, Spain
MALLET, G.	University "Sophia Antipolis", Nice, France
MARINKEV, V.	Medical University of Plovdiv, Bulgaria
M. NIKOLOVA, M.	High Naval School, Varna, Bulgaria
PRATO, F.	University of Western Ontario, Canada
ROTH, H.	University of Siegen, Germany
SAVOV, A.	Medical University of Sofia, Bulgaria
SCHADE, H-P.	Technical University of Ilmenau, Germany
SONG, L.	Technical University of Harbin, China
USHEVA, A.	University of Boston, USA

REGISTRATION

08th November, 09h - 16h

The conference registration desk will be at:

University Administration Building
Ceremonies Room (zero level of building)
National Technical University of Athens, Greece

CONFERENCE PROGRAM

8th November

Opening ceremony

9h 30min -10 h

University Administration Building
Ceremonies Room (zero level of building)
National Technical University of Athens, Greece

SCIENTIFIC PROGRAM

8th November

FIRST SESSION

10h - 12h

University Administration Building
Ceremonies Room (zero level of building)
National Technical University of Athens, Greece

Chairmen: Prof. P. Frangos, National Technical University of Athens, Greece
Prof. D. Dimitrov, Technical University of Sofia, Bulgaria

- 1. SIMULATION MODELLING AND ANALYSIS OF PHYSICAL LAYER CODING SCHEMES FOR V2X APPLICATIONS**, George Kiokes¹, Panagiotis Gkonis², Nikolaos Uzunoglu³ ¹, Hellenic Air-Force Academy, Dekeleia, Attica GR-1010, Greece^{2,3}, National Technical University of Athens, Iroon Politechniou 9, Athens, Greece
- 2. NEPHRON+: ICT-ENABLED WEARABLE ARTIFICIAL KIDNEY AND PERSONAL RENAL CARE SYSTEM**, Anastasia Garbi¹, Andreas Raptopoulos¹, Ioannis Koutras^{1,2}, Alexandros Bartzas^{1,2} and Dimitrios Soudris^{2,1} EXODUS S.A. 11527 Athens, Greece, ² National Technical University of Athens, 15780, Athens, Greece
- 3. ENERGY CONSUMPTION ANALYSIS OF WIRELESS ACCESS TECHNOLOGIES FOR V2G COMMUNICATIONS**, George C. Kiokes¹, Erietta I. Zountouridou², George S. Kliros³, Nikolaos D. Hatziargyriou⁴ ^{1,3}. Hellenic Air-Force Academy, Dekeleia, Attica GR-1010, Greece ^{2,4}. National Technical University of Athens, Iroon Politechniou 9, Athens, Greece
- 4. NETWORK PLANNING AND QOS SIMULATION SOFTWARE DESIGN FOR 4TH GENERATION BROADBAND WIRELESS TECHNOLOGIES**, Lina Narbutaitė, Rasa Brūzgienė, Eugenijus Kačerginskis, Kaunas University of Technology
- 5. COMPARATIVE ANALYSIS OF INFLUENCE OF TV CHANNEL TRANSMISSION PROCESS TO QOE FOR DVB-T/H AND IPTV SERVICES**, Rasa Brūzgienė, Lina Narbutaitė, Tomas Adomkus, Kaunas University of Technology
- 6. INDOOR MULTIPATH RADIO CHANNEL CHARACTERIZATION IN LARGE BUILDINGS**, Dimitar G. Valchev, University of Food Technologies, Plovdiv, Bulgaria
- 7. ADVANTAGES OF MFSO TO RF WIRELESS COMMUNICATION SYSTEMS**, Hristo Ivanov, Tsvetan Mitsev, Technical University of Sofia, Bulgaria

8. **INVESTIGATION OF THERMAL EFFECTS OF MOBILE PHONE TO THE HUMAN HEAD**, V. Pitkevicius, D. Kybartas, L. Svilainis, A. Lukosevicius, V. Dumbrava, Kaunas University of Technology, Lithuania

Lunch

12h - 13h30

SECOND SESSION

13h 30 - 15 h

University Administration Building
Ceremonies Room (zero level of building)
National Technical University of Athens, Greece

Chairman: Prof. V. Demirev, Technical University of Sofia, Bulgaria

1. **ON THE CAPACITY OF MIMO-WCDMA MULTICELLULAR NETWORKS WITH IDEAL POWER CONTROL**, Panagiotis K. Gkonis¹, National Technical University of Athens, Athens, Greece, George Kokes², Hellenic Air-Force Academy, Greece
2. **MODELING THE SPECTRAL RESPONSE OF BRAGG GRATINGS WRITTEN IN PHOTONIC CRYSTAL FIBERS**, George S. Kliros, Hellenic Air-Force Academy, Air-Force Base, Attica, Greece
3. **THE PERFORMANCE OF A MODULATION PASSIVELY Q-SWITCHED SOLID - STATE LASER PUMPED BY LASER DIODE, FOR FREE - SPACE LASER COMMUNICATIONS.**
¹Jassim Mohammed Jassim, ²Yaseen Hiassn Kadhim, ¹Ahmed Kadem Kodeary, ¹Laser Physics Department, College of Science for Woman, Babylon University, Iraq, ²Physics Department, College of Science, Babylon University, Iraq.
4. **A RETICULE DESIGN TO ENHANCE THE DETECTION RANGE OF A TELESCOPE FOR MOVING OBJECTS**, R. N. Ali, Ghaleb A. Al-Dahash, University of Babylon, College of Science for Women, Uraq
5. **OPTIMUM DIVERGENCE OF LASER RADIATION IN FSO SYSTEMS**, Tsvetan Mitsev, Kalin Dimitrov, Hristo Ivanov, Nikolai Kolev, Technical University of Sofia, Bulgaria

Break

15h - 15h30

THIRD SESSION

15h 30 - 17h

University Administration Building
Ceremonies Room (zero level of building)
National Technical University of Athens, Greece

Chairman: Prof. Ts. Mitsev, Technical University of Sofia, Bulgaria

1. **APPLYING THE MODIFIED FRACTAL SIGNATURE METHOD TO IMAGE CLASSIFICATION: SOME PRELIMINARY RESULTS FOR ISAR RADAR IMAGES**, C. Pandis, A. Malamou, P. Stefaneas and P. Frangos, National Technical University of Athens, Greece

2. **AN AUTOFOCUSING ALGORITHM FOR POST-PROCESSING OF SYNTHETIC APERTURE RADAR (SAR) IMAGES BASED ON IMAGE ENTROPY MINIMIZATION**, A. Malamou, A. Karakasiliotis, E. Kallitsis, G. Boultadakis and P. Frangos, National Technical University of Athens, Greece
3. **RANDOM PHASED ANTENNA ARRAYS - THE NEW CHALLENGE FOR THE MULTISTATIC RADAR NETWORKS**, Veselin Demirev, Technical University - Sofia, Bulgaria
4. **APPLICATION OF SCP TECHNOLOGY IN GLOBAL NAVIGATION SATELLITE SYSTEMS**, Veselin Demirev, Technical University-Sofia, Bulgaria
5. **MODIFIED FRACTAL KOCH CURVE ANTENNA STUDY**, Boncho G. Bonev, Technical University - Sofia, Bulgaria
6. **METHODS FOR INCREASE ACCURACY AND REDUCE THE AVERAGING TIME IN PRECIPITATION INTENSITY MEASUREMENT FOR RADIOWAVE PROPAGATION INVESTIGATIONS**, Boncho G. Bonev, Emil S. Altimirski, Kliment N. Angelov, Technical University - Sofia, Bulgaria
7. **ELECTROMAGNETIC CHARACTERISTICS OF THE "VERY - NEAR - FIELD" REGION OF A SQUARE UNIFORM APERTURE**, Antoniya Petrova Petrova, Technical University of Sofia, Bulgaria
8. **ELECTROMAGNETIC CHARACTERISTICS OF THE "VERY - NEAR - FIELD" REGION OF A CIRCULAR UNIFORM APERTURE**, Antoniya Petrova Petrova, Technical University of Sofia, Bulgaria
9. **PRACTICAL DESIGN OF MICROWAVE DIODE FREQUENCY MULTIPLIERS**, Mihail Plamenov Tonev, Technical University of Sofia, Bulgaria

09th November

FOURTH SESSION

9h - 10h

University Administration Building
Ceremonies Room (zero level of building)
National Technical University of Athens, Greece

Chairman: Prof. L. Narbutaite, Kaunas University of Technology, Lithuania

1. **ELECTROPORATOR FOR LABORATORY TESTS**, Vytautas Dumbrava, Vladas Juska, Darius Pagodinas, Marius Gailius, Linas Sidaras, Kaunas University of Technology, Lithuania
2. **ARBITRARY WIDTH AND POSITION PULSE TRAINS APPLICATION FOR ULTRASONIC IMAGING: INITIAL STUDY**, L. Svilainis, A. Aleksandrovas, K. Lukoseviciute, Kaunas University of Technology, Lithuania
3. **THE WIDEBAND ULTRASONIC PULSER FOR SONOPORATION**, L. Svilainis¹, A. Chaziachmetovas¹, R. Jurkonis², D. Kybartas¹, N. Lamanaukas³ and S. Satkauskas³ ¹Signal processing department, Kaunas University of Technology, Lithuania, ²Biomedical Engineering Institute, Kaunas University of Technology, Lithuania, ³Vytautas Magnus University, Kaunas, Lithuania

Break

10h - 10h30

FIFTH SESSION

10h 30 – 13h

University Administration Building
Ceremonies Room (zero level of building)
National Technical University of Athens, Greece

*Chairmen: Prof. K. Dimitrov, Technical University of Sofia, Bulgaria,
Prof. D. Kybartas, Kaunas University of Technology, Lithuania*

- 1. ON IMPLEMENTATION OF A NEURAL NETWORK CLASSIFIER FOR SOME CLASSES OF BIOLOGICAL AND MEDICAL PREPARATION IMAGES**, I. P. Soloviev, Comp. Sci. Dept, Math. & Mech. Faculty, St. Petersburg State University, Russia, N. B. Ampilova, Comp. Sci. Dept, Math. & Mech. Faculty, St. Petersburg State University, Russia, E. Y. Gurevich, Sofia & Jacobs Foundation, St. Petersburg, Russia
- 2. MULTIFRACTAL SPECTRUM AS A CLASSIFICATION SIGN FOR BIOMEDICAL PREPARATIONS IMAGES**, N. B. Ampilova, Comp. Sci. Dept, Math. & Mech. Faculty, St. Petersburg State University, Russia, I. P. Soloviev, Comp. Sci. Dept, Math. & Mech. Faculty, St. Petersburg State University, Russia, Y. V. Shupletsov, Math. & Mech. Faculty, St. Petersburg State University, St. Petersburg, Russia
- 3. 2-D FILTERS SYNTHESIS USING METHOD OF COMPRESSED COSINES**, Peter Apostolov¹, College of Telecommunications and Posts, Sofia, Bulgaria, Dimitar Valchev², Technical University of Varna, Varna, Bulgaria
- 4. PRACTICAL OBJECT TRACKING SYSTEM ON FPGA**, Spirov, Rosen Petrov, Technical University of Varna, Varna, Bulgaria
- 5. DESIGN OF POWER UNIT OF SYSTEM FOR THERAPY USING “RUNNING” LOW FREQUENCY MAGNETIC FIELD**, Atanas Dimitrov, Technical University of Sofia, Bulgaria
- 6. INVESTIGATION ON MOTION OF IONS IN ALIVE TISSUE UNDER INFLUENCE OF TOROIDAL LOW FREQUENCY MAGNETIC FIELD**, Atanas Dimitrov*, Dimitar Dimitrov**, Sasho Guergov***, Anton Savov**** *Technical University of Sofia, Bulgaria, **Technical University of Sofia, Bulgaria, *** Technical University of Sofia, Bulgaria****, Specialised Hospital for Rehabilitation “St. Mina”, Warshet, Bulgaria
- 7. MEDICAL INFORMATION SYSTEM FOR SELF MONITORING AND DISTANCE CONSULTATION „PATIENT’S DIARY“**, Simona Lincheva, Technical University of Sofia, Bulgaria
- 8. EXPERIMENTAL INVESTIGATION ON COMPUTER RESTORATION OF FREQUENCY SPECTRUM OF ECG – SIGNALS IN THE CASE OF INFLUENCE OF NOISE**, Tzvetia Dimitrova, Lidia Jordanova, Technical University of Sofia, Bulgaria
- 9. A REGION GROWING SEGMENTATION ALGORITHM BASED ON CLAHE AND WAVELET TRANSFORMATION FOR ULTRASOUND IMAGES**, Veska M. Georgieva, Technical University of Sofia, Bulgaria
- 10. GUI FOR SEGMENTATION OF MEDICAL IMAGES**, Veska M. Georgieva, Technical University of Sofia, Bulgaria, Antonia D. Nankova, Technical University of Sofia, Bulgaria
- 11. PROCESSING AND TRANSMISSION OF EEG SIGNALS**, Dejan Milev, Technical University of Sofia, Bulgaria

12. **METHOD AND SYSTEM FOR REMOTE MONITORING MULTIPLE MEDICAL PARAMETERS**, Dejan Milev, Technical University of Sofia, Bulgaria
13. **CREATING A WEB SITE FOR MEDICAL EQUIPMENT**, Silvia Bankova, Technical University Sofia, Bulgaria
14. **EUROPEAN CENTRE FOR PROJECT/INTERNSHIP EXCELLENCE**, Nuno Escudeiro¹, Paula Escudeiro² ^{1,2}Instituto Superior de Engenharia do Porto, Portugal

CLOSING SESSION

13 h- 13h 30

University Administration Building
Ceremonies Room (zero level of building)
National Technical University of Athens, Greece

SOCIAL PROGRAM

Social Program SCHEDULE

- **Conference Dinner** (optional) will be given in the heart of the old city of Athens, near Acropolis of Athens, on Friday, November 8th, in the evening. Participants can pay for this on site. More information regarding Conference Dinner will be provided during the first day of the Conference (November, 8th).
- Furthermore, a **tour** to the famous ‘**Acropolis of Athens**’, and its corresponding ‘**New Acropolis Museum**’, will take place on Saturday November, 10th, beginning 11:00 a.m. Participants can also pay on site.
- In addition, more touristic information about Athens and Greece can be provided by the Conference Organizers.

Contact us:

http://tu-sofia.bg/eng_new/fktt/cema12

*General Information
Submission of contributions*

Prof. Dr. Dimiter Dimitrov

Faculty of Telecommunication
Technical University of Sofia

8, Kliment Ohridsky str.
1756 Sofia, Bulgaria
Phone: ++359 2 9652278
Fax: ++359 2 9652278
E-mail: dcd@tu-sofia.bg

*Cultural programme
and hotel reservation*

Prof. P. Frangos

National Technical University of Athens
School of Electrical and Computer
Engineering

9, Iroon Polytechniou Str.,
157 73 Zografou, Athens, Greece
Phone: 00 30 210 772 3694
Fax: 00 30 210 772 2281
E-mail: pfrangos@central.ntua.gr

TABLE OF CONTENTS

SIMULATION MODELLING AND ANALYSIS OF PHYSICAL LAYER CODING SCHEMES FOR V2X APPLICATIONS	1
<i>George Kiokes, Panagiotis Gkonis, Nikolaos Uzunoglu</i>	
NEPHRON+: ICT-ENABLED WEARABLE ARTIFICIAL KIDNEY AND PERSONAL RENAL CARE SYSTEM	5
<i>Anastasia Garbi, Andreas Raptopoulos, Ioannis Koutras, Alexandros Bartzas, Dimitrios Soudris</i>	
ENERGY CONSUMPTION ANALYSIS OF WIRELESS ACCESS TECHNOLOGIES FOR V2G COMMUNICATIONS	8
<i>George C. Kiokes, Erietta I. Zountouridou, George S. Kliros, Nikolaos D. Hatziargyriou</i>	
NETWORK PLANNING AND QOS SIMULATION SOFTWARE DESIGN FOR 4TH GENERATION BROADBAND WIRELESS TECHNOLOGIES	12
<i>Lina Narbutaitė, Rasa Brūzgienė, Eugenijus Kačerginskis</i>	
INDOOR MULTIPATH RADIO CHANNEL CHARACTERIZATION IN LARGE BUILDINGS	15
<i>Dimitar G. Valchev</i>	
ADVANTAGES OF MFSO TO RF WIRELESS COMMUNICATION SYSTEMS	19
<i>Hristo Ivanov, Tsvetan Mitsev</i>	
INVESTIGATION OF THERMAL EFFECTS OF MOBILE PHONE TO THE HUMAN HEAD	23
<i>V. Pitkevicius, D. Kybartas, L. Svilainis, A. Lukosevicius, V. Dumbrava</i>	
ON THE CAPACITY OF MIMO-WCDMA MULTICELLULAR NETWORKS WITH IDEAL POWER CONTROL	26
<i>Panagiotis K. Gkonis, George Kokes</i>	
MODELING THE SPECTRAL RESPONSE OF BRAGG GRATINGS WRITTEN IN PHOTONIC CRYSTAL FIBERS	30
<i>George S. Kliros</i>	
THE PERFORMANCE OF A MODULATION PASSIVELY Q-SWITCHED SOLID - STATE LASER PUMPED BY LASER DIODE, FOR FREE - SPACE LASER COMMUNICATIONS	34
<i>Jassim Mohammed Jassim, Yaseen Hiassn Kadhim, Ahmed Kadem Kodeary</i>	
A RETICULE DESIGN TO ENHANCE THE DETECTION RANGE OF A TELESCOPE FOR MOVING OBJECTS	38
<i>R. N. Ali, Ghaleb A. Al-Dahash</i>	
OPTIMUM DIVERGENCE OF LASER RADIATION IN FSO SYSTEMS	42
<i>Tsvetan Mitsev, Kalin Dimitrov, Hristo Ivanov, Nikolai Kolev</i>	
COMPARATIVE ANALYSIS OF INFLUENCE OF TV CHANNEL TRANSMISSION PROCESS TO QOE FOR DVB-T/H AND IPTV SERVICES	46
<i>Rasa Brūzgienė, Lina Narbutaitė, Tomas Adomkus</i>	
APPLYING THE MODIFIED FRACTAL SIGNATURE METHOD TO IMAGE CLASSIFICATION: SOME PRELIMINARY RESULTS FOR ISAR RADAR IMAGES	50
<i>C. Pandis, A. Malamou, P. Stefaneas, P. Frangos</i>	
AN AUTOFOCUSING ALGORITHM FOR POST-PROCESSING OF SYNTHETIC APERTURE RADAR (SAR) IMAGES BASED ON IMAGE ENTROPY MINIMIZATION	53
<i>A. Malamou, A. Karakasiliotis, E. Kallitsis, G. Boultadakis, P. Frangos</i>	

RANDOM PHASED ANTENNA ARRAYS – THE NEW CHALLENGE FOR THE MULTISTATIC RADAR NETWORKS	57
<i>Veselin Demirev</i>	
APPLICATION OF SCP TECHNOLOGY IN GLOBAL NAVIGATION SATELLITE SYSTEMS	61
<i>Veselin Demirev</i>	
MODIFIED FRACTAL KOCH CURVE ANTENNA STUDY	64
<i>Boncho G. Bonev</i>	
METHODS FOR INCREASE ACCURACY AND REDUCE THE AVERAGING TIME IN PRECIPITATION INTENSITY MEASUREMENT FOR RADIOWAVE PROPAGATION INVESTIGATIONS	67
<i>Boncho G. Bonev, Emil S. Altimirski, Kliment N. Angelov</i>	
ELECTROMAGNETIC CHARACTERISTICS OF THE “VERY - NEAR - FIELD” REGION OF A SQUARE UNIFORM APERTURE	70
<i>Antoniya Petrova Petrova</i>	
ELECTROMAGNETIC CHARACTERISTICS OF THE “VERY - NEAR - FIELD” REGION OF A CIRCULAR UNIFORM APERTURE	75
<i>Antoniya Petrova Petrova</i>	
PRACTICAL DESIGN OF MICROWAVE DIODE FREQUENCY MULTIPLIERS	80
<i>Mihail Plamenov Tonev</i>	
ELECTROPORATOR FOR LABORATORY TESTS	84
<i>Vytautas Dumbrava, Vladas Juska, Darijus Pagodinas, Marius Gailius, Linas Sidaras</i>	
ARBITRARY WIDTH AND POSITION PULSE TRAINS APPLICATION FOR ULTRASONIC IMAGING: INITIAL STUDY	87
<i>L. Svilainis, A. Aleksandrovas, K. Lukoseviciute</i>	
THE WIDEBAND ULTRASONIC PULSER FOR SONOPORATION	91
<i>L. Svilainis, A. Chaziachmetovas, R. Jurkonis, D. Kybartas, N. Lamanauskas, S. Satkauskas</i>	
ON IMPLEMENTATION OF A NEURAL NETWORK CLASSIFIER FOR SOME CLASSES OF BIOLOGICAL AND MEDICAL PREPARATION IMAGES	94
<i>I. P. Soloviev, N. B. Ampilova, E. Y. Gurevich</i>	
MULTIFRACTAL SPECTRUM AS A CLASSIFICATION SIGN FOR BIOMEDICAL PREPARATIONS IMAGES	98
<i>N. B. Ampilova, I. P. Soloviev, Y. V. Shupletzov</i>	
2-D FILTERS SYNTHESIS USING METHOD OF COMPRESSED COSINES	102
<i>Peter Apostolov, Dimitar Valchev</i>	
PRACTICAL OBJECT TRACKING SYSTEM ON FPGA	106
<i>Rosen Petrov Spirov</i>	
DESIGN OF POWER UNIT OF SYSTEM FOR THERAPY USING “RUNNING” LOW FREQUENCY MAGNETIC FIELD	110
<i>Atanas Dimitrov</i>	
INVESTIGATION ON MOTION OF IONS IN ALIVE TISSUE UNDER INFLUENCE OF TOROIDAL LOW FREQUENCY MAGNETIC FIELD	114
<i>Atanas Dimitrov, Dimitar Dimitrov, Sasho Guergov, Anton Savov</i>	

MEDICAL INFORMATION SYSTEM FOR SELF MONITORING AND DISTANCE CONSULTATION „PATIENT’S DIARY“	118
<i>Simona Lincheva</i>	
EXPERIMENTAL INVESTIGATION ON COMPUTER RESTORATION OF FREQUENCY SPECTRUM OF ECG - SIGNALS IN THE CASE OF INFLUENCE OF NOISE	121
<i>Tzveta Dimitrova, Lidia Jordanova</i>	
A REGION GROWING SEGMENTATION ALGORITHM BASED ON CLAHE AND WAVELET TRANSFORMATION FOR ULTRASOUND IMAGES	125
<i>Veska M. Georgieva</i>	
GUI FOR SEGMENTATION OF MEDICAL IMAGES	128
<i>Veska M. Georgieva, Antonia D. Nankova</i>	
PROCESSING AND TRANSMISSION OF EEG SIGNALS	131
<i>Dejan Milev</i>	
METHOD AND SYSTEM FOR REMOTE MONITORING MULTIPLE MEDICAL PARAMETERS	134
<i>Dejan Milev</i>	
CREATING A WEB SITE FOR MEDICAL EQUIPMENT	137
<i>Silvia Bankova</i>	
EUROPEAN CENTRE FOR PROJECT/INTERNSHIP EXCELLENCE	141
<i>Nuno Escudeiro, Paula Escudeiro</i>	

AUTHOR INDEX

ADOMKUS, T.	46	KADHIM, Y.	34
AL-DAHASH, A.	38	KALLITSIS, E.	53
ALEKSANDROVAS, A.	87	KARAKASILLOTIS, A.	53
ALI, R. N.	38	KIOKES, G.	1,8,26
ALTIMIRSKI, E.	67	KLIROS, G. S.	8,30
AMPILOVA, N.	94,98	KODEARY, A.	34
ANGELOV, K.	67	KOLEV, N.	42
APOSTOLOV, P.	102	KOUTRAS, I.	5
BANKOVA, S.	137	KYBARTAS, D.	23,91
BARTZAS, A.	5	LAMANAUSKAS, N.	91
BONEV, B.	64,67	LINCHEVA, S.	118
BOULTADAKIS, G.	53	LUKOSEVICIUS, A.	23
BRŪZGIENĖ, R.	12,46	LUKOSEVICIUTE, K.	87
CHAZIACHMETOVAS, A.	91	MALAMOU, A.	50,53
DEMIREV, V.	57,61	MILEV, D.	131,134
DIMITROV, A.	110,114	MITSEV, TS.	19,42
DIMITROV, D.	114	NANKOVA, A.	128
DIMITROV, K.	42	NARBUTAITE, L.	12,46
DIMITROVA, TZ.	121	PAGODINAS, D.	84
DUMBRAVA, V.	23,84	PANDIS, C.	50
ESCUDEIRO, N.	141	PETROVA, A.	70,75
ESCUDEIRO, P.	141	PITKEVICIUS, V.	23
FRANGOS, P. V.	50,53	RAPTOPOULOS, A.	5
GAILIUS, M.	84	SATKAUSKAS, S.	91
GARBI, A.	5	SAVOV, A.	114
GEORGIEVA, V.	125,128	SHUPLETZOV, Y.	98
GKONIS, P.	1,26	SIDARAS, L.	84
GUERGOV, S.	114	SOLOVIEV, I.	94,98
GUREVICH, E.	94	SOUDRIS, D.	5
HATZIARGYRIOU, N.	8	SPIROV, R.	106
IVANOV, HR.	19,42	STEFANEAS, P.	50
JASSIM M.	34	SVILAINIS, L.	23,87,91
JORDANOVA, L.	121	TONEV, M.	80
JURKONIS, R.	91	UZUNOGLU, N.	1
JUSKA, V.	84	VALCHEV, D.	15,102
KAČERGINSKIS, E.	12	ZOUNTOURIDOU, E.	8

SIMULATION MODELLING AND ANALYSIS OF PHYSICAL LAYER CODING SCHEMES FOR V2X APPLICATIONS

George Kiokos¹, Panagiotis Gkonis², Nikolaos Uzunoglu³

¹ Hellenic Air-Force Academy, Dekeleia, Attica GR-1010, Greece

^{2,3} National Technical University of Athens, Iroon Politechniou 9, Athens, Greece

¹ Tel. +306937027669; e-mail. gkiokos@iccs.gr

^{2,3} Tel. +302107722289; e-mail. ²pgkonis@esd.ntua.gr, ³nuzu@cc.ece.ntua.gr

Abstract

This paper provides a comprehensive investigation of the performance and practical implementation issues of two coding schemes, employing Turbo Codes and low-density parity-check (**LDPC**) codes, over vehicular ad-hoc networks based on IEEE 802.11p specifications. Using simulation authors present the results of an evaluation of system performance for the two different coding schemes. We concentrate our evaluation on two different environments Rayleigh Fading and Weibull Fading. BER (Bit Error Rate) and SNR (Signal to Noise Ratio) values for BPSK modulation are examined and tested.

1. INTRODUCTION

Effective use of an Intelligent Transportation System (ITS) cannot only improve vehicular safety but also enhance the efficiency of current transport systems and driving comfort. Dedicated short-range communications (DSRC) system is a critical component of ITS for the future transport telematic services. This demand leads to wireless access for vehicular environments (WAVE), which is also regulated by the IEEE 802.11p standard [1]. In **American Society for Testing and Materials** (ASTM) 2213-03 standard, IEEE 802.11 and 802.11a are modified as a medium access control (MAC) and physical layer (PHY) specifications, respectively, for the DSRC system. In 1949, Claude Shannon developed a result that has become one of the fundamental theorems of coding theory. In his analysis he quantified the maximum theoretical capacity for a communications channel, the Shannon limit, and indicated that error-correcting channel codes must exist that allowed this maximum capacity to be achieved. In [2] Irving Reed and Gus Solomon published a paper which describes a new class of error-correcting codes that are now called Reed-Solomon (RS) codes. RS codes are the most popular class of block codes. In today's systems, convolutional codes are the most widely used channel codes. They owe their popularity to good performance and flexibility to achieve different coding rates. Block codes are different from convolutional codes in the sense that the code has a definite code word length n , instead of a variable code word length. In 1993

Berrou, Glavieux and Thitimajshima [3] proposed "a new class of convolution codes called turbo codes whose performance in terms of Bit Error Rate (BER) are close to the Shannon limit". IEEE 802.11p Physical Layer (PHY) standard intends to support road transport, traffic applications and public safety over roadside and high-speed mobile units, or between high-speed vehicles. Researches have shown that multiple propagation paths or multipaths have both slow and fast aspects. The received signal for narrowband excitation is found to exhibit three scales of spatial variation such as Fast Fading, Slow Fading and Range Dependence. Moreover temporal variation and polarization mixing can be present.

This paper provides a comprehensive investigation of the performance for two different coding schemes (LDPC codes and Turbo codes), over vehicular ad-hoc networks for Rayleigh and Weibull fading channels.

2. LDPC CODES VS TURBO CODES

In information theory, Low-Density Parity-check codes [4] are a sub-class of linear error correcting coding schemes, which are methods of transmitting messages over noisy transmission channels. LDPC codes can be described as the null space of a sparse $\{0,1\}$ check matrix as well as by a bipartite graph, Tanner graph, which represents the rows and columns of the parity-check matrix. A generic LDPC decoder architecture is shown in Figure 1. It comprises K_u shared variable nodes units (VNU),

K_c shared check variable nodes units (VNUs), K_c shared check nodes units (CNU) and a shared memory fabric used to communicate messages between VNUs and CNU. The computing operations taking place in each iteration are part of the min-sum decoding algorithm, while is a type of iterative message-passing decoding, also proposed as an approximation to the belief propagation (BP) algorithm. It is also referred to as the BP-based algorithm. The min-sum algorithm is a soft-decision, iterative algorithm for decoding binary-LDPC codes and is commonly used due to its simplicity and good BER performance. During the process, each decoding iteration consists of updating and transferring extrinsic messages between neighboring variable nodes and check nodes.

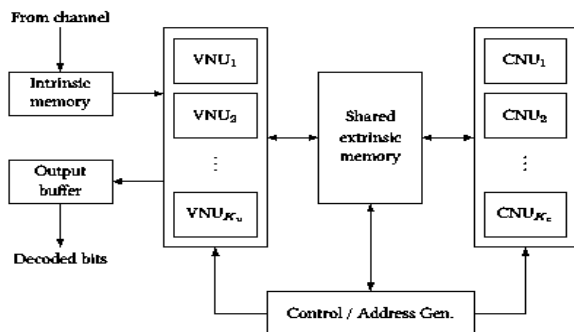


Figure 1. Generic LDPC decoder

A Turbo encoder [5] consists of two (or more) systematic block codes (Fig. 2). In a simplified Turbo encoder, there are two convolutional encoders in parallel. The interleaver is a key component of a Turbo encoder that guarantees excellent bit error rate and frame error rate performances.

A key development in Turbo codes is the iterative decoding algorithm. In the iterative decoding algorithm, decoders for each constituent encoder take turns operating on the received data. Each decoder produces an estimate of the probabilities of the transmitted symbols. The decoders are thus soft output decoders. Probabilities of the symbols from one decoder, known as extrinsic probabilities, are passed to the other decoder (in the symbol order appropriate for the decoder), where they are used as prior probabilities. The decoding algorithm thus passes probabilities back and forth between the two decoders, with each one combining the evidence it receives from the incoming prior probabilities with the parity information provided by the code. After a number of iterations, the decoding process converges to an estimate of the transmitted codeword.

The algorithm most commonly used for soft-decision decoding is the maximum a-posteriori proba-

bility (MAP) algorithm, also commonly known as the BCJR algorithm

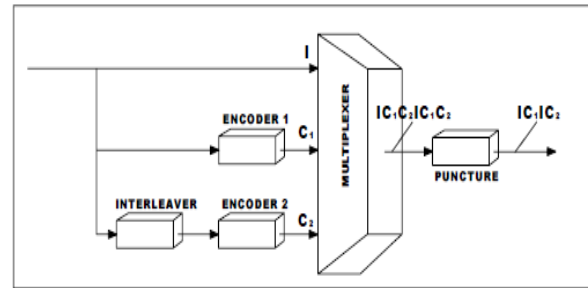


Figure 2. Block diagram of Turbo encoder

3. FADING TYPES FOR V2X COMMUNICATIONS

One of the most important problems that appears in vehicular communications is the multipath fading. This effect is causing a fluctuation in the received signal. To reduce or solve this problem we need to be able to predict this fading effect. There are two channel models for V2X communications that can be found in the literature in order to describe the multipath fading. The first propagation model [6] is proposed in the IEEE draft standard [7] and the distribution functions which can be used for modelling and designing it are either Rice or Rayleigh, with Doppler influence. The second model, presented in [8], takes into account two particularities of the mobile-to-mobile propagation channel : the inter-tap correlation and the nonstationarity modeled by a first order two-state Markov chain. In addition, the tap amplitudes are Weibull distributed. In the next paragraphs we introduce Rayleigh and Weibull distribution functions which can be used for describing the multipath fading.

3.1. Weibull distribution

The primary advantage of Weibull analysis is the ability to provide reasonably accurate failure analysis and failure forecasts with extremely small samples. Another advantage of Weibull analysis is that it provides a simple and useful graphical plot of the failure data. The Weibull distribution is often used to model the time until failure of many different physical systems. The Probability Density Function (PDF) and the Cumulative Distribution Function (CDF) of Weibull is:

$$PDF(x) = \frac{k}{\lambda} \left(\frac{x}{\lambda} \right)^{k-1} e^{-(x/\lambda)^k}, \quad CDF(x) = 1 - e^{-(x/\lambda)^k}$$

where $k > 0$ is the shape parameter and $\lambda > 0$ is the scale parameter of the distribution. The Weibull shape parameter can take values between 0 and ∞ . For $k=1$ the Weibull distribution is identical to the exponential distribution, while for $k=2$ the Weibull distribution is identical to the Rayleigh distribution.

3.2. Rayleigh distribution

The Rayleigh distribution is a special case of the Weibull distribution and is often observed when the overall magnitude of a vector is related to its directional components. This distribution represents the worst fading case because we do not consider to have Line-of-Sight (LOS). The power is exponentially distributed. The phase is uniformly distributed and independent from the amplitude. The PDF and the CDF for the Rayleigh distribution is:

$$PDF(x) = \frac{x}{\sigma^2} \exp\left(-\frac{x^2}{2\sigma^2}\right), \quad CDF(x) = 1 - e^{-\frac{x^2}{2\sigma^2}}$$

where: x is the received signal envelope voltage, σ is the rms value of received voltage before envelope detection, σ^2 is the time average power of received signal before envelope detection.

4. SIMULATION RESULTS

In order to evaluate the coding options presented in the previous sections a full system model of 802.11p PHY was implemented in Matlab – Simulink, employing LDPC code and Turbo code. We have estimated Bit Error Rate (BER) versus Signal-to-Noise Ratio (E_b/N_0). For the performance evaluation of the Turbo codes we use a recursive systematic convolutional code with constraint length $K=3$ and specific frame size. The model generates Turbo code, and decodes the code iteratively (10 iterations) using MAP detectors.

Log-Domain [9] technique was used for the decoding of LDPC codes. The comparison was performed for BPSK modulation and the relative vehicular velocity was 50 km/h. The distance which the measurements took place was 200m for the path between transmitter and receiver. For the Weibull fading according authors at [8] the shape factor was found 3.95 for small cities. We assumed 400 ns RMS delay spread. The Doppler spread was found 268 Hz. The rate of both codes is $R = 1/2$. Figure 3 shows the performance of Turbo codes and the LDPC codes for Rayleigh fading channel

with iterations one and ten respectively. Figure 4 shows the performance in Weibull path. Our simulation results for Rayleigh environment have shown that with LDPC scheme the performance was slightly better than the Turbo coding chain especially in the range between 0.5 to 3 dB. After that the two coding schemes performs equal. Regarding the second case over Weibull fading channel, our results have shown that performance obtained by LDPC coding is better than the Turbo coding by 0.5 dB in the 1st and the same in the 10th iteration.

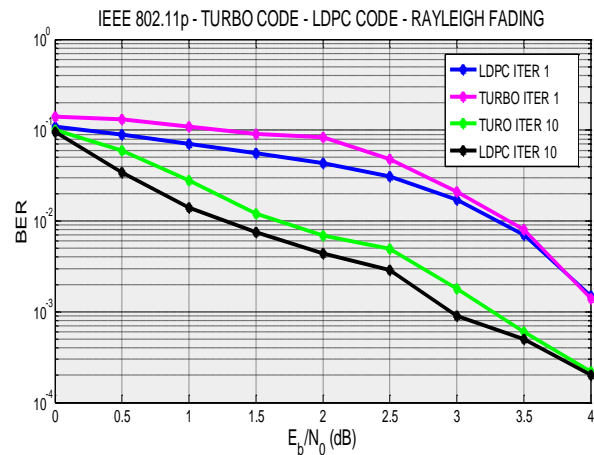


Figure 3. Simulation results for Rayleigh fading

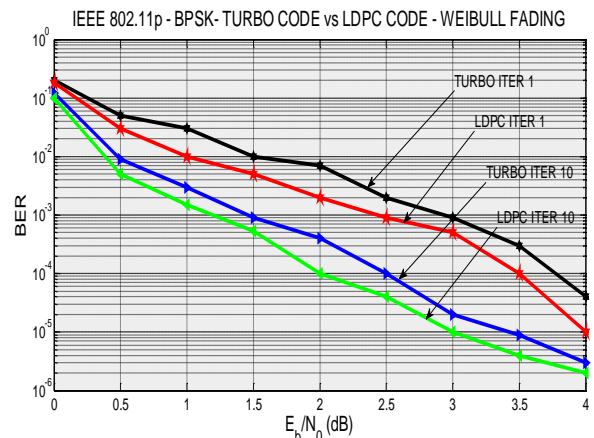


Figure 4. Simulation results for Weibull fading

5. CONCLUSION

This article presents the performance evaluation results of a comparative study for IEEE 802.11p PHY employing two different coding schemes, LDPC coding and Turbo coding. From the obtained simulation results, the BER vs SNR for BPSK modulation scheme in Rayleigh fading channel and in Weibull fading channel is calculated. In our evaluation, we have explored Turbo codes and LDPC codes and we came to the conclusion that LDPC codes tend to outperform the other coding scheme

especially in low and middle E_b/N_0 values. The results presented in this paper show that in difficult environmental cases both codes achieved significant improvement in our propagation conditions.

References

- [1] Weidong Xiang, Yue Huang, Sudhan Majhi 'The Design of a Wireless Access for Vehicular Environment (WAVE) Prototype for Intelligent Transportation System (ITS) and Vehicular Infrastructure Integration (VII)', Department of ECE, Michigan University, Vehicular Technology Conference, 2008. VTC-2008 Fall. 2008
- [2] Reed, I. S. and Solomon, G., "Polynomial Codes Over Certain Finite Fields," SIAM Journal of Applied Math., vol. 8, 1960, pp. 300-304.
- [3] Berrou, A. Glavieux, and P. Thitimajshima, Near Shannon limit error-correcting coding and decoding, in Proc. of ICC, Geneva, Switzerland, May 1993, pp. 1064–1070.
- [4] R. G. Gallager, "Low density parity check codes" IREY Transaction Information Theory, vol IT-8, pp. 21-28, Jan. 1962
- [5] W. Stallings, "Coding and Error-Control," Chapter 8 of Wireless Communications and Networks, Prentice Hall, Inc. New Jersey 2002
- [6] G. Acosta and M. A. Ingram, "Six time- and frequency-selective empirical channel models for vehicular wireless LANs," 1st IEEE International Symposium on Wireless Vehicular Comm., 2007
- [7] IEEE P802.11p/D0.26, Jan. 2006, "Part 11: Wireless LAN Medium Access Control (MAC) and Physical Layer (PHY) Specifications, Amendment 3: Wireless Access in Vehicular Environments
- [8] I. Sen and D. W. Matolak, "Vehicle-vehicle channel models for the 5-GHz band," IEEE Trans Intelligent Transportation Systems vol. 9, 2008, pp.235–245
- [9] Wymeersch, H.; Steendam, H.; Moeneclaey, M.; Log-domain decoding of LDPC codes over GF(q) IEEE ICC 2004 Volume: 2 Publication Year: 2004 , Page(s): 772 - 776 Vol.2

NEPHRON+: ICT-ENABLED WEARABLE ARTIFICIAL KIDNEY AND PERSONAL RENAL CARE SYSTEM

Anastasia Garbi¹, Andreas Raptopoulos¹, Ioannis Koutras^{1,2}, Alexandros Bartzas^{1,2}
and Dimitrios Soudris²

¹ EXODUS S.A. 11527 Athens, Greece

Emails: {arap | anastasia}@exodussa.com, {ioannis.koutras | alex.bartzas}@gmail.com

² National Technical University of Athens, 15780, Athens, Greece

Email: dsoudris@microlab.ntua.gr

Abstract

Traditional haemodialysis treatment for renal patients is known to be a suboptimal approach, although the only one tested and proven in the absence of transplantation options. We present the data management and analysis aspects of a design for an ICT-enabled wearable renal support device, offering personalized care to patients outside a hospital setting. The device features real-time functional adaptation based on sensor readings. It is supported by a mobile application as well as a clinical-back-end application; all of them communicating wirelessly to exchange control signals and patient data.

1. INTRODUCTION

NEPHRON+ will provide a major leap forward in Renal Care. It aims at a next generation, integrated solution for personalized treatment and management of patients with chronic renal failure. It presents an ideal solution for continuous dialysis outside the hospital offering better blood clearance, while patients can stay mobile and active in social and economic life. It relies on an ICT-enabled wearable artificial kidney for on-body blood purification [1].

2. THE SYSTEM

NEPHRON+ is based on realizing that the clearance rate of haemodialysis could be improved drastically if the dialysis operation can be performed continuously and matched to individual conditions and context. Continuous dialysis driven by monitoring and adjustment of the treatment is necessary, so that blood parameters constantly remain within normal ranges – thus, avoiding large peaks and rapid falls. This improved treatment results in improved well-being and quality of life of the patient and reduces the relative burden and costs imposed on the medical care system. A high-level view of the system is shown in Figure 1.

The project makes use of innovative ICT technologies, new micro-sensor principles and nanofiltration materials, medical knowledge in embedded and remotely operated analysis algorithms, safe low-power wireless connections and well-accepted

consumer devices such as blood pressure devices, with a purpose to build a system that offers controlled and personalized renal treatment outside a clinical setting.

The NEPHRON+ system consists of:

1. A Wearable Artificial Kidney Device (WAKD) for real-time treatment adaptation, accurate monitoring and purification of blood, enabled by a smart configuration of available and newly developed ICT components including:
 - Multiparametric monitoring via a set of bio-micro-nanosensors embedded in the device to measure potassium, sodium, urea, blood pressure and temperature;
 - An artificial nanofiltration component, providing sophisticated blood purification based on nanofiltration, which removes not only the small molecule toxins (salts, urea) as in traditional haemodialysis but also the middle molecules (such as β 2-microglobulin) and the protein bound toxins;
 - Embedded software for data fusion and adaptive control;
 - Secure low-power wireless connectivity.
2. Wearable on-body sensors, including ECG/ blood pressure/ body posture & activity ones.
3. A personal renal-care application for the patient, to be used in a mobile device (such as a smartphone or a tablet PC).
4. A clinical back-end renal care application that supports clinical personnel to remotely monitor

and reconfigure treatment based on receiving patient data at constant intervals throughout each day.

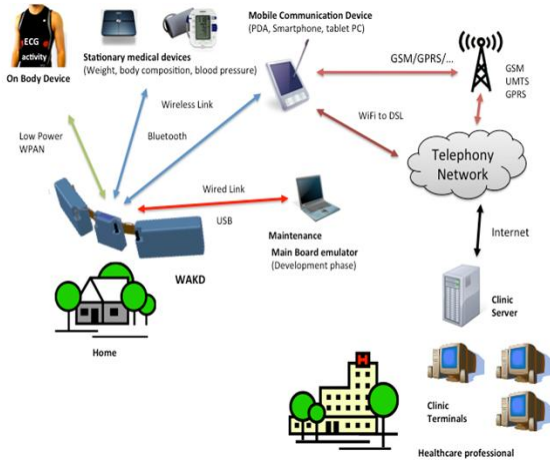


Figure 1: High level view of NEPHRON+ system

3. WAKD

The various sensors integrated within the WAKD perform measurements and produce the information on which the system's concepts and operation are based. The collected data is transferred to the WAKD control unit where the autonomous WAKD embedded software controls the dialysis process [2]. The computed values, which are extracted from the data, are used for the adaptive control of the device's function. Especially the primary function of the WAKD device, i.e. the filtration of blood, is adapted according to actual measurements. If certain predefined patterns are observed in the acquired data, notifications and alarms towards the patient and treating physician are triggered; or advice is displayed on the available screens, to initialize manual corrective measurements.

4. SMARTPHONE APPLICATION

The Smartphone/Mobile application will enable the patient, through a friendly User Interface (UI) to interact with the WAKD as well as provide information and feedback to the Clinical Back-end. More specifically, the patient will be able to receive information regarding the status of his/her disease, to safely control some functionality of the device (e.g. ultrafiltration rate etc.), to answer various questionnaires in order to provide input for his/her condition, as well as to receive alarms and reminders for remarkable variations of his/her measurements and upcoming events respectively. The UI takes care of plotting diagrams and visualizing information over-

all, but does not perform any data transformations. For instance, if a histogram is to be produced, value frequencies are calculated by the main application, and produced data is sent to the UI – which then draws diagrams and shows them to the user.

5. CLINICAL BACK-END

The main idea behind the clinical backend infrastructure is to be realized as a centralized horizontal platform on which relevant applications (vertical features) and functionalities will be implemented. This part of the system will allow the management of patients with renal disease, which includes: wireless retrieval of data produced by NEPHRON+ sensors and stored in the NEPHRON+ device; their analysis and monitoring as well as processing of the patient data for the decision making procedure on the various stages of the disease; the appropriate reconfiguration of the NEPHRON+ recognition of alarm situations and to adapt the treatment accordingly; to organize tasks of the various specific roles of clinicians within the workflow; or to manage medications and refills.

6. COMMUNICATIONS

NEPHRON+ is a complicated system combining components of different nature and scope. Thus in order to connect these various types of components a wide variety of protocols for guaranteeing stable, secure (e.g., HTTPS, SSL etc.) and reliable (e.g., SLIP) connections are applied. An overview of the various communication routes and the wireless technology employed is illustrated in Figure 2.

6.1. WAKD Physical Communications

The device will be wirelessly connected to several external devices, via two types of wireless technologies:

1. Standard Bluetooth technology will provide connection to Mobile Communication device/ Smart Phone, as WAKD device control and monitoring facility. Two Bluetooth Profiles will be considered for this purpose.
2. Bluetooth Low Energy technology will provide connection to On Body Sensor Device. The most significant available profile will be used for this purpose.

In order to keep the system as modular as possible on the hardware level as well as on the soft-

ware level, a specific board that handles both wireless technologies will be provided, its named in the rest of the document as the Communication Board. This will abstract different communication protocols for the rest of the system. The wireless communication will be fully transparent for the WAKD on the Data/Application level.

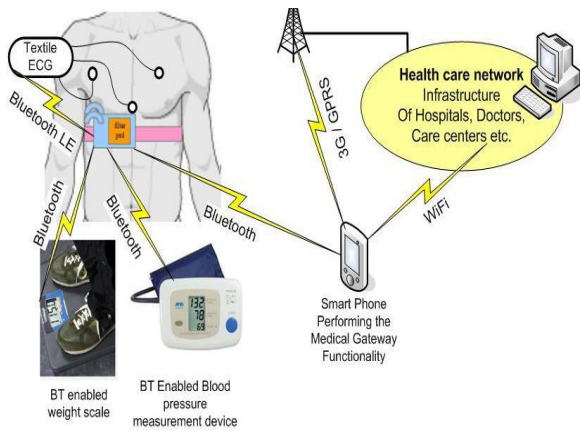


Figure 2: Supported communication routes with WAKD

6.2. Message Structure

The messages exchanged between the various parts of the system are composed of two main parts: 1) The Header that contains descriptive information on the scope of the sender of the message and 2) the payload that maintains the actual data. All the messages are transmitted in a binary format and their translation is performed internally in each application. As it was mentioned above, the communication between the WAKD and the Smartphone is done via Bluetooth and the communication between the Smartphone and the Back-end by using SOAP web services, however, the structure described is used by all sides.

The Header is a six bytes structure and it is divided in five fields:

1. *recipiendId*: One byte field that indicates the destination of the packet. The possible destinations of the packets are either the Smartphone or the Back-end.
2. *msgSize*: Two-byte field which indicates the size of the packet. The scope of this field is to recognize the where the packet ends.
3. *dataId*: One-byte field indicating the type of the message exchanged. The possible types of packets will be mentioned later in this section.
4. *msgCount*: One-byte field indicating the number of messages sent.
5. *issuedBy*: One-byte field indicating the source of the message.

The Payload part differs based on the command given and its size is defined by the *msgSize* field of the header.

The type of messages that could be exchanged between the WAKD and the rest of the NEPHRON+ system are the following:

1. Send an alarm/notification from the WAKD to the Smartphone application or the Back-end application.
2. Request from the Smartphone for the current configuration parameters from the WAKD.
3. Trigger WAKD state change.
4. Request WAKD state.
5. WAKD sends current status to the Smartphone.
6. Configuration of WAKD parameters (e.g. patient profile, thresholds).
7. WAKD sends the measurements' values to the WAKD

Each of these types of commands is characterized from a different ID found in the *dataId* field of the header file in order for the receiver to recognize the command and read the data of the packet.

7. CONCLUSIONS

The NEPHRON+ is an innovating project aiming to bring new ways of treatment in Renal Care. By combining clever self-adjusting algorithms, sensing technologies, as well as the latest trends in application development presents a solution for reducing treatment costs and improving the quality of patients' life. The project, which is in its third year, has completed the first phase of integration and system development and it is now on preparations for the initial trials in animals.

8. ACKNOWLEDGMENTS

The research leading to these results is supported by the European Community's Seventh Framework Programme FP7/2007-2013) /Objective/ Personal Health Systems" and the NEPHRON+ Project under grant agreement no.248261.

References

- [1] www.nephronplus.eu
- [2] L. Pielawa, F. Poppen, A. Hein; "Virtual Prototype of a Personal Medical Device – Simulation of a Multi Nature System"

ENERGY CONSUMPTION ANALYSIS OF WIRELESS ACCESS TECHNOLOGIES FOR V2G COMMUNICATIONS

George C. Kiokas¹, Erietta I. Zountouridou², George S. Kliros³, Nikolaos D. Hatziaargyriou⁴

^{1,3}. Hellenic Air-Force Academy, Dekeleia, Attica GR-1010, Greece

^{2,4}. National Technical University of Athens, Iroon Politechniou 9, Athens, Greece

^{1,3}. Tel. +302108193399; e-mail. gkiokas@iccs.gr, gskliros@ieee.org

^{2,4}. Tel. +302107723696; e-mail. erietta@power.ece.ntua.gr, nh@power.ece.ntua.gr

Abstract

Vehicle-to-Grid (V2G) technology can be used to interconnect electric or plug in hybrid vehicles with the power grid by either delivering electricity and level peak demands or by throttling their charging rate. Two types of wireless communications are required to a V2G system. The communications between the Aggregator, an intermediate entity, and the Control Center which will be realized through IEEE 802.16-2004 (802.16d) and between Aggregator and the Electric Vehicles which will be realized through vehicular communications (IEEE 802.11p). In this paper the two wireless communication protocols, needed for the V2G system to operate, are presented and evaluated, taking into consideration the energy consumption.

1. INTRODUCTION

V2G concept is based on the fact that most vehicles are parked an average of 95 percent of their time, so their batteries could be used to let electricity flow from the vehicles to the power lines and back. The introduction of V2G concept has been the subject of several publications [1], [2]. Electric vehicles can be connected to the electric network either in the residences of their holders, either in public spaces such as underground parking stations, airports, commercial centers etc., participating this way in power market and more specifically, depending their contract, to the peak power, ancillary services and regulation power market.

IEEE 802.16-2004 (802.16d) WiMAX [3] allows for an efficient use of bandwidth in a wide frequency range and can be used as a last mile solution for broadband internet access. IEEE 802.11p standard is being considered as a promising wireless technology for enhancing transportation safety and provides safety related services like collision avoidance and emergency breaking.

The main contribution from this paper is the energy consumption analysis and evaluation of IEEE 802.11p for the communication between the Aggregator and the EVs. and WiMAX for the communication link between Control Center to Aggregator.

2. V2G ARCHITECTURE DESIGN

The V2G concept operates when a vehicle is parked, plugged in to the electricity grid and acces-

ses a broadband connection. The V2G wireless communications architecture is shown in Fig. 1.

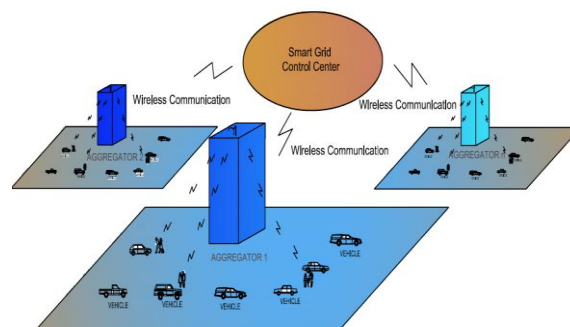


Figure 1. V2G Wireless Communication Architecture

The real time information is exchanged among the Control Centre, the Aggregator and vehicles, and the security requirements consist of source authentication, message integrity, replay attack resistance, and privacy protection. The V2G communication have the crucial requirements of fast authentication and encryption/ decryption, high bandwidth, low latency, interoperability, high reliability and accuracy and non-restrictive distance limits [4].

3. WIRELESS PROTOCOLS

The IEEE 802.16 standard was firstly designed to address communications with direct visibility in the frequency band from 10 to 66 GHz. The last revision of this specification is better known as IEEE 802.16-2004. The WiMAX standard defines the air interface for the IEEE 802.16-2004 specification working in the frequency band 2-11 GHz. IEEE

802.11p standard is being considered as a promising wireless technology for enhancing transportation safety and provides safety related services like collision avoidance and emergency breaking. At first this includes data exchange between high-speed vehicles and between the vehicles and the roadside infrastructure in the licensed ITS band of 5.9 GHz.

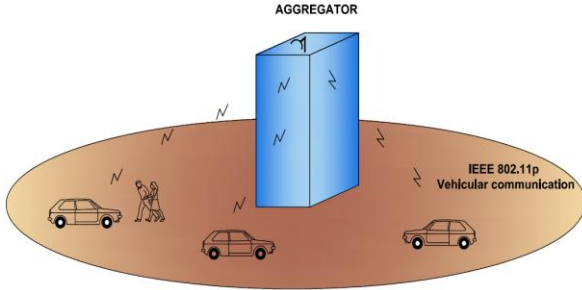


Figure 2. V2G IEEE 802.11p Communication scheme

4. ENERGY CONSUMPTION

The global Information and Communication Technology (ICT) industry is a fast growing contributor to the world wide greenhouse gas emissions, currently it has a footprint of about 2%. More importantly, this number is expected to grow drastically in the coming years. According authors at [5] the energy consumption of terminals is negligible with respect to the energy consumptions of the networks. Consequently, this study is focused on the base stations since the terminals in vehicular communications are placed in vehicles and powered from their batteries.

The power consumption of the entire base station in Watt will be:

$$P_{el} = n_{sector} \cdot (P_{EL/AMP} + P_{EL/TRANS} + P_{EL/PROC} + P_{EL/RECT}) + P_{EL/MICRO} + P_{EL/AIRCO} \quad (1)$$

with n_{sector} the number of sectors in the cell, $P_{EL/AMP}$ the power consumption of the power amplifier, $P_{EL/TRANS}$ the power consumption of the transceiver responsible for receiving and sending of signals to the terminals stations), $P_{EL/PROC}$ the power consumption of the digital signal processing responsible for system processing and coding, $P_{EL/RECT}$ the power consumption of the rectifier, $P_{EL/MICRO}$ the power consumption of the microwave link responsible for communication with the back-haul network, $P_{EL/AIRCO}$ the power consumption of the air conditioning.

The values of the WIMAX and IEEE 80211.p base station equipment can be found in Table 1. These values are retrieved from data sheets of various manufacturers of network equipment.

Table 1. Power consumption for the equipment of the base station

Equipment	IEEE 802.16d	IEEE 802.11p
Power Amplifier	100 W	80 W
Transceiver	100 W	45 W
Digital signal processing	380 W	300 W
Rectifier	80 W	80 W
Microwave link	90 W	70 W
Air conditioning	600 W	400 W

4.1. Range calculation

The next step for the determination of energy consumption of the wireless access technologies is to set up a link budget in order to relate the power consumption with the maximum wireless range of the base station. A link budget is the accounting of all of the gains and losses from the transmitter, through the medium (free space, cable, waveguide, fiber, etc.) to the receiver in a telecommunication system. Firstly, there is a need to calculate the maximum path loss PL_{max} (in dB) to which a transmitted signal can be subjected while still being detectable at the receiver. To determine the maximum path loss (PL_{max}) the parameters of [3],[6] were taken under consideration. Once the maximum path loss PL_{max} is known, the range in metres by using a path loss model can be determined

Firstly, a path loss PL_{med} function for WIMAX Erceg C model and in continuation for 802.11p model is given. For a given close-in reference distance d_0 , the median path loss (PL in dB) is given by the following equation

$$PL_{MED} = A + 10\gamma \log_{10} \frac{d}{d_0} + s \quad \text{for } d > d_0 \quad (2)$$

where $A = 20\log_{10}(4\pi d_0/\lambda)$, (λ is being the wavelength in m), γ is the path-loss exponent with $\gamma = (a - b \cdot h_b + c/h_b)$ for h_b between 10m and 80m (h_b is the height of the base station in m), $d_0 = 100m$ and a, b, c are constants dependent on the terrain category. The path loss model with the correction terms would be

$$PL_{mod} = PL + \Delta PL_f + \Delta PL_h \quad (3)$$

where PL is the path loss given in (2), ΔPL_f (in dB) is the frequency correction term given by

$$\Delta PL_f = 6 \log_{10}(f/2000) \quad (4)$$

where f is the frequency in MHz, and ΔPL_h (in dB) is the receive antenna height correction term given by

$$\Delta PL_h = -10.8 \log_{10}(h/2) \quad (5)$$

for Categories A and B

$$\Delta PL_h = -20 \log_{10}(h/2) \quad (6)$$

for Category C, where h is the receiver antenna height between 2m and 10m. For the 801.11p, we examine the case where the vehicle has no eye contact with the Aggregator's antenna, for example when the EVs are parked in underground parking stations. The log-distance path loss model is employed and the equation is:

$$PL_{MED} = PL_0 + 10\gamma \log \frac{d}{d_0} + X_g \quad (7)$$

where PL_{MED} is the total path loss measured in Decibel (dB), PL_0 is the path loss at the reference distance d_0 , d is the length of the path, d_0 is the reference distance, usually 1 km, γ is the path loss exponent, X_g is the normal random variable with zero mean, reflecting the attenuation caused by flat fading. In case of no fading, this variable is 0. In case of only shadow fading or slow fading, this random variable may have Gaussian distribution with standard deviation in dB, resulting in log-normal distribution of the received power in Watt.

5. RESULTS

This section provides computation results in order to evaluate power consumption with range dependence of the two wireless communication protocols in the V2G environment. In the most simple situation, the base station uses only one antenna for transmission and the mobile station uses only one antenna for receiving. The number of sectors was set to two Regarding the communication link between the Aggregator and the Control Center, we used the Erceg C model with the middle category (Category B). The operating frequency was set at 3.5 GHz with $\frac{1}{4}$ cycle prefix, 3.5 MHz channel bandwidth, transmitter antenna height is 30m and we considered 10m antenna height for receiver. The shadowing margin which depends on the standard deviation of the path loss model was found 12 dB. For the link between the Aggregator and the EVs

the operating frequency was set to 5.9 GHz with 400 ns RMS delay spread. Figure 3 shows the power consumption of the base station (P_{el}) needed from the electricity grid (in Watt) as a function of the range R (in metres) for the 802.16d and 802.11p technologies respectively. The power consumption of Wimax is higher than the 802.11p because of the different power consumption of the equipment and the different range of the base station.

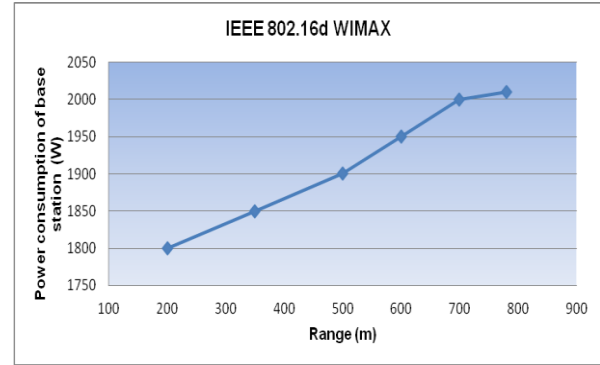


Figure 3. Power consumption vs Range for Wimax

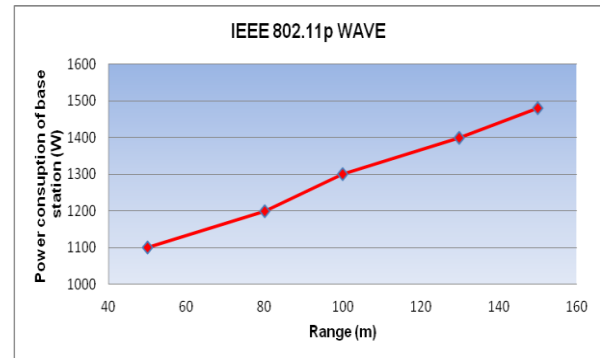


Figure 4. Power consumption vs Range for IEEE 802.11p

6. CONCLUSIONS

This article presents the power consumption evaluation of two different wireless communication protocols enabling the Control Center-to-Aggregator and the Aggregator-to-Evs communication respectively. As a first step in the evaluation Fixed WIMAX was explored for communication between Control Center-to- Aggregator at 3.5 GHz. Erceg C model was used to describe the path loss attenuation. As a second step, 802.11p standard was tested in N-LOS paths representing parked vehicles in underground stations. Log-distance path loss model was used to describe the path loss attenuation. Our results have shown that the power consumption is related to the coverage of their base stations and at the maximum range is higher than the power consumption at the minimum range.

References

- [1] P.Lopes, F.Soaes, P. Almeida, "Integration of Electric Vehicles in the Electric Power System", Proceedings of the IEEE, Volume 99, Issue: 1 pp. 168 – 183, 2011
- [2] Yonghua Song; Xia Yang; Zongxiang Lu; , "Integration of plug-in hybrid and electric vehicles: Experience from China," Power and Energy Society General Meeting, 2010 IEEE , vol., no., pp.1-6, July 2010
- [3] IEEE std 802.16 -2004 (Revision of IEEE std 802.16-2001, IEEE, Part 16: Air Interface for Fixed Broadband Wireless Access Systems, 2004
- [4] Huaqun Guo, Fan Yu, W. C. Wong, Vivvy Suhendra, and Y. D. Wu.. "Secure wireless communication platform for EV-to-Grid research". 6th International Wireless Communications and Mobile Computing Conference (IWCMC '10). New York, USA
- [5] Margot Deruyck, Emmeric Tanghe, Wout Joseph, Luc Martens 'Modelling and optimization of power consumption in wireless access networks' ELSEVIER Computer Communications 2036-2046.
- [6] IEEE P802.11p/D0.26, Jan. 2006, "Part 11: Wireless LAN Medium Access Control (MAC) and Physical Layer (PHY) Specifications, Amendment 3: Wireless Access in Vehicular Environments

NETWORK PLANNING AND QOS SIMULATION SOFTWARE DESIGN FOR 4TH GENERATION BROADBAND WIRELESS TECHNOLOGIES

Lina Narbutaitė
Rasa Brūzgienė
Eugenijus Kačerginskis

Kaunas University of Technology
Department of Telecommunications
Studentų str. 50-452, Kaunas, Lithuania, LT- 51368
E-mail: eugenijus@ntservice.eu

Abstract

Mobile network design is complex task that requires evaluation of many parameters that allow service providers to plan optimal network coverage and select mobility management solutions. It's especially relevant for such new technologies as LTE or mobile WiMAX, where ability to simulate network behavior is very important before starting real network implementation. This article presents software that was designed for 4th generation broadband wireless network planning, QoS simulation and analysis. Software consists of three major modules that allow estimating wireless propagation for different modulation techniques, simulating wireless protocols, estimating base station distribution and calculating cumulated data traffic in different types of overlapping wireless sectors. Article analyzes software functionality, operation algorithms, demonstrates possible network planning and simulation scenarios.

1. INTRODUCTION

4Th generation broadband wireless technologies, such as mobile WiMAX and LTE are entering Telco markets, offering newest and most innovative technologies that allow to meet growing demand for mobility and data throughputs. The main goal is to achieve quality similar to wired technologies, enabling seamless use of VoIP, Video and data download services. Despite standards state very high efficiency of 4th generation technologies, it's not easy to achieve it real world environment.

One of the biggest challenges for service providers is to plan and implement such networks, because it requires evolution of many complex solutions, from network planning at the start to QoS modeling at the end. These tasks must be performed at the most possible detail manner in order to achieve best solution optimizing QoS, CAPEX and OPEX.

These major tasks must be performed by network implementation team:

- network equipment selection and base station coverage estimation, enabling services providers to decide what services are possible in certain areas and what equipment is requires to achieve desired data throughputs.
- simulation of wireless protocols that allows to evaluate performance of different services, select solutions for mobility management;

- network coverage planning, that allows to decide what are optimal distances between base stations, minimize zones with overlapping base station coverage and maximize network coverage without gaps and shadow zones.
- Handover overhead estimation, ensuring that designed network will be able to handle multiple users, especially in growing networks.

Automation of these tasks requires very expensive software usually provided by different vendors. It makes network implementation even more complex and time consuming project.

This article provides overview of Authors designed software package that allows service providers to ease network design and implementation tasks. Possible network planning and simulation scenarios are provided. Package consists of three software tools:

- base station (BS) coverage estimation software;
- protocol simulation software;
- network coverage estimation and handover overhead calculation software.

2. BS COVERAGE ESTIMATION

Base station coverage estimation software allows predicting radio signal attenuation in different line of sight and non-line of sight environments. It utilizes four mathematical models that can be used for coverage estimation in urban, suburban and

rural areas: Direct line of sight, Walfish-Ikegami, Walfish-Ikegami geometrical and Stanford University Interim (SUI) models [1]. Software provides descriptions for each model and allows users to select or input required parameters.

Results are provided in graphical and text formats, showing estimated distance for different modulations used with OFDMA multiplexing technique (from QPSK to 64QAM). Higher rate modulations are more sensitive to propagation loss resulting shorter base station coverage radius. This must be taken into account when selecting what data throughput is required for planned services.

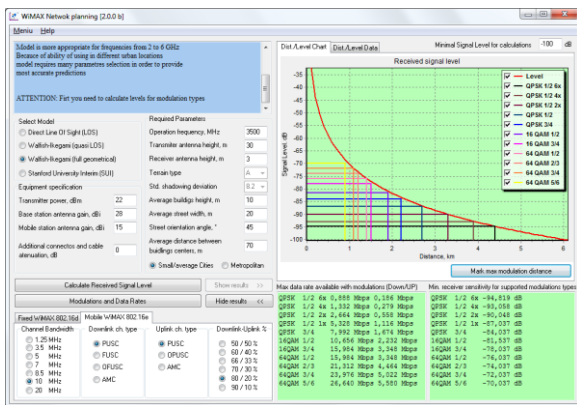


Figure 1. User interface of BS coverage estimation software

In addition to software provides fixed and mobile WiMAX data calculation plugin, which allows selecting channel bandwidth, subcarrier permutation schemes and calculating available data throughput for each modulation.

Calculation examples are provided in Fig. 2, assuming in parameters provided in Table 1.

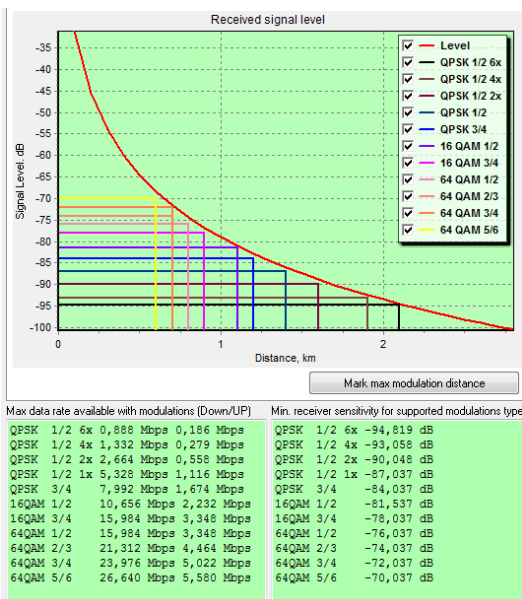


Figure 2. Distance and throughput estimation example

Table 1. Parameters used for calculation

Parameter	Value
Model	SUI-A (Urban environment)
Tx power	23 dBm
BS antenna gain	28 dBi
MS antenna gain	9 dBi
Frequency	3500 MHz
Channel size	10 MHz
Downlink/uplink ratio	80/20%

In this example case scenario we can see that radius of one base station can reach about 2 Km. Taking into account data throughput that is desired by service provider (for example 15 Mbps – 16 QAM) it is required to plan base station coverage not higher than 1,4 Km.

2. SIMULATION OF PROTOCOLS

Protocol simulation software is based on mathematical imitative simulation model which describes each network element as separate aggregate with input and output signals. Each aggregate and signal involves set of parameters and can represent behavior of mobile station, wireless channel, base station and connectivity network. Software user interface visualizes the mathematical model allowing users easily construct their network architecture and enter simulated protocol parameters such as channel latency, error probabilities, etc.

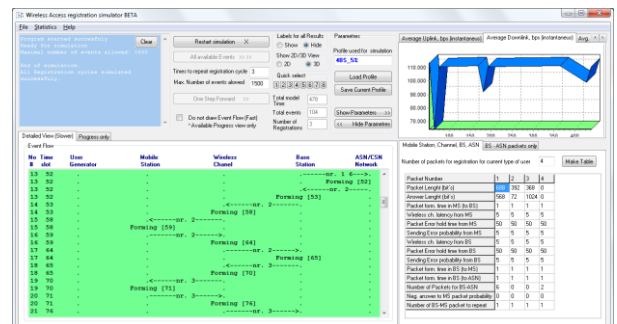


Figure 3. Simulation software GUI

Software allows creating, saving and restoring different simulation profiles for efficient comparison of investigated protocols. Simulation can be performed either step by step, analyzing each packet in time flow diagrams, either as complete simulation for thousands of simulated procedures. Software provides graphical results for different QoS characteristics of each network element – generated traffic, latency, average results, etc.

This article provides mobile WiMAX handover procedure simulation example. Procedure time flow diagram is provided in Fig. 4 [2].

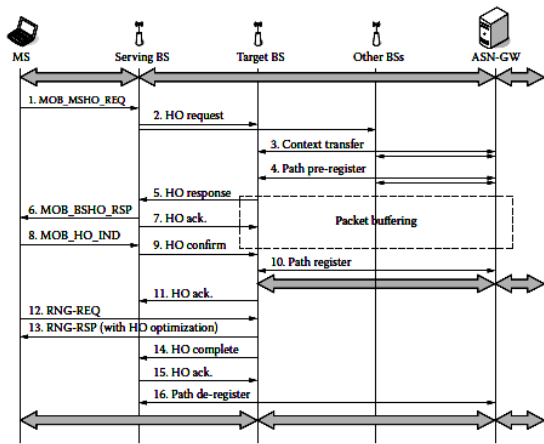


Figure 4. Handover time flow diagram

Diagram represents registration procedure and packets used for performing handover procedure. Describing each packet in simulation software was based on mobile WiMAX standard [1].

Simulation results are provided in Table 2. Values represent results when mobile station is in coverage from 2 to 4 base stations.

Table 2. Mobile WiMAX handover simulation results

QoS Characteristics	Result
Handover latency	from 92 to 180 ms
Uplink generated data load	from 2.5 to 7 kbps
Downlink generated data load	from 3 to 9.5 kbps

As we can see registration procedure of one user is acceptable from latency point of view and does not create high data traffic, but when implementing network it must be taken into account, because network consists of many mobile stations and in overlapping network zones where could be continuous handover activity.

3. NETWORK COVERAGE EVALUATION

Network coverage evaluation software utilizes results of BS coverage estimation and protocol simulation. Software suggests optimal distance between base stations, provides graphical representation of base station coverage and calculates areas between all types of overlapping sectors. It allows specifying number of mobile stations in each area type and inputting traffic load.

Calculation examples are provided in Figure 6, assuming that there are 25-75 mobile stations per sector, 2% wireless channel error probability, 50% of mobile station performs handover at sector edge. It results in up to 130 kbps for downlink and up to 120 kbps for uplink generated traffic. When lowest rate modulation QPSK1/2x6 is used (it's most probable at sector edges) handover procedure can con-

sume up to 18% and 41% sector capacity for downlink and uplink respectively. Therefore it's important to foresee what user expansion is expected in the future and initially implement required overhead.

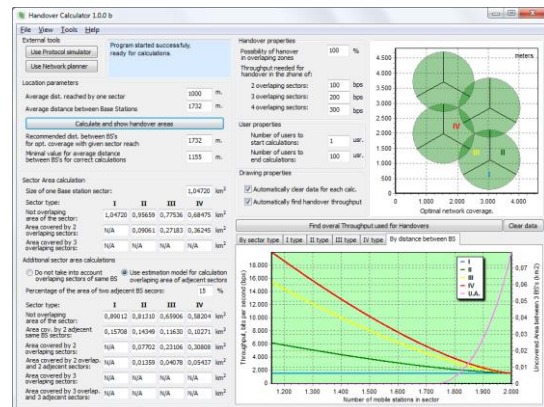


Figure 5. Network coverage evaluation software GUI

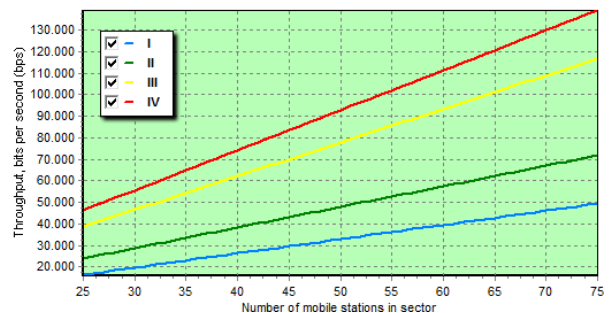


Figure 6. Handover data load dependencies from number of users by sector type

7. CONCLUSIONS

Software that is designed and presented by Authors allows automating network implementation and service simulation tasks for 4th generation wireless technologies. Software can be used as efficient tool for network providers or for educational purposes.

Example results presented in this paper show that multiple and complex tasks must be solved in order to achieve optimal network performance and even such regular procedure as handover can affect QoS. Automated software allows foreseeing and avoiding such of network behavior by choosing higher capacity equipment, selecting more efficient mobility management solutions or increasing BS density.

References

- [1] IEEE 802.16 Broadband Wireless Access Working Group. "Channel Models for Fixed Wireless Applications", 2001, 36 p.
- [2] IEEE. "IEEE Standard for Local and Metropolitan area networks / Part 16: Air Interface for Broadband Wireless Access Systems" - New York, 2009. - 864 p.

COMPARATIVE ANALYSIS OF INFLUENCE OF TV CHANNEL TRANSMISSION PROCESS TO QOE FOR DVB-T/H AND IPTV SERVICES

Rasa Brūzgienė
Lina Narbutaitė
Tomas Adomkus

Kaunas University of Technology
Department of Telecommunications
Studentų str. 50-452, Kaunas, Lithuania, LT- 51368
E-mail: rasa.bruzgiene@ktu.lt

Abstract

Digital television (TV) broadcasting offers the user an opportunity to watch higher quality television channels, compared with analog television. However, for the user, which chooses digital television instead of the analog television, the implementation of the longer channel zapping process negatively affects the user's perception of the attractiveness of service and his individual needs, so it is important for the television service provider to analyze the impact of the channel zapping process to service quality of experience (QoE). As nowadays the digital terrestrial/ handheld television (DVB-T/H) is most common TV service and digital IP television (IPTV) is considered as the most promising contender for the digital terrestrial/ handheld television, so the task of this paper is to analyze and compare the QoE of TV channel transmission process for DVB-T/H and IPTV services by TV channel zapping time.

1. INTRODUCTION

Currently actual problem for digital television is TV channel zapping time. This QoE parameter is very important for users of digital TV. Influence of channel zapping process of IPTV service to QoE is directly dependent on its main components, influencing digital television channel zapping time [1]. The main component - processing time of requests for TV channel change is reliant to the user's behaviour for TV channel searching and selection.

TV channel zapping time of DVB - T/H service is dependent on a number of components [2]. Correlation of components, that influences the TV channel zapping time, affects the transmission process of TV channel for DVB-T/H and IPTV services, so the experimental researches for TV channel zapping time of DVB-T/H and IPTV services are presented in this paper.

2. EXPERIMENTAL RESEARCHES FOR CHANNEL ZAPPING TIME OF DVB-T/H AND IPTV SERVICES

The aim of experimental researches - to measure the TV channel zapping time of DVB-T/H and IPTV services, using a different methods of TV channel searching and selection, and compare the

influence of TV channel transmission process by channel zapping time impact on the quality of experience.

The experiments were carried out in the networks of Lithuanian DVB-T/H (Fig. 1) and IPTV (Fig. 2) services' providers. During the experiments, the TV channel zapping time was recorded by assessing different behaviour of users for TV channel searching and selection to a fixed choice of selected TV channel:

- TV channel is selected sequentially;
- TV channel is selected random.

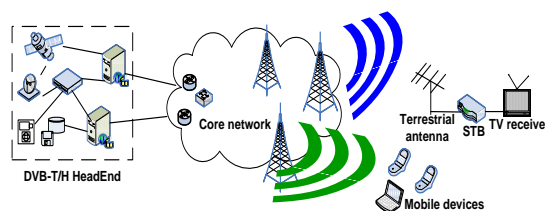


Figure 1. Experimental network for DVB-T/H service

When user selects TV channels sequentially, he/she switches one TV channel after another, recording the TV channel after the completion of the first request for channel change. When user selects TV channels random, he/she switches one TV channel after another at random, repeating the changing process not less than 2 times and not recording the selected TV channel after sending

request for its change. The transmission of selected TV channel begins when user fixes his choice for selected TV channel.

Experimental measurements was made in the hours of highest load – on Saturdays and on Sundays from 18 to 22 hours (p.m.). The duration of all experiments – 5 weeks.

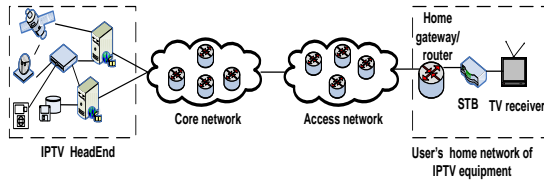


Figure 2. Experimental network for IPTV service

Total amount of TV channels: 57 IPTV channels and 14 DVB-T/H channels. The evaluation of QoE for different TV service was made by 10 respondents, who evaluated the subjective QoE using the method of Mean Opinion Score (MOS) and expressing the perceived quality of service on a scale from 1 (poor) to 5 (excellent).

3. RESULTS OF EXPERIMENTAL RESEARCHES FOR CHANNEL ZAPPING TIME OF IPTV SERVICE

Experimental results of IPTV service were processed by methods of statistical analysis. Results in Fig. 3 shows, that when TV channel is selected sequentially, only part times of TV channels changes exceed the limiting value for IPTV channel zapping time according ITU-T (2 seconds) [3].

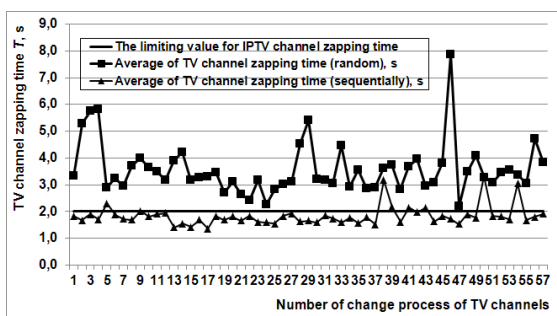


Figure 3. IPTV channel zapping time

Differentially is when IPTV channel is selected random. In this case all IPTV channel zapping times exceed the limiting value of 2 s.

However, the perceived quality of IPTV service respondents are assessing not only by the main criterion – the channel zapping time, but also on other, visible or audible factors: TV channel video

and audio desynchronization or video distortion, and et al. In order to eliminate possible errors of IPTV QoE, authors approximate results of experimental researches of IPTV service (Fig. 4). Due to this approximation, authors proposed the objective method for IPTV QoE evaluation by TV channel zapping time, when TV channel is selected

– sequentially:

$$ob_MOS = -0,665 \cdot T^5 + 7,8222 \cdot T^4 - 34,952 \cdot T^3 + 73,913 \cdot T^2 - 75,812 \cdot T + 34,935 \quad ; (1)$$

– random:

$$ob_MOS = -0,0319 \cdot T^3 + 0,6273 \cdot T^2 - 4,0203 \cdot T + 9,3723 \quad ; (2)$$

here T – TV channel zapping time in IPTV service.

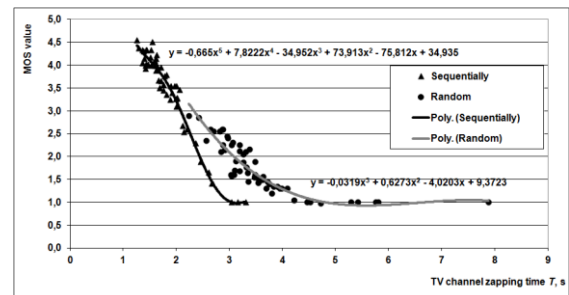


Figure 4. Approximation of results of experimental researches of IPTV

Comparision of IPTV subjective and objective QoE, when TV channel is selected sequentially and random is presented in Fig. 5 and Fig. 6. The correlation between subjective and objective QoE is 0,82 (for sequentially) and 0,87 (for random).

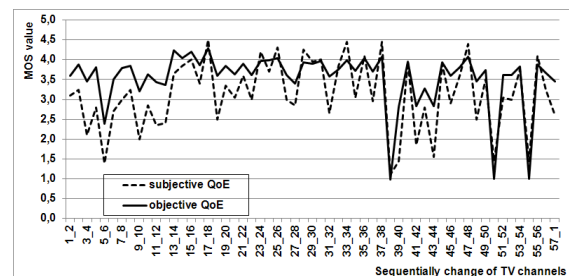


Figure 5. IPTV QoE (sequentially)

These coefficients indicate a strong correlation between the subjective QoE evaluation by respondents and proposed an objective QoE assessment.

According to the results of quality of experience evaluations, is seen that, when TV channel zapping

time exceeds the limit of 2 s, respondents of IPTV service consider this as a very long duration for change of TV channel. This duration is unacceptable for respondents and forms a negative attitude to the transmission of IPTV channels. Also it affects the negative approach to the attractiveness of IPTV service.

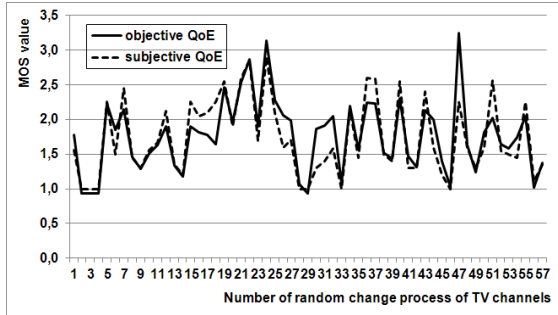


Figure 6. IPTV QoE (random)

4. RESULTS OF EXPERIMENTAL RESEARCHES FOR CHANNEL ZAPPING TIME OF DVB-T/H SERVICE

Experimental results of DVB-T/H service were processed by methods of statistical analysis are presented in illustrations below.

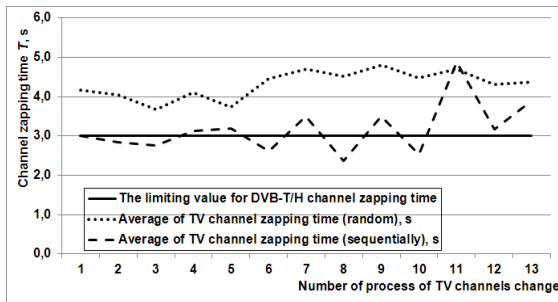


Figure 7. DVB-T/H channel zapping time

According to the Fig. 7, it is obviously, that when TV channel is selected random, in contrast to sequentially changes, all times of TV channels changes exceed the limiting value of 3 seconds [4] for DVB-T/H channel zapping time. Such TV channel zapping time respondents grade less than 3.5 in MOS scale as long duration for change of TV channel.

However, as given evaluations of the subjective QoE was scattered, the authors proposed to approximate these evaluations (Fig. 8).

In this case, the authors proposed an objective method for QoE assessment of the DVB-T/H service according TV channel zapping time, when TV channel is selected

– sequentially:

$$ob_MOS = 0,1296 \cdot T^5 - 2,8156 \cdot T^4 + 23,762 \cdot T^3 - 96,972 \cdot T^2 + 189,69 \cdot T - 138,09 \quad ; (3)$$

– random:

$$ob_MOS = 0,3315 \cdot T^4 - 6,2355 \cdot T^3 + 43,392 \cdot T^2 - 132,91 \cdot T + 153,62 \quad . (4)$$

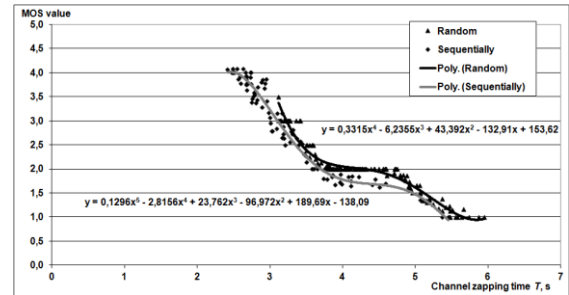


Figure 8. Approximation of results of experimental researches of DVB-T/H

Comparison of DVB-T/H subjective and objective QoE is presented in Fig.9. In this case, when IPTV channel is selected sequentially, correlation between the subjective and objective QoE is equal to 0.98; and when IPTV channel is selected random correlation is 0.93. That shows a very strong correlation between the subjective QoE evaluation and proposed an objective QoE assessment.

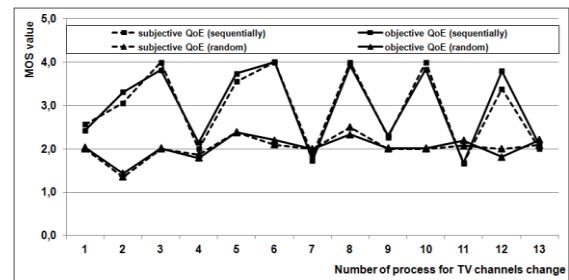


Figure 9. DVB-T/H QoE

According to the results (Fig. 9) the request for change of TV channel, when respondent is selecting a channel sequentially, was processed shorter than in a case of random selection. This results the assessment of QoE for DVB-T/H service greater than 3.5 in MOS scale as acceptable TV channel zapping time by respondents.

4. CONCLUSIONS

According to the results of experimental researches it can be stated that:

1. IPTV channel zapping time is 1 second shorter when TV channel is selected sequentially and 1 second longer when the TV channel is selected random, compared with DVB-T/H.

2. Due to this time, subjective QoE evaluation of IPTV service is 0,5 greater (for sequentially and random) in MOS scale than for DVB-T/H service.

In this paper according to the influence of TV channel transmission process for subjective QoE, authors proposed objective methods for QoE evaluation, which correlations are close to 1.

References

- [1] B. Dekeris, L. Narbutaite, "IPTV Channel Zap Time Analysis", *Electronics and Electrical Engineering*, no. 10 (106), Technologija, Kaunas, 2010, pp. 117-120.
- [2] Rezaei, M.; *et al.* "Optimal Channel Changing Delay for Mobile TV over DVB-H", *Proceedings of the International Conference on Portable Information Devices*, May 2007.
- [3] ITU – T Recommendation G.1030. *Estimating end-to-end performance in IP networks for data applications* // ITU – T study group 12, Geneva, November, 2005. 28 p.
- [4] Golgmann, L.; *et al.* "Impact of video transcoding artifacts on the subjective quality", *Proceedings of the Second International Workshop on Quality of Multimedia Experience*, June, 2010.

INDOOR MULTIPATH RADIO CHANNEL CHARACTERIZATION IN LARGE BUILDINGS

Dimitar G. Valchev

University of Food Technologies
26 Maritsa Blvd, 4000 Plovdiv, Bulgaria
Phone: +359 32 603 860; E-mail: dvalchev@ece.neu.edu

Abstract

This paper presents new mathematical developments and results for modeling three-dimensional multipath radio channels inside large buildings, such as hospitals, malls and industrial sites. Particular examples for propagation scenarios are given and the corresponding characteristics of the received signal are derived from the spatial configuration of the surrounding reflecting objects in vicinity of the receiver. The obtained results are useful for designing spatially directive reception diversity systems that effectively overcome the harmful effects of multipath propagation.

1. INTRODUCTION

An important feature of the radio communication channel is its multipath propagation due to various scattering and reflecting objects around the mobile receiver antenna. The multipath propagation is particularly characteristic to large indoor spaces where the transmitted radio signal undergoes many reflections and scatterings before reaching the mobile unit. As a result, multiple signal replicas arrive at the mobile receiver from different directions in three-dimensional space, that is, each radio wave arrives at some azimuth and some generally non-zero elevation relative to the receiver antenna which also travels at some azimuth and elevation.

In the traditional literature [1, 2, 3] the developed multipath channel model is two-dimensional (horizontal). In reality, the multipath environment is three-dimensional since the reflecting and scattering objects have some non-zero height and therefore the many radio waves arrive at the mobile unit at different non-zero elevations. Those non-zero elevations change the received signal correlation and Doppler spectrum [4]. Therefore, a three-dimensional model is the adequate analysis approach when describing realistic multipath wireless channels. In this paper the autocorrelation function of the fading signal at the mobile receiver antenna is derived. First, a mathematical model is developed for describing the multipath propagation channel and the motion of the receiver. Next, the autocorrelation function and the Doppler spectrum of the received signal are derived based on the developed mathematical model. The approach here is alternative to that developed in [5] where the authors first find the

Doppler spectrum, and then through a Fourier transform obtain the signal autocorrelation. The approach here is better when the Doppler spectrum is difficult for direct derivation.

2. MATHEMATICAL MODEL

The transmitted signal is assumed to be unmodulated with amplitude E_0 and carrier angular frequency ω_c . It is represented as

$$s(t) = E_0 e^{j\omega_c t}. \quad (1)$$

The amplitude E_0 is also called *envelope*. The multipath channel model consists of N radio waves coming to the receiver. Assuming no attenuation through the different propagation paths in a local volume, the received complex voltage signal at the mobile unit is

$$\tilde{V}(t) = E_0 \sum_{n=1}^N e^{j\psi_n}, \quad \psi_n = \omega_c t + \varphi_n \quad (2)$$

where φ_n is a random initial phase, uniformly distributed from 0 to 2π .

The N radio waves incoming to the receiver have arbitrary directions in three-dimensional space. The mobile unit travels also in an arbitrary direction in three-dimensional space, given by the azimuth-elevation pair (θ, ϕ) , where θ is the polar angle in the x - y plane and ϕ is the angle between the travel direction and the x - y plane. The different radio waves come to the receiver antenna at angles α_n relative to the travel direction of the mobile unit. The angles α_n are statistically independent of ψ_n .

For analysis simplification, only single polarization is assumed and only the electric field component is sensed by a suitable antenna with a three-dimensional radiation pattern. The antenna is assumed to have spherically uniform unit gain. The geometrical configuration of the described channel is shown in Fig. 1.

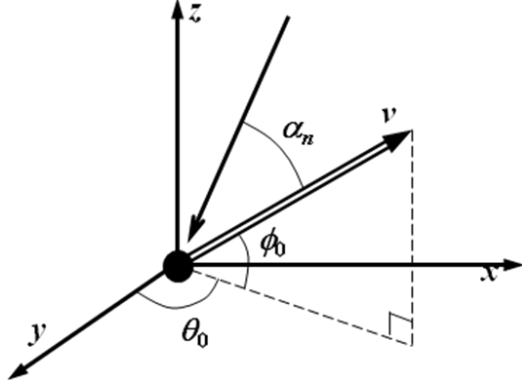


Fig. 1. Geometrical configuration of the radio propagation.

3. FADING SIGNAL CORRELATION AND SPECTRUM

The second-order statistics of the received fading signal relate to its fluctuation rate. The fluctuation rate depends on the autocorrelation and the spectrum (the Fourier transform of the correlation) of the received signal. Therefore, finding the received signal autocorrelation is very important for obtaining the different statistical measures of the channel performance.

If the mobile unit travels a distance d with velocity v , each radio wave arrives at the antenna at angle α_n relative to the travel direction, and changes its phase ψ_n by $kdc\cos\alpha_n$, where $k = 2\pi/\lambda$ is the wave number with λ being the wavelength of the transmitted signal. As a result, the received complex voltage in (2) changes to \tilde{V}^d and the correlation of the received signal can be found by the expression

$$\begin{aligned} R(d) &= E\{\tilde{V}^* \tilde{V}^d\} = E_0^2 E\left\{\sum_{n=1}^N e^{-j\psi_n} \sum_{m=1}^N e^{j(\psi_m + kd\cos\alpha_m)}\right\} = \\ &= E_0^2 \sum_{n=1}^N \sum_{m=1}^N E\left\{e^{j(\psi_m - \psi_n)} e^{jkd\cos\alpha_m}\right\} = \\ &= E_0^2 \sum_{n=1}^N \sum_{m=1}^N E\left\{e^{j(\psi_m - \psi_n)}\right\} E\left\{e^{jkd\cos\alpha_m}\right\} \end{aligned} \quad (3)$$

where $E\{\cdot\}$ is the expectation taken over the distribution of the direction of arrival α of the radio waves at the mobile unit and \tilde{V}^* is the complex conjugate of the received complex voltage \tilde{V} in (2).

The last equality in (3) follows from the statistical independence of ψ_m and α_m . The ensemble average $\sum_{n=1}^N \sum_{m=1}^N E\left\{e^{j(\psi_m - \psi_n)}\right\}$ is zero except for $m = n$ when it is equal to one. Therefore, (3) reduces to

$$\begin{aligned} R(d) &= E_0^2 E\left\{\sum_{m=1}^N e^{jkd\cos\alpha_m}\right\} = E_0^2 N \int_0^\pi p(\alpha) e^{jkd\cos\alpha} \sin\alpha d\alpha = \\ &E_0^2 N \int_0^{2\pi} \int_0^\pi p(\alpha, \beta) e^{jkd\cos\alpha} \sin\alpha d\alpha d\beta. \end{aligned} \quad (4)$$

There is a factor $\sin\alpha$ in the integral in (4) because α is a measure of a three-dimensional orientation and therefore the ensemble average in (4) involves integration over the unit sphere. The functions $p(\alpha)$ and $p(\alpha, \beta)$ in (4) are the marginal and the joint probability density functions (PDFs), respectively, of the angle (or angles) of arrival of the multipath power at the mobile unit.

3.1. A case of a uniform PDF

For a uniform PDF $p(\alpha) = 1/\pi$ for $0 \leq \alpha \leq \pi$, (4) reduces to [6]

$$R(d) = \frac{E_0^2 N}{\pi} \int_0^\pi e^{jkd\cos\alpha} \sin\alpha d\alpha = E_0^2 N j_0(kd) \quad (5)$$

with $j_0(x)$ being the zero-order spherical Bessel function of the first kind, also equal to $\frac{\sin x}{x}$ which is the unnormalized version of the sinc function.

When the travel direction of the mobile unit and the incoming radio waves all belong to a single plane in the three-dimensional space, α is a measure of a two-dimensional orientation and therefore there is no $\sin\alpha$ factor in the integral in (5). Then, the following expression for the received fading signal autocorrelation is obtained:

$$R(d) = \frac{E_0^2 N}{2\pi} \int_{-\pi}^\pi e^{jkd\cos\alpha} d\alpha = E_0^2 N J_0(kd) \quad (6)$$

and this is the classical result, obtained in [1, 2, 3].

The spatial correlation may be transformed into a temporal correlation through the distance-time proportional dependence $d = v\tau$ and the expression in (5) becomes

$$R(kv\tau) = E_0^2 N \frac{\sin(kv\tau)}{kv\tau}. \quad (7)$$

The received signal spectrum is obtained from the temporal correlation through a Fourier trans-

form. The sinc type correlation function implies a flat spectrum of the received signal within the limits $\pm f_{\max} = \pm v/\lambda$ around the carrier frequency when the angular multipath power density at the mobile unit is uniform over the unit sphere, as also shown by an alternative approach in [5], where the authors first derive the Doppler spectrum and then the autocorrelation by a Fourier transform. Usually this is the case in very densely built-up areas, as well as in large and tall corporate office buildings or industrial sites. The shape of the autocorrelation and the Doppler spectrum determine the second-order fading statistics [1, 2]. Usually of particular interest are the autocorrelation function and the power spectrum of the received signal *envelope*. The envelope correlation is approximated by the power correlation [1], equal to the square of the unnormalized sinc function for a spherically uniform angular distribution of the multipath power. The corresponding envelope spectrum is obtained through a Fourier transform of the envelope correlation, or through a self-convolution of the received signal flat spectrum, resulting in a triangular spectrum. The normalized envelope correlation $R_{|V|}(kvt)/R_{|V|}(0)$ and the envelope spectrum $S_{|V|}(f)$ in decibels for a spherically uniform angular distribution of the angle of arrival of the multipath power are shown in Fig. 2.

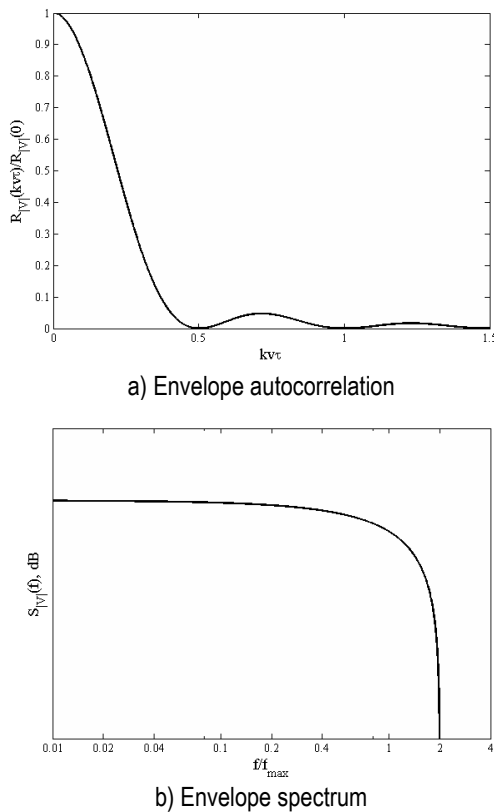


Fig. 2. Envelope autocorrelation and spectrum at the mobile unit for a uniform PDF

3.2. A case of a uniform PDF plus a line-of sight (LOS) path

This case is characteristic to situations in indoor spaces where there is a direct line (LOS) between the mobile unit and the base station. The only difference in the autocorrelation and the spectrum of the received signal envelope is that now there will be a constant term P_{LOS} added to the expression in (5) to obtain

$$R(d) = E_0^2 N_{j_0}(kd) + P_{LOS}. \quad (8)$$

Because of the constant term in (8), the autocorrelation here will never vanish.

The spectrum of the received signal envelope in the case of an additional LOS component is obtained by adding a single impulse function at the offset frequency corresponding to the angle of arrival of the LOS path to the Doppler spectrum from the previous subsection.

4. CONCLUSION

This paper develops a method for finding the fading signal correlation and the Doppler spectrum at the receiver antenna of the mobile unit in a three-dimensional multipath environment. The method is based on first deriving the autocorrelation function by averaging over the angular distribution of the incoming radio waves. It is shown that in case of uniform three-dimensional angular distribution of the multipath power at the mobile unit the autocorrelation of the received signal is a sinc function implying a flat Doppler spectrum between the minimum and the maximum Doppler offset at the receiver. For the case of a LOS component added to a uniform three-dimensional angular distribution of the multipath the autocorrelation of the received signal is a sinc function raised by the power level of the LOS component. This implies an additional impulse to the flat Doppler spectrum. From the so obtained autocorrelation function and spectrum, the corresponding approximate envelope autocorrelation and envelope spectrum at the receiver are found. The so obtained autocorrelation and spectrum form a basis for determining important second-order statistics of the fading signal at the receiver antenna of the mobile unit.

References

- [1] R. H. Clarke, "A statistical theory of mobile radio reception", *Bell Syst. Tech. J.*, vol. 47(6), pp. 957–1000, 1968.
- [2] M. J. Gans, "A power-spectral theory of propagation in the mobile radio environment", *IEEE Trans. Veh. Technol.*, vol. 21, pp. 27–38, 1972.
- [3] W. C. Jakes, ed., *Microwave Mobile Communications*, New York, IEEE Press, 1974.
- [4] T. Aulin, "A modified model for the fading signal at a mobile radio channel", *IEEE Trans. Veh. Technol.*, vol. 28(3), pp. 182–203, 1979.
- [5] R. H. Clarke and W. L. Khoo, "3-D mobile radio channel statistics", *IEEE Trans. Veh. Technol.*, vol. 46(3), pp. 798–799, 1997.
- [6] M. Abramowitz and I. A. Stegun, editors, *Handbook of Mathematical Functions with Formulas, Graphs, and Mathematical Tables*. Dover, 10-th edition, 1972.

ADVANTAGES OF MFSSO TO RF WIRELESS COMMUNICATION SYSTEMS

Hristo Ivanov, Tsvetan Mitsev

Department of Radiocommunications and Videotechnologies,
Technical University of Sofia, №8, "Kl. Ohridski", Blvd.
phone. +359 2 9653275, e-mail: hristo.dn.ivanov.87@gmail.com

Abstract

Different wireless communication systems have been increasingly utilized in many applications over the last decades in providing a link between land, air or sea subscribers. One of the most promising among them is the system of Mobile Free Space Optics (MFSSO). In this work a comparison analysis of the MFSSO with the most rapidly developing mobile technologies, namely, technologies of Fourth Generation and LMDS is done. The achievements in the field in the last few years are summarized and it is shown the most important advantages of MFSSO over other technologies. Other topics presented here are complete summary of the built MFSSO devices over recent years and pivot-table for their feasibility. In conclusion, the issue of major hurdles and future development of MFSSO is faced.

1. INTRODUCTION

FSO is laser based technology that provides wireless transmission of data on an atmospheric channel. It offers a very wide bandwidth, small size and weight, low price, huge unregulated license free spectrum, lack of electromagnetic interferences, excellent safety features. This makes it a major competitor of the developing fourth-generation systems, operating in the frequency range of 2 GHz to 11 GHz, as well as LMDS, located in the range from 10 GHz to 66 GHz [1]. Despite this advantages, FSO technology has a number of problems. The most significant of them are: limited mobility, line of sight (LOS) requirement between subscribers, influence of adverse weather conditions. An important issue about FSO systems is the eye safety measures at work. Due to the high intensity of the coherent laser source of light, there are certain limitations in the choice of its power, wavelength and beam divergence.

According to the above mentioned disadvantages there are different solutions to be built a mobile version of FSO system known as MFSSO. MFSSO systems are discussed in a lot of scientific papers due to improving their features such as modulation methods [2] working in different atmosphere conditions [3] and various types of adaptive control algorithms [4]. The main reason for this are its positive characteristics that make it not only desirable, but in many cases a compulsory decision, if there is a necessity of wireless communications. In this work we defend the above statement. As a

result we have presented MFSSO systems in all their crucial aspects.

2. TECHNOLOGY OVERVIEW

The necessity for high information capacity and security features determines the development of manifold wireless communication systems. The representative technologies with the greatest impact now and in the coming years are MFSSO, WIMAX (Worldwide Interoperability for Microwave Access), LTE (Long Term Evolution) and LMDS (Local Multipoint Distribution Service). MFSSO systems, based on stationary FSO technology, have possessed all its listed positive advantages as well as several new improvements. According to the latest results, data capacity reaches to an amazing 2.5 Gbps on a link range of 100 km, using laser source in the near-infrared spectrum [5].

In contrast of this great achievement, MFSSO systems are faced by number of challenges. The most important of them are mobile working in adverse weather conditions and constant LOS requirement. In order to enable MFSSO communication in mobile environments, we introduce different hardware solutions. In many cases they must operate in condition of severe Mie scattering, expressing in different types of smokes, fogs and cloud fields. Another attenuation factor is atmospheric turbulence, which always plays a significant role in communications. [1].

Mobile WIMAX version 802.16m and LTE technologies are the main candidates for the fourth-

generation systems. They provide relatively high information capacity. According to the most recent result the latest developed Release of WIMAX, WIMAX2, has peak data speed up to 330 Mbps (100 Mbps for mobile users). The LTE data rate is almost similar, reaching up to 300 Mbps (75 Mbps for mobile users). Coverage area of WIMAX cells is between 2 and 5 km while in case of LTE it is reaching to 10 km. The outstanding capability of both technologies is the lack of need for direct LOS. Major issue of WIMAX and LTE is because of propagation of radio signal in all directions which mean susceptibility to jamming, interference and saturation. Moreover, there is expensive licenses for network operation. **LMDS** technology is operating in the frequency range from 26 GHz to 29 GHz. This defines one of its main drawbacks. As in MFSO systems there is a need for LOS and they are strongly influenced by weather conditions. The cell is only up to about 2.4 km. The information speed is about 500 Mbps in both directions. In recent years the development of this system is suppressed by the fourth generation networks [6].

Figure 1 present summarised result of information capacity and radius of coverage for the compared technologies. As shown MFSO devices outstrips many times other systems in case of data rate feature. Although there is a limitation for the radius of coverage about 10 km this parameter is sufficiently competitive too and in some cases are possible far longer distances.

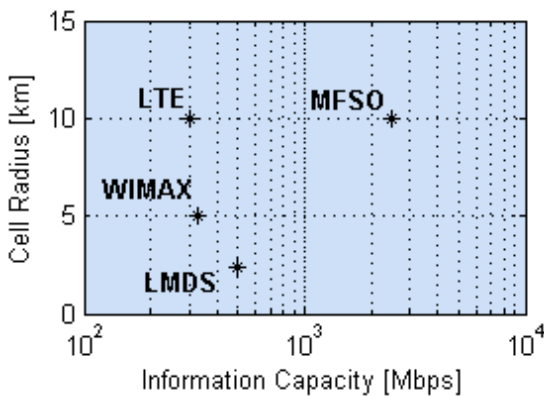


Figure 1. Comparison of communication technologies

3. MFSO SYSTEMS

The technical implementation of MFSO systems allows different types of architectures. Figure 2 shows the major achievements for connectivity between moving mobile platforms.

The structural scheme of Figure 3 provides a basic overview of general blocks of MFSO systems.

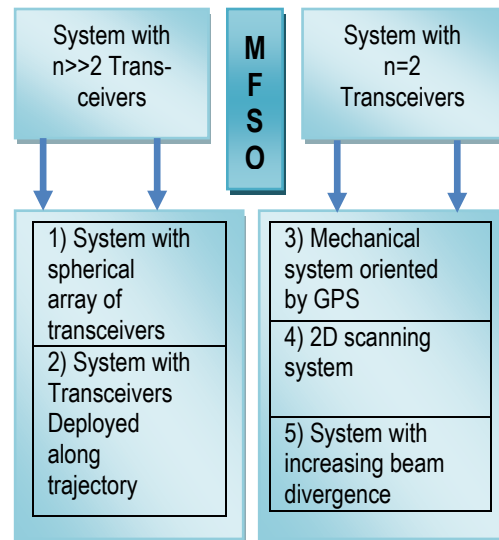


Figure 2. Classification of MFSO systems

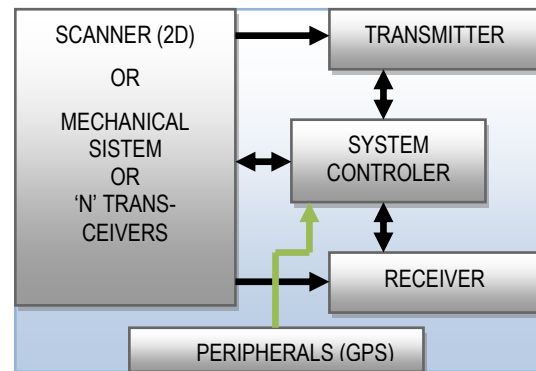


Figure 3. Basic architecture of MFSO systems

Special characteristics of individual MFSO system mainly arise from: technical realization; method for initial identification between communicating parties, ways for maintain connectivity. In the operation of each system usually are required three steps: acquisition, pointing, and tracking. In acquisition mode the two terminals try to locate each other. Pointing aims to achieve alignment between the antennas on the opposite pairs systems. Tracking is process in which there is a constant changing of direction of the laser beam transceiver due to the movement of the object.

System in Figure 2 are:

1) This system contains a number of spherical MFSO nodes. Each of them is built of hexagonal shapes and put together in a soccer ball arrangement. Thus they have 3D space coverage. Typically, each node has a auto-alignment circuit, whose task is to monitor the level of input signals and maintaining the communication link. In acquisition mode when there is absence or disconnection of

signal, the system sends simultaneously search pulses in all directions. When some of other parties responded the communication link is established again and data transmission is restored. When more than one connection are aligned it must be use signal / noise ratio priority.

In this type of MFSSO systems could be used different selection combining diversity schemes: MIMO, SIMO, MISO. Due to this multireceiving configuration, processing could be more complicated, but BER is reducing.

2) The proposed system is suitable for connection of moving platforms along a fixed terrestrial trajectory such as trains. The network is constructed of a large number of transceivers located along the track and another part of them deployed on the top of moving objects.

3) Typically are being used two MFSSO systems located at both ends of the communication channel. The GPS signals control mechanical system for acquisition, pointing, and tracking presented by 2-dimensional rotating gimbal. The acquisition and pointing are made only once in the beginning of the communication session. The tracking continue all the time. The system uses small divergence angle due to aim to minimize the geometric loss.

4) This system is utilized in case of rapidly moving mobile platforms. It combines a powerful laser and two-dimensional scanning system based on two micro mirrors with size about 1 mm. The mirrors are steered from the device using electrostatic effect. The maximum angle is 25°. The receiver consists a short focus lens with wide field of view 1 rad x 1 rad and CMOS sensor with 1000 pixels. The system uses a special protocol for transmission and connection control. It includes three modes: rough acquisition, phase of precise pointing and periodical tracking, ensuring smooth communication.

5) These systems introduce the concept of increasing divergence of the laser transmissive beam, which is controlled by precise adjustment of the collimator. Here are the typical three phases of establishing a connection. In the process of acquisition both mobile parties of the system using optical radiation with a very extended range of coverage to establish a connection. The second phase is pointing, in which the radius of the beam is changing depending on the relative speed and distance between communicating platforms. The process of tracking includes additional mechanical device that rotates MFSSO system in the right direction to ensure the communication link.

The specific feasibilities of the described MFSSO systems is shown in Table 1.

Table 1. MFSSO feasibilities

	MFSSO system	Feasibility	Characteristics
1	System with Spherical Array of Transceivers	Mobile Multi-Hop Ad-hoc Networks and MAN Networks	1 Gbps 200-300 m
2	System with Transceivers Deployed Along Trajectory	High-Speed Trains	1 Gbps 100 m
3	Mechanical System Oriented by GPS	Ground to Air Links	2,5 Gbps 100 km
4	2D Scanning System	Fast-Moving Terrestrial or Airborne Objects	1 Gbps 3 km
5	System with Increasing Beam Divergence	Ship to ship communication	1 Gbps 1-5 km

4. CONCLUSION

Mobile Free Space Optics systems are a viable alternative to communication devices of radio spectrum. With its numerous positive capabilities FSO technology has a chance to dominate almost over all modern mobile technics. Clear evidence is touched outstanding data speeds of 800 Gbps in its fixed wireless version. This shows the enormous potential of MFSSO that even in these days reaches information capacity of 2 Gbps to which fifth generation technologies are aspiring, particularly future LTE-Advanced Release. Regardless of superlatives for MFSSO Systems, RF systems also have their advantages. WIMAX and LTE technologies have almost no dependence on atmospheric conditions. They use radio signals in the frequency range, which defines no necessity of LOS. These and other challenges are addressed to mobile Free Space Optics system whose wide spreading feasibility is coming.

References

- [1] S. Nazmus, R. S. Sabbir, S. Apurba, H. Mustafa, "Free Space Optical Connectivity for Last Mile Solution in Bangladesh", ICETC 2010, V.2, June 2010, pp. 484 -487
- [2] J.R. Minch, Mitre Corp., M.A. Bedford, D.R. Gervais, ; D.J. Townsend, "A free space optical communications system", MILCOM 2006, IEEE, Washington, DC, 2006
- [3] M. K. Al-Akkoumi, A. Harris, R. C. Huck, J. J. Sluss, "Challenges Facing Mobile Free-Space Optical Communications", Atmospheric Propagation VI, SPIE, V.7324, May, 2009
- [4] A. Harris, T. Gioma, "Divergence and Power Variations in Mobile Free-Space Optical Communications", Third International Conference, 13-18 April 2008 pp. 174 -178
- [5] N. Anscombe, „Adapting to change”, Nature Photonics, January 2011
- [6] M. U. Ilyas, "A Comparison of Wireless Local Loop Technologies with Reference to their Application in Rural Areas of Pakistan", Lahore University of Management Sciences, Lahore, Pakistan

INVESTIGATION OF THERMAL EFFECTS OF MOBILE PHONE TO THE HUMAN HEAD

V. Pitkevicius, D. Kybartas, L. Svilainis, A. Lukosevicius, V. Dumbrava

Signal processing department, Kaunas University of Technology,
Studentu str. 50, LT-51368 Kaunas, Lithuania
T. +370 37 300532; F. +370 37 753998;

E. darius.kybartas@ktu.lt / linas.svilainis@ktu.lt / arunas.lukosevicius@ktu.lt / vytautas.dumbrava@ktu.lt

Abstract

An influence of electromagnetic waves radiated by mobile phones to the temperature of the human head is discussed in this paper. Several phones and thermovision camera was used in experiments and it was found a 1-2°C increase of temperature in zones where mobile phone was applied. Thermal images showed also a significant increase of temperature of mobile phone. An additional antenna and generator was used in order to separate thermal effects of the absorption of microwaves and heat radiation by case of mobile phone. Experiment was carried out with antenna on ex-vivo beef tissue sample. No thermal effect was observed. It can be concluded, that main thermal effect occurs due thermal radiation of mobile phone battery and transmitter.

1. INTRODUCTION

Influence of electromagnetic (EM) waves radiated by mobile phones to the human health and physical processes is a popular object for investigations. Microwaves are penetrating into human tissue and significant attenuation occurs due EM wave losses in water which is main component of tissues. So energy of microwaves is converted to thermal energy. This thermal effect of microwaves to the biological tissues is well known and it is widely used, e.g. in food industry for heating or cooking [1].

There is a hypothesis that use of mobile phone can heat up soft tissues of head and such influence can cause some diseases or irreversible changes in brain [2]. One of the most evident factors of influence is thermal photography. Many investigators observed increase of temperature of skin on human face after long use of mobile phone [3],[4]. On the other hand, critics of this approach noted that the same thermal effect can occur with non-radiating mobile phone.

Absorption of EM waves in body depends on electric field strength and distribution in volume. It also depends on electric properties of body. Specific absorption rate (SAR) is a parameter which represents absorption of EM power in tissue. It is expressed as

$$SAR = \int \frac{\sigma(r)|E(r)|^2}{\rho(r)} dr, \quad (1)$$

where $E(r)$ is distribution of electric field (V/m), $\sigma(r)$ is distribution of electric conductivity (S/m) and $\rho(r)$ is distribution of tissue density (kg/m³). Usually SAR is represented by power of energy absorbed in 10 g of body mass and it is marked as SAR_{10g} (W/10g).

Temperature of absorbing body depends on SAR. Goal of presented work was to investigate temperature distribution on human face and head after use of mobile phone.

2. EXPERIMENTAL SETUP AND METHODOLOGY

Thermoimaging is an effective tool for investigation of human skin and blood vessels. It can be used, e.g., in mammography [5].

In this work thermovision method is used for evaluation of temperature distribution on human face. A 160x120 pixels thermovision camera Micron MicroShot-B was used to take and analyze pictures.

Three persons participated in experiments with two different mobile phones used. The phones with different SAR was Nokia 2100 (0,55 W/kg) and LG GT540 (1,3 W/kg).

Electromagnetic field strength was monitored using Chauvin Arnoux C.A 43 field meter.

Test period of 15 minutes was selected for experiments because such duration is typical for long conversation. Two different tests were performed. The first test was with non-radiating phone attached to the head for 15 min. The second experiment was with mobile phone in call and conversation mode. Thermoimages were taken before and after experiments.

In order to examine thermal effect of GSM band microwaves, an experiment with *ex-vivo* beef tissue was performed. EM waves radiated from mobile phone and Agilent 8648C RF generator with external antenna was used.

3. RESULTS

Mobile phone radiates EM field in pulsed mode. Level of output power varies depending on distance to base station and received signal strength. Therefore maximal and mean electric field values were measured during experiments (see Table 1). It can be seen that maximal level of EM field in the beginning of call can be more than 10 times higher comparing to level at the steady period of outgoing call.

Table 1. EM field values during experiments

Call mode	Nokia 2100		LG GT540	
	E_{mean} , V/m	E_{max} , V/m	E_{mean} , V/m	E_{max} , V/m
Incoming	7,8	-	27,4	-
Outgoing (start)	10,4	39,2	20,9	> 200
Outgoing	7,4	-	11,9	-

Series of experiments with three different persons showed that increase of face temperature is 0,9 - 1,2°C when non-radiating phone is attached for 15 min. Use of mobile phone in call and conversation mode increases face temperature by 1,2 - 2,3°C. The most affected area is ear and cheek (Fig.1). This area is a contact zone of mobile phone and face skin. No correlation was found between EM field strength (SAR) and temperature increase comparing results obtained with different persons and different phones.

Temperature of mobile phones before experiment was equal to room temperature (24°C). Thermal images of mobile phone case were taken immediately after experiment. Increase of temperature up to 34,5°C was found in battery location place (Fig. 2).

A consequent hypothesis was that main thermal effect on human face is due the heat of battery and transmitter circuits. Therefore additional experiments were performed on beef tissue.

Mobile phones in call mode were placed on tissue for 15 min. Frequency of operation was controlled using frequency counter and it was in 900 MHz band.

Thermal images of tissue sample showed increase of temperature 5-6°C depending on phone used (Fig.3- A).

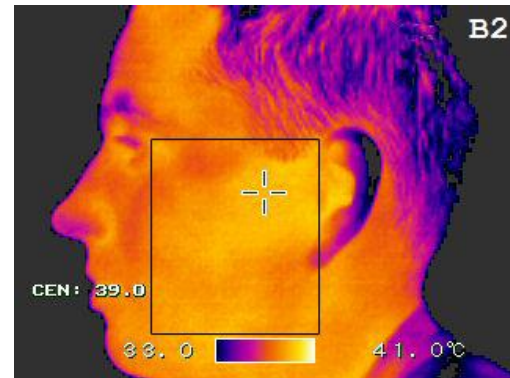
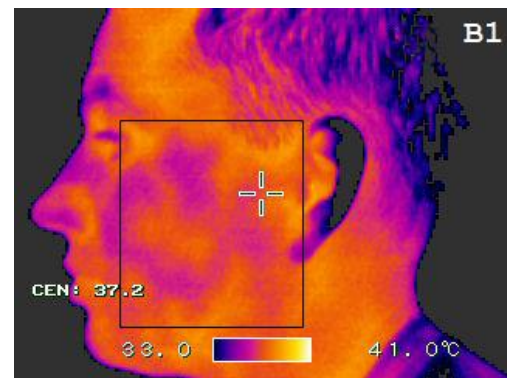


Figure 1. Thermal images of human face before (B1) and after 15 min of conversation (B2) using mobile phone Nokia 2100

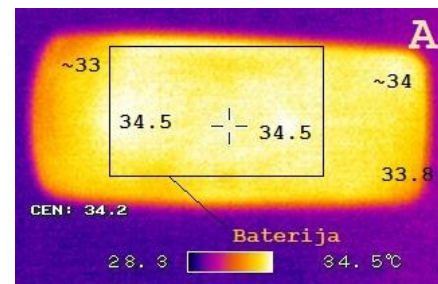


Figure 2. Thermal image of mobile phone Nokia 2100 after 15 min of call

Separation of thermal transfer effect from case of mobile phone to tissue and microwave heating effect was performed using external RF generator. A broadband antenna was used to investigate EM field absorption thermal effect. Antenna was placed on the tissue sample. RF power at 900 MHz was adjusted in order to correspond mean value of electric field (15,6 V/m) during mobile phone call. Time of this experiment was selected twice longer (30 min).

After 30 min of transmitting no thermal effect occurs in beef sample (see Fig. 3 B).

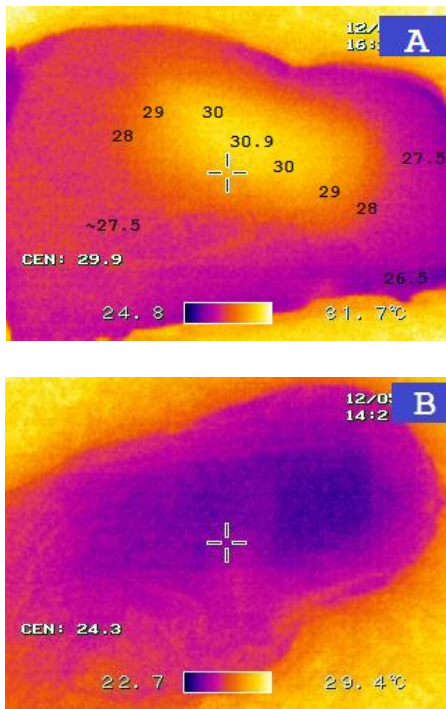


Figure 3. Thermal image of beef tissue after 15 min of exposure using mobile phone Nokia 2100 (A) and 30 min exposure using antenna and RF generator (B)

4. CONCLUSIONS

It can be concluded, that radio waves radiated by mobile phone are not able to heat up tissues. Transmitted power is too low to cause discernible thermal effect.

Effect of increase of face temperature by 1°C is related to disbalance of heat convection near skin when mobile phone case is attached to it.

The main increase of temperature on face and *ex-vivo* tissue sample is related to heat transfer from battery of mobile phone to the tissue. So it can be concluded that main source of thermal effects observed during mobile phone conversation is electronic circuits and battery of device.

References

- [1] A. C. Metaxas, "Microwave heating", Power Engineering Journal, 1991, Vol. 5, pp.237–247.
- [2] L. Salford, A. Brun, J. Eberhardt, L. Malmgren, B. Persson, "Nerve cell damage in mammalian brain after exposure to microwaves from GSM mobile phones", Environmental Health Perspectives, 2003, Vol.111, No.7, pp.881-883.
- [3] D. Mat, W. Kho, A. Joseph, K. Kipli, K. Lias, A. Marzuki, S. Sahrani, "Electromagnetic radiation towards adult human head from handheld mobile phones", International Journal of Network and Mobile Technologies, 2010, Vol.1, Issue 2, pp.60–66.
- [4] C.Kargel, "Infrared thermal imaging to measure local temperature rises caused by handheld mobile phones", IEEE Transactions on Instrumentation and Measurement, 2005, Vol. 54, Issue 4, pp.1513-1519.
- [5] E. Svitajute, A. Petrusaite, V. Veikutis, "The assessment of thermography as breast cancer screening technique", Proceedings of International Conference "Biomedical engineering", Kaunas University of Technology, 2010, pp. 206-207.

ON THE CAPACITY OF MIMO-WCDMA MULTICELLULAR NETWORKS WITH IDEAL POWER CONTROL

Panagiotis K. Gkonis¹ and George Kiokas²

1. National Technical University of Athens, Iroon Politechniou 9, Athens, Greece

2 Hellenic Air-Force Academy, Dekeleia, Attica GR-1010, Greece

e-mails: pgkonis@esd.ntua.gr, gkiokas@iccs.gr

Abstract

The goal of the study presented in this paper is to evaluate the performance of a Multiple Input Multiple Output (MIMO) network using the Wideband Code Division Multiple Access (WCDMA) physical layer protocol. In this context, several transmission techniques are evaluated. Moreover, the performance of a proposed technique that is based on the maximization of the desired signal of a Mobile Station (MS) to the total amount of interference that causes to the rest of the network is evaluated as well. As results indicate, for high data rate services this technique can achieve up to 1dB transmission power gain compared to the case where only the maximization of the desired MS's signal is considered.

1. INTRODUCTION

Modern wireless communications are coupled with high data rates over limited bandwidth areas, minimum transmission delay as well as improved Quality of Service (QoS) to mobile users. Since the adoption of the WCDMA physical layer protocol for third generation (3G) mobile wireless networks ([1]), several solutions have been proposed to further increase the spectral efficiency of these systems. 3rd Generation Partnership Project (3GPP) has recently standardized the Long Term Evolution (LTE) of 3G networks, which is an attempt to upgrade the existing infrastructure of these networks in order to support high speed data for MSs. LTE includes among others multicarrier transmission, as well as the deployment of MIMO in current networks ([2]).

In general, MIMO transmission can support either diversity combining mode or spatial multiplexing mode ([3]). In the first case, effective Bit Error Rate (BER) can be reduced, as the same information is sent and received from all links of the MIMO configuration. In the second case, independent data streams are transmitted from different transmit antennas, hence increasing the overall throughput.

However, in practical wireless orientations, effective capacity using MIMO architecture may be different than the theoretical one. The reason is that Multiple Access (MAI) interference can significantly degrade the performance of these networks. The goal of the study presented in this paper is to investigate the performance of MIMO-WCDMA networks

for complex network orientations (i.e. one tier of cells around the central cell, increased number of effective MSs). Unlike other studies, power control is performed according to 3GPP specifications in an attempt to accurately model the performance of these networks. Moreover, the performance of a proposed strategy that is based on the maximization of the desired MS's signal to the total amount of interference that causes to other MSs is evaluated as well.

The rest of this paper is organized as follows: In section 2 the MIMO-WCDMA simulator is described, while in section 3 description goes on with transmission and reception techniques for MIMO orientations. Results are presented in section 4, while concluding remarks are made in section 5.

2. MIMO-WCDMA SIMULATOR

A MIMO-WCDMA network with one tier of cells around the central cell is considered with three sectors per cell. Moreover, downlink transmission is assumed. All sectors employ conventional 120° sectors with radiation patterns as specified in [4]:

$$f(\varphi) = G_b - \min \left[12 \left(\frac{\varphi - \varphi_s}{\varphi_{3dB}} \right)^2, A_m \right] \quad (1)$$

for $\varphi_s - 60^\circ \leq \varphi \leq \varphi_s + 60^\circ$. In (1), $\varphi_s \in \{60^\circ, 120^\circ, 240^\circ\}$ is the pointing direction of the specific sector, the antenna gain G_b equals 14dBi, the 3-dB beamwidth of the antenna pattern (φ_{3dB}) is 70° and the front-to-back ratio (A_m) is 20dB.

The employed simulator is semi static; hence MSs' locations do not change during a simulation run. MSs enter the network at a sequential manner following a uniform distribution. An MS is connected to the base station (BS) with the lowest path loss (including shadowing and antenna radiation patterns). During a drop, the channel undergoes fast fading due to the motion of the MSs. For M_t antennas at the BS and M_r antennas at the MS ($M_t \times M_r$), the channel coefficient denoted as h between the q^{th} transmit antenna and the u^{th} receive antenna for the l^{th} multipath component is given by ([4]):

$$h = \sqrt{\frac{P_l \sigma_{SF}}{M}} \sum_{m=1}^M \left(\frac{\sqrt{G_{BS}(\theta_{l,m,AoD})} \exp(j[k_w d_q \sin(\theta_{l,m,AoD}) + \Phi_{l,m}]) \times \sqrt{G_{MS}(\theta_{l,m,AoA})} \exp(j[k_w d_u \sin(\theta_{l,m,AoA})])}{\sqrt{G_{BS}(\theta_{l,m,AoD})} \exp(j[k_w d_q \sin(\theta_{l,m,AoD}) + \Phi_{l,m}]) \times \sqrt{G_{MS}(\theta_{l,m,AoA})} \exp(j[k_w d_u \sin(\theta_{l,m,AoA})])} \right) \quad (2)$$

where j is the imaginary unit, P_l is the power of the l^{th} path, σ_{SF} is the lognormal shadow fading, M is the number of sub-paths per path, $\theta_{l,m,AoD}$ and $\theta_{l,m,AoA}$ are the angles of departure (AoD) and arrival (AoA) respectively for the m^{th} subpath of the l^{th} path, $G_{BS}(\theta_{l,m,AoD})$ is the BS antenna gain for each array element and $G_{MS}(\theta_{l,m,AoA})$ is the MS antenna gain for each array element for the AoD and AoA respectively. Moreover, $\Phi_{l,m}$ is the phase of the m^{th} subpath of the l^{th} path, uniformly distributed in $[0, 2\pi]$.

Finally, k_w is the wave number $2\pi/\lambda$ where λ is the carrier wavelength in meters, d_q is the distance in meters of BS antenna element q from the reference ($q = 1$) antenna and d_u and is the distance in meters of MS antenna element u from the reference ($u = 1$) antenna. The positions of the MSs, the path-losses, as well as the shadow fading remain constant during at each drop. Moreover, all AoAs and AoDs change at the beginning of each frame. Typical values for the number of multipaths and the number of subpaths per multipath are $L = 6$ and $M = 20$, respectively. All the simulation parameters are summarized in table I.

3. MIMO-WCDMA TRANSMISSION TECHNIQUES

As specified in [5], the effective Signal to Interference plus Noise Ratio (SINR) for the k^{th} MS will be given by:

$$SINR_k = \frac{P_s}{P_{ISI} + \sum_{i=1, i \neq k}^K P_{MAI,i} + P_N} \quad (3)$$

where:

$$P_{s,k} = \left(\left(\sum_{l=1}^L \mathbf{r}_{k,l} \mathbf{H}_{k,s(k),l} \mathbf{w}_k \right)^H \sum_{l=1}^L \mathbf{r}_{k,l} \mathbf{H}_{k,s(k),l} \mathbf{w}_k \right) \rho_k \quad (4)$$

$$P_{ISI} = \left| \sum_{l=1}^L \sum_{l'=1}^L \left(\mathbf{r}_{k,l} \mathbf{H}_{k,s(k),l} \mathbf{w}_k \right) \sqrt{\rho_k} \left(\rho_{k,k,l-l'} + \bar{\rho}_{k,k,l-l'} \right) \right|^2 + \sum_{l=1}^L \left(\mathbf{r}_{k,l} \mathbf{H}_{k,s(k),l} \mathbf{w}_k \sqrt{\rho_k} \right)^H \sum_{l'=1}^L \left(\mathbf{r}_{k,l'} \mathbf{H}_{k,s(k),l'} \mathbf{w}_k \sqrt{\rho_k} \right) \left(\rho_{k,k,l-l'} + \bar{\rho}_{k,k,l-l'} \right) + \sum_{l=1}^L \left(\mathbf{r}_{k,l} \mathbf{H}_{k,s(k),l} \mathbf{w}_k \sqrt{\rho_k} \right) \left(\sum_{l'=1}^L \left(\mathbf{r}_{k,l'} \mathbf{H}_{k,s(k),l'} \mathbf{w}_k \sqrt{\rho_k} \right) \left(\rho_{k,k,l-l'} + \bar{\rho}_{k,k,l-l'} \right) \right)^H \quad (5)$$

$$P_{MAI,i} = \left(\sum_{l=1}^L \sum_{l'=1}^L \left(\mathbf{r}_{k,l} \mathbf{H}_{k,s(i),l} \mathbf{w}_i \right) \left(\rho_{k,i,l-l'} + \bar{\rho}_{k,i,l-l'} \right) \right)^2 \rho_i \quad (6)$$

$$P_N = N_o \sum_{l=1}^L \|\mathbf{r}_{k,l}\|_F^2 \quad (7)$$

In (4) – (7), ρ_k is the transmission power for the k^{th} MS, $s(k)$ is the k^{th} MS's serving sector, $\mathbf{H}_{k,s(i),l}$ is the l^{th} multipath component of dimensions $M_r \times M_t$ from the i^{th} MS's serving sector to the k^{th} MS and N_o is the thermal noise power. Each element of the matrix $\mathbf{H}_{k,s(i),l}$ is calculated according to (2). Finally, \mathbf{w}_k is the $M_t \times 1$ transmit weight vector assuming diversity combining mode and $\rho_{k,i,l}$, $\bar{\rho}_{k,i,l}$ are the partial cross-correlations of the spreading sequences ([5]).

In order to exploit diversity from frequency selective fading, each MS is equipped with a 2-D RAKE receiver. The $1 \times M_r$ MRC multiplying vector is:

$$\mathbf{r}_{k,l} = \left(\mathbf{H}_{k,s(k),l} \mathbf{w}_k \right)^H \quad (8)$$

for $1 \leq l \leq L$. In this study several approaches to transmit beamforming are evaluated. With respect to [5], the performance of the uniform and random power allocation strategies, the maximization of the desired MS's signal as well as per RAKE maximization of Signal to Noise Ratio (SNR) are analysed assuming a MIMO-WCDMA orientation where power control is performed according to 3GPP specifications (i.e. closed loop power control with 1dB step). In [5], the performance of the maximization of the Signal to Jamming plus Noise Ratio was also analysed:

$$SJNR_k \approx \frac{\mathbf{w}_k^H \left(\sum_{l=1}^L \mathbf{r}_{k,l} \mathbf{H}_{k,s(k),l} \right)^H \sum_{l=1}^L \mathbf{r}_{k,l} \mathbf{H}_{k,s(k),l} \mathbf{w}_k}{\mathbf{w}_k^H \left(\sum_{i=1, i \neq k}^K \left(\sum_{l=1}^L \mathbf{H}_{i,s(k),l}^H \mathbf{H}_{i,s(k),l} \left(|\rho_{k,i,l}|^2 + |\bar{\rho}_{k,i,l}|^2 \right) \right) \right) \mathbf{w}_k} \quad (9)$$

which is a function of the desired MS's weight vector only. Hence, denoting $X_m(\mathbf{Y}_k)$ the eigenvector corresponding to the maximum eigenvalue of matrix \mathbf{Y}_k , the weight vector in the proposed transmission scheme that maximizes the SJNR ratio is given by:

$$\mathbf{w}_k = X_m(\mathbf{Y}_k) \quad (10)$$

$$\mathbf{Y}_k = \left(\sum_{i=1, i \neq k}^K \left(\sum_{l=1}^L \mathbf{H}_{i,s(k),l}^H \mathbf{H}_{i,s(k),l} \left(|\rho_{k,i,l}|^2 + |\bar{\rho}_{k,i,l}|^2 \right) \right) \right)^{-1} \times \left(\sum_{l=1}^L \mathbf{r}_{k,l} \mathbf{H}_{k,s(k),l} \right)^H \sum_{l=1}^L \mathbf{r}_{k,l} \mathbf{H}_{k,s(k),l} \quad (11)$$

At this point it should be noted that in the evaluation of the MSJNR algorithm only the co-sector MSs are included, as it is assumed that undergo greater amount of interference from the desired MS relevant to the MSs of other sectors.

4. RESULTS

All simulation parameters are summarized in Table I. Each simulation scenario consists of a network topology with one tier of cells around the central cell, while data services of 120 Kbps are also considered. Unlike [5], where power control was considered only in a frame by frame basis, in this study it is performed analytically according to 3GPP specifications. For this reason, in every frame with duration 10ms (i.e. 38400 chips assuming bandwidth equal to 3.84MHz) and 15 slots per frame, the SINR value per MS is fed back to the transmitter which decides either to increase or decrease transmission power with 1dB step in every deviation from the target SINR.

In Figures 1 and 2, in the horizontal axis is the number of active MSs per sector, while in the vertical axis is the central cell's transmission power in dBm. Note that in Figure 1 there are up to 4 MSs per sector, while in Figure 2 up to 7 MSs. For more MSs in the network then outage takes place. As it can be observed from Figure 1, where 5 dB required E_b/N_0 is assumed, then there are no significant differences among PRMSNR, MSNR and MSJNR strategies. However, from Figure 2 and 7 dB required E_b/N_0 , then for 4 active MSs there is transmission gain almost 1dB, as MSNR strategy requires 24dBm while MSJNR strategy requires 23 dBm. In this case, actual capacity is $4 \times 3 \times 120 \text{Kbps} = 1440 \text{ Mbps}$ (product of active users per sector with sectors per cell and rate per MS).

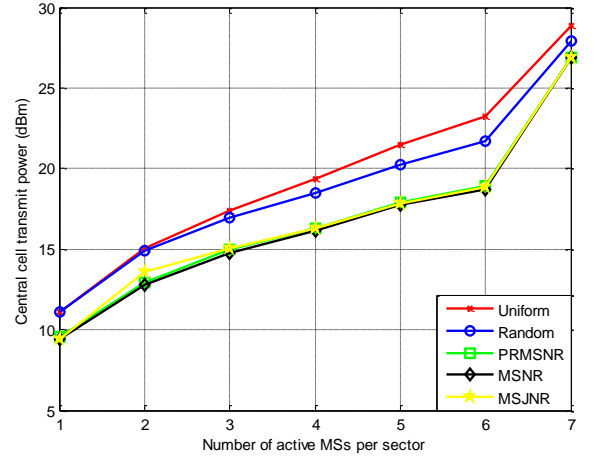


Figure 1: Total transmission power for data services of 120 Kbps and 5dB required E_b/N_0

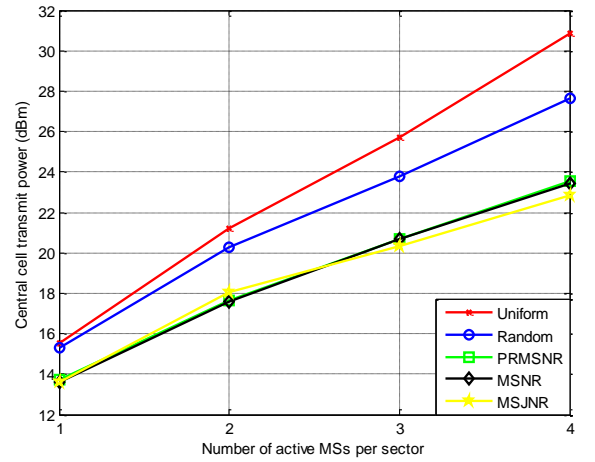


Figure 2: Total transmission power for data services of 120 Kbps and 7dB required E_b/N_0

TABLE I
SIMULATION PARAMETERS

Parameter	Assumption
Environment	Urban macrocell
Cells	7
Sectors per cell	3
Cell radius	1000 m
Carrier frequency	2 GHz
BS height	30 m
MS height	1.5 m
Propagation	Okumura - Hata, pathloss exponent 3.5
Std for shadow fading	8 dB
Power delay profile	Uniform
Number of drops (D)	1000
Frames per drop (F)	100
Bits per frame (B)	200
Multipath components (L)	6

5. CONCLUSIONS

The performance of multicellular MIMO-WCDMA networks has been analysed, according to 3GPP specifications (channel modelling and power control). Ongoing research includes among others the extension of these results for other orientations (i.e. two tiers of cells) and services as well.

References

- [1] H. Holma and A. Toskala, *WCDMA for UMTS: radio access for third generation mobile communications*, 3rd ed. John Wiley & Sons, 2004.
- [2] D. Astély, E. Dahlman, A. Furuskär, Y. Jading, M. Lindström and S. Parkvall, "LTE: The Evolution of Mobile Broadband", *IEEE Communications Magazine*, Vol. 47, No. 4, pp. 44-51, April 2009.
- [3] A. Paulraj, D. Gore, R. Nabar and H. Bolcskei, "An overview of MIMO communications - a key to gigabit wireless," *Proceedings of IEEE*, Vol. 92, No. 2, pp. 198-218, 2004.
- [4] 3GPP TR 25.996 v6.1.0, "Spatial Channel model for Multiple Input Multiple Output (MIMO) simulations", September 2003.
- [5] P. K. Gkonis, G. V. Tsoulos and D. I. Kaklamani, "Performance evaluation of MIMO-WCDMA cellular networks in multiuser frequency selective fading environments", *Wireless Communications and Mobile Computing* (Wiley), article first published online: 18/01/2011, DOI:10.1002/wcm.1096

MODELING THE SPECTRAL RESPONSE OF BRAGG GRATINGS WRITTEN IN PHOTONIC CRYSTAL FIBERS

George S. Kliros

Hellenic Air-Force Academy, Department of Aeronautical Sciences
 Division of Electronics, Electrical Power and Telecommunications Engineering
 Dekeleia Air-Force Base, Attica GR-1010, Greece
 gskliros@ieee.org

Abstract

The spectral response of photonic crystal fiber Bragg gratings (PCFG) are investigated theoretically using a full vectorial Fast Multipole Method combined with exact equations for the reflection response of the Bragg gratings. When the PCF air-holes are infiltrated with different fluids, a downward shift is observed in the power reflectivity spectra. Both relative Bragg shift and grating's bandwidth depend linearly on the effective refractive index which supports the potential use of PCFGs as liquid sensors as well as tunable filters. It is also shown that the sensitivity of PCFG is strongly influenced by the choice of the structural parameters of the photonic crystal fiber.

1. INTRODUCTION

Photonic Crystal Fibers (PCF) have recently gain a broad application in telecommunication industry as well as in the traditional sensor industry. Endlessly single mode operation, high optical nonlinearities, the freedom to engineer the chromatic dispersion and the ability to fill the cladding air holes with liquids or gases are only a few of the physical virtues that have allowed these fibers to shine in a variety of roles from fiber lasers to fiber sensors. On the other hand, as for conventional fibers, the use of Bragg gratings written in a PCF can significantly enhance the device performance in a variety of environmental, biomedical and aerospace applications.

In this paper, motivated by the recent interest in developing photonic crystal sensors [1-3], we present a numerical simulation of Bragg gratings written in a PCF, as it is shown in Fig.1, using a full-vectorial fast multimode method combined with the coupled-mode theory of gratings. The sensitivity of our device is investigated by observing the shift in Bragg resonance wavelength in the reflectivity spectrum as a function of the change in effective refractive index when the PCF-holes are infiltrated with different fluids.

2. DEVICE MODELING

2.1. COUPLED-MODE THEORY OF BRAGG GRATINGS

In order to calculate the characteristics of uniform PCF Bragg Gratings (BG), the coupled-mode theory is applied. The PCF-BGs is considered longitudinally invariant, while a perturbation is introduced in the core region according to the relation:

$$\epsilon_r(\mathbf{z}) = \epsilon_{rs} + D\epsilon_{rs}(\mathbf{z}) \square n_s^2 + 2n_s \delta n_{eff}(\mathbf{z}) \quad (1)$$

where n_s is the refractive index (RI) of pure silica with a wavelength dependence given by the Sellmeier's equation

$$n_s(\lambda) = \left(1 + \sum_{j=1}^3 A_j \frac{\lambda^2}{\lambda^2 - \lambda_j^2} \right)^{1/2} \quad (2)$$

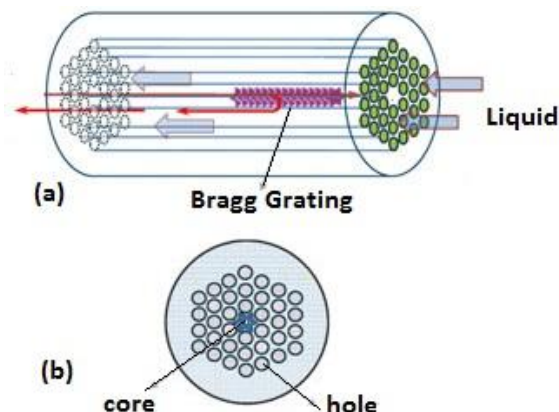


Figure 1. (a) Schematic of a photonic crystal fiber Bragg grating (b) Cross-section of the PCF.

where for A_j and λ_j are material constants with values: $A_1=0.6961663$, $A_2=0.4079426$, $A_3 = 0.8974794$, $\lambda_1=0.0684043$, $\lambda_2=0.116241$ and $\lambda_3 = 9.896161$.

For a uniform grating without chirp, the refractive index modulation can be written as

$$\delta n_{eff}(z) = \overline{\delta n_{eff}} \left[1 + v \cos\left(\frac{2\pi}{L_G} z\right) \right] \quad (3)$$

with $\overline{\delta n_{eff}}$ being the averaged refractive index change over one period, v is the fringe visibility of the index change, L_G is the period of the grating perturbation and z is the propagation distance.

In most uniform BG sensor application, only the reflection spectra of the BG are considered and the dominant interaction is between the forward propagating fundamental core mode and its counter propagating mode. Then, the system of coupled-mode equations has analytical solution [4] which leads to the following closed-form expression for the power reflection coefficient $r(L, \lambda)$ of a uniform fiber grating of length L .

$$r(L, \lambda) = \frac{\sinh^2\left(\sqrt{\kappa^2 - \hat{\sigma}^2} L\right)}{\cosh^2\left(\sqrt{\kappa^2 - \hat{\sigma}^2} L\right) - \frac{\hat{\sigma}^2}{\kappa^2}} \quad (4)$$

In Eq.(4), κ is the 'ac' coupling coefficient and $\hat{\sigma} = \sigma + \delta$ where σ is a generalized 'dc' self-coupling coefficient and the detuning parameter δ is defined as:

$$\delta \equiv \beta - \frac{\pi}{\Lambda_G} = 2\pi n_{eff} \left(\frac{1}{\lambda} - \frac{1}{\lambda_D} \right) \quad (5)$$

where λ_D is the design wavelength of the grating. For a single-mode reflection grating, the coupling parameters are given by the following simple relations:

$$\sigma = \frac{2\pi}{\lambda} \overline{\delta n_{eff}}, \quad \kappa = \frac{\pi v}{\lambda} \overline{\delta n_{eff}} \quad (6)$$

From Eq.(4), we find the maximum reflectivity for a Bragg grating is

$$r_{max} = \tanh^2(\kappa L) \quad (7)$$

which occurs at the 'Bragg wavelength'

$$\lambda_B = \left(1 + \frac{\overline{\delta n_{eff}}}{n_{eff}} \right) \lambda_D \quad (8)$$

A measurable bandwidth for the uniform Bragg grating is that between the first zeros on either side of the maximum reflectivity and is given by

$$\frac{D\lambda}{\lambda_D} = \frac{v \overline{\delta n_{eff}}}{n_{eff}} \sqrt{1 + \left(\frac{\lambda_D}{v \overline{\delta n_{eff}} L} \right)^2} \quad (9)$$

2.2. FAST MULTIPOLE METHOD

Multipole method (MPM) is a simulation method which is based on the principle of electromagnetic scattering properties for PCF. The method was first proposed by White and Kuhlmeier [5] for the simulation of PCF with circular holes. According to MPM the mode field is expanded by Fourier-Bessel function in the ℓ^{th} - hole, as

$$E_z = \sum_{m=-\infty}^{\infty} a_m^{(\ell)} J_m(k_{\perp}^i r_{\ell}) \exp(jm\varphi_{\ell}) \exp(j\beta z) \quad (11)$$

and in the adjacent medium of the circular ℓ^{th} - hole, the mode field is expanded as

$$E_z = \sum_{m=-\infty}^{\infty} \left[b_m^{(\ell)} J_m(k_{\perp}^s r_{\ell}) + c_m^{(\ell)} H_m(k_{\perp}^s r_{\ell}) \right] \times \exp(jm\varphi_{\ell}) \exp(j\beta z) \quad (12)$$

where

$$k_{\perp}^i = (k_0^2 n_i^2 - \beta^2)^{1/2}, \quad k_{\perp}^s = (k_0^2 n_s^2 - \beta^2)^{1/2} \quad (13)$$

n_i and n_s the refractive indexes of air and silica, respectively, $k_0=2\pi/\lambda$ is the free space wave-number and, β is the modal propagation constant. Magnetic field component H_z can be expressed by similar equations to Eqs. (11) and (12). We can obtain the relation between $a_m^{(\ell)}$, $b_m^{(\ell)}$, $c_m^{(\ell)}$ applying the electromagnetic field boundary conditions and then, the modal effective refractive index can be calculated as $n_{eff}=\beta/k_0$. Vector-based computations are employed instead of element-based ones using MATLAB technical language in order to reduce the computation time considerably.

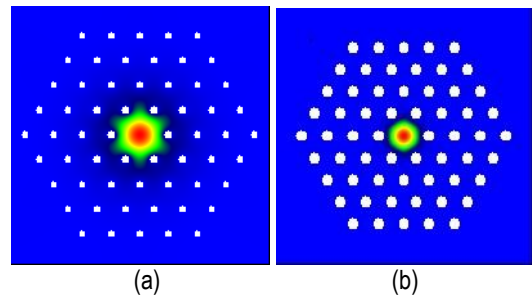


Figure 2. Energy flux distribution for the fundamental mode in PCF with air-holes of diameter a) $d/\Lambda=0.2$ and b) $d/\Lambda=0.4$ at the wavelength $\lambda=1.55 \mu\text{m}$.

3. RESULTS AND DISCUSSION

The PCF used to inscribe the Bragg grating has a structure with hexagonal symmetry with four layers of air-holes in the silica matrix and a missing hole in the center. The hole pitch is $\Lambda=2.3 \mu\text{m}$ and the ratio of hole diameter over pitch d/Λ is chosen to meet the condition of single-mode transmission. The structure of the PCF under study and the energy flux distribution of the fundamental mode calculated by MPM, for two different ratios $d/\Lambda=0.2$ and 0.4 , is depicted in Fig.2(a) and (b), respectively. It is clear from this figure that at larger ratios d/Λ the modes tends to be more confined in the core part of the structure. Furthermore, we consider the following parameters for the uniform grating written in the PCF-core: initial design wavelength $\lambda_D=1.55 \mu\text{m}$, refractive index modulation of $\delta n_{\text{eff}}=8.0 \times 10^{-4}$, visibility of the index change $v=0.02$ and grating length $L=70 \text{ mm}$.

In order to explore the spectral sensitivity of Bragg gratings written in the PCF, several fluids with refractive indexes varied from 1.25 (salol) to 1.40 (octane), are inserted into the holes. The effective RI of the guided fundamental mode in the PCF infiltrated by fluids, as a function of the operational wavelength, is calculated by MPM and the results are shown in Fig. 3. The red dots in Fig. 3 correspond to the effective refractive indexes at the design wavelength $\lambda_D=1.55 \mu\text{m}$.

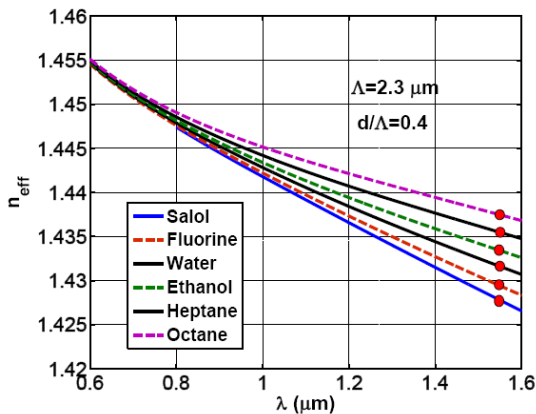


Figure 3. Energy flux distribution for the fundamental mode in PCF with air-holes of diameter a) $d/\Lambda=0.2$ and b) $d/\Lambda=0.4$ at the wavelength $\lambda=1.55 \mu\text{m}$.

Then, the power reflection spectra of the Bragg grating can be calculated using Eq.(4) as it is shown in Fig.4 for PCFs infiltrated by three different fluids.

The insertion of a fluid changes the cladding RI and modifies strongly the interaction between the

evanescent field of the guided mode and the medium in the holes. The effective index of the guided mode increases together with the RI of the holes. As a result, when a given fluid reaches the grating, the Bragg resonance experiences a downward shift, as depicted in Fig. 4. Additionally, it was found that the maximum reflectivities are almost the same. The Bragg wavelength λ_B at which the maximum reflectivity occurs can be calculated by Eq.(8).

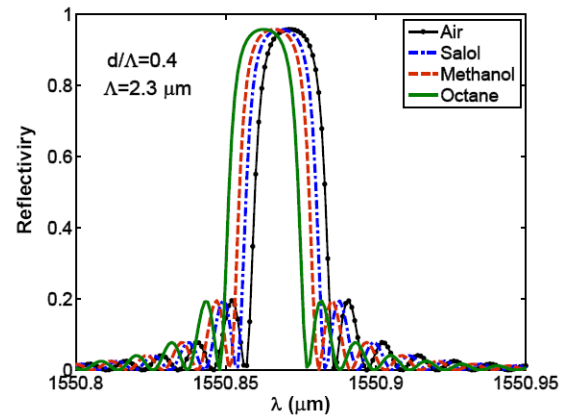


Figure 4. Computed power reflectivity spectra when different liquids are inserted in the PCF air-holes.

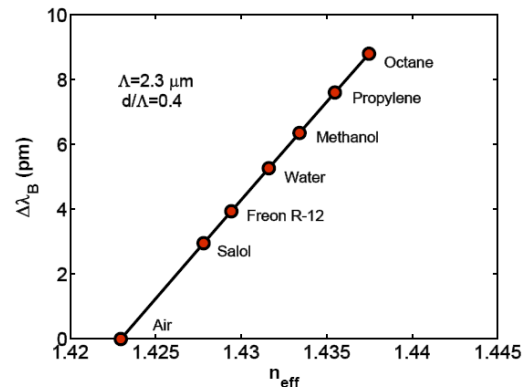


Figure 5. Sensitivity characteristic curve showing the simulated changes in Bragg wavelength versus the effective RI.

Figure 5 shows the relative Bragg wavelength shift as a function of the fluid RI, where the reference wavelength is taken the Bragg wavelength for air-filled PCF holes. It is worthy to note that the Bragg shift, although relatively weak, is linear and hence, the device is extremely suitable for sensor applications. Moreover, Fig. 6 shows the linear dependence of the relative bandwidth on the effective RI.

Finally, we explore the dependence of relative Bragg shift on the ratio d/Λ , for a PCF grating with air-filled holes. As it is seen in Fig. 7, the relative Bragg shift increase as the hole diameter increases.

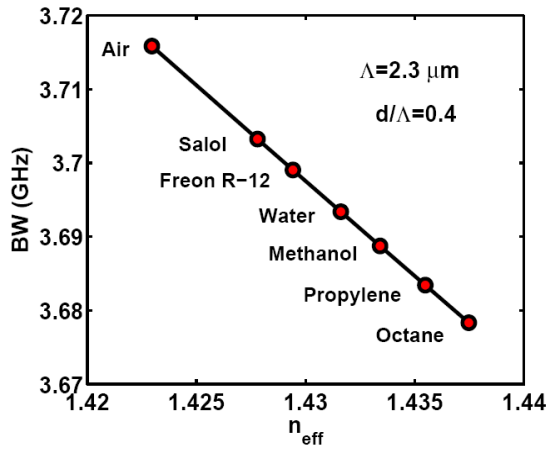


Figure 6. Bandwidth of the PCF Bragg grating versus the effective RI

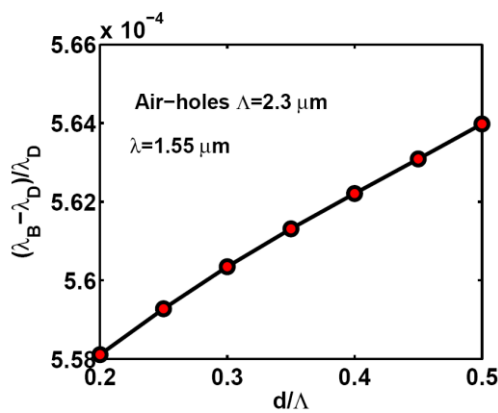


Figure 7. Relative Bragg shift of the PCF grating versus air-hole diameter.

4. CONCLUSION

The characteristics of PCF Bragg gratings are simulated utilizing a full-vectorial multipole method combined with coupled mode theory. For the design wavelength of $\lambda_D \sim 1.55 \mu\text{m}$, the reflectivity spectrum has been explored by filling the holes of PCF with different fluids. The shift in both the Bragg wavelength and bandwidth is found to be linear and hence, the device can be used as fluidic sensor or as tunable filter

References

- [1] O. Frazão et. al., Optical Sensing with Photonic Crystal Fibers, *Laser and Photonics Reviews*, Vol. 2 (6), 2008, pp. 449-459.
- [2] G. Kliros, K. Papageorgiou, Refractometric Optical Sensor based on Tapered Photonic Crystal Waveguide, *Journal of Optoelectronics and Advanced Materials*, Vol.12 (7), 2010, pp. 1530-1533.
- [3] G. Kliros, K. Papageorgiou, Fdtd Modeling of Refractometric Optical Sensors based on Quasi-1D Photonic Crystals, *Journal of Applied Electromagnetism (JAE)*, Vol.12 (3), 2010, pp. 39-45.
- [4] A. Othonos, K. Kalli, *Fiber Bragg Gratings: Fundamentals and Applications in Teleco-munications and Sensing*. Norwood, MA: Artech House, 1999.
- [5] T.P. White et. al., Multipole method for microstructured optical fibers, *J. Opt. Soc. Am. B*, Vol. 19 (10), 2002, pp. 2322-2340.

THE PERFORMANCE OF A MODULATION PASSIVELY Q-SWITCHED SOLID – STATE LASER PUMPED BY LASER DIODE, FOR FREE – SPACE LASER COMMUNICATIONS

¹Jassim Mohammed Jassim, ²Yaseen Hiassn Kadhim, ¹Ahmed Kadem Kodeary

¹Laser Physics Department, College of Science for Woman, Babylon University, Iraq.

² Physics Department, College of Science, Babylon University, Iraq.

E-Mail: jassimm2007@yahoo.com

Abstract

The aim of this project is to demonstrate a simple method of a multiple-frequency operation of passively Q- switched Nd: YAG optically pumped by an RF modulation Injection Laser Diode (ILD) at (808 nm wavelength), and controllable repetition rate (100 Hz – 4 KHz). A stable gain –switched pulse train of (1.064 nm) wavelength is obtained with a maximum repetition rate of 4 KHz and (17 ns) pulse duration.

Key words: Modulation, free-space communication, Q- switch

1. INTRODUCTION

Free-space optical communication (FSO) systems (in space and inside the atmosphere) have developed in response to a growing need for high-speed and tap-proof communication systems. Links involving satellites, deep-space probes, ground stations, unmanned aerial vehicles, high altitude platforms, aircraft, and other nomadic communication partners are of practical interest. Moreover, all links can be used in both military and civilian contexts. FSO is the next frontier for net-centric connectivity, as bandwidth, spectrum and security issues favor its adoption as an adjunct to radio frequency (RF) communications [1]. The optical carrier can be modulated in its frequency analog or digital. Analog modulation simply means that waveform is continuously varying in amplitude. A sine wave is a perfect example. Digital modulation, on the other hand, implies a discontinuous change in amplitude. A Square wave is the prime example of digital modulation [2]. Communication system consists of three main units, a transmitter, propagation medium and receiver [3]. Today, diode-pumped solid-state lasers it's used as transmitter, they offer significant advantages in terms of efficiency, compactness, lifetime and high beam quality. So satisfy requirements (FSO) [4].

2. OPTICAL SIGNAL LINK ANALYSIS

The overall system performance of a lasercom is quantified using a link budget derived from the ran-

ge equation, which combines attenuation and geometrical aspects to calculate the received power. The process of finding the link margin through the system link calculation transmitter power, propagation losses, receiver sensitivity. The receiver's sensitivity determines the amount of received optical power needed to achieve the required signal-to-noise ratio (SNR) for a given expected communication performance [6]. The purpose of this section is to develop the parameters necessary to calculate the performance of an optical communication link. We shall consider the situation of optical propagation between points in free-space. Consider a laser transmitter antenna with gain G_T transmitting a total power P_T at the wavelength. The signal power received (P_R) at the communications detector can be expressed (from the range equation) [7].

$$P_R = P_T T_{ATM} G_T G_R (\lambda/4\pi L)^2$$

where P_T is the power transmitted, T_{ATM} is the value of the atmospheric transmission at the laser transmitter wavelength (λ), G_T is the transmitter antenna gain

$$G_T = 16/(\theta_T)^2$$

where θ_T is the full transmitting divergence angle, G_R is the receiver antenna gain

$$G_R = (\pi D_R/\lambda)^2$$

where D_R is the receiver diameter, and where L is the link range. Normally an optical link typically consists of two transceivers, each made up of one (or

more) transmitting laser and receiving photo detector. Transmitting optics (telescope, lenses, mirrors) shape the transmitted laser beam which is collected by the receiver optics so that the received signal is focused onto the photo detector. The parameters of the communications are chosen so that sufficient signal from the lasers on one transceiver reaches the photo detector on the other transceiver through the atmosphere to differentiate ones (signal) and zeros (no signal) with negligible error [8]. If Given a laser transmitter power P_T , with transmitter divergence of θ_T , receiver telescope area A , transmit and receive optical efficiency T_{opt} , the achievable data rate R can be obtained from [9].

$$R = \frac{P_T T_{opt} T_{ATM} A}{\pi (\theta_T / 2)^2 L^2 E_p N_b}$$

where $E_p = hc/\lambda$ is the photon energy and N_b is the receiver sensitivity in photons/bit.

3. EXPERIMENTAL SETUP

Fig. 1 shows a schematic of our experimental Setup. A (0.1 %) doped, Nd:YAG crystal with diameter of 5 mm and length of 5 mm, was utilized as laser medium. Both ends of the crystal were parallel, which created a flat-flat cavity. A coating a highly reflective at the laser wavelength of 1064 nm, has been vapour deposited onto one end of the rod that also forms the left resonator mirror. The vapour deposited system of layers is designed such that the maximum pump-light radiation can penetrate the highly reflective layer with only 20% losses. The other end of the rod has a vapour deposited, high-quality antireflex layer for 1064 nm in order to keep the internal resonator losses as low as possible. The pump source (ILD) at 808 nm, which operates in either CW mode or pulsed mode. A Peltier's cooling element for the control of the diode temperature and a thermistor for the measurement of the temperature are all located inside the laser diode. The (ILD) output beam was collimated and focusing onto the Nd:YAG crystal by sequence of three lens system it consists of a three-lens system with a short focal length ($f=6$ mm) in addition to a focal length of 60 mm lens. The Nd- YAG output beam was filtered by a narrow band pass interference filter to reject the (ILD) wavelength (808 nm) and allow the (1.064 nm) only. Which is then detected by a PIN Photo diode and displayed by a storage oscilloscope.

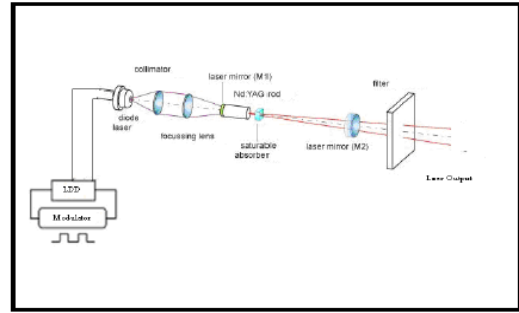


Fig. 1. Schematic of experimental Setup

4. RESULTS

4.1. Modulation Laser Diode

Light output of a laser diode can be directly modulated. The laser output is either amplitude or pulse modulated by controlling the current flow through the device. In figure 2 a,b shows the photodetector output of laser pulse modulated at low frequency (100 Hz) and high frequency (4 KHz) channel 2 (yellow trace). Channel 1 (red trace) is the input modulation signal.

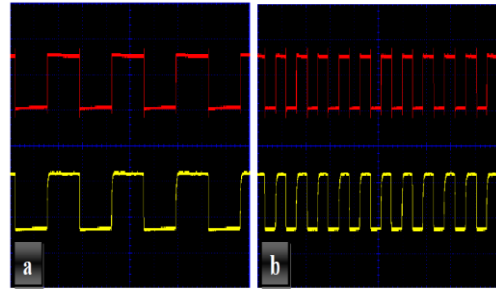


Fig. 2. Digital modulation signals of laser diode, (a) at low frequency, (b) at high frequency.

4.2. Pulse Repetition Rate (PRR)

The life time of the upper state of the active medium is very important parameter to limited the PRR of DPSSLT. Increased the life time decrease the PRR. The life time for active medium (Nd:YAG) used in this system is measured about (230 μ s) as shown in figure (3), which mean that the DPSSLT can controlled about (4.3 KHz).

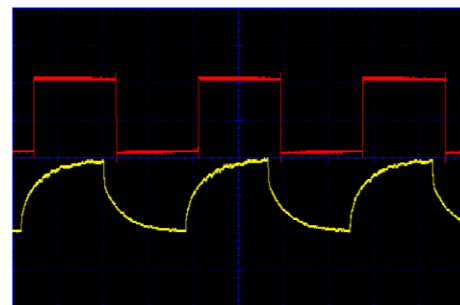


Fig. 3. Signals of the fluorescence life time level for Nd: YAG laser

4.3. Modulation DPSSSLT

Fig. 4a shows the photodetector output of a laser modulated by low frequency (100 Hz) digital signal Channel 2 (yellow trace). Hence at free – running mode, the pulse duration of laser is in microsecond. Channel 1 (red trace) represents the input modulation signal (ILD) pumping source. Fig 4b shows the high frequency (4 KHz) modulation case.

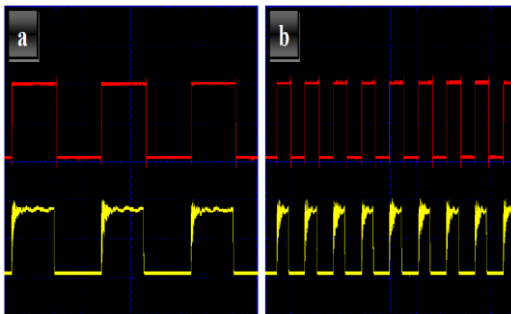


Fig. 4. Digital modulation signals free -running Nd:YAG laser, (a) at low frequency, (b) at high frequency

Fig. 5 show the output gain –switched pulse train with stable peak values, narrow pulse duration at the low frequency (100 Hz), channel 2 (yellow trace) in fig. (5a) and high frequency (4 KHz) channel 2 (yellow trace) modulation case in fig. (5b). Correspondingly the diode laser output is a rectangle pulses, channel 1 (red trace).

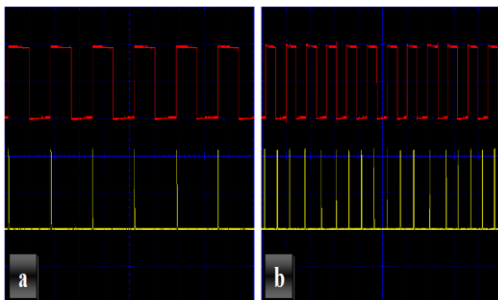


Fig. 5. Digital modulation signals, gain switched, (a) at low frequency, (b) at high frequency.

4.4. Optical signal link and data rate calculations

At the system parameters such as laser power, gain receiver, gain transmitter operation wavelength and visibility conditions, which are calculated the received power with versus link range atmosphere transmitter. As shown in the fig. 6, $T_{ATM} = 0.9$ is available for clear condition for the system operation over a (2Km) span, for $T_{ATM} = 0.6$ over a (1.5 Km) span, for $T_{ATM} = 0.4$ just under a (1 Km) span.

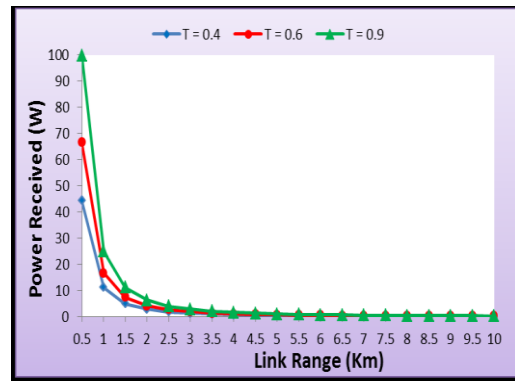


Fig. 6. Power received as a function of link range for three atmospheric conditions

Fig. 7 illustrates available optical data rate versus link range for the same system parameters. As shown in this figure, the link is available for very clear condition for the system operating over a 3.5-km span, for clear weather over a 3 km span, and for bad weather just under a 2.5-km span. The curve shows how system operation, parameters defining channel capacity can be varied to accommodate link availability under varying atmospheric conditions.

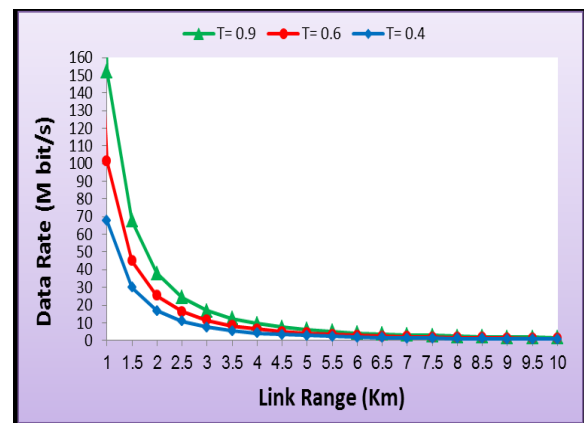


Fig. 7. Data rate as a function of link range for three atmospheric conditions

5. CONCLUSION

The Passively Q-switched Nd:YAG laser (1.064 nm) pumped by an RF modulated (ILD) demonstrated as stable pulse repetition rate of (100 Hz-10 KHz) and a pulse width of (17 ns). The pulse width and the modulation frequency dependence of the passively Q-switched, repetitively modulated laser output vs. the diode pump power for Nd:YAG crystals. Choosing the proper pumping current & pulse width makes system usable in a (FSOC) system.

References

- [1] E. Kozachenko ,and M. Anderson, "A Free Space Optical Communications System", IEEE Journal, Vol. 1, No. 3, (2011), PP. 195- 201.
- [2] H. G. yong, C. C. ying, and C. Z. qiang, "Free-Space Optical communication using visible light", Journal of Zhejiang University, Vol.8, No.2, (2007),PP.186-191.
- [3] H. HENNIGER , "An Introduction to Free-space Optical Communications", Radio engineering, VOL. 19, NO. 2, (2010).
- [4] K. Morrison and M. Sosa, "Application of COTS High Speed 980 nm Pump Laser Diode and Driver for Free Space Laser Communication Terminal", SPIE, Vol. 3708, April (1999).
- [5] V. Chan, "Free-Space Optical Communications", Journal of Lightwave Technology, Vol. 24, No. 12, (2006), PP.4750-4762.
- [6] G. Gilbreath and W. Rabinovich, "Research in Free Space Optical Data Transfer at the U. S. Naval Research Laboratory", Journal SPIE, Vol. 5160, No.4, (2004), PP.225-233.
- [7] A. Komaee, P. Krishna, and P. Narayan, "Active Pointing Control for Short Range Free-Space Optical Communication", Communications in Information and Systems Journal, Vol.7, No. 2, (2007) , PP. 177-194.
- [8] D. Aviv, "Laser Space Communications", ARTECH HOUSE, USA, (2006).
- [9] R. E. Ziemer and W. H. Tranter, "Principle of communications, systems, modulation, and noise", Wiley, New York, (1995).

A RETICULE DESIGN TO ENHANCE THE DETECTION RANGE OF A TELESCOPE FOR MOVING OBJECTS

R. N. Ali, Ghaleb. A. Al-Dahash

University of Babylon/College of Science for Women. Iraq.

Abstract

In this work a stationary opto-mechanical reticule is designed to be utilized with a terrestrial telescope to improve its detection range for moving objects. The design calculations based on the psycho-physical characteristics of the human eye. The results obtained show that the optimum ocu-reticule co-performances may be obtained for the case where the object angular velocity fluctuates between (10^{-2} rad/s) and ($5 \cdot 10^{-2}$ rad/s), or may be extended with certain limits, to a decade more or less than the pronounced value.

1. INTRODUCTION

The purpose of an optical instrument is to improve the performance of the eye by improving the details perceived in the observed scene especially under low contrast. Some magnification of the object makes it easily identifiable but the field of view is usually reduced in proportion. If magnification exceeds the diffraction limit no further enhancement of details is possible. In any optical system design the magnification has to be considered with all other interdependent factors which often lead to a compromise. In general, relatively lower magnifications and larger fields of view are used for surveillance instruments, whilst relatively higher magnifications and smaller fields of view are necessary for target acquisition. However, the question now is, for an optical design of a telescope, is there any probability of enhancing its detection range? The answer may be given in the following theoretical proposal in this paper.

2. THEORY

Considering the visual system as a part of a communication system, the transfer, spatial, and temporal characteristics are the most important parameters of interest, while the noise of the system, usually, considered next in importance where in conjunction with the other parameters, sets the limits on the system performance. The study of these parameters is usually based on psychophysical concepts.

2.1. Spatial Characteristics

In the optical stage diffraction, aberration, and scattering contribute to the spreading of the light in

the retinal image of a point source. The total diameter of the point spread function, (PSF) for white light, and a pupil diameter of (2 mm), is found to be approximately one arc minute, while it almost equal to the Airy disc⁽⁴⁾. However, for this case, about half of the image flux falls within a radius of (1.2 mm) of point source image. The radius is doubled for a (6.6mm) pupil diameter⁽⁵⁾.

Spatial threshold performance of an optical system is usually stated in terms of resolution. It is the system ability to separate or resolve two close objects, that is, to recognize them as two. In vision, the term acuity is often used instead. The visual acuity of the eye is a measure of its ability to perceive details in a scene and it is the ophthalmic analogue of the resolution. Acuity is defined as the reciprocal of the visual angle subtended, at the eye, by the resolved object details. When the visual angle is measured in minutes of arc, the reciprocal is called decimal acuity⁽⁶⁾.

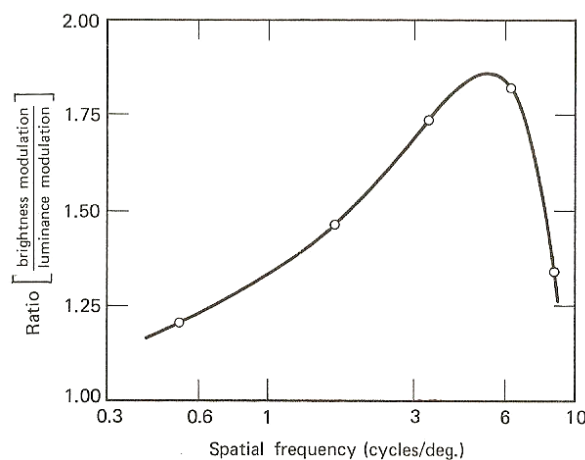


Fig. 1. Brightness-to-Luminance Ratio
{After Ref. (8)}

The reciprocal of the threshold contrast is called the contrast sensitivity. It represents the spatial

frequency response of retina-brain section of human visual system⁽⁸⁾, that is, the optical transfer function, (OTF), of the visual system.

Contrast sensitivity maximizes at (1-6 cycles/deg), fall off at lower frequencies due to ocular and at low frequencies due to aberrations, diffraction, and finite receptor size, Fig. (1).

2.2. Temporal characteristics

The frequency, of periodic signals, at which the flicker ceases to be perceptible, is called the critical flicker frequency (CFF). The flicker phenomenon is often described by means of de-Lange curve, which show the threshold modulation as a function of (CFF), Fig. (2)⁽⁹⁾. At intensity levels above (0.5 Td) these curves start at a threshold modulation of (0.6-0.7) at low frequencies, rise to a peak some where between (5 & 20 Hz) and then drop rapidly.

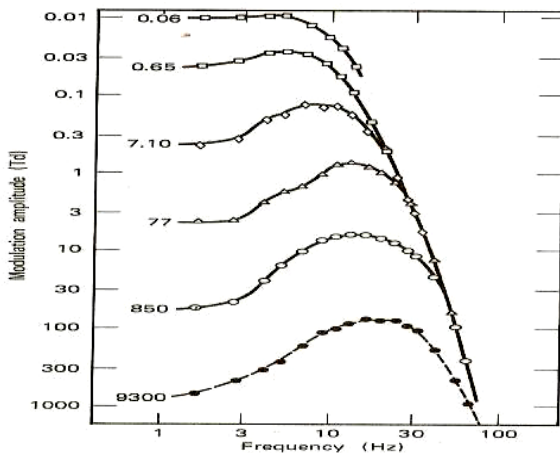


Fig. 2. Threshold Modulation as a function of CFF {After Ref.(9)}

The frequency response of the visual system is another characteristic of spatiotemporal behavior, signals varying sinusoidally both in time and space. Suprathreshold experiments showed that at low frequencies (~ 2 Hz) the perceived modulation of sinusoidal luminance pattern was more than two folds. While at (~ 5 Hz) it appeared to be equal to that of the steady pattern, and at (10-20 Hz) it dropped to about half this value⁽¹⁰⁾.

Ocular motion is another important example of the spatiotemporal interaction where any motion of the eye, while viewing a bar pattern, resulting in image motion across the retina will translate the spatial pattern into a temporal one. The eye's motion prevents the fading of the image, which quickly disappears when it is stabilized on the retina. The coupling between spatial and temporal effects in-

duced by the eye motion optimizes the visual response to luminance fluctuation and the ocular scanning may contribute to edge enhancement⁽¹¹⁾.

2.3. The Spectral Characteristics

A representative curve of the change in wavelength, required to make the difference just noticeable, is plotted as a function of wavelength in Fig. (3)⁽¹²⁾. It shows that the maximum sensitivity appears, mainly at the wavelengths (0.49 μm) and (0.59 μm) and also at (0.44 μm).

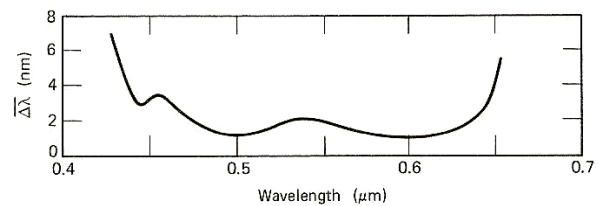


Fig. 3. Human's eye Spectral Sensitivity {After Ref. (12)}

3. UTILIZATION OF A RETICULE IN A TELESCOPE

A reticule is an opto-mechanical chopper, occasionally it referred to as an episcotister⁽¹³⁾. It suppresses unwanted signal from the background of the object scene by converting a DC-signal to an AC-one, that is, improving the signal-to-noise ratio. The use of a reticule to increase the detectability of a particular target in the presence of extraneous background details is called spatial filtering. This type of filtering is used to enhance the signals from object of larger subtending angles. The reticule is placed at the image plane of the optics, and its center coincides with the optical axis. There must be a relative movement between the reticule and the object's image. Therefore two types of reticules may be used to initiate this relative motion, a rotating reticule or stationary reticule.

The movement of the object across the spatial patterns of the reticule creates temporal frequencies while improves the eye response, within certain limits, and an enhancement in the detection range of the overall optical system is expected.

3.1. A Suggested Design for a Reticule Pattern

A suggested reticule pattern designed for a tripod binocular terrestrial telescope is described below. Its field of view (7 deg.) and focal length (280

mm), that is, the image plane diameter is about (34.25 mm). A proper reticule pattern for this case is of a concentric annular circles Fig. (6). These annular circles are divided into three groups of different spatial frequencies which are successively increasing toward the reticule center.

The external group consists of five concentric circles of one millimeters width for each of them. they are ordered in pairs, from the external circle toward the center, alternatively, as a transparent – semitransparent annular circles are made yellowish, the complement of the blue color, where the sensitivity for the eye, at these wavelengths at, the low spatial frequencies, is the best as indicated in Fig. (3). The spatial frequency is made to be (2.5 cycles/deg.) (or 0.5 cycles/mm). The spatial frequency of this the intermediate group is doubled (5 cycles/deg). Similarly the internal group spatial frequency is (6.25 cycles/deg).

3.2. The Temporal Frequency Calculations

If the object under investigation crossing the scene at an angular velocity, ω , then the temporal frequency u^t , results from crossing the image reticule's annular rings, can be estimated using the relation⁽¹⁴⁾.

$$u^s f \omega = u^t \tag{3.1}$$

where f is the focal length and u^s , the spatial frequency of the reticule, for each group of its annular rings.

The temporal frequencies produced at external group of the annular circles ($u^s = 2.5 \text{ c/deg.}$) varies from (1.4 Hz for $\omega = 0.01 \text{ rad/s.}$) to (14 Hz for $\omega = 0.1 \text{ rad/s.}$) For the intermediate group ($u^s = 5 \text{ c/deg.}$), the temporal frequencies fluctuates between (2.8 Hz for $\omega = 0.01 \text{ rad/s}$) and (33.6 Hz (for $\omega = 0.1 \text{ rad/s}$). Finally the calculated temporal frequencies for inner group of the annular rings ($u^s = 6 \text{ c/deg}$) fluctuate between (3.4 Hz for $\omega = 0.01 \text{ rad/s}$) and (17 Hz for $\omega = 0.05 \text{ rad/s}$).

The spatial frequencies have been selected to fit the band of the best spatial response of the eye, that is (1-6) cycles per degree. Consequently the temporal frequencies obtained fluctuate between (1.4 Hz and 16.8 Hz) in the range of angular velocities of (10^{-2} rad/s) to ($5 \cdot 10^{-2} \text{ rad/s}$). However the best response of the eye to the temporal frequencies (2-5 Hz) and the critical flicker frequency is about (20 Hz).

4. DISCUSSION

The results obtained in this work are utilized in a suggested design of a reticule pattern that can be applied to terrestrial or astronomical telescopes to improve their detection ranges against moving objects.



Fig. 4. The Reticule Design

The reticule design is illustrated in Fig. (4). Calculations of the spatial and temporal frequencies results utilized in this reticule are summarized in Fig. (5).

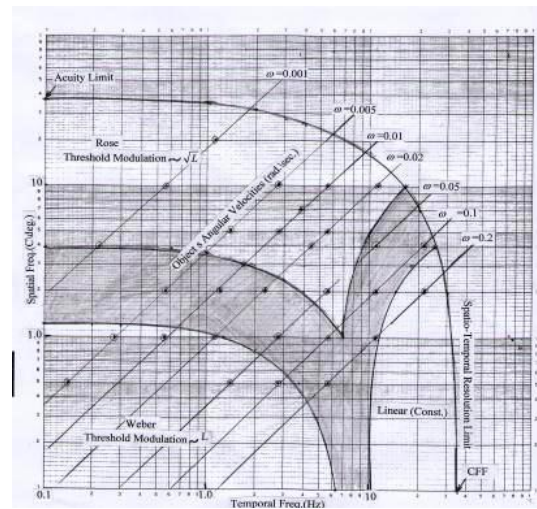


Fig. 5. The applicable range of the targets angular velocities

The device performance against moving objects can be deduced from this figure. The ranges of object's angular velocities that expected to induce the optimum performance of the eye-telescope system fluctuates between ($5 \cdot 10^{-2} \text{ rad/s}$) and (10^{-2} rad/s). The best performance may be obtained at the angular frequency ($2 \cdot 10^{-2} \text{ rad/sec}$), where spatial frequencies of (1 to 6 c /degree), the optimum response of the human eye, produce temporal frequencies of (1.12 Hz) to (6.72 Hz). This is approximately fulfills the requirements of the human-eye

response to the temporal frequencies (2-5 Hz). However, one may work properly in the spatial frequency range of about (1-8 c/deg), and temporal frequency range of about (1-9Hz). It can be seen from Fig (7) that these frequency ranges located at the Rose region of the threshold –luminance relationship, that is threshold modulation is proportional to the square root of the object luminance. The relation between the ratio of the brightness modulation to luminance modulation, and the spatial frequencies is illustrated in Fig 1), which shows that the best ratio, takes place at the spatial frequency (6 cycles/degree), is about (1.8)

References

- [1] Mansfield, R. J. W., (Brightness Function: Effects of Area and Duration), J. Opt. Soc. Am.63, 913-920, (1973).
- [2] Cornsweet T. N., (Visual Perception), Academic Press New York, (1974).
- [3] Campell F. W. and R. W. Gubish, (Optical Quality of the human-Eye), J. Physiol. (London.) 186,558-578, (1966).
- [4] Fry, G. A. (The Optical performance of the human eye),
- [5] Progress in optics, Vol. 8, E. Wolf, Ed., North- Holland, Amsterdam, (1970).
- [6] Rodgers A. L. et al (Surveillance and Target Acquisition system), Brassey's Defense Publishers Ltd., (1983).
- [7] Levi, L. (Applied Optics, A Guide to Optical system Design), Vol.2, John Wiley and sons,Inc. VSA,(1980).
- [8] Campell, F.W. (The Human Eye as an Optical Filter), Proc. IEEE 56,1009-1014,(1968).
- [9] Patel, A. S. (Spatial Resolution by the Human Visual System: The Effect of mean retinal illuminance), J. Opt. Soc. Am., 56,689-694, (1966).
- [10] De Valois R. L. and MORGAN, H. (Psycho physical studies of Monky Vision.III. Spatial Luminance Contrast Sensitivity Test of Macaque and Human Observer), Vision Res.14, 75-81,(1974).
- [11] De Lange, H. (Research in to the Dynamic Nature of the Human Fovea –Cortex
- [12] System with intermittent and Modulated Light. I- Attenuation characteristics with white and colored Light), J. Opt. Soc.Am.48, 774-784,(1958).
- [13] Kelly, D. H. (Visual response to time – dependent stimuli), J. Opt. Soc. Am. 51,422-429,(1961).
- [14] Hiltz, R, and Cavanaugh, C. R., (Wavelength Discrimination Measured with Square-Wave Gratings), J. Opt. soc. Am, 60, 273-277,(1970).
- [15] Biberman, L. M. (Reticles in Electron–optical device), New York, Pergamon, (1966).
- [16] Ali, R. N. (Design Study on Laser Guidance System Employing an Optical Reticule) A Ph. D. Thesis University of Technology Baghdad Iraq (2004).

OPTIMUM DIVERGENCE OF LASER RADIATION IN FSO SYSTEMS

Tsvetan Mitsev, Kalin Dimitrov, Hristo Ivanov, Nikolai Kolev

Faculty of Telecommunications, Technical University of Sofia,
8 Kliment Ohridski Blvd., 1000 Sofia, Bulgaria,
E-mail: mitsev@tu-sofia.bg

Abstract

The necessity for higher information capacity and for better operational reliability of FSO systems require more precise selection and adjustment of their parameters. Many factors cause random fluctuations in the direction of propagation of the transmitter radiation, respectively, in the angle of incidence of the optical flow on the receiving aperture. Due to this effects is drawn a serious deterioration in the quality of transmitted information and reducing of the reliability of systems. A significant improvement can be achieved by determining of the optimum divergence of the transmitter optical beam in FSO systems under specific operating conditions. In the work mathematical equations for calculating of optimum deviation angle $\theta_{t,opt}$ of a laser beam are derived. Setting a FSO with this parameter, will provide operation with the highest possible deviation from the main beam direction. This paper deals with studying of dependence on maximal divergence from the power of laser source and the length of communication channel. Calculations are made for two different wavelengths of optical radiation. Manifold graphics, showing the importance of correct setting for the system reliability, are attached.

1. INTRODUCTION

The feasibility of FSO technology in the group of wireless communication systems is increasing constantly. Its mobile version known as MFSO has significant progress over recent years too [1, 2]. The increased interest in FSO systems, however, creates new requirements for improvement of their characteristics, as well as for optimizing some of their parameters, in particular those of the divergence of the transmitter optical radiation [3-7]. In [8] the dependence of $\theta_{t,opt}$ on the BER, the eye-diagram and the quality factor of the system are investigated by numerical simulations under different atmosphere effects. Despite numerous researchs so far has not offered a clear statement to calculate the optimal divergence $\theta_{t,opt}$ of the laser radiation, depending on the FSO system parameters and characteristics of the atmospheric communication channel.

2. STATEMENT OF THE LASER BEAM DIVERGENCE PROBLEM

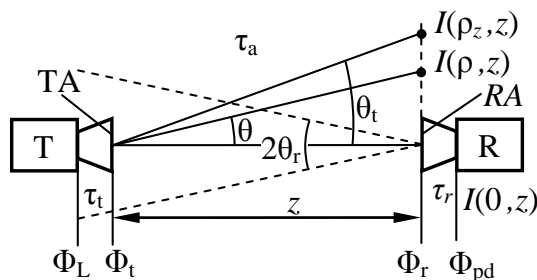


Figure 1. Block diagram of an FSO link between two sites

Figure 1 outlines a block diagram of FSO system when the optical axes of the transmitter (TA) and the receiver (RA) antennas are aligned. The distribution of the optical radiation intensity $I(\rho, z)$ in the plane $z = \text{const}$ depends mainly on the phase and amplitude distribution of the field in the TA. For our case we will accept equiphase and Gaussian amplitude distribution. In the figure is shown the optical flux: Φ_L – transmitted by the laser, Φ_t and Φ_r – through the apertures, namely, TA and RA, and at the entrance of the photodetector Φ_{pd} . $I(0, z)$ is the optical radiation intensity along the axis of the antenna. The radius ρ_z of the Gaussian laser beam (with azimuthal symmetry of the radiation) is calculated by the mathematical expression

$$I(\rho_z, z) = \frac{I(0, z)}{e^2} \quad (1)$$

and defines the divergence θ_t of the radiation in the far-field region. With τ_t and τ_r are denoted losses in the defined antennas and τ_a is the transparency of atmospheric channel. $2\theta_r$ is the diagram width of the receiving antenna.

Radial distribution of the optical radiation intensity in the plane $z = \text{const}$, in which receiving aperture is situated, is shown in Figure 2.

According to the assumption for receiving aperture radius $R_r \ll \rho_z$, it can be approximately determined the received optical flux Φ_r as a product of the intensity of optical radiation in the center of the receiving antenna and the surface of antenna, A_r .

$$\begin{aligned}\Phi_r &= I(\rho, z)A_r, \\ A_r &= \pi R_r^2, \\ \rho &= \theta z, (tg\theta = \rho/z).\end{aligned}\quad (2)$$

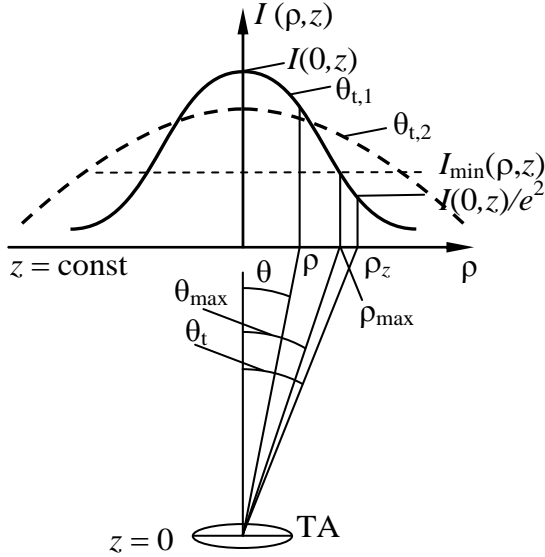


Figure 2. Distribution of intensity in a plane $z = \text{const}$ for two values of divergence of optical radiation θ

The intensity I_{\min} shown in Figure 2 corresponds to the minimum power of optical radiation through the aperture of the receiver for which FSO system works reliably. The respectively magnitude of ρ defines the angle θ_{\max} . This is the value of bearable angular misalignment of the laser beam axis from the main direction ($\theta = 0$) due to the different random factors.

With $\theta_{t,1}$ and $\theta_{t,2}$ are shown two distributions of $I(\rho, z)$, corresponding to divergence $\theta_{t,1}$ и $\theta_{t,2}$ ($\theta_{t,1} < \theta_{t,2}$) of the beam transmitter. Figure 2 outlines the case of $\theta_{\max}(\theta_{t,2}) > \theta_{\max}(\theta_{t,1})$. But it is obvious that this trend will continue to the limit value $\theta_{t,\text{opt}}$. After this point with increasing θ_t , there will be a decrement in the magnitude of θ_{\max} .

The task of our following analysis is to calculate $\theta_{t,\text{opt}}$, and to investigate its dependence on the parameters of the FSO system.

3. MATHEMATICAL DESCRIPTION

Due to Gaussian amplitude distribution of the optical field in the aperture of the transmitting antenna the intensity distribution in the far-field region, in which the receiving antenna is positioning, is also Gaussian.

$$I(\rho, z) = I(0, z) \exp\left(-2 \frac{\rho^2}{\rho_z^2(z)}\right) \quad (3)$$

When $\rho = \rho_{\max}$ (Fig. 2), the optical radiation intensity $I = I_{\min}$, i.e.

$$I_{\min} = I(0, z) \exp\left(-2 \frac{\rho_{\max}^2}{\rho_z^2(z)}\right) \quad (4)$$

The optical radiation intensity along the axis of the laser beam depends on the characteristics of the transmitter and the atmospheric communication channel [7]

$$I(0, z) = \frac{2 \cdot \tau_t \cdot \tau_a(\lambda_0, S_M, z) \cdot \Phi_L}{\pi \cdot \rho_z^2(z)}. \quad (5)$$

The transparency of the atmosphere is related to meteorological visual range S_M and the wavelength of the transmitter.

$$\tau_a(\lambda_0, S_M, z) = \exp\left[-\frac{3,92 \cdot z}{S_M [\text{km}]} \left(\frac{\lambda [\mu\text{m}]}{0,55}\right)^{-q}\right] \quad (6)$$

In case of $S_M \leq 10$ km, $q = 0,585 \sqrt{S_M [\text{km}]}$.

From (4) and (5) we draw the formula

$$\rho_{\max} = \frac{1}{\sqrt{2}} \rho_z \sqrt{\ln \frac{2 \cdot \tau_t \cdot \tau_a \cdot \Phi_L}{\pi \cdot \rho_z^2 \cdot I_{\min}}}. \quad (7)$$

This mathematical equation allows determination of the extreme magnitude of ρ_{\max} as a function of ρ_z . The value of ρ_z , for which has a maximum ρ_{\max} , is

$$\rho_z \equiv \rho_{z,\text{opt}} = \sqrt{\frac{2 \cdot \tau_t \cdot \tau_a \cdot \Phi_L}{\pi \cdot e \cdot I_{\min}}}, \quad e = 2,7183. \quad (8)$$

I_{\min} is calculated by the condition

$$I_{\min} = \frac{\Phi_{\text{pd}}}{\pi \cdot \tau_r \cdot R_r^2} \Big|_{\text{SNR}=\text{const}}. \quad (9)$$

When SNR value is given, Φ_{pd} is calculated from the expression [7]

$$\text{SNR} = \frac{R_1 \cdot \Phi_{\text{pd}}}{\sqrt{C_1 \left[\frac{2 \cdot k_B \cdot T \cdot A}{R_{\text{Fb}}} + e^{-\cdot} \cdot R_1 \cdot (\Phi_{\text{pd}} + \Phi_B) \right]}} \quad (10)$$

In (10) R_I is the integral sensitivity for current of the photodetector

$$R_I(\lambda_0) = 8,06 \cdot 10^5 \eta(\lambda_0) \lambda_0, \quad (11)$$

$\eta(\lambda_0)$ is the quantum efficiency of the photodetector material, C_I is the information capacity of digital communication system, $k_B = 1,38 \cdot 10^{-23}$ J/K is the Boltzmann constant, T is the absolute temperature, A is a constant of receiver, R_{Fb} is the value of the resistor in the feedback of the preamplifier, $e^- = 1,602 \cdot 10^{-19}$ C is the charge of the electron.

Background optical flux Φ_B depends on the spectral brightness of the background radiation $L_{\lambda,B}$ and the parameters of receiver: the aperture radius R_r , the transmission coefficient τ_r and the angular width of the receiving antenna θ_r [7]

$$\Phi_B = \pi^2 \cdot \tau_r \cdot L_{\lambda,B} \cdot R_r^2 \cdot \theta_r^2 \cdot \Delta\lambda_F. \quad (12)$$

With $\Delta\lambda_F$ is denoted the transmission wavelength of the interference filter before the photodetector.

From (10) and from physical considerations we reach to a clear result for calculating the value of the optical signal flux in the entrance of the photodetector

$$\Phi_{pd} = \frac{1}{2} \left[\frac{SNR^2 \cdot C_I \cdot e^-}{R_I} + \left(\left(-\frac{SNR^2 \cdot C_I \cdot e^-}{R_I} \right)^2 + \frac{4SNR^2 \cdot C_I \left(\frac{2k_B \cdot T \cdot A}{R_I \cdot R_{Fb}} + e^- \cdot \Phi_B \right) \right)^{\frac{1}{2}} \right] \quad (13)$$

Having used the expression (13), (9) and (8) we compute $\rho_{z,opt}$, respectively,

$$\theta_{t,opt} = \frac{\rho_{t,opt}}{z} \text{ [rad]} \quad (14)$$

as a function of parameters of FSO system and communication channel.

4. SIMULATION RESULTS

For numerical calculations we choose the following typical values of the parameters of the FSO system and atmospheric communication channel: $C_I = 100$ Mbps; $\eta(\lambda_0) = 0,7$; $SNR = 11,2$ (corres-

ponds to $BER = 10^{-8}$); $\lambda_0 = 0,85$ and $1,55 \mu\text{m}$; $T = 300$ K; $A = 5$; $R_{Fb} = 1 \text{ k}\Omega$; $\tau_r = \tau_t = 0,85$; $R_r = 5,5$ cm; $\Delta\lambda_{F} = 10 \text{ nm}$; $L_{\lambda,B} = 10^{-2}$ (corresponds to bright day); $\theta_r = 5 \text{ mrad}$; $S_M = 10 \text{ km}$.

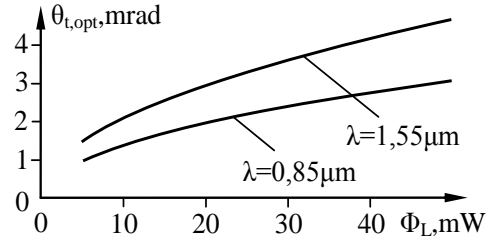


Figure 3. Dependence of $\theta_{t,opt}$ from Φ_L ($z = 2 \text{ km}$)

Figure 3 shows the $\theta_{t,opt}$ dependence from the power of the transmitter, and Figure 4 from the length of the communication channel.

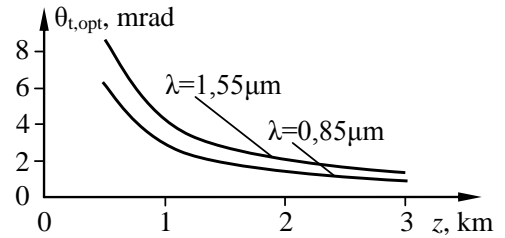


Figure 4. Dependence of $\theta_{t,opt}$ from z ($\Phi_L = 10 \text{ mW}$)

We see the strong dependence on $\theta_{t,opt}$ within an order of magnitude (1 mrad to 10 mrad). This is a prerequisite for the importance of the correct selection of the optimal divergence of the laser beam for the reliable operation of FSO system in each one case.

5. CONCLUSION

The optimal magnitude of the laser beam divergence is influenced much more by the length of the communication channel than the power of the laser source. In case of six times increasing in the distance between communication parts the value of optimal divergence decreases eight times. In comparison, five times reducing of transmitter power leads to four times decreasing of the optimal divergence. The dependence of the optimal divergence of the transmitter on the wavelength is much weaker.

References

- [1] M. K. Al-Akkoumi, A. Harris, R. C. Huck, J. J. Sluss, "Challenges Facing Mobile Free-Space Optical Communications", Atmospheric Propagation VI, SPIE, V.7324, May, 2009.
- [2] A. Harris, T. Giama, "Divergence and Power Variations in Mobile Free-Space Optical Communications", Third Int. Conf., pp. 174 –178. 13-18 April 2008.
- [3] Zh. Zhao, R. Liao, Y. Zhang, "Impact of Laser Beam Diverging Angle on Free-Space Optical Communications", Aerospace Conference, IEEE, pp. 1-10, 2011.
- [4] A. Farid, S. Hranilovic, "Outage Capacity Optimization for Free-Space Optical Links with Pointing Errors", Journal of Lightwave Technology, Vol. 25, Issue 7, pp. 1702-1710, 2007.
- [5] Y. Ren, A. Dang, B. Luo, H. Guo, „Capacities for Long-Distance Free-Space Optics Links Under Beam Wander Effects“, Photonics Technology Letters, IEEE, vol. 22, issue 14, pp. 1069-1071, 2010.
- [6] Shlomi Arnon, "Effects of Atmospheric Turbulence and Building Sway on Optical Wireless Communication Systems", Opt. Lett., vol. 28, No. 2, pp. 129-131, 2003.
- [7] Mitsev Ts., N. Kolev, Hr. Ivanov, K. Dimitrov, „Optimum Divergence of the Transmitter Optical Radiation in FSO Systems“, Conf. Proceedings ICEST 2012.
- [8] Gaurav Soni, Jagjit Singh Malhotra, "Impact of Beam Divergence on the Performance of Free Space Optical System", Int. Journ. of Scientific and Research Publ., v.2 (2), Febr. 2012.

APPLYING THE MODIFIED FRACTAL SIGNATURE METHOD TO IMAGE CLASSIFICATION: SOME PRELIMINARY RESULTS FOR ISAR RADAR IMAGES

(Scientific area of interest: 'Image Classification')

C. Pandis, A. Malamou, P. Stefaneas and P. Frangos

National Technical University of Athens
9, Iroon Polytechniou Str., GR 157 73, Zografou, Athens, Greece
Tel. +30 210 772 1869, E-mail: petros@math.ntua.gr

Abstract

The Modified Fractal Signature (MFS) method uses the 'blanket' technique to provide useful information for image classification. It has been used in [1] and [2] in order to provide classification results for document analysis purposes [1] and biomedical image classification [2]. It is based on the calculation of the volume of a 'blanket', corresponding to the image to be classified, and then on the calculation of the corresponding fractal signature (MFS) of the image. We present here some preliminary results concerning the application of MFS method to the classification of Inverse Synthetic Aperture Radar (ISAR) images. In these results it is clearly seen that the focusing of the ISAR radar image clearly correlates with the value of MFS signature.

1. INTRODUCTION

MFS method has been introduced by Y. Tang et al. for the purpose of document analysis, classification and pattern recognition [1]. N. Ampilova et al. applied similar methods for biomedical image classification [2]. This method includes fractal analysis [3,4] of surfaces and uses a 'blanket' technique [1,2], which is explicitly provided in Section 2, below. The concept in this technique is that different classes of images yield different values of fractal signature (MFS) and fractal dimension, upon which classification of different types of images is possible. In particular, in this paper we are interested for the classification of ISAR radar images, and, in particular, for discrimination of 'focused' or 'unfocused' ISAR images [5]. In [5], the criterion for image focusing is based on the 'image entropy', while in the present the criterion of fractal signature value is investigated.

2. MATHEMATICAL FORMULATION OF THE PROBLEM

The 'blanket' (MFS) method [1,2], as implemented by our research group in this paper, is summarized as following: initially, the whole image is divided into several non-overlapping sub-images and the

fractal signature is calculated for each sub-image, as explained below (the overall fractal signature of the initial image will be calculated ultimately by summation of the corresponding values of the sub-images, as it will be explained below). Subsequently, each sub-image is converted to a gray – level function $g(x,y)$ [1].

According to [1] and [2], the covering blanket is defined by its upper surface $u_\delta(x,y)$ and its lower surface $b_\delta(x,y)$. Initially, $\delta=0$ and $u_0(x,y) = b_0(x,y) = g(x,y)$. For $\delta=1,2,\dots$ we have the following iterative formulae:

$$\begin{aligned} u_\delta(x,y) &= \max \left\{ u_{\delta-1}(x,y) + 1, \max_{|(m,n)-(x,y)| \leq 1} u_{\delta-1}(m,n) \right\} \\ b_\delta(x,y) &= \min \left\{ b_{\delta-1}(x,y) - 1, \min_{|(m,n)-(x,y)| \leq 1} b_{\delta-1}(m,n) \right\} \end{aligned} \quad (1)$$

Subsequently, the volume of the 'blanket' is calculated

$$\text{Vol}_\delta = \sum_{(x,y)} (u_\delta(x,y) - b_\delta(x,y)) \quad (2)$$

Furthermore, the fractal signature A_δ is calculated by

$$A_\delta = \frac{\text{Vol}_\delta}{2\delta} \quad (3)$$

or

$$A_{\delta} = \frac{\text{Vol}_{\delta} - \text{Vol}_{\delta-1}}{2} \quad (4)$$

(see also Fig. 1)

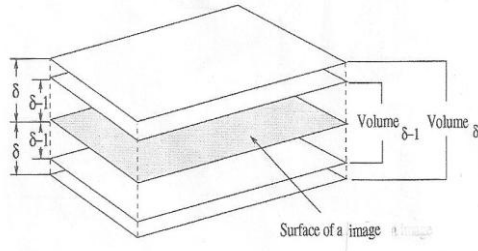


Fig. 1. Volumes of the 'blanket' involved in our proposed algorithm for fractal signature calculation [1]

Finally, concerning the calculation of the corresponding fractal dimension D , the following formula is used [1]

$$A_{\delta} \approx \beta \delta^{2-D} \quad (5)$$

where β is a constant, from which the fractal dimension can be calculated from successive fractal signature values as following

$$D \approx 2 - \frac{\log_2 A_{\delta_1} - \log_2 A_{\delta_2}}{\log_2 \delta_1 - \log_2 \delta_2}, \quad \delta=1,2,\dots \quad (6)$$

3. PRELIMINARY NUMERICAL RESULTS

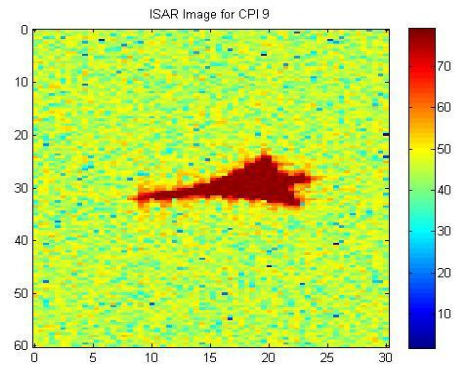
In this paper our simulations of the proposed algorithm concern ISAR radar images of the authors' previous research [5], see Fig. 2 below [similarly, in the near future, our research group will investigate, in a similar fashion, classification issues of direct Synthetic Aperture Radar (SAR) images [6]].

As well expected, the image of Fig. 2(a) is characterized from small value of entropy, as opposed to the image of Fig. 2(b) [5]. In the present study, the criterion of fractal signature and fractal dimension will be used instead. Fig. 3, below, shows the fractal signature A_{δ} as a function of iteration δ for the cases of the 'focused' and the 'unfocused' image of Fig. 2.

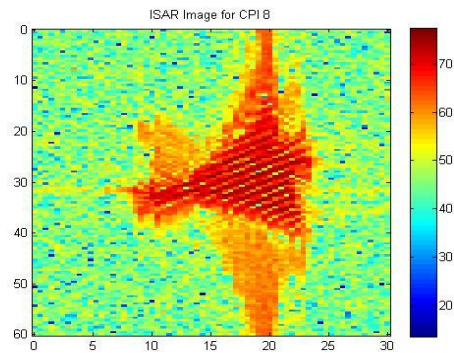
From the results of Fig. 3 above, through the use of Eq. (6) above, the following results of Fig. 4 for the corresponding fractal dimension are derived.

From the numerical results of Figs. 3,4 above, it is apparent that the criteria of 'fractal signature' and 'fractal dimension' for ISAR image characterization work in a satisfactory way for the above simulations (besides to the criterion of entropy values, examined in [5] and [6]). Furthermore, from the first simulations presented above, we can provide here some preliminary remarks, as following. First, it appears

that conclusions about image characterization follow for small values of iteration δ . Furthermore, for the particular case of Fig. 3, above, note that information about image characterization is lost for number of iteration $\delta=13$. Finally, we easily can understand that, for large number of iterations (δ), the proposed algorithm of Eq. (1) appears to select the ± 1 values of the previous iteration, so that the value of fractal signature equals, in this limit, the number of the pixels of the image. This final statement can be very easily proved from Eq. (4), where, in the current simulations, this situation occurred for $\delta=148$ ('focused' case) and $\delta=129$ ('unfocused' case).



(a)



(b)

Fig. 2. ISAR images used in the present simulations, (a) 'focused' ISAR image of airplane, (b) corresponding 'unfocused' image [5]

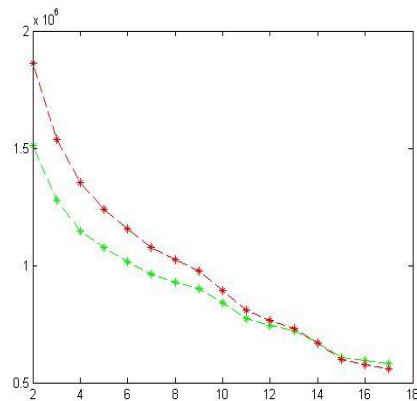


Fig. 3. Fractal signature A_{δ} as a function of iteration δ for the cases of the 'focused' and the 'unfocused' image of Fig. 2 (red = unfocused, green=focused).

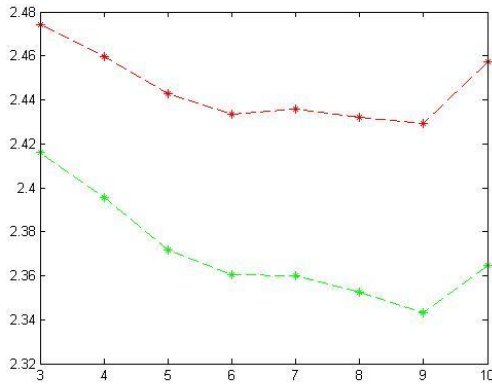


Fig. 4. Fractal dimension D as a function of iteration δ for the cases of the 'focused' and the 'unfocused' image of Fig. 2 (red = unfocused, green=focused)

4. CONCLUSION – Future Work

In this paper we applied an iterative MFS technique [1,2] for ISAR radar image characterization. It appears that for small values of iteration δ the proposed algorithm provides interesting characterization results. In the near future, our research group will also examine the behavior of direct SAR images, as well, further comparisons with the entropy value criterion, and other fractal image characterization methods, such as 'Regny spectrum' method, as well [2].

Acknowledgements

The authors would like to acknowledge very interesting relative discussions with Professors N. Ampilova and I. Soloviev, St. Petersburg State University, Russia, which initiated this research.

This research has been co-financed by the European Union (European Social Fund - ESF) and Greek national funds through the Operational Program "Education and Lifelong Learning" of the National Strategic Reference Framework (NSRF) - Research Funding Program: THALES:Reinforcement of the interdisciplinary and / or inter-institutional research and innovation.

References

- [1] Yan Y. Tang, Hong Ma, Dihua Xi, Xiongmao Mao, Ching Y. Suen, 'Modified Fractal Signature (MFS): A New Approach to Document Analysis for Automatic Knowledge Acquisition', IEEE Transactions on knowledge and data engineering, Vol. 9, No. 5, Sept. – Oct. 1997, pp. 747-762.
- [2] N.B. Ampilova, E.Y. Gurevich, I.P. Soloviev, 'Application of modified fractal signature and Regny spectrum methods to the analysis of biomedical preparation images, CEMA'11 Conference, Sofia, Bulgaria, October 2011, pp. 96 - 100.
- [3] K. J. Falconer, 'Fractal Geometry : Mathematical Foundations and Applications', J. Wiley and Sons, 1990.
- [4] D. Jaggard, A. Jaggard and P. Frangos, 'Fractal electrodynamics : surfaces and superlattices', in 'Frontiers in Electromagnetics', IEEE Press, Edited by D. Werner and R. Mittra, 2000.
- [5] E. Kallitsis, A. Karakasiliotis, G. Boultadakis and P. Frangos, 'A Fully Automatic Autofocusing Algorithm for Post-processing ISAR Imaging based on Image Entropy Minimization', 'Electronics and Electrical Engineering' Journal, Vol. 110, No. 4, pp. 125 – 130, 2011.
- [6] A. Malamou, A. Karakasiliotis, E. Kallitsis, G. Boultadakis and P. Frangos, 'An Autofocusing Algorithm for Post-processing of Synthetic Aperture Radar (SAR) Images based on Image Entropy Minimization', accepted for presentation to CEMA'12 Conference, National Technical University of Athens, Greece, November 2012.

AN AUTOFOCUSING ALGORITHM FOR POST-PROCESSING OF SYNTHETIC APERTURE RADAR (SAR) IMAGES BASED ON IMAGE ENTROPY MINIMIZATION

A. Malamou, A. Karakasiliotis, E. Kallitsis, G. Boultadakis and P. Frangos

National Technical University of Athens
9, Iroon Polytechniou Str., GR 157 73, Zografou, Athens, Greece
Tel. +30 210 772 3694, Fax. +30 210 772 2281, E-mail : pfrangos@central.ntua.gr

Abstract

In this paper, a two-dimensional (2D) Synthetic Aperture Radar (SAR) geometry is presented for a ship target which is located on the sea surface. The ship is considered at first to be stationary, and subsequently an oscillatory movement is induced to its position along the vertical axis, due to sea surface motion. Moreover, the mathematical expressions of the backscattered signal (magnitude, and, in particular, phase) are presented for the two cases of a ship target mentioned above. Furthermore the 'CPI-split algorithm' [3] (CPI = Coherent Processing Interval) is applied in the SAR scenario examined here, and the numerical results, based on simulated radar data, are presented. These results show the effectiveness of the CPI-split algorithm [3] for the case of SAR imaging.

1. INTRODUCTION

Synthetic aperture radar (SAR) has been widely used for long-range imaging of stationary ground objects. This radar can perform with high image resolution at long range, regardless the weather conditions, because it is a radio frequency (RF) sensor. Hence, one of its main uses is in target detection and recognition for civilian or military applications. Provided that the target remains stationary, it is feasible from the SAR data to construct the target SAR image with high resolution by exploiting the range-Doppler information collected by the SAR antenna [1,2].

As far as moving targets are concerned, the reconstruction of the target image using SAR data is a more difficult task [1]. The SAR image of the target is usually defocused due to target movement. As moving targets are of great interest, the purpose of this paper is to apply the post processing CPI-split autofocusing algorithm [3] in the SAR geometry in order to get a focused SAR image of a moving target.

2. SIMULATED SAR GEOMETRY AND MATHEMATICAL FORMULATION

The simulated SAR geometry is presented in Fig. 1. The antenna of the radar, as it is common in SAR geometry, is mounted on a platform such as an aircraft and illuminates the target [1]. The aircraft is assumed to travel along a flight path from $-N/2$ to

$N/2$ (N is the number of bursts during one CPI) with constant velocity v . The center of the flight path is considered to be the point A , as it is shown in Fig. 1. Furthermore, the radar is assumed to emit linear frequency modulation (LFM) pulses, where M stepped frequencies are emitted per burst ($m=1$ to M) and N pulses per CPI [1,2].

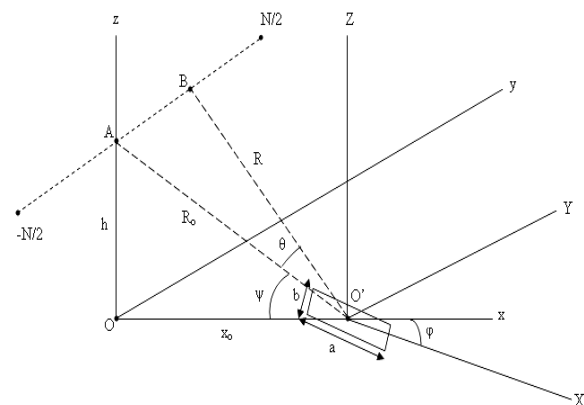


Figure 1. SAR geometry

The target is a ship on the sea surface with length and width b (2D geometry of the ship is assumed here, without loss of generality). The origin O' of the 'local' coordinate system [i.e. of the target (ship) to be imaged] is placed in the mass center of the ship. The distance R_0 is the distance between the center of the flight path and the origin O' of the local coordinate system. The angle ψ is the grazing angle of the incident radar electromagnetic (EM) wave and the angle θ is the angle of observation of the target within the CPI. The angle φ determines

the orientation of the ship with respect to the 'earth' coordinate system Oxyz (axis Ox, in particular).

In the simulations of Section 3, below, the ship is considered in most CPI's of observation to be stationary. However, in some specific CPI's, an oscillatory movement is induced to its position along the vertical axis, due to sea surface motion. The SAR images that are obtained for these CPI's are blurred due to the ship movement. The main idea is to apply the CPI-split autofocus algorithm [3] in order to eliminate the SAR image smearing.

In order to fully clarify the simulated geometry, the main mathematical expressions of the backscattered signal (magnitude, and, in particular, phase) are presented below, for the two cases of a ship target (e.g. stationary and in movement).

The backscattered radar data are simulated through the following formula:

$$x(m, n) = \sum_d s_{i,j} \exp[j\phi_{i,j}^m] + u(m, n) \quad (1)$$

where d is the number of the scatterers of the target and $s_{i,j}$ is the scattering intensity for the (i,j) scatterer. In the simulations below we can assume, without loss of generality, that all scatterers have the same strength in amplitude ($s_{i,j}=1$ for all i,j). The term $\phi_{i,j}$ is the phase of the backscattered signal, while $u(m,n)$ is the two dimensional additive white Gaussian noise component.

Assuming that the ship is stationary, the phase $\phi_{i,j}$ for the (i,j) scatterer of the target, $\phi_{i,j} = 2\mathbf{k} \cdot \mathbf{R}_{i,j}$, is calculated by our research group from analytic (geometric) calculation of the distance $\mathbf{R}_{i,j}$ between the radar and the (i,j) scatterer, and from the analytic expression for the incident wavevector \mathbf{k} , as well. These calculations lead to the following 'local' phase, assuming that the target is stationary:

$$\phi_{i,j}^m = \frac{4\pi f_m}{c} [\cos\theta \cos\psi (X_{i,j} \cos\phi + Y_{i,j} \sin\phi) + \sin\theta \cdot (X_{i,j} \sin\phi - Y_{i,j} \cos\phi)] \quad (2)$$

where m is the stepped frequency index ($m=1, \dots, M$); n is the burst index ($n=1, \dots, N \cdot N_{CPI}$) for a number of simulated CPI's (N_{CPI}); N is the number of bursts during one CPI and $(X_{i,j}, Y_{i,j})$ are the local coordinates of the ship scatterers.

When the vertical movement of the ship, due to the sea motion, is taken into account, the phase formula changes. In the ship motion model, that we adopt here, an extra term is added due to the ship movement along the z-axis and it depends on the

period T_{osc} of the oscillation. As a result, the phase of the backscattered signal is given by:

$$\phi_{i,j,osc}^m = \phi_{i,j}^m - \frac{4\pi f_m}{c} z_0 \sin(\omega_{osc} \cdot t) \quad (3)$$

where z_0 is the oscillation amplitude and ω_{osc} is the angular frequency of oscillation.

In the numerical simulations of Section 3, below, the vertical movement of the ship is induced only for specific CPI's, where the raw data matrices are formed through Eq. (1) [dependence on 'slow - time' index n in eqns. (2) and (3) becomes effective through the aspect angle θ].

The SAR images for all CPI's are constructed from the raw data matrices through the traditional 'Range - Doppler' imaging technique, involving FFT processing in both range and Doppler directions [2]. In order to compare the quality of the SAR images obtained, the entropy values of each image are computed. It is expected that the SAR images which correspond to those specific CPI's in which the ship movement is induced, will have greater entropy values than the SAR images corresponding to no ship movement.

3. NUMERICAL RESULTS

The simulated ship geometry is shown in Fig. 2. It is a point scatterer model which consists of 233 scatterers. The corresponding radar and geometry parameters are shown in Table 1.

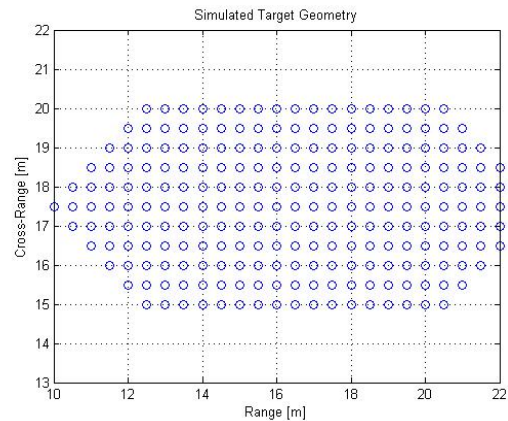


Figure 2. Geometry of the simulated ship target

The CPI-split autofocus algorithm [3] is employed in those CPI's whose entropy values exceed a threshold that represents an acceptable SAR image quality. The images with entropy values below the entropy threshold are called "focused" images, while the images with entropy values over the threshold are called "unfocused". In this simulation

scenario the value of the entropy threshold was set equal to 6.0 [3].

Table 1. SAR simulation parameters

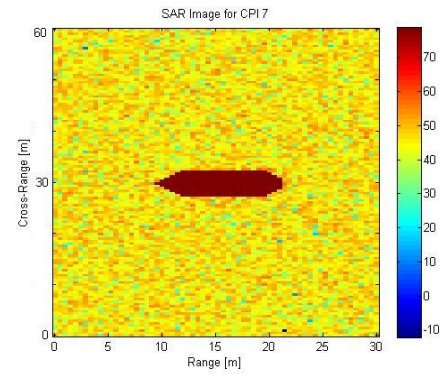
Parameter	Value [units]
carrier frequency, f_0	10 [GHz]
radar bandwidth, B	300 [MHz]
number of frequencies, M	64
frequency step, Δf	4.76 [MHz]
pulse repetition frequency, PRF	2.74 [KHz]
burst duration, T_b	0.0234 [sec]
coherent processing interval, CPI	3 [sec]
number of bursts, N	128
number of CPIs, NCPI	13
range distance to center of target, R_0	10 [km]
height of SAR platform, h	2 [km]
position angle of the ship, φ	0°
velocity of platform, v_p	100 [m/sec]
oscillation amplitude, z_0	0.2 [m]
oscillation period, T_{osc}	1.3 [sec]

In this simulation, the flight duration is considered to be 13 CPI's. The ship movement is induced only in the 4th and 8th CPI. In Fig. 3, four (4) SAR images are presented. Images 3a, 3b and 3c represent the reconstructed SAR images for the 7th, 8th and 9th CPI respectively. It is clear that the SAR image of the 8th CPI (image 3b) is unfocused due to sea motion, as modeled in our simulations. In image 3d the SAR image of the 8th CPI is shown after the application of the CPI-split autofocus algorithm [3]. Clearly the SAR image is now focused and has an acceptable entropy value. The CPI-split autofocus algorithm is effective in this simulation scenario.

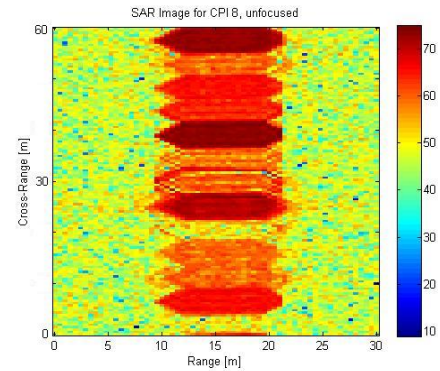
In Table 2 the entropy values for the CPI's related to the application of the algorithm are presented. Note that the entropy values of the 4th and 8th CPI are within the acceptable entropy value range (e.g. below the entropy threshold), after our proposed algorithm is applied [3].

Table 2. Entropy values of SAR images

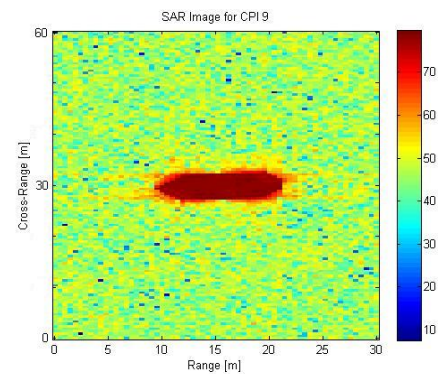
SAR Image	Entropy	Minimum Entropy Combination
3rd CPI 4th CPI, unfoc. 5th CPI	5.7635	
	7.8581	
	5.7540	
4th CPI, foc.	5.7648	stage 3, segment 1, comb. 1
7th CPI 8th CPI, unfoc. 9th CPI	5.6786	
	7.3654	
	5.7572	
8th CPI, foc.	5.7581	stage 3, segment 2, comb. 4



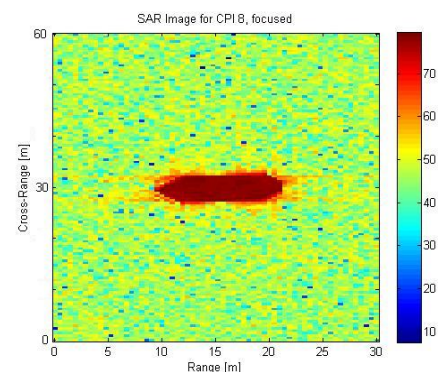
3a)



3b)



3c)



3d)

Figure 3. Reconstructed SAR images for the: a) 7th; b) 8th; c) 9th; CPI and d) the 8th CPI after application of the CPI-split algorithm

4. CONCLUSION – Future Research

In this paper, a 'CPI-split autofocusing algorithm' [3] is applied to a Synthetic Aperture Radar (SAR) scenario. The simulation results presented above show that the proposed algorithm is effective in producing focused SAR images, at least for the simulated data used in this research. One basic idea for near future research of our research group is to incorporate the proposed 'CPI-split autofocusing algorithm' also for the cases of real – field data.

References

- [1] D. Wehner, *High-Resolution Radar*, Artech House, 2nd edition, London, 1995.
- [2] V. Chen, H. Ling, *Time-Frequency Transforms for Radar Imaging and Signal Analysis*, Artech House, London, 2002.
- [3] E. Kallitsis, A. Karakasiliotis, G. Boultadakis, P. Frangos, "A Fully Automatic Autofocusing Algorithm for Post-processing ISAR Imaging based on Image Entropy Minimization", *Electronics and Electrical Engineering Journal*, No. 4 (110), April 2011, pp. 125 – 130.
- [4] A. Lazarov, C. Minchev, "ISAR Signal Modeling and Image Reconstruction with Entropy Minimization Autofocusing", *Proc. DASC*, Portland, USA, Oct 2006, pp. 3E5-1-3E5-11.

RANDOM PHASED ANTENNA ARRAYS – THE NEW CHALLENGE FOR THE MULTISTATIC RADAR NETWORKS

Veselin Demirev

Radio Communications and Video Technologies Department, TU-Sofia,
Kl. Ohridski blv. № 8, 1756-Sofia,
Tel: 3592-965-26-60; e-mail:demirev_v@tu-sofia.bg

Abstract

In this report an effective solution of the “beam scan-on-scan losses” problem in Bistatic radars and Multistatic Radar Networks is proposed. It is based on random phased antenna arrays approach, as well as correlation signal processing in the radar receiver. Similar approach was proposed by the author to solve the antenna problems of the mobile satellite communications, named Spatial Correlation Processing – Random Phase Spread Coding. Matrix presentation of the signals in such radar systems is given, as well as the computer simulated Spatial Correlating Function, which is the virtual antenna patterns at baseband.

1. INTRODUCTION

Bistatic radars and Multistatic Radar Networks (MRN) are subject to problems and special requirements that are either not encountered or encountered in less serious form by monostatic radars [1]. One of the main problems are beam scan-on-scan losses. If high gain narrow-beam antennas are used by both the transmitter and the receiver in bistatic surveillance radar, inefficient use is made of the radar energy because only the volume common to both beams can be observed by the receiver at any given time. Several techniques have been proposed and used [1], but all of them suffer different disadvantages. Another problem, typical for all kind high gain antenna radar systems, is the sequential target search in the space due to the steering of the narrow antenna pattern. It leads to low illumination/scan period ratio and low probability of target detection.

The goal of this report is to propose effective solution of the above mentioned problems, based on Random Phased Antenna Arrays (RPAA) approach, as well as correlation signal processing in the radar receiver. Similar approach was proposed by the author to solve the antenna problems of the mobile satellite communications in Ku frequency band [2]. The name of the proposed new technical solution is Spatial Correlation Processing – Random Phase Spread Coding (SCP-RPSC).

2. SCP TECHNOLOGY – THE NEW APPROACH TO SOLVE THE MRN SCAN ON SCAN PROBLEMS

The basic SCP bistatic radar geometry is shown in fig. 1. It consists of transmitter site, radar target

and receiver site. The last is given in more details in fig. 3. The transmitted by the radar transmitter CW signals are phase modulated with slow “coarse” PN-code C and fast “precise” PN-code P .

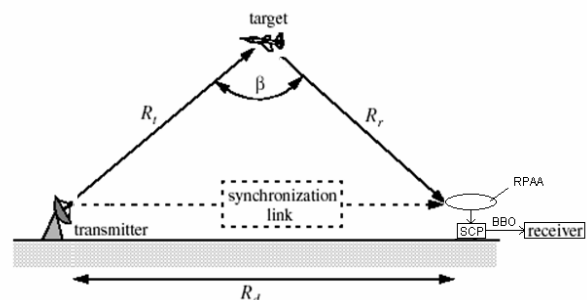


Figure 1. The basic SCP bistatic radar geometry

The frequency spectrum of the transmitted wave is shown in fig. 2.

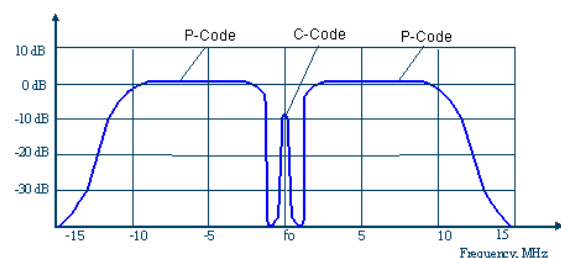


Figure 2. The frequency spectrum of a SCP bistatic radar system

3. BASIC MATRIX EXPRESSIONS OF THE SIGNALS IN A SCP BISTATIC RADAR SYSTEM

The receiver site of a SCP bistatic radar system can be represented by a block diagram, shown in

fig. 3. It involves a radar target located in a position, given with its angular coordinates in the coordinate system, centred in the receiver RPAA [fig. 4]. To analyze such a system, the most suitable mathematical tools available involve matrix and vector algebra.

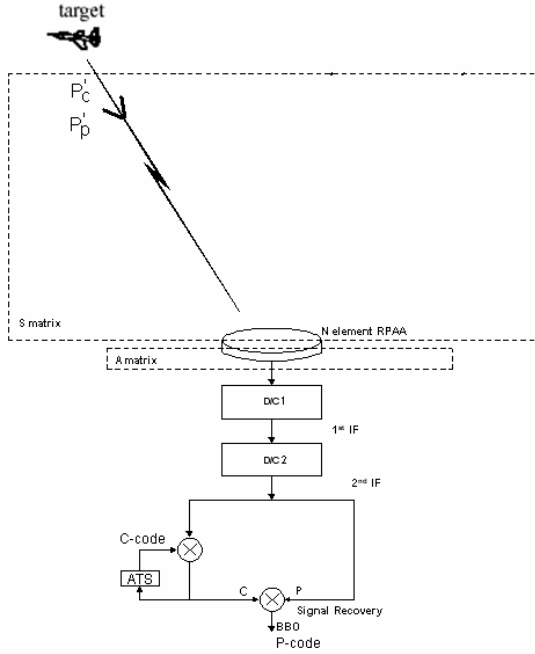


Figure 3. The SCP bistatic radar receiver site

The reflected by the radar target SCP signals involve both the coarse signal with power P_c' and precise P_p' . For simplicity target point scattering model is considered. These signals travel through space to reach the RPAA, where they are picked up by every antenna element and collected by the summing network to the input of the receiver. Here, after several steps of down-conversion, the collected random phase spread P signals correlate with the recovered phase spread in the same manner C signals for precise signal recovery. The radar target is located at angular coordinates ϕ_r, θ_r and distance R_r .

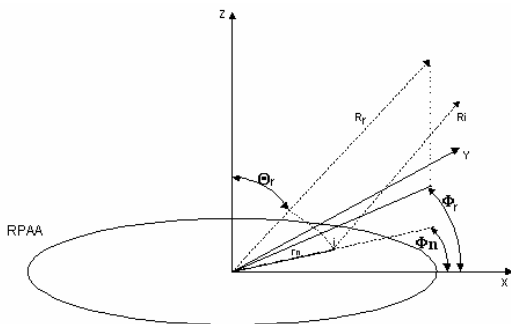


Figure 4. The SCP bistatic radar coordinate system

Each element of the N-elements RPAA pick up the reflected by the target signals and deliver them to its output. Let s_n be the transfer function between the radar target and the n -th element of RPAA. Then

$$s_n = L_{sn} \cdot e^{-j\psi_n} \quad (1)$$

where L_{sn} are the space propagation losses, $\psi_n = kr_n \sin \theta_r \cos(\phi_r - \phi_n)$ is the phase of the signal received by n -th element of RPAA relative to its centre, $k = 2\pi / \lambda$ - free space phase constant, r_n, ϕ_n - the coordinates of the n -th element of RPAA, ϕ_r, θ_r - the angular coordinates of the radar target.

The transfer function for the C and P signals from the radar target to the RPAA will be given by:

$$\mathbf{s}_c = \begin{bmatrix} s_{c1} \\ s_{c2} \\ \dots \\ s_{cn} \\ \dots \\ s_{cN} \end{bmatrix} \quad \text{and} \quad \mathbf{s}_p = \begin{bmatrix} s_{p1} \\ s_{p2} \\ \dots \\ s_{p3} \\ \dots \\ s_{pN} \end{bmatrix} \quad (2)$$

The signals, reflected by the radar target, at the RPAA elements will be given by:

$$x_{cn} = s_{cn} P_c', x_{pn} = s_{pn} P_p' \quad (3)$$

All RPAA elements will also receive the reflected C and P signals, as follows:

$$x_c = s_c P_c', x_p = s_p P_p' \quad (4)$$

The summing networks of the RPAA will transport all signals, received by the different elements, to its output and the SCP receiver. Let the transfer functions between all RPAA elements and its output be represented by the column vector \mathbf{a} :

$$\mathbf{a} = \begin{bmatrix} a_1 \\ a_2 \\ a_3 \\ \dots \\ a_n \\ \dots \\ a_N \end{bmatrix} \quad (5)$$

where $a_n = L_{an} \cdot e^{j\varphi_n}$, L_{an} - gain of a single element, internal propagation losses are included, $\varphi_n = 2\pi r_n / \lambda_g + \Delta\varphi_n$, where $2\pi r_n / \lambda_g$ - phase shift due to summing network, $\Delta\varphi_n$ - phase shift due to the element inclination if Circular Polarization (CP) is used.

Due to the finite transfer function that exists between the input and output ports of the RPAA and the summing network, the signals appearing at the output, will be those at the input modified by the transfer function \mathbf{a} . The signal vectors, combining all C and P signals, will be given by:

$$C = \mathbf{a}x_c \quad (6)$$

$$P = \mathbf{a}x_p \quad (7)$$

The received by RPAA signals are amplified in Low Noise Amplifier (LNA), down converted, amplified and correlated in the Correlator unit. Consider for simplicity the process without math description of C -code spreading and despreading. The total receiver gain G , product of the above mentioned procedures, will be:

$$G = G_{LNA} \cdot G_{DC1} \cdot G_{IFA1} \cdot G_{DC2} \cdot G_{IFA2} \quad (8)$$

where G_{LNA} is the gain of the LNA, G_{DC1} is the gain of the first down converter, G_{IFA1} is the gain of the first IFA, G_{DC2} is the gain of the second down converter and G_{IFA2} is the gain of the second IFA.

The output signal, product of the multiplication process, will be:

$$G(C \cdot P) = G \begin{pmatrix} c_1 \cdot p_1 & c_2 \cdot p_1 \dots & c_n \cdot p_1 \dots & c_N \cdot p_1 \\ c_1 \cdot p_2 & c_2 \cdot p_2 \dots & c_n \cdot p_2 \dots & c_N \cdot p_2 \\ \dots & \dots & \dots & \dots \\ c_1 \cdot p_n & c_2 \cdot p_n \dots & c_n \cdot p_n \dots & c_N \cdot p_n \\ \dots & \dots & \dots & \dots \\ c_1 \cdot p_N & c_2 \cdot p_N \dots & c_n \cdot p_N \dots & c_N \cdot p_N \end{pmatrix} \quad (9)$$

A basic requirement of the SCP technology (in order to obtain smooth omnidirectional receiving pattern) is the sum of the off-diagonal terms of the matrix (9) to be zero. This requirement is fulfilled when the RPAA output signals phase probability density function (PDF) is uniform in the interval $0 - 360$ degrees, the channel is real with AWGN and the signal processing is digital. The real part of the n -th diagonal term of matrix (9) consists of:

$$\text{Re}(c_n \cdot p_n) = c \cdot p \cdot \cos^2[\omega_{II} t - kr_n \sin \theta_r \cdot \cos(\phi_r - \phi_n) + k_g r_n] \quad (10)$$

Equation (10) can be presented by means of eq. $\cos^2 A = 0,5 \cdot (1 + \cos 2A)$ as follows:

$$\text{Re}(c_n \cdot p_n) = \frac{+}{-} 0,5 \cdot c \cdot p + 0,5 \cdot c \cdot p \cdot \cos(2\omega_{II} t + \dots) \quad (11)$$

The second term of eq. (11) vanishes after Low Pass Filtering. The first term represents the demodulated reflected signal per antenna element at baseband for the precise PN-code, used later for precise distance measurement. The total baseband output signal will be N times more, equal to the trace of the matrix (9) (the N diagonal elements are in phase):

$$BBO_{cp} = \frac{+}{-} 0,5 \cdot G \cdot c \cdot p \cdot N \quad (12)$$

The formal mathematical way to describe the above mentioned correlation process and the result (12) in matrix form is:

$$BBO_{cp} = \text{timeaver } G \cdot (c \cdot p) = G \cdot \text{Tr}(c \cdot p^H) \quad (13)$$

where \mathbf{p}^H is the Hermitian (transpose and conjugate) matrix of \mathbf{p} .

If there is another radar target, interfering with the same reflected power over the system, the Spatial Cross - Correlation Function (SCCF) can be introduced for the spatial interference analysis, as follows:

$$SCCF(\phi, \theta)(dB) = 10 \lg \left[\frac{BBO_{c.inter.}(\phi, \theta)}{BBO_{cp}} \right] \quad (14)$$

The matrix simulations of the SCCF of a SCP system for $\lambda = 2,5 \text{ cm}$, $r_n = 5 - 28,5 \text{ cm}$, $\phi_n = 0 - 360^\circ$ are shown in fig. 5.

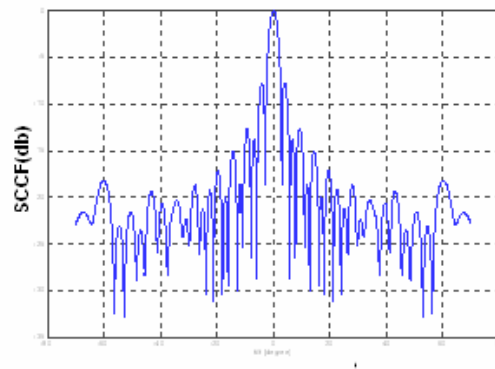


Figure 5. The SCCF for $\theta_r = 0$ deg.

The simulated SCCF, which is the virtual RPAA antenna pattern, is pointed to the radar target direction when the Acquisition and Tracking System (ATS) is locked to the reflected C signal. The interference, coming from targets with different directions and distances, will be attenuated with the corresponding value of the P -code autocorrelation function and SCCF.

4. CONCLUSION

The application of SCP-RPSC technology in radar bistatic and MRN,s, is proposed in this paper. Matrix presentation of the signals in a bistatic radar

SCP systems is given too. The implementation of the RPSC technology in the transmitter site will give another important benefits and will be subject of future research work. A promising feature is the typical for the RPSC technology random space coding, which will improve the anti jamming resistance of the radar system in the case of jamming targets.

References

- [1]. J. Willis, *Bistatic Radar*. Artech House, Boston, 1991.
- [2]. V. Demirev, *Mobile and Personal Satellite Communications*, TU-Sofia, 2010.

APPLICATION OF SCP TECHNOLOGY IN GLOBAL NAVIGATION SATELLITE SYSTEMS

Veselin Demirev

Radio Communications and Video Technologies Department, TU-Sofia,
Kl. Ohridski blv. № 8, 1756-Sofia,
Tel: 3592-965-26-60; e-mail:demirev_v@tu-sofia.bg

Abstract

Historically, the Global Navigation Satellite Services (GNSS) have been delivered through the use of satellites transmitting in L-band. Targeted to military navigations at first, these services have evolved towards hundreds of civil applications, some of them (for example railway transport) with great accuracy. The use of L-band gives important benefits, such as small onboard antenna size and little or no attenuation due to rain. However, the amount of L-band available, and more specifically the portion allocated to GNSS, is limited. The possible transport applications require a much greater accuracy than normally in L-band because of the ionosphere propagation effects.

An analysis of the possibilities to create new GNSS, working in Ku –band, is given in the report. SCP technology is proposed as solution of the antenna problems. The possible advantages of such kind systems are discussed, as follows:

- Improving the fade margin of GNSS in Ku-band.
- Drastically decrease of ionosphere propagation errors.
- Improving the GNSS system parameters due to directivity of the SCP virtual antenna pattern – better isolation among different satellites, better pseudo-satellite compatibility, better anti-jamming and multi-path propagation properties.

1. INTRODUCTION

Historically, the Global Navigation Satellite Services (GNSS) have been delivered through the use of satellites transmitting in L-band (out of which only a few tens of MHz are assigned to GNSS use from regulatory authorities). Targeted to military navigations at first, these services have evolved towards hundreds of civil applications, some of them (for example railway transport) with great accuracy. The use of L-band gives important benefits, such as small onboard antenna size and little or no attenuation due to rain. However, the amount of L-band available, and more specifically the portion allocated to GNSS, is limited. Moreover, frequency reuse due to different orbital slots is extremely limited. The possible transport applications require a much greater accuracy than normally in L-band because of the ionosphere propagation effects.

To definitely overcome the problems due to the L-band, the only choice is to move GNSS to a higher frequency band. Ku-band (frequencies between 11 and 14 GHz, out of which 2+2 GHz assigned to satellite use) is an ideal candidate to offer error free GNSS. An analysis of the possibilities to create new GNSS, working in Ku–band, is given in the report. SCP technology [1,6] is proposed as solution of the existing antenna problems. The possible advantages of such kind systems are discussed.

2. SCP GNSS SYSTEM ARCHITECTURE

A possible architecture of a SCP based GNSS is shown in fig.1. The signals from different navigation satellites (Sat.1....Sat.M) are received by a random phased Radial Line Slot Antenna (RLSA), down-converted and separated by means of coarse code recovery circuits (C1, C2,...CM recovery). The sum of the output signals is Gaussian random with Rayleigh distribution. It is strong correlated with the sum of the precise code signals (P1,P2....PM), coming from the corresponding satellites. The outputs of the P-codes recovery units are used for pseudo range navigation measurements in convenient way. In fig. 2 the frequency spectrum of the navigation signals in the proposed SCP-GNSS is shown.

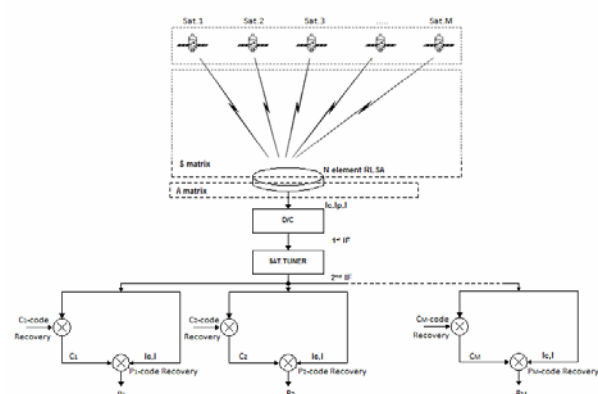


Figure 1. Architecture of the proposed SCP GNSS

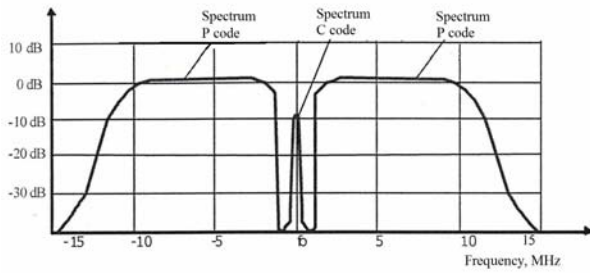


Figure 2. Frequency spectrum of the navigation signals in a SCP GNSS

3. ADVANTAGES OF GNSS IN KU-BAND

3.1. Improving the fade margin of GNSS in Ku-band

A basic parameter of the satellite communications channels is the Carrier to Noise Density Ratio [2]:

$$C/N_0 = C/kT_s = C/T_s + 228,6 \text{ (dBHz)}, \quad (1)$$

where:

$$C/T_s = EIRP - L + G_r / T_s \text{ (dBW/K)}, \quad (2)$$

where $EIRP$ is the Equivalent Isotropically Radiated Power of the transmitter site, L –propagation losses and G_r is the gain of the receiving antenna,

$$L = L_0 + L_{add} \text{ (dB)}, \quad (3)$$

where L_0 are the Free Space Path Losses,

$$L_0 = 201g R + 201g f + 92,45 \text{ (dB)}, \quad (4)$$

and L_{add} are the additional losses in the atmosphere and hydrosphere, f is the frequency in GHz, and R is the distance between the ground station and the satellite in km.

Bearing in mind eq. 1, 2, 3 and 4, it is possible to compare different GNSS on the basis the parameter C/N_0 .

L - band:

- The used antennas are semi omni directional in order simultaneous receiving of navigational signals from all visible satellites. Antenna gain is about 3 dB.
- $L_{add} = 2$ dB in heavy rain.

Ku -band:

- By means of SCP technology [1], it is possible to develop antenna system with 36 dBi gain and diameter about 60 cm, with several virtual beams directed towards different navigation satellites.

The antenna dimensions are suitable for proper antenna mounting over cars, boats, planes or trains roofs.

- The additional losses, due to heavy rain conditions, are in order of 10 dB. The increase of the free space losses will be in order of 8,8 dB.

The common increase of the propagation losses due to the use of Ku-band will be about 17 dB. On the contrary, due to the much higher antenna gain, the parameter C/N_0 will be about 14 dB higher. The result will be drastically decrease of the thermal noise User-Equivalent Range Error (UERE), which is now about 11,1 m [3, fig. 5.10].

3.2. Drastically reduce of the ionosphere propagation errors

One of the main source of UERE are the propagation effects in the Earth Ionosphere. They are result of the Sun activity and often they are unpredictable. The root mean square Ionosphere delays UERE in normal activity is equal to 9,9 m, but in the case of high sun activity and low satellite elevation it could reach even 50 m [3]. There are many ways to reduce these kinds of errors, but all of them suffer from different disadvantages.

The frequency dispersion of the root mean square Ionosphere delays UERE could be approximated with $1/f^2$. The transfer of GNSS frequencies from L to Ku –band will lead to about 50 times decrease of this error, which will delete the importance of Ionosphere delays UERE over satellite navigation systems.

3.3. Improving the GNSS system parameters due to the directivity of the SCP virtual antenna patterns

- better isolation among signals of the different satellites
- better pseudo-satellite compatibility
- better anti-jamming properties

In particular GNSS applications the down-links will be well protected from jamming, coming from the side-lobes of the Spatial Cross-Correlation Function (SCCF), an important parameter of the SCP technology. The level of the side-lobes will be very low (in order of -25, -30 dB). It leads to good protection rations of SCP down-links against ground based terrorist jamming.

- better anti multi-path propagation properties.

One of the main reason for navigation errors in GNSS are the reflected signals (fig. 3), causing s.c. multi-path errors. In some cases UERE, due to multi-path, can reach 12,6 м [4,5]. In a SCP-GNSS the down-links are well protected from multi-path reflections, coming from the low side-lobes of the SCCF.

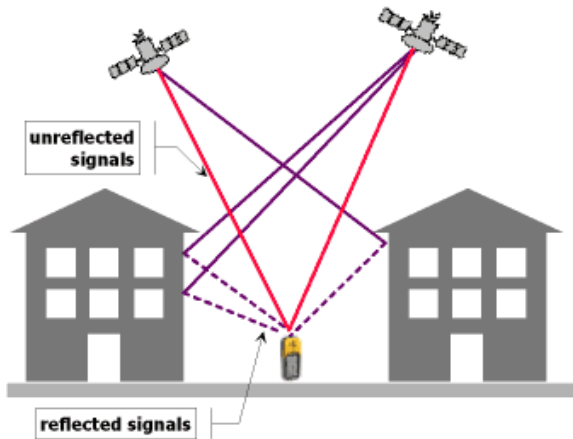


Figure 3. Multi-path of GNSS signals in urban environment

4. CONCLUSION

The preliminary analysis of the possible transition from L to Ku-band of the future high accuracy GNSS, based on SCP technology, gives good first results and impressions. In the future this possibility should be studied in details, based on funded research projects.

Referencies

- [1] В. Демирев, Мобилни и Персонални Спътникови Комуникации, Изд. ТУ-София, 2010.
- [2] G.Gordon, W. Morgan, Principles of Communications Satellites, John Willey&Sons, 1993.
- [3] M.Grewal, L. Weill, A. Andrews, Global Positioning Systems, Inertial Navigation and Integration, Wiley, 2001.
- [4] E. Kaplan, Understanding GPS – Principles and Applications, Artech House, 1996.
- [5] Error analysis for the Global Positioning System, Wikipedia, Internet.
- [6] В. Демирев, "Приложение на технологията SCP в системите за спътникова навигация", Трудове на Бултранс, 2011, стр. 47-50, Септември, 2011, Созопол.

MODIFIED FRACTAL KOCH CURVE ANTENNA STUDY

Boncho G. Bonev

Technical University of Sofia
8 Kliment Ohridski Blvd., 1700 Sofia, Bulgaria
Tel. +35929652870; E-mail: bbonev@tu-sofia.bg

Abstract

Most of recent wireless communications technologies need multi-band and miniaturized antennas. The fractal antennas advantages fit these challenges. Koch curve fractal structure is one that is often used in antenna design, because of its simplicity.

In this work modified fractal antenna that can be used in wireless communication systems is suggested. This antenna is combination of 1st and 2nd iteration Koch curve.

This antenna has been tested and some main characteristic like SWR dependence on frequency for UHF band, resonance frequencies and radiation pattern have been obtained. The comparison with 1st and 2nd iteration Koch curve antennas have been also performed.

1. INTRODUCTION

Communications development in last years defines more and more requirements towards communication devices. The operation of a single device with several technologies (GSM-900, GSM-1800, UMTS etc.), that work in different frequency bands demands usage of antennas working in these bands. Moreover the tendency of devices miniaturization is also referred to its antennas. Therefore in the last decade there is a strong interest in possibilities of fractal designed antennas usage in telecommunication devices. Their characteristics fit these requirements – multiband usage and small size due to their shape [1-5].

In this paper is presented an experimental investigation on fractal monopole antennas, shaped as Koch curve. The modified monopole Koch curve antenna is suggested. It is combination of 1-st and 2-nd iteration of Koch curve and will be called 1.5 iteration in this paper. The standing wave ratio (SWR) dependence on frequency and radiation pattern in H-plane of the suggested antenna and of the 1-st and 2-nd Koch curve monopole antennas are experimentally obtained.

2. KOCH CURVE

Fractals are geometry objects and each part of them consist their small shapes. The Koch curve monopole is one of the first fractal antennas used in communication. Geometrical shape of zero, 1-st and 2-nd iteration of the Koch curve is showed on Figure 1. The 1-st iteration is obtained as the zero

one is partitioned into three equal parts and the middle part is replaced with two elements with the same length. This process is reused for each part of this 1-st iteration and in that way is obtained the 2-nd iteration etc. The total length of the Koch curve can be given with equation [6]

$$L = L_0 \left(\frac{4}{3} \right)^n, \quad (1)$$

where L_0 is the zero iteration length, also called initiator, and n is the iteration number.

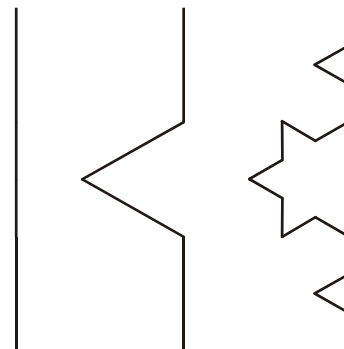


Figure 1. Zero, 1-st and 2-nd iteration of Koch curve

The fractal dimension of the Koch curve is

$$D = \log 4 / \log 3 = 1.2618. \quad (2)$$

3. EXPERIMENTAL INVESTIGATION ON KOCH CURVE FRACTAL MONOPOLE ANTENNAS

On Figure 2 are showed the antennas that are object of the experimental study. The antenna in the

middle is suggested 1.5 iteration of Koch curve. It is obtained from the 1-st iteration by changing only the two side elements with these of 2-nd iteration. That allows increase of the total length of the antenna and respectively decrease of working frequency bands according to the 1-st iteration, but the shape of this antenna is simpler than the 2-nd order antenna. The total length of the 1.5 iteration is $L_0 \cdot \frac{14}{9}$.

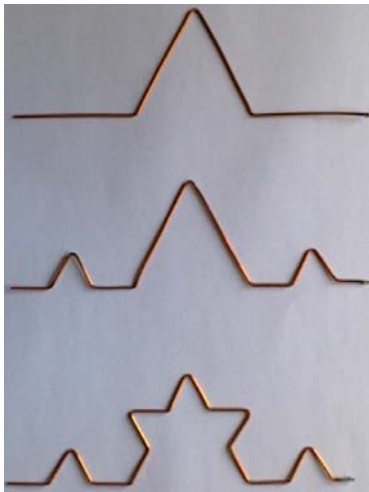


Figure 2. Studied antenna models

3.1. SWR

For obtaining the SWR dependence on frequency have been used microwave generator and network analyser. The results are given on Figure 3 – 5, and the resonance frequencies in Table 1. During the experiment the antennas have being placed over conductive surface.

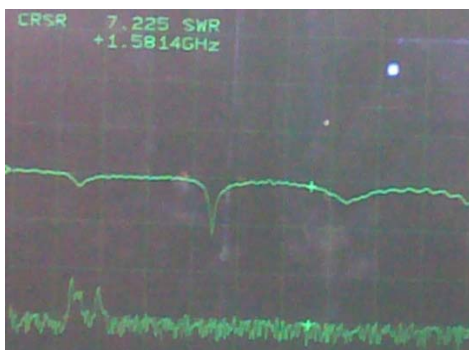


Figure 3. SWR (f) for 1-st iteration

These figures show that when the number of iteration increases the resonance frequency decreases because of bigger length of the antenna model.

The antenna models have 3 resonance frequencies in the frequency band 300 - 2100 MHz. The

SWR for the first resonance frequency of all models $SWR > 2$ but it can be improved by using methods described in [7]. The bandwidth ($SWR < 2$) for 2-nd and 3-rd resonance of suggested 1.5 iteration antenna is respectively 32.25 MHz and 77,5 MHz, while for 1-st iteration it is maximum 50 MHz and for 2-nd iteration maximum 56,3 MHz.



Figure 4. SWR (f) for 1.5 iteration

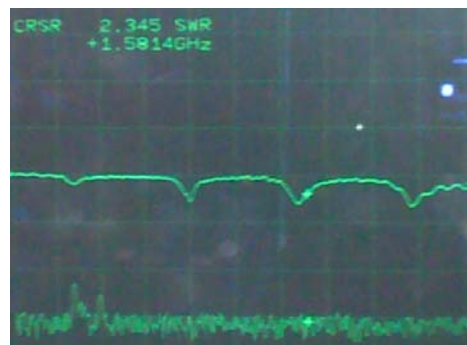


Figure 5. SWR (f) for 2-nd iteration

Table 1. First three resonance frequencies of studied models

1-st iteration	1.5 iteration	2-nd iteration
366 MHz	356.5 MHz	359 MHz
1.069 GHz	1 GHz	966 MHz
1.763 GHz	1.623 GHz	1.544 GHz

3.2. Radiation patterns in H-plane

On Figures 6, 7, 8 are given radiation patterns of the studied models in H-plane.

They were measured in open area. In this measurement two equivalent antennas in the transmitter and in the receiver were used. The investigation was fulfilled for the 2-nd resonance frequency of each antenna model – see Table 1. The antennas were situated in distance of 5 m over conductive surface.

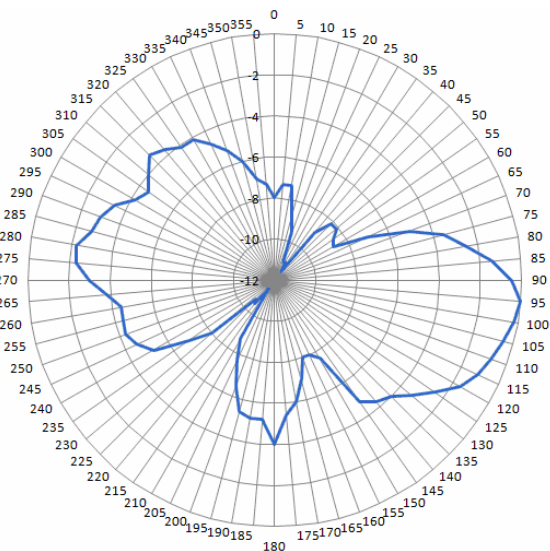


Figure 6. Radiation pattern in H-plane for 1-st iteration antenna model

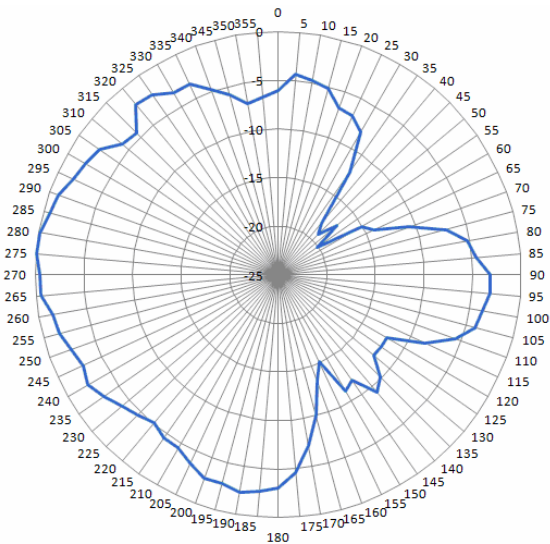


Figure 7. Radiation pattern in H-plane for 1.5 iteration antenna model

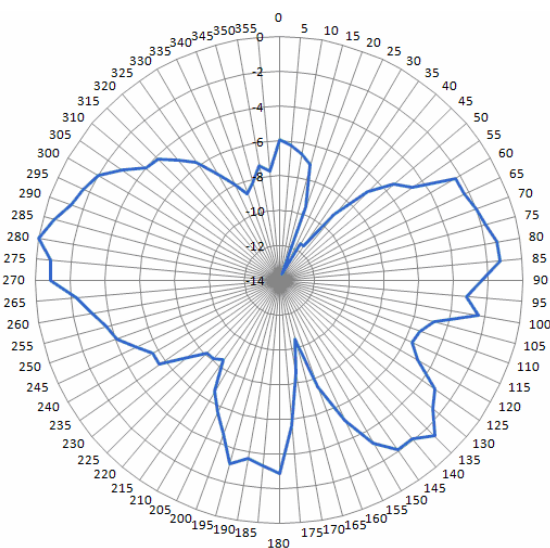


Figure 8. Radiation pattern in H-plane for 2-nd iteration antenna model

4. CONCLUSIONS

Maximums of the radiation patterns are approximately in the same directions for all studied models. The radiation patterns have two basic lobes like classical monopole antennas but 2-nd iteration has also some small side lobes.

The radiation pattern of the 1.5 iteration antenna has main lobe that is wider than of other two antennas. That allows this antenna to be used for some radio links that required almost isotropic radiation in given sector for example in point-to-multipoint systems, security systems, observation systems etc. The bandwidth of 1.5 iteration antenna is bigger than of 1-st and 2-nd iteration antennas. That allows this antenna to be used in communication technologies that required wider bandwidth.

5. ACKNOWLEDGMENTS

This work was supported under Project INDECT - "Intelligent Information System Supporting Observation, Searching and Detection for Security of Citizens in Urban Environments."

References

- [1] R. S. Aziz, M. A. S. Alkanhal, and A. F. A. Sheta, Multi-band Fractal-like antennas, *Progress In Electromagnetics Research B*, Vol. 29, pp. 339-354, 2011.
- [2] Y. Lee, J. Yeo, R. Mittra, S. Ganguly, J. Tenbarger, *Fractal and Multiband Communication Antennas*, 2003 IEEE Topical Conference on Wireless Communication Technology, pp. 273-274, 2003.
- [3] Munish Kumar, Trisha Garg, *Antenna Miniaturization using Fractal Antenna and its Design*, International Journal of Enterprise Computing and Business Systems, Vol. 1 Issue 2 July 2011, <http://www.ijecbs.com>.
- [4] Kulbir Singh, Vinit Grewal, Rajiv Saxena, *Fractal Antennas: A Novel Miniaturization Technique For Wireless Communications*, International Journal of Recent Trends in Engineering, Vol 2, No. 5, November 2009.
- [5] Anagnostou D., M.T. Chryssomallis, J.C. Lyke, C.G. Christodoulou, *Improved multiband performance with self-similar fractal antennas*, 2003 IEEE Topical Conference on Wireless Communication Technology, pp. 271-272, 2003.
- [6] Karim M.N.A., M.K.A. Rahim, M. Irfan, T. Masri, *Fractal Koch curve for UHF band application*, 2007. APACE 2007. Asia-Pacific Conference on Applied Electromagnetics, pp. 1-4, Dec. 2007.
- [7] Angelov, K., B. Bonev, P. Simeonov, R. Tsochev, *Fractal Designed Antenna Matching*, ICEST'2011, Nis, Serbia, pp. 675-678, June 2011.

METHODS FOR INCREASE ACCURACY AND REDUCE THE AVERAGING TIME IN PRECIPITATION INTENSITY MEASUREMENT FOR RADIOWAVE PROPAGATION INVESTIGATIONS

Boncho G. Bonev, Emil S. Altimirski, Kliment N. Angelov

Technical University of Sofia
8 Kliment Ohridski Blvd., 1700 Sofia, Bulgaria
Tel.: +35929652870; Fax: +35929652230; E-mail: bbonev@tu-sofia.bg

Abstract

Accurate measurement of the precipitation intensity and collection of sufficient data for them is an essential prerequisite for precise prediction of attenuation of radio waves and the reliability of the radio links at frequencies above 10 GHz. The available data from meteorological services are not appropriate because their intensity averaging time is great and it does not allow recording peaks of the intensity. Moreover, some of the methods of measurement do not allow sufficient measurement accuracy for heavy precipitation, which have an important role in the interruption of the radio links.

Two methods of measurement to improve accuracy and reduce time for averaging are proposed in this paper. The first is a combination of the two main existing approaches - the tipping bucket and weighing methods. It allows more accurate registration of heavy rainfall intensity. The second method is based on the non-linear transformation of precipitation (water flow) in water level (weight) and measurement of this level. It allows maintaining good relative accuracy of measurement and it is relatively simpler than the first one.

1. INTRODUCTION

The attenuation of the radio waves in hydrometeors significantly affects the functioning of the radio links operating at frequencies above 10 GHz [1]. The methods for predicting and evaluating the attenuation in such conditions, are largely based on rainfall data from the meteorological services in different regions of the world. This data is not always suitable for the needs of the communications [2, 3]. Most often, the period of time taken in consideration for averaging the rainfall rate is relatively large and this leads to not accounting of the peak values of the rain rate, which would result in extreme attenuation of the radio waves and therefore to a possibility of disruption of the radio links for a certain, although relatively small, period of time.

In some cases, are made attempts, based on the collected precipitation data with relatively large averaging time to be restored the true picture of the rain rate, i.e. to be obtained the actual values of the rain rate for smaller intervals of time during the period of averaging only by the average rain rate for this period based on a statistics for the relationship between these parameters for other regions.

Moreover, some of the main methods for measuring the rain rates does not allow sufficient accuracy at extreme values of the rain rate [4].

In the present work, two methods for measuring the rain rate are proposed, they are based on the previously existing methods, but allow avoidance of the disadvantages in terms of communications, in particular averaging the values for small enough period of time and providing higher accuracy at high values of rain rates. Furthermore they are complied with the achievement of relatively low price of the monitoring devices.

In the analysis of the main parameters of the devices, which will be developed, based on these methods, is taken into consideration the statistics of precipitation for the territory of Bulgaria and the attenuation model for radio wave propagation in precipitation.

2. METHODS FOR PRECIPITATION INTENSITY MEASUREMENT, ALLOWING REDUCTION OF THE AVERAGING TIME AND INCREASING THE ACCURACY

2.1. Method for precipitation intensity measurement, based on measurement of weight and tipping bucket system

2.1.1. Structure and principle of operation

A major problem in determining of the rain rate, by measuring the weight of collected water from

given area covered by collecting device, is providing of fast enough procedure of emptying the container in which the water is collected, in order to measure water's weight. If this container is with small volume, which will allow its rapid emptying, then it will be difficult to be registered the rain rates with high values. If the volume is large enough to allow registering of high values of rain rates, the container will be emptying for a relatively long period of time and this will lead to failure measurements for this period and thereby the loss of data, especially at high values of rain rate. Therefore, in the proposed method, the water from the precipitations is collected and measured in the reservoirs on tipping bucket mechanism (Figure 1), which allows fast emptying after filling. Their volume should be large enough so that not to be necessary too frequent emptying of them and therefore losing of measurement records.

The principle of operation of the proposed device consists of the following: water from the precipitations covered by the surface of the collecting device (1) falls into one of the reservoirs of the tipping bucket mechanism (2) and is measured by the weight sensor (4).

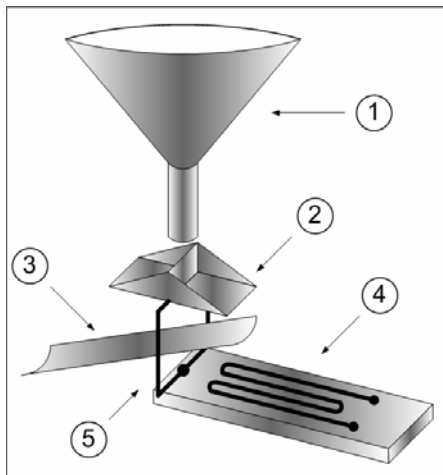


Figure 1. Scheme of device for measuring the rain rate based on measurement of weight and tipping bucket mechanism

When one of the reservoirs fills up, the rocker turns upside down and the reservoir empties, while the other reservoir starts to fill. The water from the reservoir is conveyed by special furrow (3) in order not to fall on the sensor. Thus, the release of water from the container in which it is collected for measuring is relatively fast compared with the time for its filling.

2.1.2. Analysis of some of the main parameters of the measuring devices

For the purposes of the measuring of instantaneous values of rain rates it is necessary to select a suitable averaging time t_{av} . It is the interval between two records of the weight of the water from the fallen precipitations and for the purposes of measuring the attenuation of radio waves from the millimeter range it should be small enough. For example, when the desired reliability of the radio link is 99.9999% of the time, i.e. on an annual basis is allowed no more than 32 seconds disability. Therefore the interval t_{av} must be much smaller and can be chosen $t_{av} = 1$ s. On the other hand the operating range of the udometer should be selected, in order to ensure accurate reporting of the rains that could affect the propagation of the radio waves. For maximum value of the intensity of the rain can be chosen $RR_{max} = 400$ mm/h. When choosing the minimum value RR_{min} on the other hand, some parameters from constructive character must be considered. It will depend on the size of the collecting device S , the averaging time t_{av} and the resolution of the sensor weight Δm . The following equation (1) shows this relationship:

$$RR_{min} = \frac{3,6 \cdot \Delta m}{S \cdot t_{av}} \quad (1)$$

In Figure 2 is shown the graph of relation (1) for several values of Δm from weight sensors that are available on the market.

From the graph can be selected reasonable values for the size of the area of the collecting device and the minimum value of rain rate, which can be recorded since they can determine other constructive parameters in terms of the maximum rain rate value.

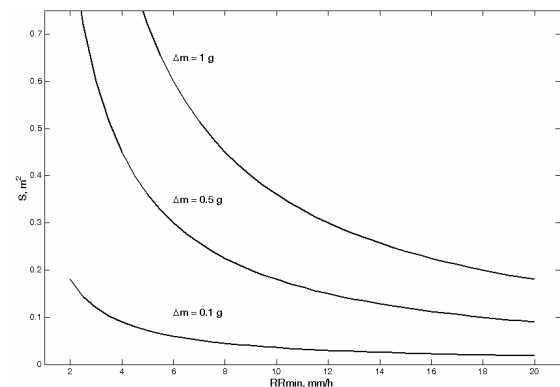


Figure 2. Dependence of the area of the collecting device and the minimum rain rate

Equation (2) reflects the relationship between the volume of the one chamber of the tipping bucket system V in cm^3 and the surface of the collecting device S for a maximum rain rate:

$$V = \frac{t_{\max} \cdot RR_{\max} \cdot S}{3.6}, \quad (2)$$

where t_{\max} is the time to rollover the tipping bucket mechanism. This reversal is associated with short-term interruption of the recording process and should happen on large intervals of time in order to approximate the lost reports based on the other values. According to our estimates, it should be 20 to 50 times greater than the averaging time.

Figure 3 shows a graph of relation (2) for several values of t_{\max} at $RR_{\max} = 400 \text{ mm/h}$.

Through the thus obtained relationships it can be selected an optimal combination of construction and operating parameters of the udometer so that it will allow measurements for the purposes of accounting of the attenuation of electromagnetic waves from the centimeter and millimeter bands in rain, which will be the subject of future research and experiments.

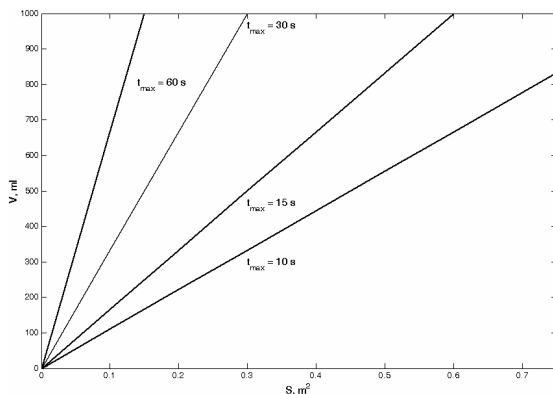


Figure 3. Dependence of the volume of the one chamber of the tipping bucket mechanism from the area of the collecting device

2.2. Method for measuring the rain rate through nonlinear transformation of the intensity of precipitation in weight

In the second proposed method, the rain rate is transformed into water level, respectively, in the weight of the water collected by the device shown in Figure 4.

The water from the collecting device (1) is poured into measuring cone (2), which has a slot with variable width from which a part of the water flows into a special furrow (3). When the precipitation is weak, the water level in the measuring cone

will be low, therefore the water that will flow through the slot will be less. In heavy rains, the level will increase and the amount of water that pours from the measuring cone will also increase and in such manner a non-linear transformation of the intensity of precipitation to water level (respectively the weight of water in the measuring funnel) is obtained, which can be register with the weight sensor (4).

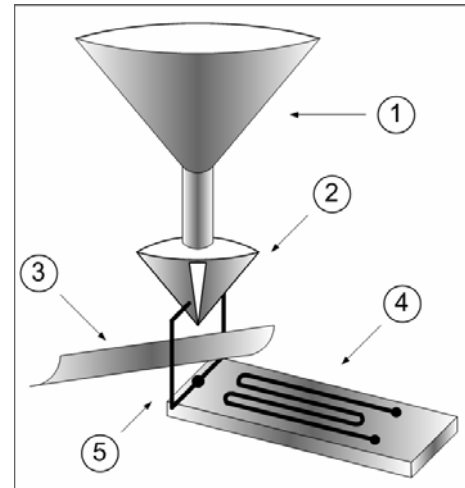


Figure 4. Scheme of the device for measuring the rain rate with nonlinear transformation of the amount of the precipitation in level (weight)

Thus the rain rate is transformed into water level, while it is kept a relatively constant accuracy throughout the whole range of variation in the rain rate values. The shape of the slot, its size and the size of the measuring funnel will be the subject of future experimental work.

3. ACKNOWLEDGMENTS

This work is supported under Project Nr DUNK-01/03 – 12.09 “University Scientific and Research Complex for Innovation and Transfer of Knowledge in Areas of Micro/Nano Technologies and Materials, Power Effectiveness and Virtual Engineering”.

References

- [1] ITU-R P.838-3.
- [2] Duchon, C. E. and Biddle, C. J.: Undercatch of tipping-bucket gauges in high rain rate events, *Adv. Geosci.*, 25, 11-15, doi: 10.5194/adgeo-25-11-2010, 2010.
- [3] Hassan M., A. Ali, M. Alhaider, Rain Measurements for MM-Wave Propagation: A Review, *J. Eng. Sci, King Saud Univ.*, Vol. II, 179-200, 1985.
- [4] Habib E., W. Krajewski, A. Kruger, Sampling Errors of Tipping-Bucket Rain Gauge Measurements, *Journal of Hydrologic Engineering*, 159-166, March/April 2001.

ELECTROMAGNETIC CHARACTERISTICS OF THE “VERY – NEAR – FIELD” REGION OF A CIRCULAR UNIFORM APERTURE

Antoniya Petrova Petrova

Technical University of Sofia, Bulgaria
Faculty of Telecommunication, TU-Sofia, “Kl.Ohridsky” str. 8, 1000 Sofia, Bulgaria
E-mail: tony.petrova@gmail.com

Abstract

The main purpose of this paper is to investigate the behavior of the electromagnetic field in the region of “near-field reactive” or “very-near field”. In this unusual and rather unknown region, trying to explore the specific characteristics of the radiated fields, the wave impedance, and the power density. Based on this parameters, it is succeed in determining, the outer boundary of the “very-near field” region of a circular aperture with a uniform illumination law. The big interest of the “near-field reactive” due to the fact that the antennas for physiotherapy are located very close to the human body and the propagation of the electromagnetic waves is precisely in this field. The study and visualization of the electromagnetic field would lead to more effective treatments to patients.

1. INTRODUCTION

Two main regions can be divided into the space around the antenna: far field and near field. In the far field, electric and magnetic fields propagate outside as an electromagnetic wave and are perpendicular to each other and to the direction of propagation. The angular field distribution does not depend on the distance from the antenna. The fields are uniquely related to each other through free-space impedance and decay as $1/r$. In the near field, the field components have different angular and radial dependence. The near field region includes two sub-regions: radiating, where angular field distribution is dependent on the distance, and reactive, where the energy is stored but not radiated.

2. THEORETICAL SOLUTION

The first in the “far-field” region, at distances greater than $2D^2/\lambda$, where the angular field distribution is independent of the distance from the antenna and the radiated wave is spherical. The second is the “near-field radiating” (Fresnel) region, at distances less than $2D^2/\lambda$, wherein the angular field distribution is dependent upon the distance from the antenna. In this region, the radiated wave, which is first a plane wave, is progressively transformed into a spherical wave. The third is the “near-field reactive” region, located between 0 and $\lambda/2\pi$ from the antenna, wherein the reactive field predominates.

For circular aperture is determined the “very-near-field” region as an interference region, inside

which the radiated wave presents the following characteristics: the electric and magnetic fields are out of phase; the wave impedance is different from 120π (i.e., the free-space impedance); and the power density has a complex formulation, with a real part and an imaginary part. This region is extended up to one-quarter of the Rayleigh distance: up to $D^2/8\lambda$.

$$\vec{E}(P) = -j \frac{k^2}{4\pi} \int_s^{-\infty} \left\{ -jZ_0(\hat{n} \times \vec{H}) + Z_0(2 + 3j)[\hat{r} \cdot (\hat{n} \times \vec{H})] \hat{r} + (1 - j)\hat{r} \times (\hat{n} \times \vec{E}) \right\} \exp(-jkr) dS \quad (1)$$

$$\vec{H}(P) = -j \frac{k^2}{4\pi} \int_s^{-\infty} \left\{ \frac{j}{Z_0}(\hat{n} \times \vec{H}) - \frac{1}{Z_0}(2 + 3j)[\hat{r} \cdot (\hat{n} \times \vec{E})] \hat{r} + (1 - j)\hat{r} \times (\hat{n} \times \vec{H}) \right\} \exp(-jkr) dS \quad (2)$$

where Z_0 is a wave impedance and $Z_0 = 120\pi$, r is a distance, \hat{n} is the unit normal to the surface.

Consequently, the Poyting vector $\vec{p} = \frac{1}{2} \vec{E} \times \vec{H}$, is a complex vector. A direct computation of this has shown us that for various apertures the real and the imaginary parts of \vec{p} are nearly equal. So, can say that at the distance $r = \lambda/2\pi$ there is as much reactive as active power density. Thus, this distance cannot represent the end of the “near-field-reactive” region. It seems more convenient to investi-

gate the distance at which the ratio between the reactive and the active power density becomes lower than -30dB, for example. Beyond this distance could consider that the reactive power density is negligible. Moreover, for the same reason as why \vec{p} is complex, the wave impedance, which is the ratio between E and H , is also complex. This feature could also characterize the “near-field-reactive” region.

So, I think that the distance beyond which

- The reactive power density is negligible
- The wave impedance is equal to 120π

Would really show the limit of the “near-field-reactive” region.

The fact that these two electromagnetic characteristics, \vec{p} and Z , are complex is linked to an interference phenomenon of the fields near the aperture. In the reference case of a circular aperture with uniform illumination, such interference is noteworthy, and may be interpreted thanks to the Huygens – Fresnel principle. This will allow us to conclude that the “near-field-reactive” region is located between 0 and $D^2/8\lambda$, i.e. one – quarter of the Rayleigh distance.

3. ELECTROMAGNETIC PARAMETERS OF THE “VERY-NEAR-FIELD” REGION OF A CIRCULAR UNIFORM APERTURE

If we compare the interference lobes of the E and the H fields for a 5λ – radius aperture with a uniform illumination, can see that the E and H maximum magnitudes are not exactly similar. We can then assume that these two fields are not exactly in phase. Figure 1 shows the phase shift between the E and H fields. This difference, first equal to $\pi/8$, tends to zero when the observation point moves away from the aperture. So, close to the aperture, the E and H fields are out of phase. Each peak of the plot (Figure 2) corresponds to a minimum of the interference lobes of the field magnitude. The last one, located at one – quarter of the Rayleigh distance, points to a phase difference about 2° , beyond, the fields can be considered to be in-phase.

The first consequence of this shift is that the wave impedance is complex, and therefore different from the free – space propagation impedance, which is $Z_0 = 120\pi$. The presence of some reactive power is the second consequence. Indeed, the power density is complex in this region, and it under-

lines the presence of a stationary wave, confined near the surface, in addition to a travelling wave that radiates. Both features are characteristics of the “very-near-field” region.

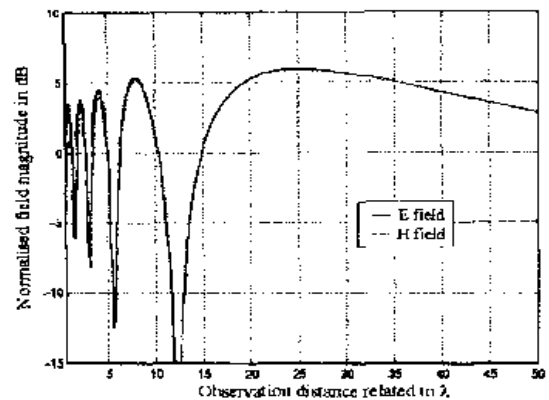


Figure 1. The E and H interference lobes in the “very-near-field” region of a 5λ radius aperture.

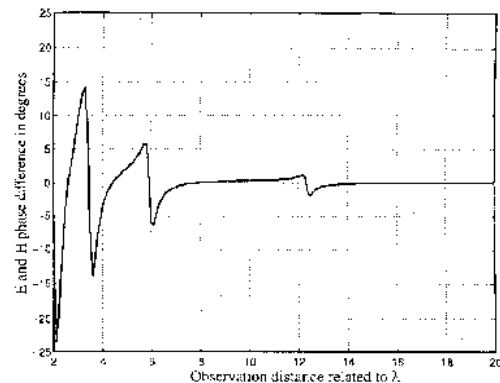


Figure 2. The phase shift between the E and H fields.

3.1. Wave Impedance

Concerning the wave impedance, is used a criterion that is the relative difference between Z and Z_0 , that is $|Z - Z_0| / Z_0$, where $Z = E/H$ is the complex wave impedance and $Z_0 = 120\pi$. Point out that close to the aperture, Z is different from Z_0 , and it is considered that outside the “very-near-field” region, the wave impedance has to be equal to Z_0 . To characterize the “very-near-field” region of a dipole antenna, the limiting value has been set there to be 0.01.

Figures 3a, 3b and 3c show the variations of this criterion on the central perpendicular axis of the circular apertures studied in the previous section. They also present definite peaks, corresponding once again to the minima of the field magnitude. It is noticed that the value of the criterion, 0.01, is reached exactly for one – quarter of the Rayleigh distance, i.e., just after the last peak, for the 5λ

radius aperture, and just on the last peak for the 10λ and the 25λ radii apertures. Further than one-quarter of use Rayleigh distance, the criterion will be less than this limiting value, and we can consider that Z and Z_0 .

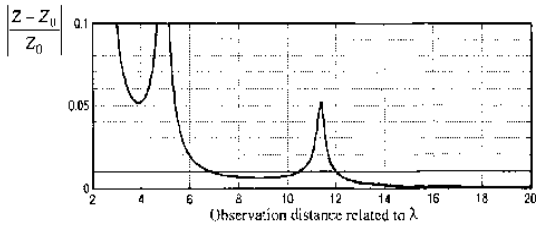


Figure 3a. The wave impedance criterion for 5λ radius circular aperture ($R_r/4 = 12,5\lambda$).

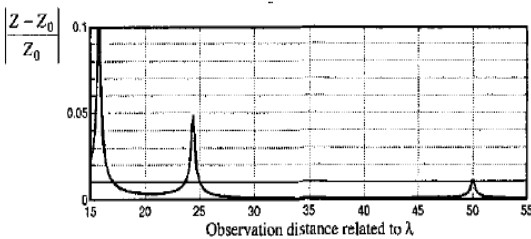


Figure 3b. The wave impedance criterion for 10λ radius circular aperture ($R_r/4 = 50\lambda$).

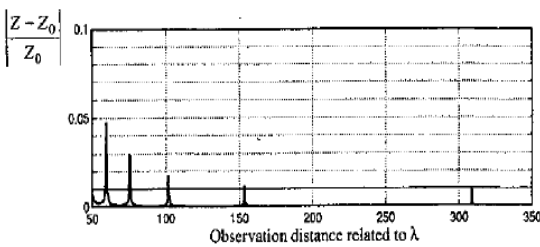


Figure 3c. The wave impedance criterion for 25λ radius circular aperture ($R_r/4 = 312,5\lambda$).

3.2. Power Density

The criterion is used relative to the power density is the ratio of the imaginary and the real parts of the Poynting vector in the direction of propagation. This ratio, characterizes the presence of reactive power near the aperture and a pertinent limit value was set at -30dB (i.e., 10^{-3} in linear value). Indeed, for such a proportion can consider that the reactive power is negligible, and so conclude that outside the: "very-near-field" region there is no more reactive power.

Figures 4a,4b and 4c illustrate the variations of the power-density criterion on the central perpendicular axis of the same circular apertures as in Section 3.1. For the wave-impedance criterion can notice that the limiting value of the power-density

criterion is reached for one-quarter of the Rayleigh distance, i.e., just after the last peak for the 5λ and 10λ radii apertures, or just on the last peak for the 25λ radius aperture.

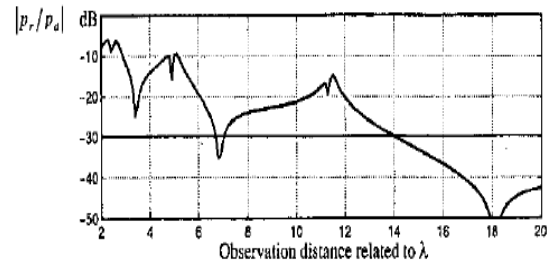


Figure 4a. The power density criterion for 5λ radius circular aperture ($R_r/4 = 12,5\lambda$).

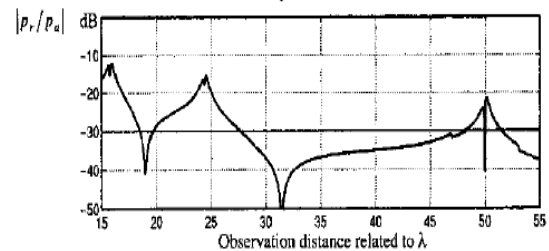


Figure 4b. The power density criterion for 10λ radius circular aperture ($R_r/4 = 50\lambda$).

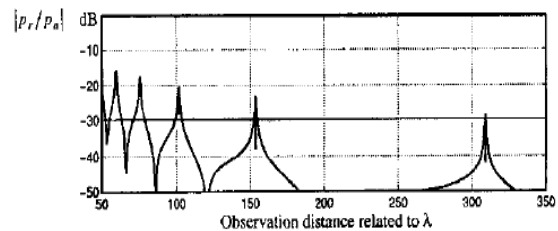


Figure 4c. The power density criterion for 25λ radius circular aperture ($R_r/4 = 312,5\lambda$).

3.3. Transverse Section Analysis in the "Very-Near-Field" Region

On the next figures are shown the variations of these criteria, not only along the central perpendicular axis, but also on the transverse planes. Figures 5a, 5b and 5c, concern the wave - impedance criterion for the aperture for 10λ radius, and Figures 6a,6b and 6c illustrate the power-density criterion. For such an aperture, we saw that the upper boundary of the "very-near-field" region was located at 50λ . These graphics display the variations of both criteria on the transverse planes, located at distances of 15λ and 30λ from aperture - thus, inside the "very-near-field" region - and at a distance of 60λ , outside this region. The radiation in the "near-field or Rayleigh" region in concentrate in a tubular beam.

That is the reason why the transverse views are focused on this beam inside a circle of 10λ radius.

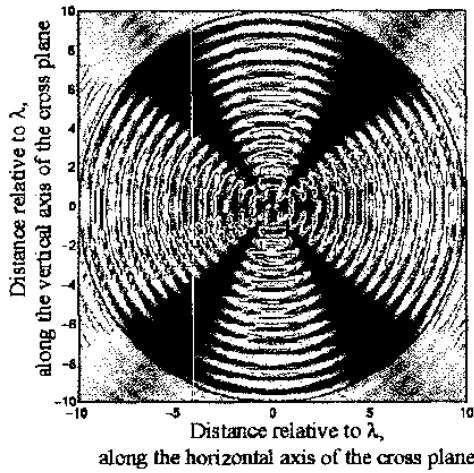


Figure 5a. The variations of wave impedance criterion for 10λ radius aperture ($R_r/4 = 50\lambda$) on the transverse plane at 15λ from the aperture.

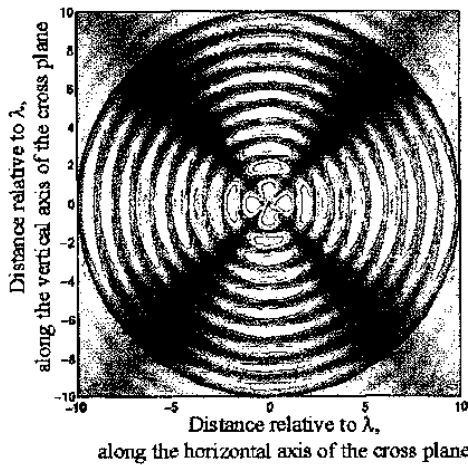


Figure 5b. The variations of wave impedance criterion for 10λ radius aperture ($R_r/4 = 50\lambda$) on the transverse plane at 30λ from the aperture.

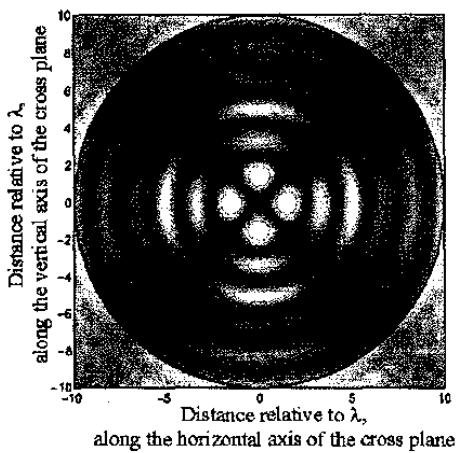


Figure 5c. The variations of wave impedance criterion for 10λ radius aperture ($R_r/4 = 50\lambda$) on the transverse plane at 60λ from the aperture.

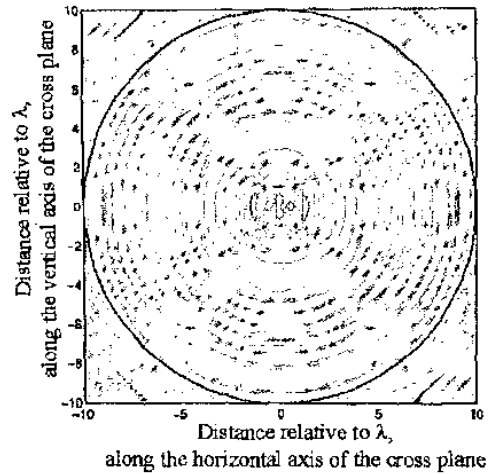


Figure 6a. The variations of power density criterion for 10λ radius aperture ($R_r/4 = 50\lambda$) on the transverse plane at 15λ from the aperture.

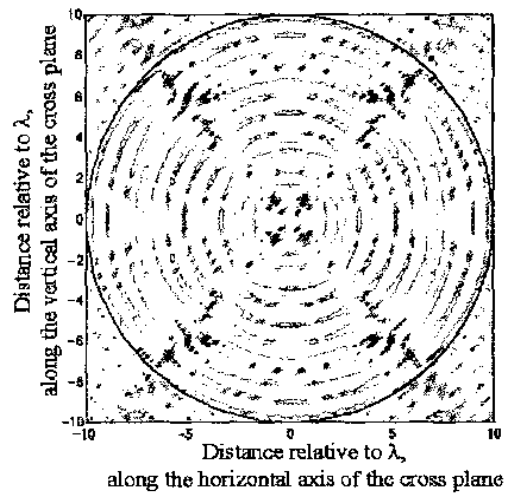


Figure 6b. The variations of power density criterion for 10λ radius aperture ($R_r/4 = 50\lambda$) on the transverse plane at 30λ from the aperture.

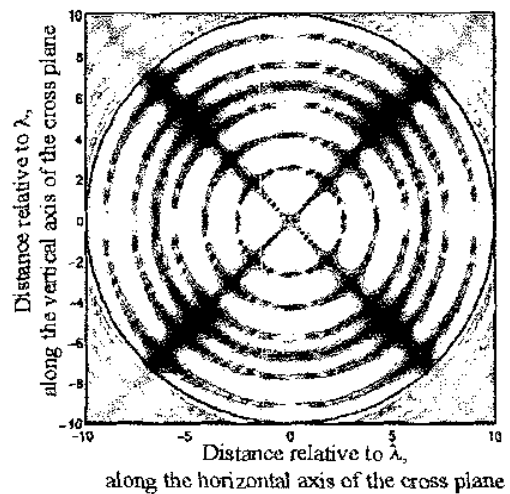


Figure 6c. The variations of power density criterion for 10λ radius aperture ($R_r/4 = 50\lambda$) on the transverse plane at 60λ from the aperture.

The transverse views in Figures 5 show that the impedance criterion, really disturbed inside the beam for a short observation distance, is higher than the limiting value of 0.01. According to these variations can conclude that inside the "very-near-field" region, Z isn't equal to Z_0 . It tends to be uniform moving away up to the "very-near-field" region boundary (50λ). At 60λ – so just after this limit – can see that almost everywhere in the tubular beam the wave – impedance criterion is less than 0.01. There, Z is equal to Z_0 .

The power-density criterion presented in Figures 6 lead to the same conclusions as the impedance criterion. At 15λ , the ratio of the reactive power density is not negligible compared with the active power density, and up to 50λ , note some reactive power. So, all along the "very-near-field" region, there is still reactive power, first comparable to the active power, and then more and more negligible. At 60λ from the aperture and in the tubular beam of 10λ radius, there are as many points where the reactive – power criterion is greater than -30dB as points where this criterion is less than -30dB. But can clearly see that the levels less than -30 dB often decrease down to -50dB, whereas for only a few points do the levels greater than -30dB reach -20dB. So, can say that the mean level is lower than -30dB. Outside the "very-near-field" region, there is no more reactive power.

4. CONCLUSION

We can state that for a uniform circular aperture, the behavior of the criteria along the central axis is representative of what happens inside all of the tubular radiated beam. In view of these results can claim that the criteria for the wave impedance and the power density and their limiting values are adequate to define the boundary of the "very-near-field" region at $R_r/4$. So getting to know the electromagnetic field with its characteristics can more easily focus antennas for physiotherapy, which will result in more effective treatment of the patient.

Acknowledgments

The paper will be included in the Proceedings of 7th INTERNATIONAL CONFERENCE on Communications, Electromagnetics and Medical Applications (CEMA'12) Athens, Greece, November 08th - 10th, 2012 on the base of financial support of contract 121пд0009-07, Sector for scientific research of Technical University-Sofia, Bulgaria

References

- [1] D. Dimitrov, Medical systems influence of electromagnetic fields on human, education book, TU-Sofia, 2007
- [2] W. Y. Riadh, "Electromagnetic Fields and Radiation (Human Bioeffects and Safety)", Marcel Dekker Inc. Canada, 2001, ISBN 0-8247-0877-3
- [3] Shoogo Ueno, Biological Effects Of Magnetic And Electromagnetic Fields (The Language Of Science)
- [4] C. A. Balanis, Advanced Engineering Electromagnetics, 2nd Edition, New York, John Wiley, February 2012
- [5] C. A. Balanis, Antenna Theory : Analysis and Design, 3rd Edition, New York, John Wiley, April 2005
- [6] S. Laybros and P. F. Combes, "On Radiating Zone Boundaries of Short, $\lambda/2$ and λ Dipoles", IEEE Antennas and Propagation Magazine, 45, 5, October 2004, pp. 53-64.

ELECTROMAGNETIC CHARACTERISTICS OF THE “VERY – NEAR – FIELD” REGION OF A SQUARE UNIFORM APERTURE

Antoniya Petrova Petrova

Technical University of Sofia, Bulgaria
Faculty of Telecommunication, TU-Sofia, “Kl. Ohridsky” str. 8, 1000 Sofia, Bulgaria
E-mail: tony.petrova@gmail.com

Abstract

The big interest of the “near-field reactive” due to the fact that the antennas for physiotherapy are located very close to the human body and the propagation of the electromagnetic waves is precisely in this field. The study and visualization of the electromagnetic field would lead to more effective treatments to patients. The main purpose of this paper is to investigate the behavior of the electromagnetic field in the region of “near-field reactive” or “very-near field”. In this unusual and rather unknown region, trying to explore the specific characteristics of the radiated fields, the wave impedance, and the power density. It is observed the influence of the illumination law and of the aperture shape on the extent of this region, through the cases of parabolic or cosine laws, and the case of square-shape aperture.

1. INTRODUCTION

The space around the reader antenna can be divided into two main regions: far field and near field. In the far field, electric and magnetic fields propagate outward as an electromagnetic wave and are perpendicular to each other and to the direction of propagation. The angular field distribution does not depend on the distance from the antenna. The fields are uniquely related to each other via free-space impedance and decay as $1/r$. In the near field, the field components have different angular and radial dependence. The near field region includes two sub-regions: radiating, where angular field distribution is dependent on the distance, and reactive, where the energy is stored but not radiated.

2. THEORETICAL SOLUTION

For antennas whose size is comparable to wavelength, the approximate boundary between the far field and the near field region is commonly given as $r=2D^2/\lambda$, where D is the maximum antenna dimension and is the wavelength. For electrical small antennas, the radiating near field region is small and the boundary between the far field and the near field regions is commonly given as $r = \lambda/2\pi$.

We are interesting in the “near-field radiating” (Fresnel) region, at distances less than $2D^2/\lambda$, wherein the angular field distribution is dependent upon the distance from the antenna. In this region, the

radiated wave, which is first a plane wave, is progressively transformed into a spherical wave. The third is the “near-field reactive” region, located between 0 and $\lambda/2\pi$ from the antenna, wherein the reactive field predominates.

$$\begin{aligned} \vec{E}(P) = & -j \frac{k^2}{4\pi} \int_s^{-\infty} \{ -jZ_0(\hat{n} \times \vec{H}) \\ & + Z_0(2 + 3j)[\hat{r} \cdot (\hat{n} \times \vec{H})]\hat{r} \\ & + (1 - j)\hat{r} \\ & \times (\hat{n} \times \vec{E}) \} \exp(-jkr) dS \end{aligned} \quad (1)$$

$$\begin{aligned} \vec{H}(P) = & -j \frac{k^2}{4\pi} \int_s^{-\infty} \left\{ \frac{j}{Z_0} (\hat{n} \times \vec{H}) \right. \\ & - \frac{1}{Z_0} (2 + 3j)[\hat{r} \cdot (\hat{n} \times \vec{E})]\hat{r} \\ & \left. + (1 - j)\hat{r} \times (\hat{n} \times \vec{H}) \right\} \exp(-jkr) dS \end{aligned} \quad (2)$$

where Z_0 is a wave impedance and $Z_0 = 120\pi$, r is a distance, \hat{n} is the unit normal to the surface.

For square aperture is determined the “very-near-field” region as an interference region, inside which the radiated wave presents the following characteristics: the electric and magnetic fields are out of phase; the wave impedance is different from 120π (i.e., the free-space impedance); and the power density has a complex formulation, with a real part and an imaginary part. This region is ex-

tended up to one-quarter of the Rayleigh distance: up to $D^2/8\lambda$. Consequently, the Poynting vector $\vec{p} = \frac{1}{2} \vec{E} \times \vec{H}$, is a complex vector. A direct computation of this has shown us that for various apertures the real and the imaginary parts of \vec{p} are nearly equal. So, can say that at the distance $r = \lambda/2\pi$ there is as much reactive as active power density. Thus, this distance cannot represent the end of the “near-field-reactive” region. It seems more convenient to investigate the distance at which the ratio between the reactive and the active power density becomes lower than -30dB, for example. Beyond this distance could consider that the reactive power density is negligible. Moreover, for the same reason as why \vec{p} is complex, the wave impedance, which is the ratio between E and H, is also complex. This feature could also characterize the “near-field-reactive” region.

So, I think that the distance beyond which

- The reactive power density is negligible
- The wave impedance is equal to 120π

Would really show the limit of the “near-field-reactive” region.

The fact that these two electromagnetic characteristics, \vec{p} and Z, are complex is linked to an interference phenomenon of the fields near the aperture. In the reference case of a circular aperture with uniform illumination, such interference is noteworthy, and may be interpreted thanks to the Huygens – Fresnel principle. This will allow us to conclude that the “near-field-reactive” region is located between 0 and $D^2/8\lambda$, i.e. one – quarter of the Rayleigh distance.

3. ELECTROMAGNETIC PARAMETERS OF THE “VERY-NEAR-FIELD” REGION OF A CIRCULAR UNIFORM APERTURE

Now deepen the influence of the aperture-illumination law. This is why, it is determined the “very-near-field” region upper boundary for square aperture with a nonuniform illumination. As for the uniform square case, the “very-near-field” region boundary will be set at the distance where the field magnitude reaches its last minimum.

Four nonuniform equiphase laws are reviewed here: parabolic, squared parabolic, cosine and square cosine distributions. Figure 1 displays the variations of the E-field magnitude along the central axis in the case of a 10λ radius square surface with the four different illumination laws. We can notice that

the variations present less pronounced peaks than for the uniform case. Due to these illuminations, the fields of each Fresnel zone do not present the same magnitude, which decreases and lends to zero on the edge of the aperture. So, even if the fields from the Fresnel zones have opposite phases, their magnitudes do not have the same weight. This explains why the interference phenomena are all the more damped as the illumination law is tapered.

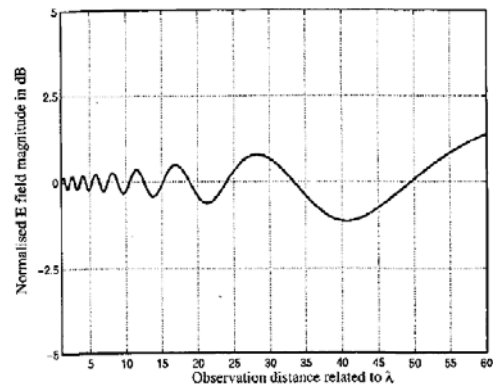


Figure 1a. The axis magnitude of the E field for an aperture of radius equal to 10λ with parabolic illumination

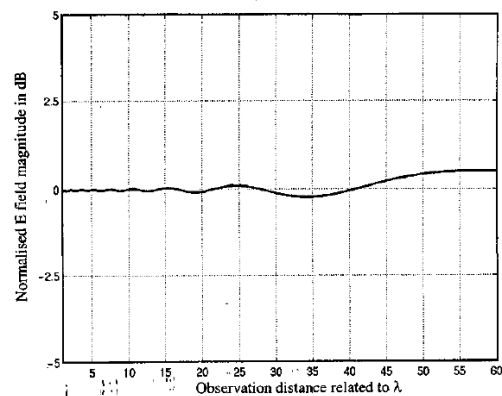


Figure 1b. The axis magnitude of the E field for an aperture of radius equal to 10λ with square parabolic illumination

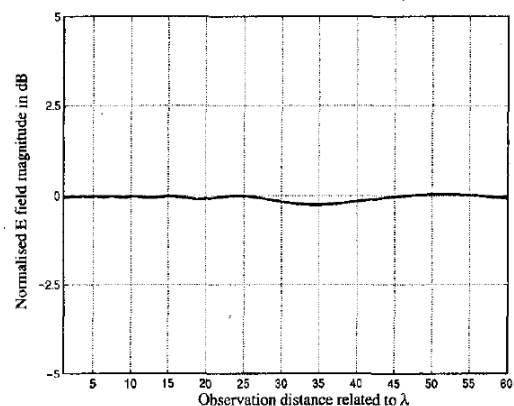


Figure 1c. The axis magnitude of the E field for an aperture of radius equal to 10λ with square cosine illumination

Even so, it is still possible to determine the location of the last minimum. For the 10λ radius aper-

ture presented here, succeeded in concluding with a coefficient applied to $R_r/4$. Indeed, for the parabolic law, for example, the last minimum is located at $0,82 R_r/4$.

So, reasoning in the same way as for the uniform-illumination aperture, it is determined the upper boundary of the "very-near-field" region of apertures with a nonuniform illumination. These boundaries are defined as a fraction of a quarter of the Rayleigh distance, R_r .

Some square apertures with a uniform illumination have been studied. Figures 2 display the variations of the E-field magnitude along the central axis of such apertures. The square apertures under study are 10λ , 20λ and 50λ wide. Also, in these cases, the interference is less pronounced than in the case of the circular aperture. Indeed, the Fresnel zones – which present a rotational symmetry – are not matched for the square aperture.

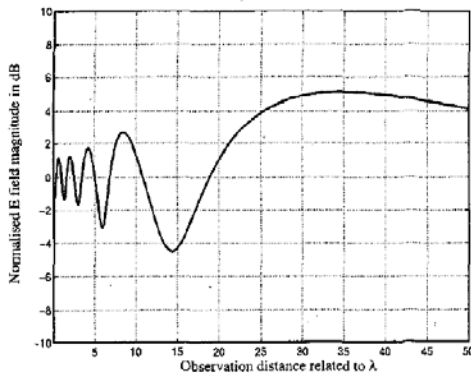


Figure 2a. The axis magnitude of the E field for a 10λ wide ($R_r/4 = 12,5\lambda$) square aperture

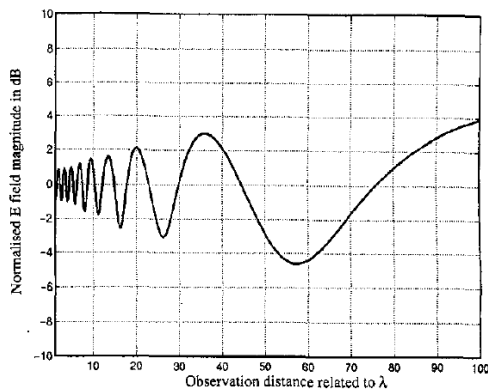


Figure 2b. The axis magnitude of the E field for a 10λ wide ($R_r/4 = 50\lambda$) square aperture

In order to determine the upper boundary of the "very-near-field" region of these apertures, we pinpointed the last minimum of the E-field magnitude. Once again, it is arrived at a coefficient to apply to $R_r/4$. This time, the coefficient is higher than 1. For the three apertures of different dimensions, the coefficient is equal to 1.14.

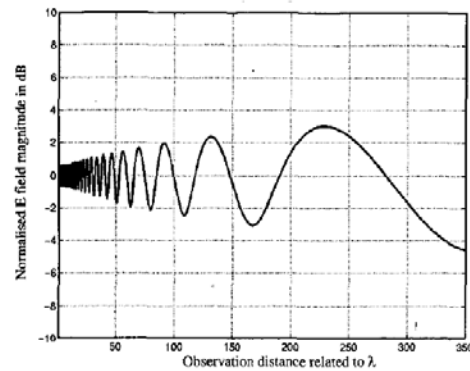


Figure 2c. The axis magnitude of the E field for a 10λ wide ($R_r/4 = 312,5\lambda$) square aperture.

3.1. Wave Impedance

The interference along the central axis is less noteworthy in the square case than in the circular case. Consequently, the wave impedance criterion variations for the square apertures do not present notable peaks. These variations are shown in Figures 3a, 3b and 3c for the 10λ to 50λ wide apertures. The limiting value of 0.01 is reached at distances really suitable for the square apertures, because it does not present a circular symmetry around this axis.

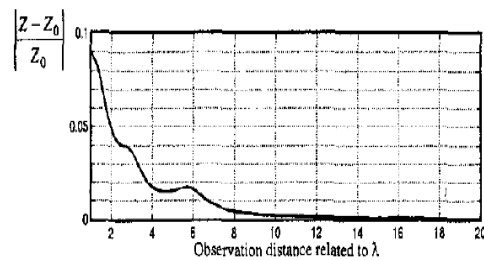


Figure 3a. The wave impedance criterion for 10λ wide square aperture ($1,14R_r/4 = 14,5\lambda$).

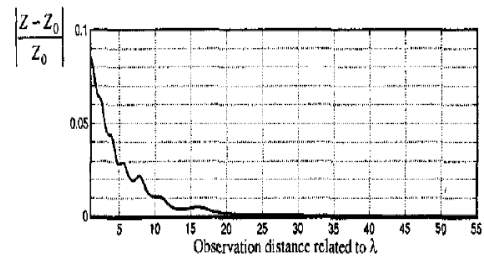


Figure 3b. The wave impedance criterion for 20λ wide square aperture ($1,14R_r/4 = 57\lambda$).

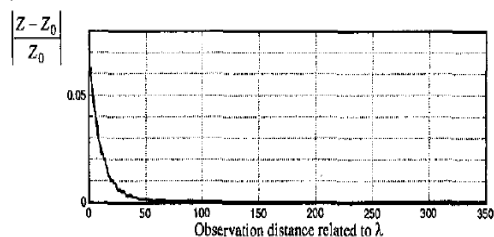


Figure 3c. The wave impedance criterion for 50λ wide square aperture ($1,14R_r/4 = 356\lambda$).

3.2. Power Density

Figures 4a, 4b and 4c present the variations of the power density criterion for the same square apertures. In the way can notice that the limiting value of -30dB does not occur at distances about $1,14R_r/4$, but closer to the aperture. Moreover, the distances deduced from this criterion are also different from the distances obtained from the impedance criterion. So, in the square-aperture case can assume that these two criteria are not consistent on the central axis.

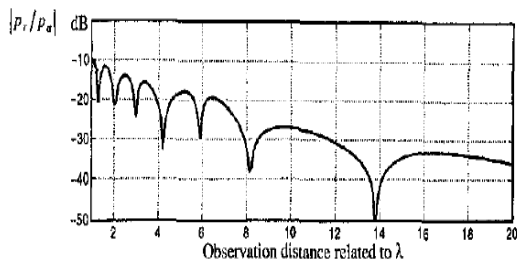


Figure 4a. The power density criterion for 10λ wide square aperture ($1,14R_r/4 = 14,5\lambda$).

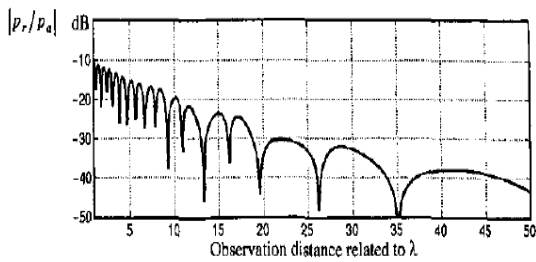


Figure 4b. The power density criterion for 20λ wide square aperture ($1,14R_r/4 = 57\lambda$).

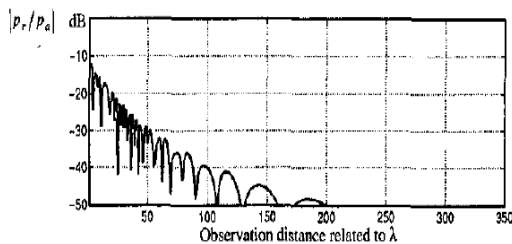


Figure 4c. The power density criterion for 50λ wide square aperture ($1,14R_r/4 = 356\lambda$).

3.3. Transverse section analysis in the "very-near-field" region

The radiation in the "very-field or Rayleigh" region is concentrated inside a square tubular beam. Figures 5a, 5b and 5c display the variations of the wave impedance criterion for a 20λ wide square aperture, for which the "ver-near-field" region is extended up to 57λ . The first two figure show this criterion on the transverse planes located at 15λ

and 30λ , below this boundary. Referring to them can say that Z is not yet to Z_0 . At 60λ – that is, just after the "very-near-field" region boundary – the criterion is lower than the limiting value of 0,01. It can note from these views that the maximum values of the criterion are not located on the central axis, contrary to the circular case. This justified the observation that the criterion on the central axis is not conclusive.

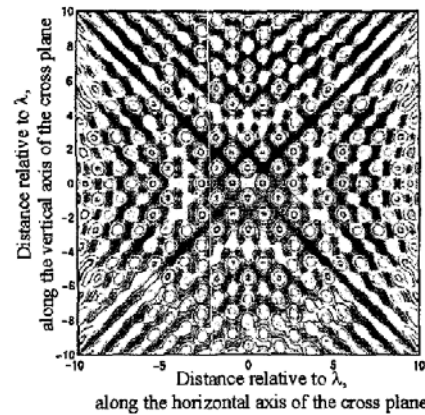


Figure 5a. The variations of wave impedance criterion for 20λ radius aperture ($1,14R_r/4 = 57\lambda$) on the transverse plane at 15λ from the aperture

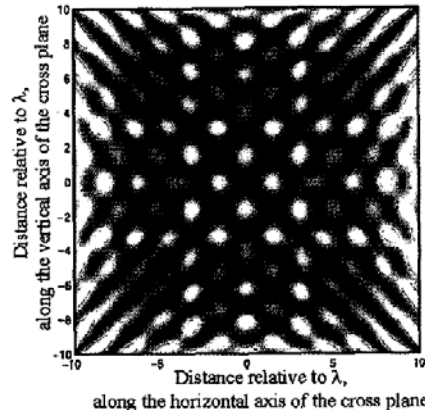


Figure 5b. The variations of wave impedance criterion for 20λ radius aperture ($1,14R_r/4 = 57\lambda$) on the transverse plane at 30λ from the aperture

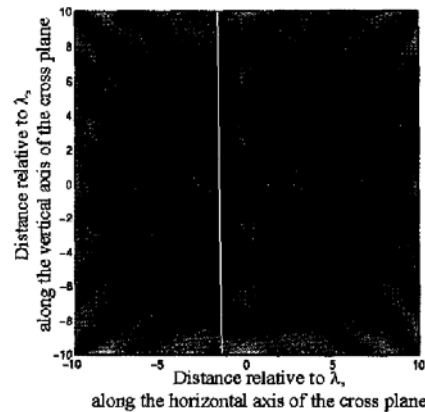


Figure 5c. The variations of wave impedance criterion for 20λ radius aperture ($1,14R_r/4 = 57\lambda$) on the transverse plane at 60λ from the aperture

Figures 6a, 6b and 6c concern the power density criterion. It emphasizes that the “very-near-field” region boundary set at 57λ seems coherent. Indeed, the figures for the distances of 15λ and 30λ let us see that the reactive power density is not negligible compared with the active power density at such distance. For a distance of 60λ – just after the “very-near-field” region boundary – we can see that the power density criterion is more or less than -30dB inside the square tubular beam. As for the circular case do not have to consider the maximum value of the criterion inside the tubular beam, but rather its mean value. Indeed, the most important characteristics is the flux of the power density across the transverse section. So, at 60λ , the mean value of the power density criterion is actually -30dB .

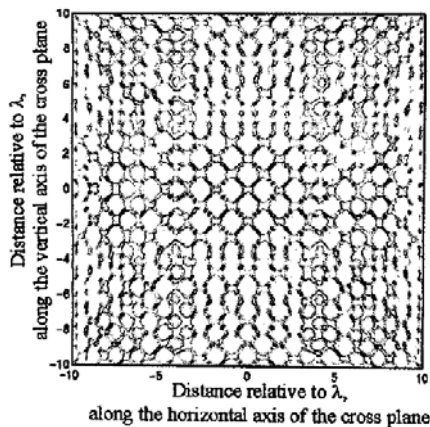


Figure 6a. The variations of power density criterion for 20λ radius aperture ($R_r/4 = 57\lambda$) on the transverse plane at 15λ from the aperture

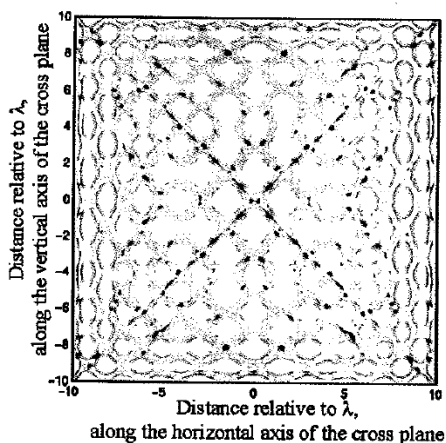


Figure 6b. The variations of wave impedance criterion for 20λ radius aperture ($R_r/4 = 57\lambda$) on the transverse plane at 30λ from the aperture

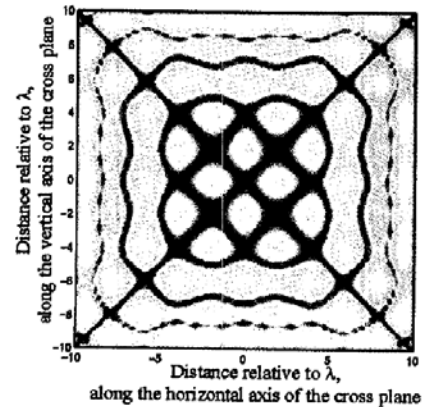


Figure 6c. The variations of wave impedance criterion for 20λ radius aperture ($R_r/4 = 57\lambda$) on the transverse plane at 60λ from the aperture

4. CONCLUSION

We can assume that the boundary of $1,14R_r/4$ for the “very-near-field” region is well suited for the uniform square apertures. Can also conclude that the two criteria are consistent, even for the square-aperture case, providing that they are studied inside all of the tubular beam and not only along the central axis. So getting to know the electromagnetic field with its characteristics can more easily focus antennas for physiotherapy, which will result in more effective treatment of the patient.

Acknowledgments

The paper will be included in the Proceedings of 7th INTERNATIONAL CONFERENCE on Communications, Electromagnetics and Medical Applications (CEMA'12) Athens, Greece, November 08th - 10th, 2012 on the base of financial support of contract 121нд0009-07, Sector for scientific research of Technical University-Sofia, Bulgaria

References

- [1] D. Dimitrov, Medical systems influence of electromagnetic fields on human, education book, TU-Sofia, 2007
- [2] W. Y. Riadh, “Electromagnetic Fields and Radiation (Human Bioeffects and Safety)”, Marcel Dekker Inc. Canada, 2001, ISBN 0-8247-0877-3
- [3] Shoogo Ueno, Biological Effects Of Magnetic And Electromagnetic Fields (The Language Of Science)
- [4] C. A. Balanis, Advanced Engineering Electromagnetics, 2nd Edition, New York, John Wiley, February 2012
- [5] C. A. Balanis, Antenna Theory: Analysis and Design, 3rd Edition, New York, John Wiley, April 2005
- [6] S. Laybros and P. F. Combes, On Radiating Zone Boundaries of Short, $\lambda/2$ and λ Dipoles, IEEE Antennas and Propagation Magazine, 45,5, October 2004, pp. 53-64.

PRACTICAL DESIGN OF MICROWAVE DIODE FREQUENCY MULTIPLIERS

Mihail Plamenov Tonev

Technical University of Sofia, Bulgaria,
Faculty of Telecommunication, TU-Sofia, "Kl.Ohridsky" str. 8, 1000 Sofia, Bulgaria
E-mail: mihail_tonev@abv.bg

Abstract

Phase noise is a critical performance parameter of frequency synthesizers for wireless communications. In phase modulated equipment the integrated phase noise in frequency synthesizer directly impacts to bit error rate of communication system. Design of frequency synthesizers with low phase noise is related to using low noise voltage controlled oscillators. Realizing such oscillators in microwave frequencies is hampered by low quality factor of tuning elements. A method to generate high frequency signal with low phase noise is to generate high quality lower frequency signal and perform frequency multiplication to deliver desired frequency. The purpose of this sheet is to give some theoretical insight for frequency multiplication and some practical guidelines for microwave diode multipliers design.

1. INTRODUCTION

The key element in designing microwave equipment is availability of clean local oscillator. Clean means a signal free from any sort of spurious frequencies or parasitic modulation effects. In most cases spurious frequencies can be filtered by using appropriate filter. The parasitic modulation with low frequency noises of active element, known as phase noise can not be filtered. Unfortunately frequency multiplication process degrades this parameter. The reason about this unfortunate characteristic is that the frequency multiplier in fact is phase multiplier. So it multiplies phase deviations as well as the frequency of input signal. The minimum carrier to noise degeneration, ΔCNR in decibels, caused by frequency multiplier is:

$$\Delta CNR = 20 \log N ,$$

where N is multiplication factor

In spite of this fact, multiplying a very stable low-frequency reference signal can still produce signals with better phase noise than producing them directly in microwave frequencies range.

Frequency multiplication is obtained by applying nonlinear distortion to sinusoidal signal. The spectrum of distorted input signal contains a number of harmonics and suitable harmonic number can be filtered and amplified to obtain output signal with desired frequency and amplitude. Frequency multipliers can be realized either with transistors or diodes. Transistors provide better efficiency but in

microwave frequencies may occurs problem with upconverting low frequency noise. The reason for this effect is that almost all transistors have high gain at low frequencies. This problem is not presented in diode frequency multipliers but they have worse efficiency. Diode multipliers are divided into two groups – reactive multipliers and resistive multipliers. Reactive multipliers can be realized by using varactor or step recovery diodes. They have good efficiency but bandwidth is narrow. Good decision to realize microwave frequency multipliers with relatively high bandwidth is to use resistive diode approach. This type of multipliers has bad efficiency but wide bandwidth and good noise performance. That's why they are main topic in this article.

Depending on how diodes distort sinusoidal signal, multipliers are divided into two groups – odd order and even order. The schematics and output waveforms of these multipliers are shown on fig. 1 and fig. 2. In odd order frequency multipliers the spectrum of output signal contain only odd harmonic numbers and in even order multiplier is the opposite.

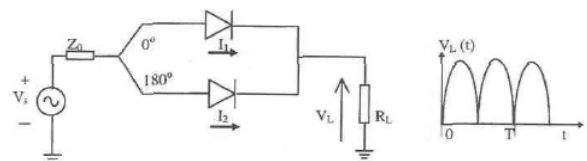


Fig. 1. Even order frequency multiplier

Unwanted harmonics must be filtered and their level has to meet requirements by standard for designed communication equipment. If unwanted har-

monics are not suppressed enough, at the output of multiplier need to be placed more complicated band pass filter. Designing of such filter is difficult and sometimes impossible because it can not be manufactured within acceptable tolerances. That's why harmonic suppression is critical parameter for frequency multipliers. Since the bad efficiency can be compensated by amplifier with higher gain, the bad unwanted harmonic suppression can make design impossible. Improving this parameter is the main topic of this paper.

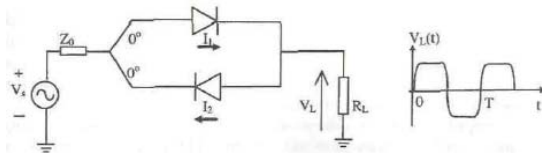


Fig. 2. Odd order frequency multiplier

2. UNWANTED HARMONIC SUPPRESSION IN MICROWAVE FREQUENCY MULTIPLIERS

As was explained above, harmonic content at the output of multiplier depends on how diodes distort the input sinusoidal signal. The generation of odd order harmonics requires paralleling the diodes as shown in fig. 2. In this case the first diode conducts during the positive semi cycle while the second conducts during the other semi-cycle. If applied voltage is high enough, the result is a symmetrical distortion in waveform, resembling square waveform. Theoretically if the duty cycle of this square waveform is 50%, its spectrum will contain only odd harmonics, and even harmonics suppression would be infinity. Unfortunately, in practice 50% duty cycle can't be obtained because ideally symmetrical structure is impossible to be manufactured. Theoretically the influence of duty cycle can be evaluated by performing Fast Fourier Transforming to a square wave signal and results of this research are presented in Table 1. In this case is performed multiplication x5 and suppression of fourth and sixth harmonics is most important, because they are closest the desired harmonic. If we assume 20dB to be good even harmonic suppression, duty cycle of the output signal can be in range of 49.4 to 50.6%.

Table 1. Evaluating influence of duty cycle to even harmonic suppression

Duty cycle [%]	Fourth harmonic suppression [dB]
50	infinity
49.5	22
49	17

In general microwave resistive diode multipliers are realized with dual in package shotky diodes. In this case the diodes have almost the same parameters and asymmetry due to their difference can be neglected. Here more substantial parameter, which influence the duty cycle is parasitic capacitances in diode package and asymmetry in layout due to manufacturing tolerances. Most critical element from PCB layout in microwave frequencies is grounding holes. In fig. 3 is shown equivalent circuit of two shotky diodes in package SOT23. This model was used for designing frequency multiplier x5. The input signal is in frequency range from 1.9 GHz to 2.3 GHz. The circuit was simulated with harmonica simulator, provided by ansoft.

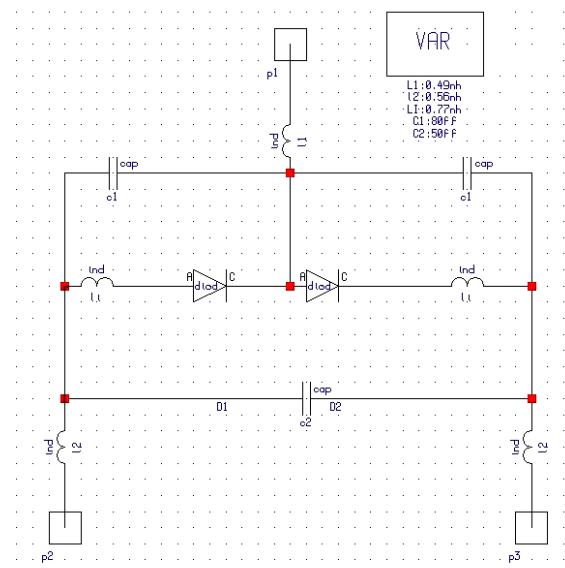


Fig. 3. Nonlinear model for dual shotky diodes in SOT23 package

It wasn't surprising, that simulator shows perfect even harmonic suppression. Here asymmetry in layout is not taken into account. To gain real insight how circuit works the simulated layout of frequency multiplier was manufactured. Material used in design is Arlon25N with dielectric permeability 3.38, substrate thickness 0.51mm and loss tangent 0.0025. In fig.4 is shown measured test fixture.



Fig. 4. Test fixture for microwave diode multiplier x5

To measure even harmonic suppression was used input signal with frequency 2.1 GHz and po-

wer level of 10dBm. Measured output spectrum is shown in fig. 5.

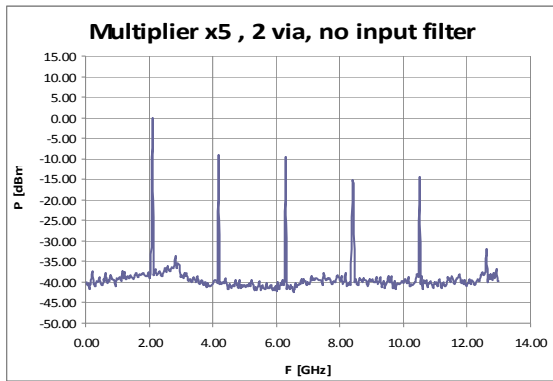


Fig. 5. Measured output spectrum of diode frequency multiplier x5

It's obvious that fourth and fifth harmonic have almost the same levels and we can't speak for any even harmonic suppression. At first sight the design is absolutely failed. To reduce the influence of asymmetry in grounding holes, a big solder drop was put between grounded pins of diode, as shown in fig. 6.



Fig. 6. Diode frequency multiplier with added solder drop between grounded pins

The result of this experiment is shown in fig. 7. Here we notice improvement in harmonic suppression with about 8 dB.

This decision is not good from a manufacturing point of view. This solder drop must be put manually and the manufacturing process cannot be automated.

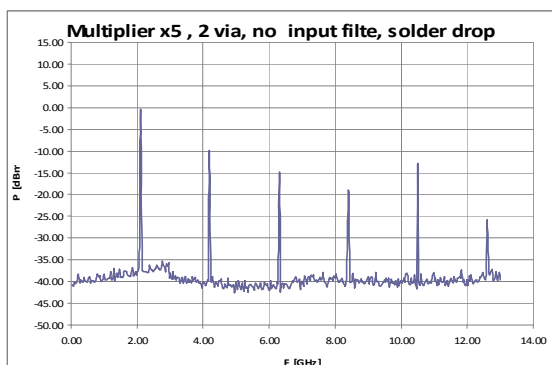


Fig. 7. Measured output spectrum of diode frequency multiplier x5 with added solder drop between grounded pins

To decide this problem was manufactured another test fixture with six grounding holes as shown in fig. 8.

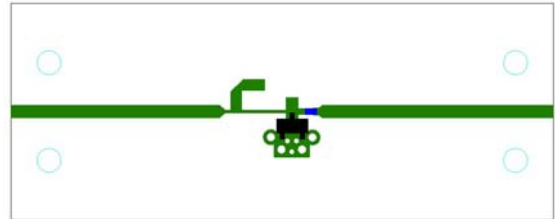


Fig. 8. Redesigned multiplier with 6 grounding holes

Measurement results show that the redesigned test fixture has almost the same harmonic suppression as the first one with a solder drop, fig. 6. This solves the problem with manufacturing automation, but 8dB harmonic suppression is still not enough. This frequency multiplier is suitable for use in VSAT down converters and VSAT standards require unwanted harmonic suppression to be at least -60dBc. If we assume that even harmonic suppression of a frequency multiplier is 8dB, to meet the standard we need a filter which attenuates the fourth and sixth harmonic at least 52dB. This requirement makes filter design very complicated.

To improve even harmonic suppression of a frequency multiplier, the influence of the input signal was researched. Most of the signal sources do not generate a clean sinusoidal signal. It always contains high-order harmonics – second, third, etc. The question is "How harmonic content of the input signal affects the even harmonic suppression". To find an answer to this question, an analogy with a frequency up converter was used. The first harmonic from the spectrum of the input signal acts as a local oscillator frequency for the up converter. Its power is high enough to change the diode's nonlinear transconductance. The second harmonic has a much lower power level than the first harmonic. It can be represented as an RF signal for the assumed up converter. Furthermore, if higher-order harmonics exist, they will also be mixed with the first harmonic, and the products of this mixing will appear at the output of the frequency multiplier. We assume that their level is low enough and they can be neglected. The second harmonic is the major factor, which contributes to the harmonic content at the output of the multiplier. Below are listed some products formed from mixing the first and second harmonics of the input signal and the resultant harmonics which they appear at the output.

$$H1 + H2 = H3$$

$$H1 + 2H2 = H4$$

$$H1 + 3H2 = H5$$

$$H1 + 4H2 = H6$$

It's obvious that they increase levels of all harmonics higher than third and this impact to even harmonic suppression of frequency multiplier. This statement was proved in practice by using frequency multiplier test fixture shown in fig. 4. Let's remind that harmonic suppression was improved with 8 dB by putting additional grounding holes. Now will be shown how even harmonic suppression can be improved further, by filtering the second harmonic of input signal. In fig. 8 is shown spectrum of original input signal and in fig.9 is depicted spectrum after filtering.

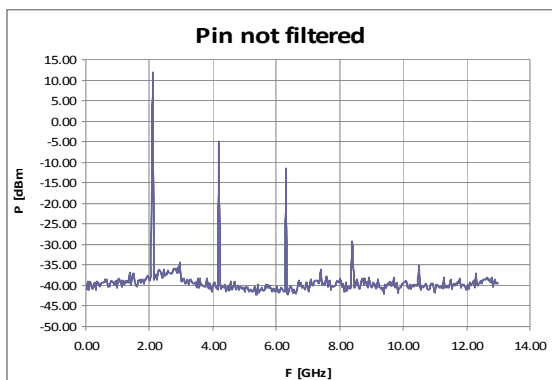


Fig. 8. Spectrum of input signal without low pass filter

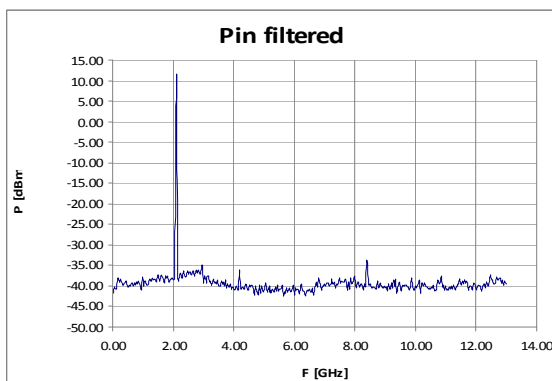


Fig. 9. Spectrum of input signal after filtering high order harmonics

Measurement results without low pass filter are shown in fig. 5 and results with filtered input signal are shown in fig. 10.

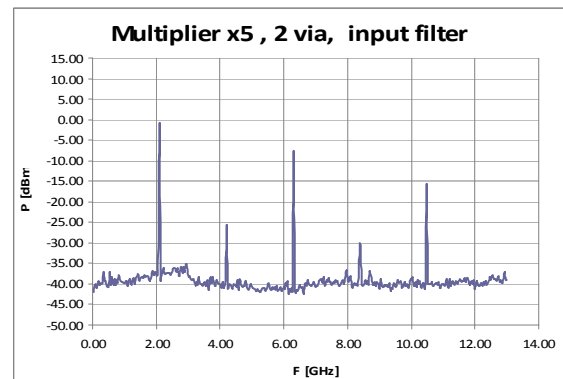


Fig. 10. Measured spectrum of frequency multiplier with filtered input signal

It can be easily seen that improvement in even harmonic suppression by filtering second harmonic is about 15dB.

3. CONCLUSION

A low cost frequency multiplier with uncomplicated design was described. As was explained the harmonic suppression is critical parameter in multiplier design. Practically were proved two methods for enhancing this parameter. The first is to ensure good grounding to diodes. This can be obtained by increasing number of grounding holes in PCB layout of frequency multiplier. And the second method is to use clean input signal. Its second and high order harmonics must be filtered.

References

- [1] Edmar Camargo, Design Of FET Frequency Multipliers And Harmonic Oscillators
- [2] Stephen Maas, Nonlinear Microwave and RF Circuits 2d edition
- [3] Stephen Maas, RF and Microwave Circuit Design Cookbook

ELECTROPORATOR FOR LABORATORY TESTS

Vytautas Dumbrava, Vladas Juska, Darijus Pagodinas, Marius Gailius, Linas Sidaras

Signal processing department , Kaunas University of Technology
Studentu str. 50, LT-51368, Kaunas , Lithuania
T.+37037 300531; F.+37037753998; E. vytautas.dumbrava@ktu.lt

Abstract

In recent years the molecular therapy was successfully developed. Its aim is to achieve an active agent penetration into damaged cells only. This way the agent is getting more effective and causes less side effects. It is often that the membranes of damaged cells are closed and aggravates the active agent penetration inside the cells. It is find out that the use of electroporation methods enables us to solve this problem effectively.

Industry produces a lot of electroporators for clinical work. Laboratory equipment, however, has to have a broader range of parameters, to be able to optimize the electrical parameters and vary them in a relatively wide range.

The electroporator designed in Kaunas University of Technology, Signal processing department is intended for laboratory research purposes to find out more electroporation effects on cell membranes. This paper presents the already done electroporator with the enhanced facilities, its structure and technical parameters. The device has a personal computer (PC) to control parameters of electroporator and has the capabilities for data acquisition on PC and the subsequent digital processing. It also provides synchronization signals for electroporation with programmable temporal shift control.

1. INTRODUCTION

Since that time when the electroporation methods were invented it found more and more application for medical [1-3], and biotechnological [4-5] purposes. Elektroporation (EP) is one of possible methods in which DNA molecules can be delivered into cells by using a short electric pulses. Electrical breakdown of cell membranes can be either reversible or irreversible [3]. Each of them is widely used in a field medicine as well as in biotechnology. In medicine drug regimen traditionnally has been used in various ways: injection, infusions, inhalations, creams, and transdermal patches. In this case, the active agent is distributed throughout the body and this requires the introduction of much higher doses. Since at 1987 successfully was developed molecular therapy, during which an effort is made to reach the active agent only cells that are damaged. Then this agent is becomes more effective and cause fewer side effects. However, the cell membrane is closed and prevents the active agent to enter the cells, so the techniques used, allowing up to facilitate an active agent to enter the cells. It was found that the electroporation (EP) methods to perform duty in an effective way to overcome the cell membrane barriers.

The electroporation is also used to accelerate a green mass drying. [4]. Such a method enables us to save energy used during the drying process.

Electroporation is a new way for the mash treatment of vinification process. Electroporation the mash of red wine enables a fast extract the red pigments from the skin without remarkable heating of the mash. [5].

The aim of this article is to provide the structural scheme of created electroporator for medical purposes, describe the main parameters of the device and the present really output signals using the experimental time diagrams.

2. STRUCTURE

The industry has developed a whole range of industrial electroporators which are used in practice [6] and/or for scientific research in a field of biomedicine [7]. Such devices are rather expensive and are mostly used for standard techniques. The laboratory prototype of the electroporator was designed in Kaunas University of Technology, Signal Processing Department. The prototype has an enhanced facilities and it is made for scientific researches to find the optimal parameters. The quantity of energy absorbed into a cell depends direct from the electrical parameters and for each material it should be chosen and optimised separately [8].

Electroporation of cells in common theory are divided into the high (HV) (up to 1200V) and low amplitude (LV) (up to 100V) packets pulses with variable-frequency and then is observed the state of cell membrane barriers.

The common structure of given electroporator is shown in Fig. 1. The device can be controlled by local keyboard or using the virtual panel from PC. Using the local keyboard it is possible to control and change the electrical parameters in autonomic mode. All functions may also be accomplished by special PC program, which retains the values of operating parameters. In both cases the parameters are shown on local LCD placed within the device.

The values of HV and LV voltages are set up by microprocessor (CPU) and controlled by separate controller, which signals control the AC – DC converter.

Time settings are set by CPU, and the commutation is produced by HV and LV pulse generator. U and I sensors are engaged with the monitoring controller, which consequently informs the CPU about possible failure. Here as well the sequences of HV and LV pulses are summed up. The two dangerous situations of short circuit in the back stage and a failure of back switches can be displayed on the monitor. In both cases the HV voltage is switched off, and the control of switches is blocked. The power unit forms galvanically separated voltages for all of the electroporator units.

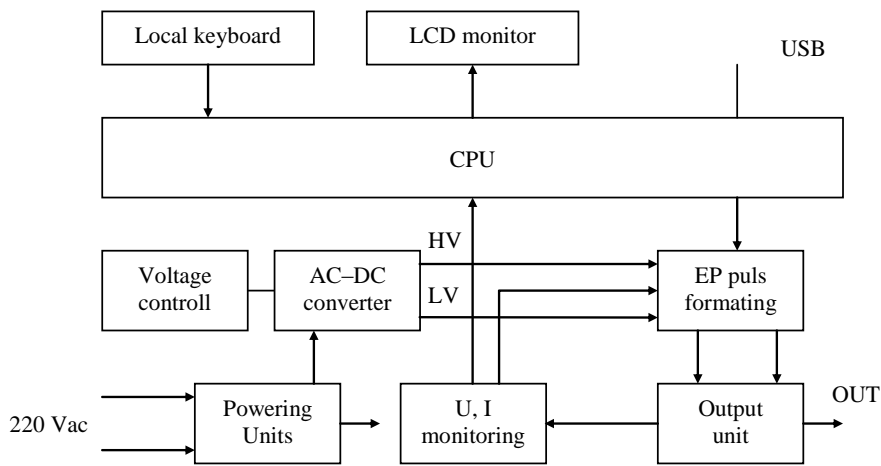


Figure 1. Structure scheme

EP is controlled by three Atmega 64 CPU units. Atmega 16 performs voltage control, while Attiny 13 serves for U and I monitoring. Such a function division between different CPU units made the main CPU software (which performs communication between PC and keyboard, arranges and indicates the parameters) to be much simpler. It also allows to start the EP pulse sequence by using an external pedal, and to indicate the parameter values on the PC monitor and LCD screen at the same time.

For the EP we use a special solution which has sufficiently high electrical conductivity in comparison with 1.5% salt solution used before. When the volume resistance equals around 80 Ohms and HV pulse amplitude of 1000 V as a result we get 12,5 kW pulse power. For that reason the Corner Dubilier capacitor with small parasitic inductance L_P was chosen. The equivalent experimental scheme showed in Fig.2. Apart from the above mentioned values the experimental scheme includes circuit capacitance C_M and the capacitance between electrodes and solution C_S .

The augmentation rate of pulse current can be defined as follows:

$$I(t) = [C_M + C_S] \frac{du_c}{dt} \tag{1}$$

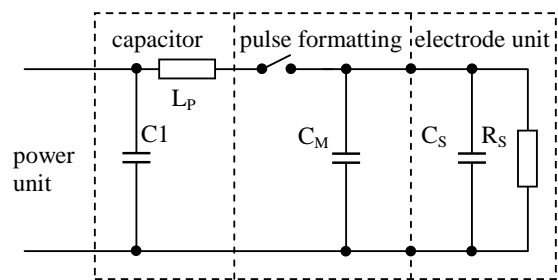


Figure 2. Equivalent scheme of electroporator output



Figure 3. View of the electroporator

The common view of electroporator is shown in Fig. 3. The main parameters of EP device are shown in Table 1.

3. EXPERIMENTAL RESULTS

The oscillograms of an output signal are represented in Fig. 4. It is obvious that HV and LV signals can be supplied to the load simultaneously. The number of positive HV pulses in a sequence may vary from 1 to 9 and their amplitude is in a range between 100 and 1100 V., while duration varies between 1 and 1000 μ s. LV voltage may be changed in its polarity up to max. 100 V. It means that LV pulses are at about 10% of HV amplitude value. The detail electrical parameters of the EP device are shown in Table 1.

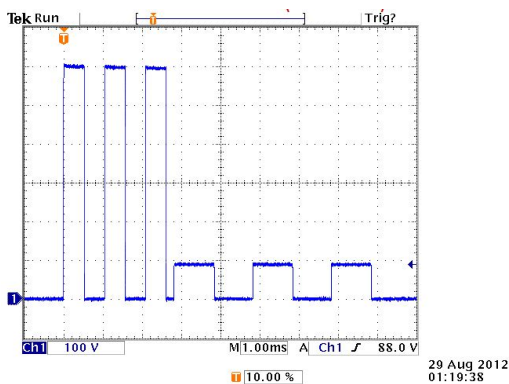


Table 1. Electrical parameters of electroporator"

No.	Parameter	Value
1	HV pulse amplitude	(100 – 1100) V
2	HV pulse duration	(1 – 1000) μ s
3	HV pulse number	(1 – 9)
4	HV pulse polarity	positive
4	LV pulse amplitude	(4 – 100) V
5	LV pulse duration	(1 – 1000) ms
6	LV pulse number	(1 – 9)
7	LV pulse polarity	positive or negative
7	Delay between HV ir LV sequence	(5 μ s – 1 s)
8	Protectors activation rate	< 30 μ s
9	Emergency HV voltage shutdown speed	< 5 ms

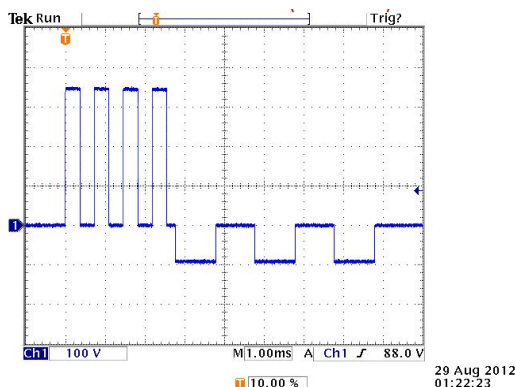


Figure 4. Experimental time diagram

The control of electrical parameters is performed on virtual PC display (Fig. 5).



Figure 5. Virtual panel

It is possible here to set all needed output signal combinations. Management of the multiprocessor system is used with typical peer communication channels SPI and USART interfaces. All system components are galvanically separated, because initial tests showed an absolute necessity of these methods. Bandwidth is achieved using a 10 Mbps optical separation. On the final stages are used IGBTs field transistors with maximal breakdown voltage 1700 V.

Due to a low reliability were abandoned standard driver's stages and used schemes with discrete transistors.

5. CONCLUSION

The structural scheme of the electroporator used the methods and developed electroporator parameters, experimental results of output signals are presented. Laboratory model of electroporator has a wider possibilities and used for medical applications

References

- [1] A. J. H. Sale and W. A. Hamilton, "Effects of high electric fields on microorganisms: I: Killing of bacteria and yeasts", *Biochim. Biophys. Acta*, Volume 148, 1967 pp. 781–788.
- [2] Sukhendu B. Dev, Dietmar P. Rabussay, Georg Widera, and Gunter A. Hofmann, "Medical Applications of Electroporation", *IEEE Transactions on Plasma Science*, Volume 28, No. 1, February, 2000, pp.207-223.
- [3] T. Kotnik, P. Kramar, G. Pucihar, D. Miklavčič, M. Tarek, "Cell Membrane Electroporation—Part 1: The Phenomenon", *IEEE Electrical Insulation Magazine*, Volume 28, No. 5, pp.14-23.
- [4] M.Sack, C. Eing, L. Buth, Th. Berghöfer, W. Frey, and H. Bluhm, "Electroporation as an optimizing step in drying of green biomass", *Pulsed Power Conference, 16th IEEE International*, Volume 1, 2007, pp.756-759.
- [5] M. Sack, G. Müller: "Optimisation of an Electroporation Device for Mash". *Proc. OPTIM2008*, Brasov, Romania, May 2008, pp. 113-118.
- [6] "Cliniporator EPSo2. Technical sheet", *IGEA S.p.A. Via Parmenide 10/A, Carpi, Modena, Italy*, pp.1-4.
- [7] Congo Tak-Shing Chinga, Tai-Ping Suna, Wei-Ti and etc. Huang "A circuit design of a low-cost, portable and programmable electroporation device for biomedical applications". *Sensors and actuators B: Chemical*, 2012, pp. 292-300.
- [8] S. Rodamporn. "Optimal Parameters of Electroporation for Gene and Tissue", *Biomedical Engineering International Conference (BMEICON-2011)*, pp. 279-282.

ARBITRARY WIDTH AND POSITION PULSE TRAINS APPLICATION FOR ULTRASONIC IMAGING: INITIAL STUDY

L. Svilainis, A. Aleksandrovas, K. Lukoseviciute

Signal processing department, Kaunas University of Technology,
Studentu str. 50, LT-51368 Kaunas, Lithuania
T. +370 37 300532; F. +370 37 753998; E. linas.svilainis@ktu.lt

Abstract

Novel spectrum spread technique is presented: the arbitrary width and position pulse trains. We suggest to use specially formed square pulse sequences (APWP), applying specific limitations on duration and positions in time and use the discrete time: this would increase temporal stability and save system resources. Efficiency of excitation electronics would increase, maintaining small size, cost of the spread-spectrum equipment can be reduced. Such signals would allow increasing imaging resolution and quality, increasing the sensitivity of the measurements.

Initial investigation results of the influence on signal spectral and correlation properties are presented. Results are applicable in ultrasonic imaging systems and high accuracy measurements employing the time of flight information.

1. INTRODUCTION

Requirements for non-destructive testing and biomedical imaging systems resolution and sensitivity are increasing, and greater flexibility of the equipment is demanded [1]. In case of straight bandwidth increase, shorter excitation pulses are required. But short pulses do not possess the high energy, required for sensitivity [2-4]. Complex, spread spectrum, excitation signals are used which inherit both long duration (high energy) and wide bandwidth. Most popular, arbitrary waveform signals are complicated to excite, hard to deliver the high power, such equipment is inefficient, not portable and expensive. Chirp signals have relatively simple spectrum which can be easily controlled if nonlinear modulation is used. Binary single pulse or CW pulse trains were used for decades in ultrasonic imaging. Scientific papers report binary chirps use for excitation. Phase manipulated sequences are close to this class, but do not allow to have a full control of the shape the correlation function and spectrum. The novel spectrum spread technique did not receive the proper attention in ultrasound: the arbitrary position and width pulse trains (APWP) [5,6]. Technique is using a chaotically placed train of square pulses with arbitrary position and duration. We suggest new technique – use specially formed square pulse APWP sequences, applying specific duration and position in time limitations and use the discrete time: this would increase temporal stability and save system resources. APWP signals would allow for increased imaging resolution and

precision, sensitivity. Excitation electronics efficiency can be increased, size and cost reduced.

Initial study of such signals spectral and correlation properties is presented. Results are documented as figures and numerical values.

2. APWP SIGNALS

Resolution of any imaging system operation on pulsed signal reflection principle is defined by the envelope bandwidth of the signals used for probing. Improving the resolution can be accomplished by using short rectangular pulses. But such signals will have low energy; therefore the accuracy of imaging will be reduced. SS signals offer high energy, wide bandwidth and possess spectral spread in time (Figure 1).

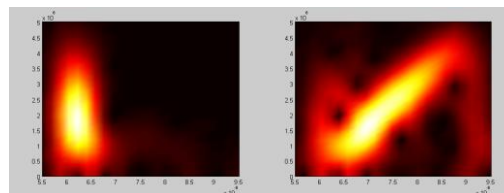


Figure 1. Pulse (left) vs. chirp (right) spectrograms

Several techniques can be applied for SS: phase manipulated sequences, chirp or arbitrary waveform excitation [2-4]. Narrow, matched properties single pulse and chirp were used in our study as reference signals. APWP sequences (Figure 2) [7] should also possess the spectral spread properties.

Aim of our investigation was to perform the initial study on how these signals can be optimized and

what correlation and spectral properties can be obtained compared to the aforementioned signals.

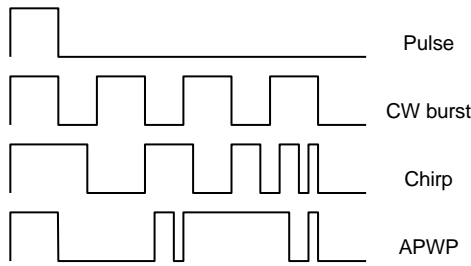


Figure 2. Pulse, CW burst, chirp and APWP signals comparison

3. ANALYZED PARAMETERS

Both chirp, pulse and APWP signals content can be optimised (Figure 3) based on one of the convergence parameters:

- i) maximum value of all the side lobes beyond the first zero crossing ($\max(\text{SL})$: Figure 3);
- ii) energy of sidelobes ($E(\text{SL})$);
- iii) main lobe duration minimum.

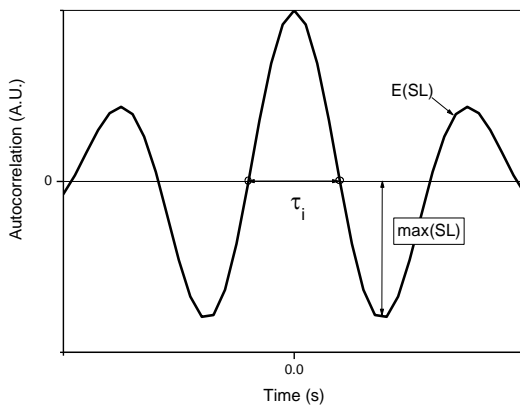


Figure 3. Explanation of pulse width, peak sidelobe and sidelobes variation

4. ULTRASOUND TRANSMISSION MEASUREMENT

The ultrasound propagation frequency response was determined by probing the system input with a chirp signal (0.5 MHz to 15 MHz) while measuring the input and the output signals u_{in} and u_{out} and the channel frequency response was obtained by taking the ratio of Fourier transforms of the two:

$$G(f) = \frac{u_{out}(f)}{u_{in}(f)}, \quad (1)$$

Results obtained were used for ultrasonic signals propagation modeling in iterative optimization.

5. NUMERICAL MODELING AND OPTIMIZATION RESULTS

Ultrasound transmission was used to calculate the transmitted signal as if it was used in real-world experiment. If for pulse all duration were used in optimum search, one combination (f_{min} to f_{max}) was used for chirp and Monte Carlo was used for APWP. Total 10000 Monte Carlo iterations were used. Results obtained for narrowest mainlobe duration are presented in Figure 4 (RF cross-correlation) and Figure 5 (cross-correlation envelope taken using magnitude of the Hilbert transform of the original cross-correlation function).

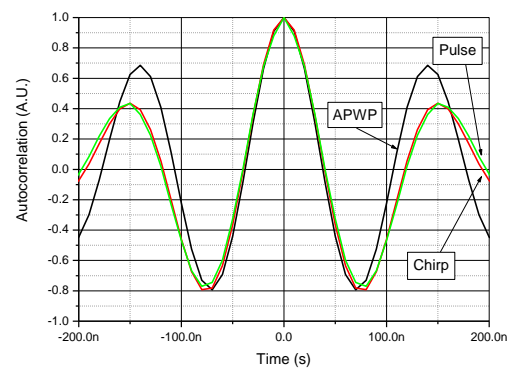


Figure 4. Mainlobe duration minimization result for three signals, cross-correlation function

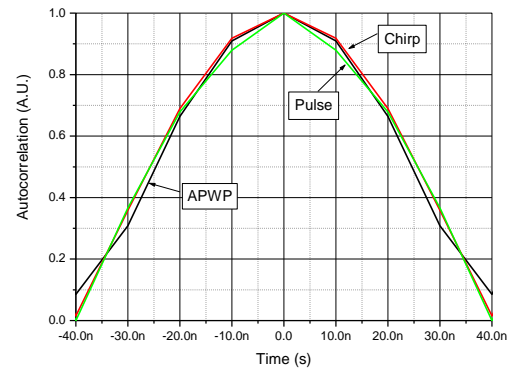


Figure 5. Mainlobe duration minimization, cross-correlation function Hilbert-envelope

It would be expected that pulse would possess lowest sidelobes. It can be seen that optimized APWP has similar to pulse performance and in case of correlation envelope has slightly better performance over the other signals.

Same optimization was performed on lowest variation on spectral response (refer Figure 6 and Figure 7 for correlation functions for such case).

APWP has the worst performance. Reason could be that performance of the spectrum was optimized not in transmission window but in whole 0 to Nyquist region.

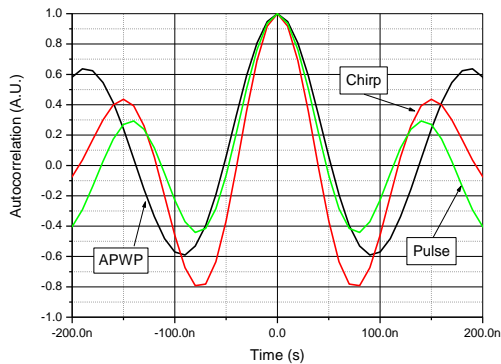


Figure 6. Spectral optimization cross-correlation function

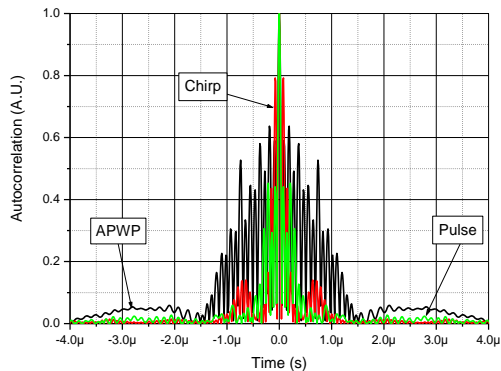


Figure 7. Spectral optimization result for three signals, Hilbert-envelope of the cross-correlation function

Results for sidelobes maximum reduction are presented in Figure 8 and Figure 9.

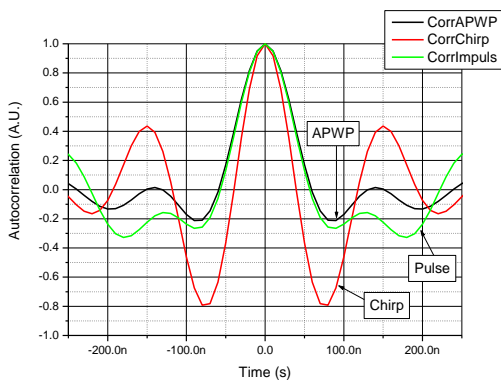


Figure 8. Sidelobes' maximum reduction result: correlation function

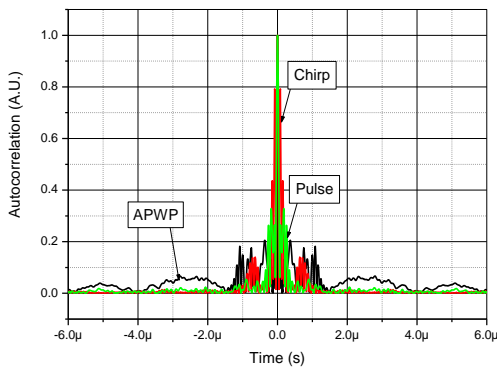


Figure 9. Sidelobes' maximum reduction result: correlation magnitude

Results for sidelobes' energy reduction are presented in Figure 10 and Figure 11.

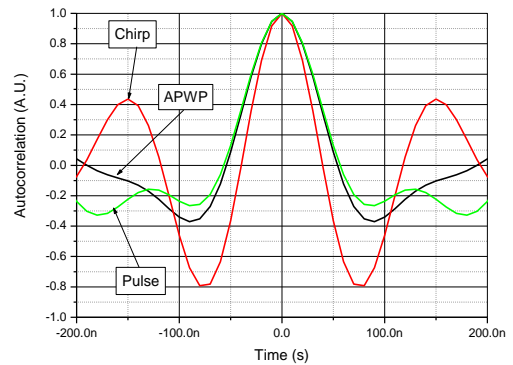


Figure 10. Sidelobes' energy reduction result: correlation function

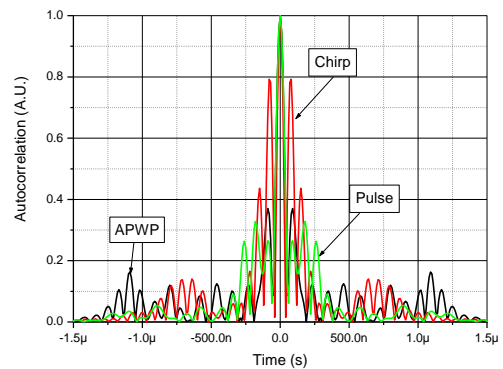


Figure 11. Sidelobes' energy reduction result: correlation magnitude

It can be noted that APWP performance in this initial investigation allows to expect better or similar performance to classical chirp and pulse signals: in some cases APWP performance was the best among the classical signals.

6. CONCLUSIONS

Initial investigation indicates that APWP signals can have properties similar to those of chirp and pulse signals. After optimization, some gain in correlation mainlobe width or sidelobes level compared to pulse or chirp signals can be obtained.

Acknowledgment

This research was funded by a grant (No. MIP-058/2012) from the Research Council of Lithuania.

References

- [1] U.Schnars, R.Henrich, "Applications of NDT Methods on Composite Structures in Aerospace Industry", in. Proc. Conference on Damage in Composite Materials, 2006, pp. 1-8.
- [2] M. Pollakowski and H.Ermert, "Chirp signal matching and signal power optimization in pulse-echo mode ultrasonic nondestructive testing", IEEE Trans. Ultrason., Ferroelectr., Freq. Control, 1994, vol. 41, no.5, pp. 655-659.
- [3] D. Cowell, S. Freear, "Quinary excitation method for pulse compression ultrasound measurements", Ultrasonics, 2008, vol.48, pp. 98-108.
- [4] A.Nowicki, I.Trots, P.A.Lewin, et.al. "Influence of the ultrasound transducer bandwidth on selection of the complementary Golay bit code length", Ultrasonics, 2007, vol.47, pp. 64-73.
- [5] L. Fortuna, M. Frasca, and A. Rizzo, "Chaotic pulse position modulation to improve the efficiency of sonar sensors", IEEE Trans. Instrum. and Meas, 2003, vol.52, pp. 1809-1814.
- [6] Z.-J. Yao, Q.-H. Meng, et al., "Non-crosstalk real-time ultrasonic range system with optimized chaotic pulse position-width modulation excitation," Proc. IEEE Ultrasonics Symp., 2008, pp. 729-732.
- [7] L. Svilainis, V. Dumbrava, A. Chaziachmetovas and A. Aleksandrovas, "Pulser for Arbitrary Width and Position Square Pulse Trains Generation", Proc. IEEE Ultrasonics Symp., 2012, in press.

THE WIDEBAND ULTRASONIC PULSER FOR SONOPORATION

L. Svilainis¹, A. Chaziachmetovas¹, R. Jurkonis², D. Kybartas¹, N. Lamanaukas³ and S. Satkauskas³

¹Signal processing department, Kaunas University of Technology,
Studentu str. 50, LT-51368 Kaunas, Lithuania

² Biomedical Engineering Institute, Kaunas University of Technology,
Studentu str. 65, LT-51369 Kaunas, Lithuania

³ Department of Biology, Faculty of Natural Sciences, Vytautas Magnus University.,
Vileikos str. 8. LT-44404, Kaunas, Lithuania

T. +370 37 300532; F. +370 37 753998; E. linas.svilainis@ktu.lt / rytis.jurkonis@ktu.lt / darius.kybartas@ktu.lt / andrius.chaziachmetovas@ktu.lt / nlanaukas@gmail.com / s.satkauskas@gmf.vdu.lt

Abstract

The transient nature of membrane permeability requires extensive study to develop the most efficient sonoporation parameters: the ultrasound energy, frequency content or signal shape. Other investigators use the arbitrary function generator and linear RF power amplifier. We consider such setup expensive and oversized. More compact design can be achieved if binary or unipolar pulser is used in excitation. Dedicated hardware was developed and the performance investigated. We achieve up to 500 Vpp voltages, frequencies beyond 3 MHz, ability to have both unipolar and bipolar pulses, burst lengths up to 40 periods and pulse repetition frequency up to 3 kHz on transducers with capacitance of 3000 pF.

1. INTRODUCTION

Sonoporation has some advantages over electroporation in modifying the permeability of the cell membrane for drugs or foreign genes delivery: non-bactericidity, safety, ability for specific volume are named [1]. It is assumed that the acoustic field causes the inertial cavitation which in turn develops some microstreaming facilitating the membrane permeability. Alternative hypothesis propose that microbubble's rupture can be the cause of the sonoporation. Assuming that excitation parameters can be fine tuned to inhibit the most bioeffective [2,3] oscillations, there is a need for extensive study to develop the most efficient sonoporation parameters: the ultrasound energy, frequency content or signal shape. Such experiments where the arbitrary function generator and linear RF power amplifier are used we consider expensive and oversized. More compact design can be achieved if binary/unipolar pulser is used for excitation. Design of the dedicated electronics hardware and performance investigation is presented below. Such system could be applied for ultrasound contrast agent microbubble properties investigation.

2. PULSER REQUIREMENTS

Results of Apfel and Holland presented in [4] indicate that at 1 MHz frequency the inertial cavitation

threshold is 0.25 MPa of peak negative pressure; 0.6 MPa at 5 MHz and 0.85 MPa at 10 MHz. Assuming high ultrasonic transducer impedance and low coupling, we aimed at to achieve the variable, up to 300 V output voltages, frequencies beyond 3 MHz, ability to have both unipolar and bipolar pulses, burst lengths up to 40 periods and pulse repetition frequency up to 3 kHz for relatively high capacitance (up to 3000 pF) transducers. Experimental system (Figure 1) used hydrophone HNP-1000 from Onda and digital storage oscilloscope Yokogawa DLM2054 for sound pressure waveforms registration.

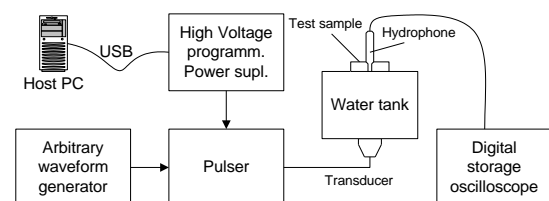


Figure 1. Hardware setup

The excitation signal generation was planned to be performed by arbitrary waveform generator generating low voltage CW bursts. These signals were fed into pulser input and positive and negative waves selected to drive different output channels. Our own design high voltage source was used for excitation voltage supply.

3. TOPOLOGY SELECTION

Main part of the piezoelectric transducer impedance is capacitive. This capacitance has to be charged and discharged every excitation cycle. Then, half bridge topology with two active elements (Figure 2, left) should offer an advantage in achieving both high efficiency and high frequencies.

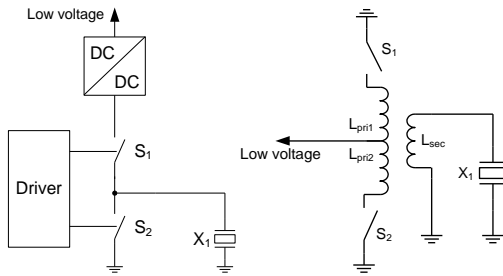


Figure 2. Half bridge (left) and transformer push-pull (right) topologies

Such topology was presented in [5], where also the analysis and theory for components selection is given. But driving the high side switch presents a challenge: high dV/dt will be present on floating driver. Therefore, such topology is limited to 3-4 MHz operating frequencies. Though, it has an advantage in achieving high excitation voltages [6]. Another, transformer coupled push-pull topology (Figure 2, right), is using only low side drivers and transformer coupling [7].

On the other hand such design requires (Figure 3) careful transformer construction and material selection.



Figure 3. Pulser photo

But the result is the simple and compact design.

3.1. High voltage source

The high voltage power source was designed using a DC/DC converter CA05P from EMCO. Main control tasks including consumed current, supply voltage monitoring, USB connectivity, and control knob encoding servicing, indication is accomplished

(Figure 4) by MSP430 microcontroller. Whole high voltage source is encapsulated into separate box and power supplied from 24V wall-plug SMPS.

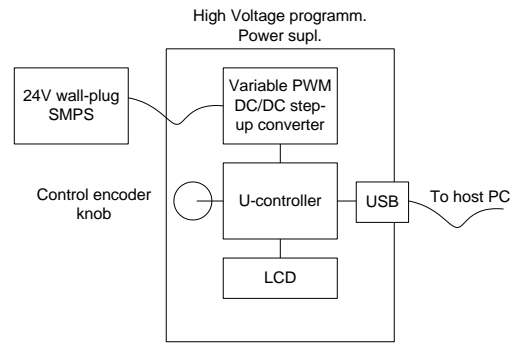


Figure 4. Programmable high voltage power source structure

Voltage control is either manual, using control knob (Figure 5) or via USB interface.



Figure 5. High voltage source photo

Such design allow for reuse of the high voltage source.

4. EXPERIMENTAL PULSER PERFORMANCE EVALUATION

Comparison to commercially available standalone sonoporation generator from Medelcom was performed. Same load and operation conditions were used: 3 MHz at 50 Ω and 3nF load at 500 Vpp programmed voltage. Results for 50 Ω output are presented in Figure 6.

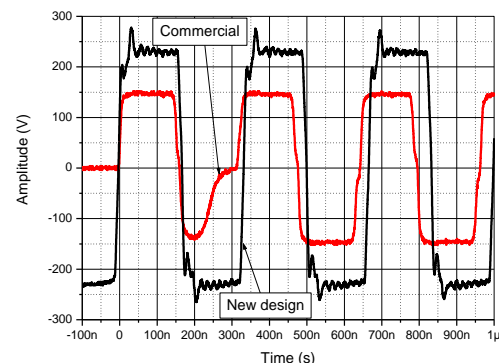


Figure 6. Generators output comparison at 50 Ω load

It can be seen that commercial device does not adhere to the frequency stability requirement. Furthermore, output voltage is lower than specified in control software.

Refer Figure 7 for generators output for 3000 pF load case.

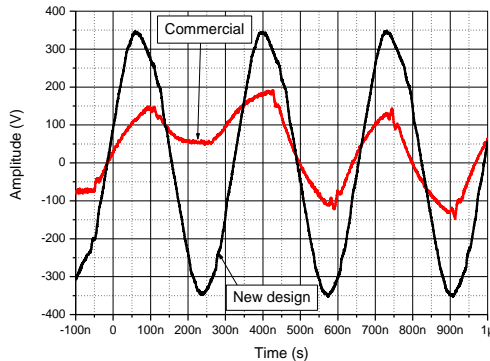


Figure 7. Generators output comparison at 3000 pF load

Results indicate that commercial device is not capable to deliver the signal to capacitive load. New design pulser is capable of programmed output delivery.

5. CONCLUSIONS

Push-pull topology with symmetric transformer output was used. Such approach allows for N-channel MOSFETs application for both positive and negative wave, avoiding complicated high side driver structure. New solution allows for high voltage yet high speed pulse trains generation into capacitive load. Voltages up to 500 Vpp and frequencies beyond 3 MHz can be achieved. Pulser is capable of both unipolar and bipolar pulses, burst lengths beyond 40 periods and pulse repetition frequency up to 3 kHz on transducers with capacitance up to 3000 pF.

Acknowledgment

This research was funded by a grant (No. MIP-058/2012) from the Research Council of Lithuania and by the grant VPI-3.1-SMM-01-V-01-001 No. 88 (postdoc program for N. Lamanaukas).

References

- [1] C. M. H. Newman and T. Bettinger, "Gene therapy progress and prospects: ultrasound for gene transfer", *Gene Therapy*, 2007, vol. 14, pp.465–475.
- [2] M.Kinoshita, K.Hynynen, "Key factors that affect sonoporation efficiency in In Vitro settings", *IEEE Ultrasonics Symposium*, 2006, pp.852–855.
- [3] S. Samuel, J. Fowlkes, D. Miller, "An in vitro study of the correlation between bubble distribution, acoustic emission, and cell damage by contrast ultrasound", *IEEE Trans. Ultrason. Ferroelectr. Freq. Control*, 2009, vol. 56, pp.589–593.
- [4] R. E. Apfel, and C. K. Holland, "Gauging the likelihood of cavitation from short-pulse, low duty cycle diagnostic ultrasound", *Ultrasound in Med. and Biol.*, 1991, vol.17, pp.179-185.
- [5] L. Svilainis, A. Chaziachmetovas, V. Dumbrava, "Efficient high voltage pulser for piezoelectric air coupled transducer", *Ultrasonics*, In Press, DOI:10.1016/j.ultras.2012.06.004.
- [6] L. Svilainis, A. Chaziachmetovas, D. Kybartas, R. Jurkonis, "Advanced hardware for fine-tuning and optimization of sonoporation efficiency in vitro", *IEEE Conf. Intelligent Data Acquisition and Advanced Computing Systems*, 2011, vol.6, pp. 65 – 70.
- [7] B.Haider, "Power Drive Circuits for Diagnostic Medical Ultrasound", *IEEE Proc. Symposium on Power Semiconductor Devices & IC's*, 2006, pp. 1–8.

ON IMPLEMENTATION OF A NEURAL NETWORK CLASSIFIER FOR SOME CLASSES OF BIOLOGICAL AND MEDICAL PREPARATION IMAGES

I. P. Soloviev

Comp. Sci. Dept, Math. & Mech. Faculty, St. Petersburg State University
Universitetsky pr. 28, Starii Peterhof, St.Petersburg 198504
soloviev@math.spbu.ru

N. B. Ampilova

Comp. Sci. Dept, Math. & Mech. Faculty, St. Petersburg State University
Universitetsky pr. 28, Starii Peterhof, St. Petersburg 198504
ampilova@math.spbu.ru

E. Y. Gurevich,

Sofia & Jacobs Foundation, Itlyanskaya str. 10/5, St.Petersburg 191186, info@organicproduct.ru

Abstract

The paper is devoted to the investigation of the applicability of textural and morphological analysis to the images of some biomedical preparations.

The obtained feature vectors are input of an artificial network classifier. All the groups of images can be successfully classified by any of 3 methods considered, being for blood crystals images the morphological method is the best one.

1. INTRODUCTION

In this work we investigate the applicability of textural and morphological image analysis methods to the images of blood crystals and plant extract crystals obtained by the Pfaifer sensitive crystallization method [6,7], and brain tumor images [1].

Medical experimental research showed that structural features of blood crystals characterize both clinical signs of diseases and the presence of tendencies to get a disease. This reason stimulates designing reliable algorithms to classify such preparations images.

In the proposed implementation an artificial neural network is used as a classifier. The input of the network consists of different variants of classifying signs of analyzed images: statistical textural signs obtained with the help of the gray-tone spatial dependence matrix or Grey Level Co-occurrence Matrix (GLCM) [3], Gabor filter [2] and morphological signs (skeleton representation) [5]. For adjustment of modeled neural network parameters RProp (Resilient Propagation) algorithm that speeds up Back Prop algorithm is used [4].

Experimental data obtained for images of different classes show that the constructed model makes good progress for all the groups of features. How-

ever, the best classification results for blood crystals images are achieved when morphological signs are used.

2. IMAGES DESCRIPTION

We analyzed 3 groups of images: (1,2) were obtained by the Pfaifer sensitive crystallization method (addition a small quantity of blood or plant extract to cuprous chloride solution) and (3) is brain tumors images. All the images are supposed to be monochrome.

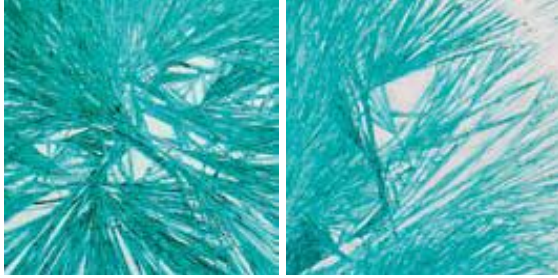
2.1. Blood images

It was revealed that in a health organism needles in crystals are radiating from the centre to periphery. In the case of a disease there is an interruption in the crystal growth, the change of its form, etc.

Moreover, it has been stated empirically that there is a relation between the position of the parts having changed form and structure and the malfunctioning an organ or the organs system.

This method helps to detect a disease on infancy, which is very important for early diagnosis. It may be useful to estimate the efficiency of taken therapeutic actions.

The next figure illustrates the following typical forms of crystals: hole structure of crystals – typical of degenerative processes (left); hollow form of the crystal with transversal structures, malignant tumor (right).



2.2. Plant extract images

We analyze the following images: orange juice, wheat flour solution and wheat extract crystals.

2.3. Brain tumor images

Images are classified according to the tumor kind. We consider the tumors of 3 types: astrocytoma, nevirinoma, oligodendroglioma.

The images were given in [1], where the textural analysis was performed basing expert knowledge and here we used them for comparative analysis.

3. METHODS OF IMAGES FEATURES GENERATION

3.1. Gray tone spatial dependence method

GLCM is a matrix containing co-occurrence pairs of pixels of a given intensity that are in a definite spacing defined by the angle and the distance that are the matrix parameters.

We use the following texture features based on the normalized GLCM $P_{i,j}^{Norm}$ (i and j are intensities of neighboring pixels) [3].

Contrast specifies a measure of intensities contrast between a pixel and its neighbor:

$$Contrast = \sum_{i,j=0}^{N-1} P_{i,j}^{Norm} (i-j)^2$$

If all pixels have the same intensity $Contrast = 0$.

Homogeneity characterizes the density of distribution of GLCM elements relative to its diagonal:

$$Homogeneity = \sum_{i,j=0}^{N-1} \frac{P_{i,j}^{Norm}}{1+(i-j)^2}$$

Correlation is a correlation measure between a pixel and its neighbor:

$$Correlation = \sum_{i,j=0}^{N-1} P_{i,j}^{Norm} \left[\frac{(i-\mu I)(j-\mu J)}{\sqrt{(\sigma I^2)(\sigma J^2)}} \right]$$

where μI , μJ , σI and σJ are respectively mathematical expectation and dispersion of pixel intensities that are calculated using a current pixel and its neighbors.

3.2. Gabor filters

We introduce the 2-D Gabor function [2]:

$$g(X, Y) = \frac{1}{2\pi\sigma_x\sigma_y} e^{-\frac{1}{2}\left(\frac{X^2}{\sigma_x^2} + \frac{Y^2}{\sigma_y^2}\right) + 2\pi i\omega x}$$

Gabor wavelets are obtained by using the generating functions:

$$g_{mn}(X, Y) = a^{-m} \cdot g(X', Y'),$$

$$X' = a^{-m}(X \cos \theta + Y \sin \theta)$$

$$Y' = a^{-m}(X \sin \theta + Y \cos \theta)$$

$$\theta = n\pi/N, a > 1,$$

where integers m, n characterize the wavelet scale and orientation: $m = 0, 1, \dots, M, n = 0, 1, \dots, N$ and M, N are the numbers of scales and orientations respectively.

Let $I(x, y)$ be a gray level distribution for an image. Then the image convolution with the Gabor kernel g_{mn} is defined as:

$$W_{mn}(x, y) = \int I(x, y) g_{mn}^*(x-x_1, y-y_1) dx_1 dy_1$$

where* denotes complex conjugation. We assume that areas with local texture are spatially homogeneous, then the mean value of the amplitude of reduction coefficient μ_{mn} and the mean-square deviation of the amplitude σ_{mn} may be used as a characteristics of the image:

$$\mu_{mn} = \iint |W_{mn}(x, y)| dx dy,$$

$$\sigma_{mn} = \sqrt{\iint (|W_{mn}(x,y)| - \mu_{mn})^2 dx dy}$$

The feature vector has the form:

$$\vec{f} = [\mu_{00} \quad \sigma_{00} \quad \mu_{01} \quad \sigma_{01} \dots \mu_{mn} \quad \sigma_{mn}]$$

3.3. Morphological Method

Mathematical morphology is a method to obtain structural components of an image that are useful for its representation and description: boundaries, skeletons and convex hulls. In this work we use so called image skeleton, which allows us to decrease the task dimension [5]. To extract the image skeleton the tools of mathematical packages are applied [8].

4. NEURAL NETWORK CLASSIFIER

In this work we use multilayered feedforward network, because it is known that such a model is sufficient for the problems of this class [4].

The number of neurons in the input layer N_{in} is defined by the feature vector size that by-turn is defined by the method of construction of the vector.

The number of neurons in the second layer N_{av} is defined as the integer part of $N_{in}/2$ (empirical recommendation).

In our experiments the number of output neurons in the third layer N_{out} is defined by the number of classes of images that are considered in each groups of test models: for medical preparations $N_{out} = 5$, for biological ones $N_{out} = 3$ and for brain tumors $N_{out} = 3$.

For the network training RProp (Resilient Propagation) algorithm [4] was applied. Its principal advantage over Backprop method is the simplicity, high rate of convergence and low specifications for the gradient calculating error. As opposed to Backprop based on gradient descent method, RProp uses only signs of partial derivatives but not their values to adjust weighting coefficients.

5. RESULTS OF EXPERIMENTS

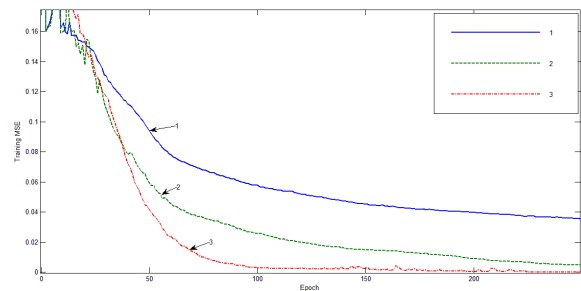
The algorithm testing was performed on the computer with Intel Core i5™ 2.27GHz processor.

Further 1 denotes medical preparation images, 2 – biological preparation images, 3 – brain tumor images.

5.1. GLCM based method

Let the number of directions to a neighbor pixel be 3 ($0^\circ, 45^\circ, 90^\circ$), the number of distances to a neighbor pixel be 10 (i.e. distances = 1,2, ..., 10), the number of textural features – 3 (Contrast, Homogeneity, Correlation), then the number of input neurons $N_{in} = 3 \cdot 10 \cdot 3 = 90$ [har]. Hence $N_{av} = 45$. The size of GLCM (64x64) was defined by the given number of gray levels $N=64$.

For 3 groups of images the graphics of the dependences network parameter training mean-square error (MSE) σ on the number of iteration N are shown below.



The time of the construction of feature vectors and the network training is shown in the table below.

Image group number	Feature vector generation time (sec)	Network training time (sec)	Summary time (sec)
1	10.619	9.437	20.056
2	10.239	4.701	14.940
3	35.607	4.901	40.508

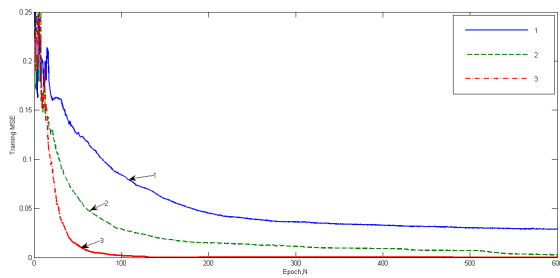
It takes 2-4 sec for the trained network to classify different images by this method.

5.2. Gabor filter

Let the number of wavelet scales be 8, the number of wavelet orientation — 5 and the number of used textural features (mathematical expectation and mean-square deviation) – 2. Then

$$N_{in} = 8 \cdot 5 \cdot 2 = 80, N_{av} = 45.$$

The graphics of the dependences network parameter training MSE σ on the number of iteration N are:



The time of the construction of feature vectors and the network training is shown in the table below.

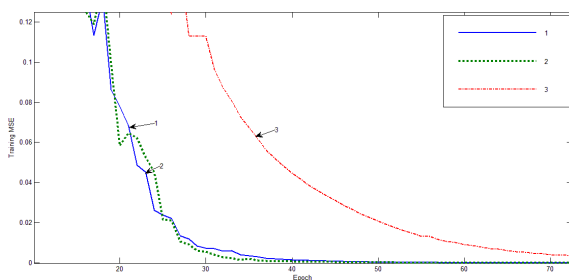
Image group number	FV gene-ration time (min:sec)	Network training time (min:sec)	Summary time (min:sec)
1	14:17.964	2:31.928	16:49.892
2	14:34.104	0:6.554	14:40.658
3	26:45.027	0:4.099	26:49.126

It takes 3-4 min for the trained network to classify different images by this method.

5.3. Morphological method

Here N_{in} depends on the image size and equals 1/100 image height multiplied by image width (pixels). If $N_{in} > 4096$ the image is partitioned into small areas.

The graphics of the dependences network parameter training MSE σ on the number of iteration N are:



The time of the construction of feature vectors and the network training is shown in the table below.

Image group number	FV gene-ration time (min:sec)	Network training time (min:sec)	Summary time (min:sec)
1	0:5.397	0:30.735	0:36.132
2	0:8.519	17: 12.592	17:21.111
3	1:02.447	39-59 min	40-60 min

Classification time is 3-4 min.

6. CONCLUSION

To summarize, in accordance with accuracy criteria all the groups of images can be successfully classified by any of 3 methods. As for time criteria, the best results for the first group of images were obtained by the morphological method and by GLCM method for group 2 and 3.

Acknowledgements

Authors wish to express their thanks to the Sofia & Jacobs Foundation for support.

References

- [1] Ampilova N., Gurevich E., Soloviev I. Texture recognition as a quantitative analysis of underdoses in pharmacology and medicine. — Proc.5 Int. Conf. CEMA10, 7-10 Oct. 2010, Athens, pp.78-81.
- [2] Boogaart C. G. v. d., Lienhart R. Fast Gabor Transformation for processing high quality audio. — Technical Report, Institute of Computer Science, University of Augsburg, October 2005.
- [3] Haralick R.M. Statistical and Structural Approaches to Texture. — Proc. of the IEEE, 67, 1979, pp. 786-804.
- [4] Riedmiller M., Braun H. A direct adaptive method for faster backpropagation learning: The RPROP algorithm. San Francisco, 1993.
- [5] J. Serra. Image analysis and Mathematical morphology. London, 1982.
- [6] Beatrix Walburger. Ehrenfried Pfeiffer's Sensitive Crystallisation Method Applied to Blood. Goetheanum Research Institute. The Laboratory for Sensitive Crystallisation. Dornach, 2007.
- [7] Beatrix Walburger. Die Empfindliche Kristallisation. Eine Methode zur Qualitatatsforschung. Goetheanum Research Institute. The Laboratory for Sensitive Crystallisation. Dornach, 2007.
- [8] <http://www.mathworks.com/products/matlab/>

MULTIFRACTAL SPECTRUM AS A CLASSIFICATION SIGN FOR BIOMEDICAL PREPARATIONS IMAGES

N. B. Ampilova

Comp. Sci. Dept, Math. & Mech. Faculty, St. Petersburg State University
Universitetsky pr. 28, Starii Peterhof, St. Petersburg 198504
ampilova@math.spbu.ru

I. P. Soloviev

Comp. Sci. Dept, Math. & Mech. Faculty, St. Petersburg State University
Universitetsky pr. 28, Starii Peterhof, St. Petersburg 198504
soloviev@math.spbu.ru

Y. V. Shupletzov

Math. & Mech. Faculty, St. Petersburg State University
Universitetsky pr. 28, Starii Peterhof, St. Petersburg 198504
shupaag@mail.ru

Abstract

The paper is devoted to the application of methods of multifractal image analysis to classify biomedical preparations images.

We use two methods for calculation of multifractal spectrum: the direct determination and the moment-based method, being the last one does not use Regny dimensions with the following application of the Legendre transform. Such an approach results in increasing the precision of calculation.

For 4 classes of biomedical preparation images (histological preparations, blood cells, connective tissue and bone tissue) two classes (histological preparation and bone tissue) for which multifractal spectrum is a reliable classification sign have been marked out. At the same time the analysis of images of blood cells with leukemia and connective tissue shows that it is necessary to apply additional methods to obtain proved results.

1. INTRODUCTION

It is now widely accepted that physical systems that exhibit chaotic behavior are generic in Nature. Since it is possible to follow and predict their motion in any detail only for short time scales, one must use suitable statistical descriptions to describe the system asymptotic.

Considering an image as the phase portrait of a complex dynamical system we can use for its description multifractal formalism as a statistical characteristics. The multifractal formalism relies on the fact that highly nonuniform probability distributions arising from the nonuniformity of the system often possess rich scaling properties such as self-similarity. Hence we can associate a characterization of the fractal properties of a measure with the nonuniform distribution.

Spatial distribution of dissipative regions in a turbulent flow, the invariant probability distribution on a strange attractor and the distribution of growth probabilities on the external surface of a diffusion-limited aggregate are some examples.

The multifractal formalism describes the statistical properties of these singular measures in terms of their singularity (multifractal) spectrum or their generalized dimensions.

Cover the support of the measure with disjoint boxes of size l and define for each box a measure as l^{α_i} , where α_i are real numbers. Then the subsets of points (E_{α}) for which values α_i are equal or close are defined. For each subset its fractal dimension $f(\alpha_i)$ is calculated. So, the image is considered as a union of interwoven subsets, being each of them has own fractal dimension. The set of these dimensions forms multifractal spectrum (MFS).

The method of MFS direct determination is described in [6]. It should be noted that the finding of

E_{α} sets means a categorization of an image points. In fact, it is the box measure that describes a categorization. Different methods lead to different multifractal spectra. For digital images the measure is defined through pixel intensities [4].

Generalized (Regny) dimensions D_q provide an alternative description of the singular measure. They correspond to scaling exponents for the q th moment of the measure. The generalized dimensions were introduced earlier than multifractal spectrum and they are easier to compute than the latter.

Since these two characteristics describe the same measure, there is a connection between them. Namely, when $f(\alpha)$ and D_q are smooth functions of α and q , they are related by a Legendre transformation. It was believed that for measures arising from real experiments it is easier to calculate generalized dimensions and then obtain multifractal spectrum using the Legendre transform.

But, as was shown in [1], the D_q corresponding to large negative q may have large error bars and Legendre transforming the D_q curve may decrease precision considerably. The authors elaborated a new direct method of determining multifractal spectrum based on a canonical method of computing thermodynamic averages. Both $f(\alpha)$ and α are obtained as functions of the parameter q .

It should be noted that multifractal spectrum is widely used in image analysis because it is globally invariant under bi-Lipschitz transform (general transform including brightness changing, rotation, scaling and general texture surface deformations) [3].

In this work we use both the MFS direct determination method and the moment-based method without using Regny dimensions. They may be successfully applied for a classification of 4 classes of biomedical preparation images.

2. METHODS OF ANALYSIS

2.1. MFS direct determination

2.1.1. Method description

Let μ be a measure defined through pixel intensities. For $x \in R^2$ we denote $B(x, r)$ a square of length r with center x . We describe

$\mu(B(x, r)) = kr^{d(x)}$ with $d(x)$ the density function and k some constant. The local density function of x is defined as

$$d(x) = \lim_{r \rightarrow 0} \frac{\log \mu(B(x, r))}{\log r}. \quad (1)$$

The set of all image points x with local density α is

$$E_\alpha = \{x \in R^2 : d(x) = \alpha\}. \quad (2)$$

Thus we obtain a point categorization $\{E_\alpha : \alpha \in R\}$ of the image with a multifractal spectrum defined as

$$\{f(\alpha) : \alpha \in R\} = \{\dim(E_\alpha) : \alpha \in R\}. \quad (3)$$

The density function describes how locally the measurement μ satisfies the power law behavior. It measures the non-uniformity of the intensity distribution in the square $B(x, r)$. It should be noted that in this method the measurement $\mu(B(x, r))$ is the sum of intensity pixels in the square. The density $d(x)$ is obtained as the slope of the line fitted to the data $\{\log r, \log \mu(B(x, r))\}$ by the least square method. Then we take a discrete set $\{\alpha_i\}$ from an interval and find for each α_i the point set E_{α_i} according to (2). This set contains all pixels whose densities are close to α_i . The example of such a set near the source image is shown below with $\alpha_i \in (1.5, 1.6)$. The fractal dimension $f(\alpha_i)$ is computed as the slope of the line fitted to the data $\{\log \frac{1}{\delta}, \log N(\delta, E_{\alpha_i})\}$, where $N(\delta, E_{\alpha_i})$ is the smallest number of sets of diameter less than δ that cover E_{α_i} .

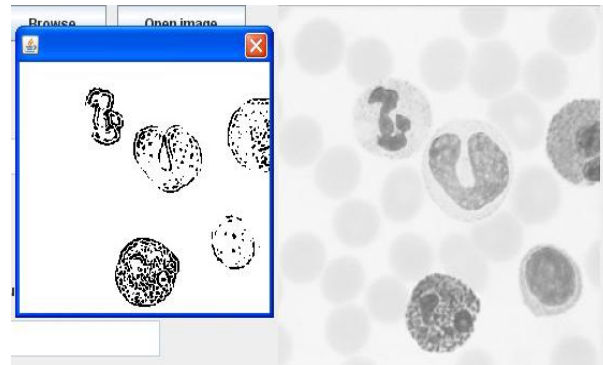


Figure 1. The example of E_α set with $\alpha \in (1.5, 1.6)$

2.1.2. Numerical experiments

Multifractal spectra were obtained for health and affected histological preparations (liver). The following pictures show the images of the preparations and the graphic illustrates their spectra.

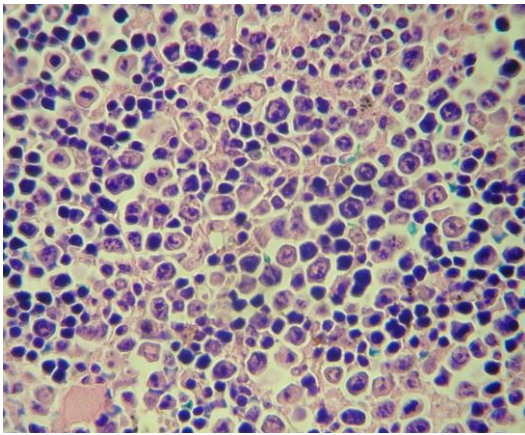


Figure 2. The health liver preparation

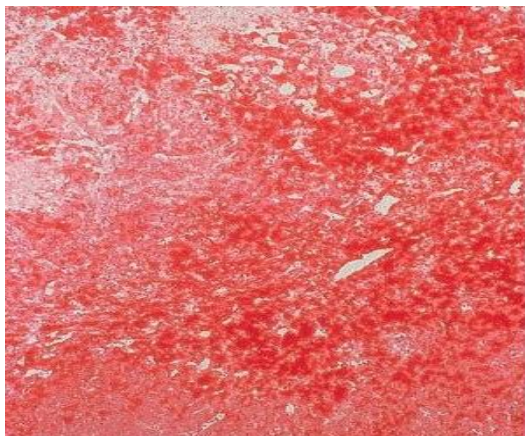


Figure 3. The affected liver preparation

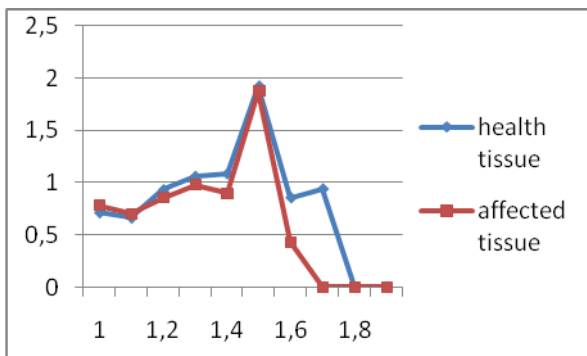


Figure 4. MFS spectra

2.2. Moment-based method

2.2.1. Method description

Let $p_i(r)$ be a normalized i th box measure (the sum of box pixel intensities divided by the sum of all pixel intensities), $i \in [1, N]$. Construct a one-parameter family of normalized measures $\mu(q)$, where for i th box we have

$$\mu_i(q, r) = \frac{(p_i(r))^q}{\sum (p_j(r))^q} \quad (4)$$

According to [2] the Hausdorff dimension of the support of $\mu(q)$ is given by

$$f(q) = \lim_{r \rightarrow 0} \frac{\sum_{i=1}^N \mu_i(q, r) \ln \mu_i(q, r)}{\ln r} \quad (5)$$

In addition we can compute the average value of the singularity strength $\alpha_i = \frac{\ln p_i(r)}{\ln r}$ as

$$\alpha(q) = \lim_{r \rightarrow 0} \frac{\sum_{i=1}^N \mu_i(q, r) \ln p_i(r)}{\ln r} \quad (6)$$

Thus, both α and $f(\alpha)$ may be obtained as explicit functions of the parameter q .

2.2.2. Numerical experiments

Multifractal spectra were calculated by using formulas (4)-(6) for images of 4 classes of biomedical preparations. The most reliable results were obtained for bone tissue and histological preparation images. Below the graphics for health and affected bone tissue (osteoporosis) are shown.

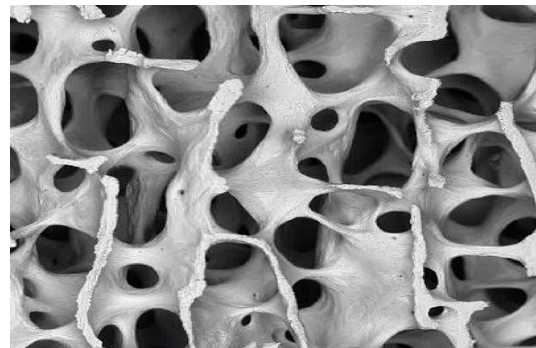


Figure 5. The health bone tissue

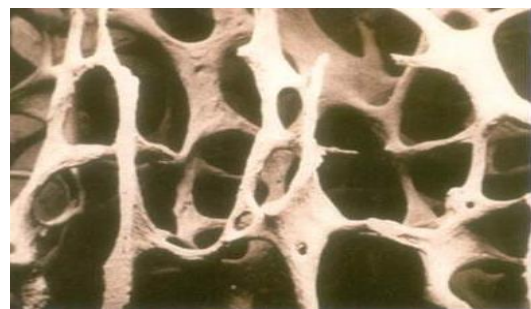


Figure 5. The affected bone tissue

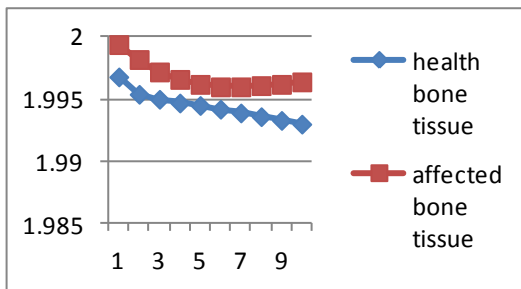


Figure 6. Graphics of (q)

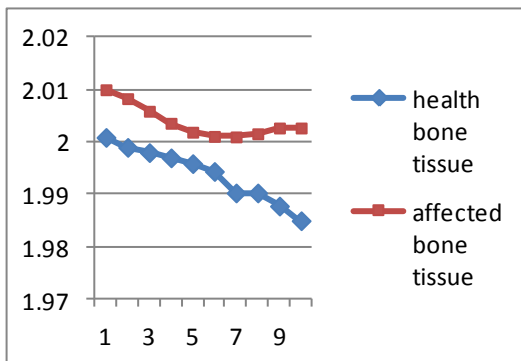


Figure 7. Graphics of f(q)

3. CONCLUSION

For 4 classes of biomedical images: histological preparations, blood cells, connective tissue and bone tissue classification signs have been obtained. The comparison of multifractal spectra for bone tissue allows us to define osteoporosis. At the same time the analysis of images of blood cells with leukemia and connective tissue shows that it is necessary to apply additional methods to obtain reliable results.

References

- [1] Ashvin B. Chhabra, Charles Meneveau, Roderick V. Jensen and K.R. Sreenivasan. Direct determination of the $f(\alpha)$ singularities spectrum and its application to fully developed turbulence – *Physical Review A*, Volume 40, Number 9, November 1, 1989. pp. 5284-5294.
- [2] P. Billingsley. *Ergodic theory and information* (Wiley, New York, 1965)
- [3] Falconer K.J. *Fractal Geometry. Mathematical Foundations and Applications*. — John Wiley & Sons, 1990.
- [4] R. Gonzalez, R. Woods. *Digital image Processing*, 2002, Prentice Hall.
- [5] Halsey T., Jensen M. Fractal measures and their singularities. — *Phys. Rev. A*, no. 33, 1986, pp. 1141-1151.
- [6] Xu Y., Ji H., Fermüller C. Viewpoint Invariant Texture Description Using Fractal Analysis. — *International Journal of Computer Vision*, no. 83, 2009, pp. 85–100.

2-D FILTERS SYNTHESIS USING METHOD OF COMPRESSED COSINES

Peter Apostolov¹

Department of Wireless Communications and Broadcasting at the College of Telecommunications and Posts, Sofia 1700, 1 Acad. Stefan Mladenov St, Bulgaria, e-mail: p_apostolov@abv.bg

Dimitar Valchev²

Department of Radioengineering, Technical University of Varna, 1 Student St, 1910 Varna, Bulgaria, phone: +359 52 383596, e-mail: D.Valchev@tu-varna.bg

Abstract

The method of compressed cosines is used for mathematical approximations. With it, polynomials of a low order are obtained that approximate with high accuracy ideal functions with rectangular contours. Up till now it has been used for synthesis of digital filters for one-dimensional signals. This paper considers the application of the method for synthesis of two-dimensional digital filters. Filters are obtained with characteristics close to the ideal ones.

1. INTRODUCTION

In every technical device using information signals the purpose of filters is to separate the signals necessary for its functioning and to suppress all others that are interference to it. The ideal filter is a rectangular contour. This is a function of the frequency ω having two regions: passband (PB) – the function is equal to unity, and stopband (SB) – the function is equal to zero. It is defined by the expression

$$H_d(\omega) = \begin{cases} 1, & \omega \in [0, \omega_c] \\ 0, & \omega \in (\omega_c, \pi] \end{cases} \quad (1)$$

where ω_c is the cutoff frequency.

A filter with an ideal response cannot be realized. This is why the ideal function is approximated with another one that can be realized by technical means. The task is to define such an approximation function that is very close to the ideal one, and that has a low computational complexity. The approximating functions can be fractional rational, spline functions, polynomials, etc. For technical devices the fractional rational approximations have the best properties but in many cases they are not applicable. In such cases polynomial approximations are used.

A very important factor in these mathematical tasks is the criterion (metric) L_p , $p = 1 \div \infty$ used for approximating the ideal function. Fig. 1 shows a comparison among the most used metrics L_1 , L_2

and L_∞ in approximations with polynomials of 32nd degree. It is seen that in filter synthesis a compromise has to be found between two contradictory requirements: the amplitude of the oscillations and the steepness of the function in the transition band – the band in which the function goes from unity to zero. In all the criteria the function has oscillations in the passband and the stopband that are proportional to the degree of the polynomial.

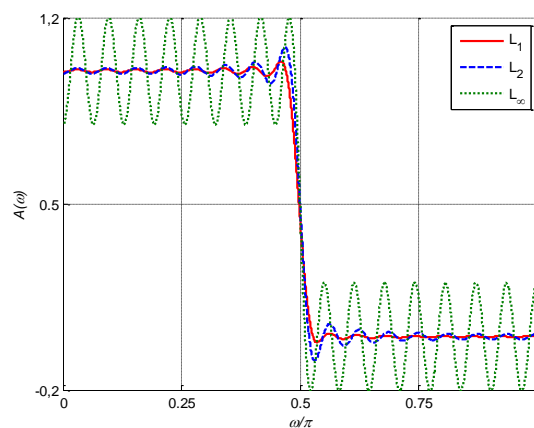


Fig.1. Approximations with polynomials of 32nd degree in an L_1 , L_2 and L_∞ metric

These oscillations are undesirable. Their amplitude reflects the approximation error ε . The purpose in filter synthesis is to obtain the rectangular contour of the ideal function that is maximally flat characteristics in the passband and stopband, and the narrowest possible transition band. With L_1 and

L_2 metrics the oscillations increase near the transition band of the function. This is due to the Gibbs effect [1].

Numerous methods exist for reducing this effect. It can be generalized that every action towards decreasing the amplitude inevitably leads either to broadening the transition band or to increasing the degree of the polynomial which decreases the accuracy of the approximation and increases its computational complexity.

The approximations in an L_∞ metric are performed with the well-known method of Parks-McClellan [2], which is a modified version of the second algorithm of Remez [3]. It is a minimax, equiripple approximation relative to the Chebyshev distance. It is performed with a trigonometric polynomial of degree m :

$$A_m(x) = \sum_{n=0}^m b_n \cos(nx); \quad x \in [0,1], \quad (2)$$

where b_n are the polynomial coefficients, $x = \omega/\pi$. With this method the transition band can be precisely defined and arbitrary narrow. The latter, however, leads to an increase of the approximation error, resp. the amplitude of the oscillations. An important advantage of the method is that the synthesis is performed by an iterative algorithm of Remez that has a fast convergence and a low computational complexity. It is established that with equal specification (non-uniformity in PB and SB and equal transition bandwidth) with the Parks-McClellan method the approximation is performed by a polynomial of the lowest degree. This determines the broad applicability of the method in many technical tasks.

2. ESSENCE OF THE METHOD OF COMPRESSED COSINES

In [4] a new approximation method called, "compressed cosines", using chebyshev's norm is proposed. With the method a low degree trigonometrical polynomials with small approximation error are determined. The analytical expression of the polynomial is

$$A_m(x) = \sum_{k=1}^{m+1} b_k \cos\left\{(k-1) \frac{-\pi}{2} [\operatorname{erf}(\beta(2x-1)) + 1]\right\} = \sum_{k=1}^{m+1} b_k \cos[(k-1)\varphi(x)], \quad x \in [0,1]. \quad (3)$$

It is seen that the argument of cosine consist modulating function

$$\varphi(x) = -\frac{\pi}{2} [\operatorname{erf}(\beta(2x-1)) + 1], \quad (4)$$

The function $\operatorname{erf}(\cdot)$ is the Gauss integral error function. It has S-shaped graph. The slope of the graph depends on the parameter β , and compresses the oscillations of cosine – fig. 2.

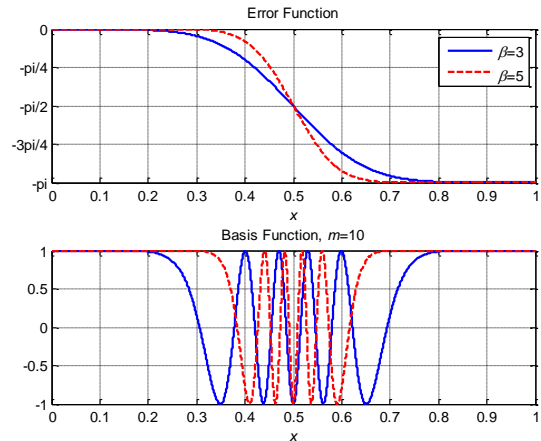


Fig. 2. Modulating function $\operatorname{erf}(\cdot)$ and compression of cosine

Fig. 3 shows an optimal approximation by a polynomial of the lowest possible degree (fourth).

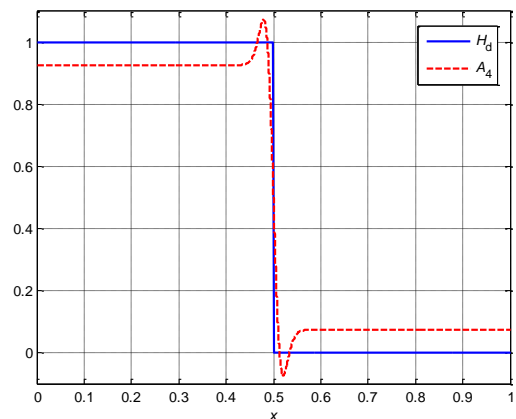


Fig. 3. Optimal approximation of fourth degree

It is seen from the figure that the approximation has only two extreme points, while with the other methods the extreme points are much more (Fig. 1), which is due to the low degree of the polynomial. In this regard this approximation is closest to the ideal function. The polynomial coefficients are obtained by the Remez algorithm that is an iterative solution to a system of $m+2=6$ linear equations. With the other two approximations the equations are much more. For filters with specifications close

to the ideal function, the reduction of the computation operations is more than 100 times.

On the other hand, in the proposed method the magnitude of the “jump” of the function decreases with the increase of the parameter β , without change of the transition bandwidth or increasing the polynomial degree. Fig. 4 shows this valuable property of the method for a fixed transition band and two different values of the parameter β .

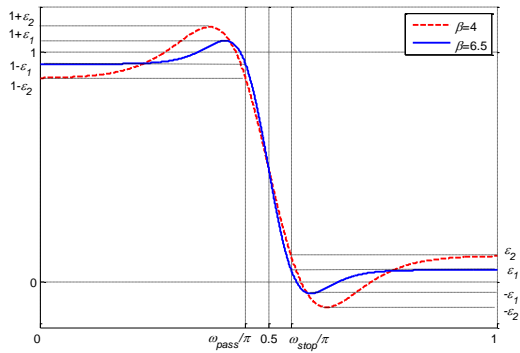


Fig. 4. Approximation error ε depending on the parameter β for a fixed transition band

The parameter β can be arbitrarily large and the transition band – arbitrarily narrow. With the proposed method approximations to ideal functions with a very high accuracy and a very low computational complexity can be done. With a transition bandwidth equal to zero and $\beta = \infty$ the fourth degree polynomial coincides with the ideal transfer function. Instructively speaking, the proposed polynomial of fourth degree is the shortest way to the ideal function.

3. APPLICATION OF THE METHOD TO COMPUTING 2D FILTERS

The magnitude response of one-dimensional digital filters is a function of one variable which designates the frequency. The general form of the transfer function is

$$H(x) = h_0 + \sum_n h_n \cos(nx), \quad (5)$$

where h_n are the filter coefficients. The plot of the magnitude response (MR) is a plane figure (fig. 4). The abscissa is the argument and the ordinate is the amplitude value.

In the two-dimensional filters the transfer function is of two variables

$$H(x, y) = \sum_{n_1} \sum_{n_2} 2h(n_1, n_2) \cos(n_1x + n_2y). \quad (6)$$

The MR is a spatial figure whose base is the plane defined by the values of the two arguments. The values of the arguments are on the abscissa x and the ordinate y , and the amplitude is on the applicate z . The ideal transfer function of a lowpass two-dimensional filter is a rectangular contour whose rotational body is a cylinder.

Approximation in a two-dimensional space is a complicated and time-consuming operation [5]. This is why the fastest way is to perform a one-dimensional approximation and to obtain the spatial figure by a program as a rotational body with respect to the ordinate.

Fig. 5 shows an MR of a one-dimensional lowpass filter with a specification: degree of the approximating polynomial $m = 4$, attenuation in the stopband $DS \geq 10$ dB; normed transition frequency $f_c = 0.5$; normed transition bandwidth $\Delta f = 0.1$

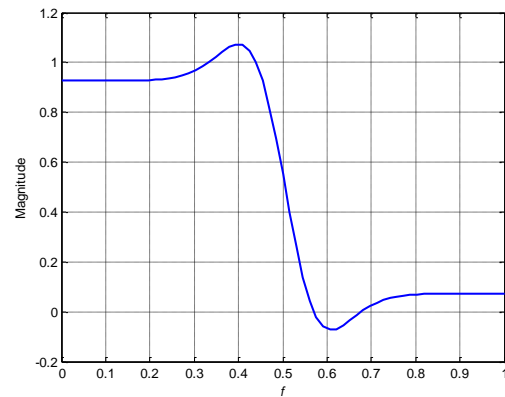


Fig. 5. MR of a one-dimensional LP filter

An MR of the derived two-dimensional filter is obtained by the rotation of the one-dimensional MR with respect to the ordinate Fig. 6.

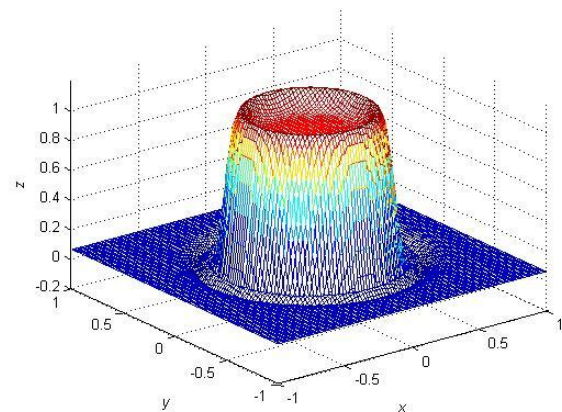


Fig. 6. Two-dimensional lowpass filter

In the example shown the filter specification is deliberately chosen to have a low selectivity in order to obtain a better visualization of the plots. Obviously, if the transition bandwidth is decreased and the value of the parameter β is increased, the filter with compressed cosines will have a characteristic closer to the ideal one – a cylinder.

In a similar way a two-dimensional highpass filter is obtained. Fig. 7 shows a highpass two-dimensional filter, mirroring the prototype from Fig. 6.

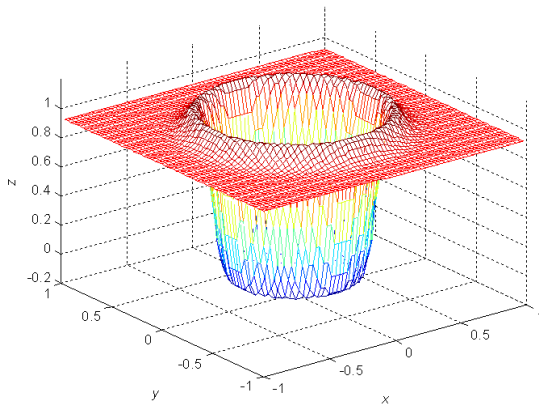


Fig. 7. Two-dimensional highpass filter

Fig. 8 show characteristics of a two-dimensional bandpass filter.

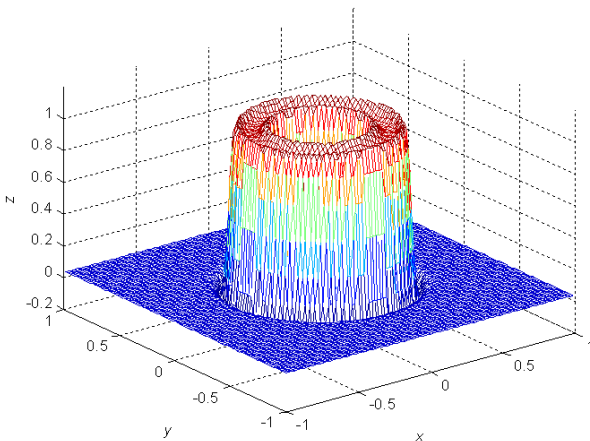


Fig. 8. Two-dimensional bandpass filter

4. CONCLUSION

With the method of compressed cosines two-dimensional filters with characteristics close to the ideal ones are obtained. It has to be noted that achieving optimal characteristic close to the ideal one requires a high resolution in the transition band of the filter. Otherwise, a Gibbs phenomenon is observed. The calculation of the spatial figure can be considerably alleviated, since in a large part of the passband and the stopband it has constant values $1 - \varepsilon$ and ε , respectively (Fig. 4).

The proposed filters can find application to image processing with a high precision in such areas as astronomy, medicine, criminology, etc.

References

- [1] B. Porat, *A Course in Digital Signal Processing*. New York: Wiley, 1997.
- [2] T. W. Parks, J. H. McClellan, "A Program for the Design of Linear Phase FIR Digital Filters", *IEEE Trans. on Audio and Electroacoustics*, Vol. AU – 20, August 1972, pp. 196-199.
- [3] E. Ya. Remez, "Fundamentals of numerical methods for Chebyshev approximations", *Naukova Dumka*, Kiev, 1969
- [4] P. Apostolov, *Approximations with compressed cosines and their applications*. Marin Drinov Academic Publishing House, Sofia, Bulgaria, 2012.
- [5] D. E. Dudgeon, R. M. Mersereau, *Multidimensional signal processing*. Prentice-Hall, Inc, Englewood Cliffs, 1984.

PRACTICAL OBJECT TRACKING SYSTEM ON FPGA

Spirov Rosen Petrov

Technical University of Varna
1, Studentska str.
9010, Varna, Bulgaria
Tel.+35952383488; E-mail: rosexel@abv.bg.

Abstract

In this thesis the author proposed the hardware application of algorithm based on a new representation of the objects with the graph pyramids. The objects are examined at different, increasing, resolutions until it is possible to separate the multiple region in the objects belonging to the occlusion. The graph matching algorithm is performed. For describing its behavior use the VHDL language and the Altera's Quartus tools to synthesize and Altera DE2 board to implement a simple hardware FPGA design.

Keywords: Image processing, object Detection, FPGA, VHDL

1. INTRODUCTION

One of the most interesting applications is that of the video surveillance systems [1]. Video surveillance systems are employed in airports, etc. where cameras are installed are installed to control docks, areas customers, etc. There are two main categories of active sensors. The ones based on structured light triangulation and the laser range scanners. Sensors belonging in the first class project a light stripe on the scene and use a camera to view it in Fig. 1.

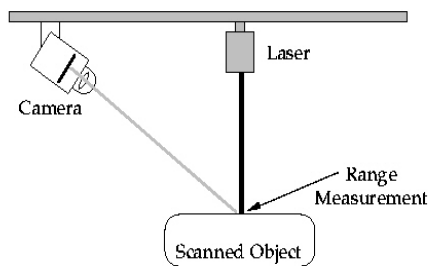


Fig. 1. The optical paths of structured light triangulation

The second category of sensors emit and receive a laser beam and by measuring difference of phase, time of flight or frequency, shift depth is measured and widely used in robotics applications.

A video analysis system has a modular structure. The first step of the processing is the segmentation of the scene, that is the separation of the frame in two set: the static part of the scene-background and the set of the moving objects of interests. This phase is called object detection. Detected moving objects are compared with moving objects in the previous frame to find correspond-

dences. The trajectories of the objects, at point of the processing, are expressed in pixels. Pixel is marked as foreground if the inequality is satisfied:

$$| I_t(x, y) - B_t(x, y) | > T \quad (1)$$

Where T is a predefined threshold. The background image B_t is updated by the use of a first order recursive filter as shown in:

$$B_{t+1} = \alpha I_t + (1 - \alpha) B_t \quad (2)$$

Where α is an adaptation coefficient. The basic idea is to provide the new incoming information into the current background image. Therefore transformation from pixel coordinates to real world coordinates is required. That is an Inverse Perspective Mapping Processing [2] is required and define two Euclidean Spaces: $W = \{(x, y, z)\} \in E^3$ is the 3-D space representing the real world; $I = \{(u, v)\} \in E^2$ is the 2-D space representing image in which the three-dimensional space is projected as image plane. The acquired image by camera belongs to the two-dimensional space I , while the transformed image by the IPM is defined with $z=0$ and belongs to the 3-D space W . The relationship between W and I is illustrated in Figure 2.

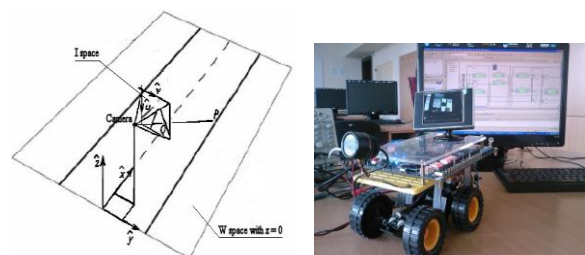


Fig. 2. Relationship between real world and image plane and camera model

2. THE SYSTEM TRACKING ALGORITHM

A number of objects is identified in each frame and a different label is associated to each object. Let $B^t = \{b_1^t, \dots, b_n^t\}$ be the set of boxes belonging to the frame t , moreover let $L = \{l_1, \dots, l_k\}$ be a set of labels. The element (i, j) of the matrix is 1 if the label assigned to the element b_j^t is the same as the label of b_i^{t-1} , it is 0 otherwise. Since there exists no duplicate label in set B^{t-1} , each row contains no more than one value set to 1. If the j -th row contains only zeros, it means that there exists no correspondence between an object belonging to the set B^{t-1} and b_j^t , i.e. b_j^t is a new box. If the j -th column contains only zeros, it means that there exists no correspondence between an object belonging to the set B^t and b_i^{t-1} .

As anticipated, the object tracking problem can be solved by computing a suitable injective mapping $\tau^t: B^t \rightarrow L$. This mapping solves a suitable Weighted Bipartite Graph Matching problem [3]. This is a graph where nodes can be divided into two sets such that no edge connects nodes in the same set. In our problem, the first set is B^{t-1} , while the second set is B^t . Before the correspondence is determined, each box of the set B^{t-1} is connected with each box of the set B^t , thus obtaining a Complete BG [4], as shown in Figure 3.

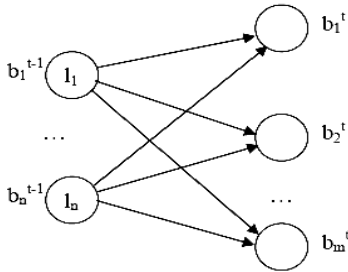


Fig. 3. The complete bipartite graph

Each box b_i^{t-1} is uniquely identified in the set B^{t-1} by its label. In general, an assignment between two sets B^{t-1} and B^t is any subset of $B^{t-1} \times B^t$, i.e., any set of ordered pairs whose first elements belongs to B^{t-1} and whose second elements belongs to B^t , with the constraint that each node may appear at most once in the set. A maximal assignment containing a maximal number of ordered pairs is known as a matching BGM [4].

The height h and the width w of each box is considered. The cost element (i, j) is the Euclidean distance between the (h, w) vectors of b_i^{t-1} and b_j^t . If the distance is greater than a threshold, the cost is ω . Now, let $H_c^b(x)$ the histogram of the color c inside the box b . The correlation $\lambda(i, j)$ index can compute as follows:

$$\lambda(i, j) = \sum_{c \in \{r, g, b\}} \frac{1}{3} \frac{\sum_{k=0}^{q-1} \min(H_c^{b_i^{t-1}}(k), H_c^{b_j^t}(k))}{\sum_{k=0}^{q-1} \max(H_c^{b_i^{t-1}}(k), H_c^{b_j^t}(k))} \quad (4)$$

Where $\lambda(i, j)$ is the average of three indices, computed on the histograms of red, green and blue. The value of λ belongs to the interval $[0, 1]$. The histogram of brightness $H_b(x)$ is then computed, and its correlation λ is obtained. The cost function is computed as $1/\lambda$. In the next step let $G_c(k)$ is the chromaticity histogram of the color c of a frame. The contribution of a color $c \in \{r, g, b\}$ of a pixel to $G_c(k)$ is given:

$$\lambda(i, j) = \frac{1}{3} \sum_{c \in \{r, g, b\}} \sum_{k=0}^{q-1} (G_c^{b_i^{t-1}}(k) - G_c^{b_j^t}(k)) \quad (5)$$

to the histogram is an integer value belonging to $(0, \dots, q-1)$. We compute the correlation index $\lambda(i, j)$ as follows:

$$\lambda_{tot} = \alpha \cdot \lambda_{metric1} + (1 - \alpha) \cdot \lambda_{metric2} \quad (6)$$

Our method is based on a more complex representation, based on a graph pyramid, which in absence of occlusions retains the simplicity and effectiveness of the bounding box, but enables a more accurate object matching to take place during an occlusion. At lowest level there is an adjacency graph, where the nodes represent single pixels, and the edges encode the 4-connected adjacency relation. The intermediate levels are obtained by a bottom-up process, using the classical decimation-grouping procedure described in [5], where a colour similarity is used to decide which nodes must be merged. We decide to use the absolute difference between the mean R, G and B levels of the regions. For two regions R_1 and R_2 the colour similarity is defined as follows:

$$C = |\mu_1^R - \mu_2^R| + |\mu_1^G - \mu_2^G| + |\mu_1^B - \mu_2^B| \quad (7)$$

Where μ_1^R, μ_2^R are the mean of R for regions R_1 and R_2 , μ_1^G, μ_2^G are the mean of G for regions R_1 and R_2 , μ_1^B, μ_2^B are the mean of B for regions R_1 and R_2 . The representation differs from the quad-tree structure [5]. Each intermediate node represents a sub region of the whole region, and its attributes are the position and size of the sub region bounding box and average colour of that sub re-

gion. In particular a node attribute is a set of 7 numbers $\{w, h, avR, avG, avB, cx, cy\}$

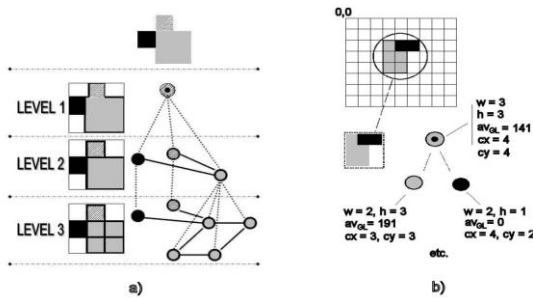


Fig. 4. The graph pyramid: a) the hierarchical structure; b) the nodes attributes

$\{w, h, avGL, cx, cy\}$ where w, h are the width and height of the sub region bounding box, avR, avG, avB ($avGL$) are the average colour/grey level of the sub region, cx, cy are the position of the sub region bounding box centre in the image on Figure 4. Tracking of the object is based on the features, requires selecting the right features, which plays a critical role in tracking.

In image processing, the RGB colour space is usually used to represent colour. Object boundaries usually generate strong changes in image intensities [6]. Edge detection is used to identify these changes. An important property of edges is that they are less sensitive to illumination changes compared to colour features. The Center of mass is vector of 1-by-n dimensions in length that specifies the center point of a region. For each point it is worth mentioning that the first element of the centroid is the horizontal x-coordinate of the center of mass, and the second element is the vertical y-coordinate [4,6] as in fig. 5.

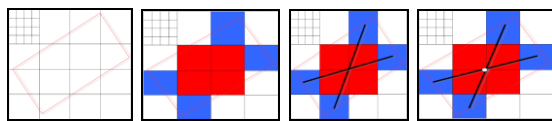


Fig. 5. The center point of a region

Texture is used for classification as well as tracking purpose. This feature is used to identify region or object in which we are interested. It is a measurement of the intensity variation of a surface which quantifies properties such as smoothness and regularity [6].



Fig. 6. The tracking object and system overview

In this method we compute the distance between the centroid that is smaller than a predefined threshold T . Suppose two objects O_c and O_p , c for current frame and p for previous frame with center of mass (x_c, y_c) and (x_p, y_p) respectively, then the Euclidian distance between centers expressed as shown in equation:

$$\sqrt{(x_c - x_p)^2 + (y_c - y_p)^2} < T \quad (8)$$

There are varies number of objects blobs in the current and previous frame I_n and I_{n-1} . Let I_{n-1} and I_n be the number of objects in these frames.

The board Altera DE2 has an Analog Devices ADV7181 TV decoder chip which can convert NTSC composite video from camera to a digital format. Object recognition will be accomplished through software on the Nios II. The processes capture shown in fig. 7.

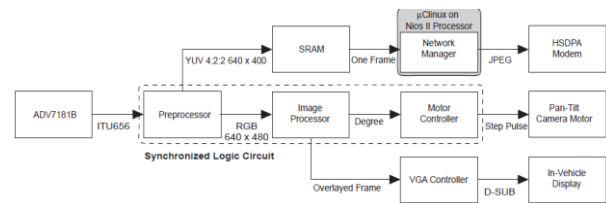


Fig. 7. The image processes capture

The ADV7181 decoder controller takes digital video input from the ADV each pixel from YUV to 16-bit RGB. A double line buffer in the FPGA's block RAM is used for data transfer between the 27 MHz frequency domain of the video controller and the 50 MHz frequency domain of the Avalon bus [7].

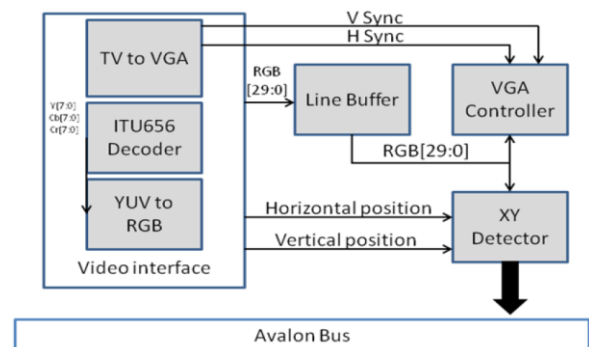


Fig. 8. Video interface and Avalon bus

The Nios II then performs processing on the buffer in SDRAM in order to find the center of the object we are tracking and to mark up the image.

The image processing software analyzes an image, termines the orientation of the target compared

to the center of the screen, and then issues a command to turn either right or left to the Platform until the tracked object is in the center of the camera's field of view.

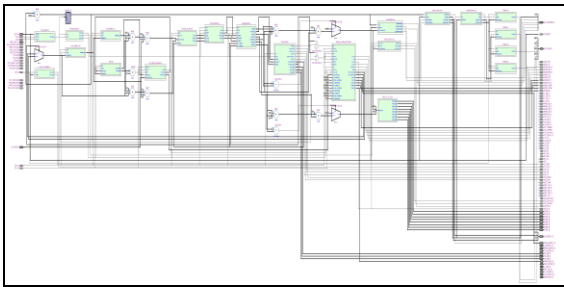


Fig. 9. The RTL project of object tracking system

3. CONCLUSION

In this thesis we propose an algorithm based on a new representation of the objects: the graph pyramids. This representation allows the resolutions of occlusions also in complex cases. The objects are examined at different, increasing, resolutions until it is possible to separate the multiple regions in the objects belonging to the occlusion. Furthermore, to detect the identities of the objects in the current frame beginning from the identities of the objects in the previous frame, a graph matching algorithm is performed.

References

- [1] M. Bertozzi, A. Fascioli, "Vision-based intelligent vehicles: State of art and perspectives", Robotics and Autonomous Systems 2000
- [2] Poupard M, "Road edge tracking using filtering theory" Palaiseau Ecole 2000.
- [3] R. Sedgewick, Algorithms in C. Pt. 5, Graph algorithms. 3rd Edition Harlow : Addison-Wesley 2002, p. 482.
- [4] Kuhn, H.W "The Hungarian Method for the Assignment Problem", Naval Research Logistics Quarterly, 2002
- [5] J. M. Jolion, A. Montanvert. "The Adaptive Pyramid: A Framework for 2D Image Analysis". CVGIP: Image Understanding, Academic Press. Vol. 55 – 3, pp. 339 – 348. 1992.
- [6] H. Buxton and S. G. Gong, "Visual surveillance in a dynamic and uncertain world," Artif. Intell., vol. 78, Oct. 1995
- [7] www.altera.com

DESIGN OF POWER UNIT OF SYSTEM FOR THERAPY USING "RUNNING" LOW FREQUENCY MAGNETIC FIELD

Atanas Dimitrov

Technical University of Sofia, Bulgaria), Faculty of Telecommunication, "Kl.Ohridsky" str. 8, 1000 Sofia, Bulgaria,
T.+359(2)9652278; E-mail: atanasdimitrov@gmail.com.

Abstract

One very important problem in the process of design of systems for magnetotherapy is connected with design of power unit. The systems for magnetotherapy, which use running low frequency magnetic field are new generation of systems for magnetotherapy. It is well known that familiarization of patients with parameters of external influence is a big disadvantage of systems for physiotherapy. This problem can be avoided in systems for low frequency magnetic field by running of this field around the human body. The possibility for simultaneously influence of low frequency magnetic field on different part of the human body is one additional advantage of systems for magnetotherapy, using moving magnetic field. The basic requirements and method for design of above mentioned system for magnetotherapy and especially design of power unit is described in the paper.

1. INTRODUCTION

The power unit should provide enough high amplitude of output current for all patients coils which are situated on the patient's bed (Fig. 1). The input signals of power unit are provided by generator for rectangular electrical impulses with special parameters. Now more and more digital systems are applied to therapy. The use of digital elements for their construction offers greater flexibility, economy and more functions in one system. The data which pass through various digital modules can be saved in memory, subject to various digital processing, and also can be displayed on digital display. In the design of pulse generators can be used and one-chip microcomputers, characterized by low consumption and a limited number of external components.

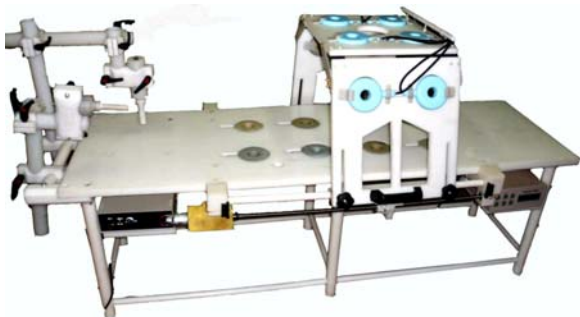


Fig. 1. Patient's bed

Great advantage over the basic generators is the programmable logic. Any functional change can be implemented easily without any hardware changes (making a new board, adding / replacing components).

2. DESIGN OF POWER UNIT

To ensure the amplitude manipulation of the output signals device was used with sixteen transformer output voltage in the secondary coil. Managing stress how to manipulate the output signals of the apparatus at a time is done programmatically by way microprocessor management. In the production of the device is provided at the outlet to be used with a large inductive load inductance. Besides handling the voltage provided an opportunity to determine to which output is directed to output. For this switching are provided five separate and completely equal steps. This makes the device more versatile and easy to use and "animation" as-entitling the choice of the designer to choose which output to use enhancements. Given the characteristics of the inductive load for the apparatus final steps are realized by choosing powerful triacs. The use of transistor stages is not desirable because the application of inductive load is observed instability in their work. Powerful Hill-relays are characterized by a finite number of switch and losses caused by mechanical contact of the switch plates, large switching time, high cost and risk of injury. Given the stable operation of the triacs work with inductive load, low market price, compact size and good working parameter's choice for the thesis is the most appropriate. For the final steps is possible to conduct high currents up to 3A and relatively high voltage 24V. Used triacs model BTA12-600B. They are characterized by low current opening 50mA, 12A maximum current in the control circuit and

600V maximum voltage. Repeatedly higher characteristics of triacs to set in the assignment of work provide more reliable operation of the elements and less waste heat process. Used Six triacs (Q12-Q17) for the amplitude manipulation provided with six and five strains (Q18-Q22) to provide switching and management outcome of five sets.

The maximum of output current signal from the microprocessor is 25mA. The use of such power will not be enough to clear a triacs, and will also lead to strong and increase of temperature of microprocessor. Ensuring adequate power to clear triacs, and also the simplification of the CPU is achieved through the use of transistor stages placed between the ruling and findings of the microcomputer gates of triacs. Transistors are connected in a circuit common collector (emitter repeater). For this type of scheme is characterized by low voltage amplifier, high gain in current and power. Depending on the given signal on the basis they operate in standby mode or route of saturation. The maximal current for the gate triacs in a performance is 50mA. Therefore, to ensure reliable and stable operation of transistor stages are designed for currents less than 50mA.

$$I_{c_{max}} = V_{cc} / R_e \Rightarrow$$

$$R_e = V_{cc} / I_{c_{max}} = 12 / 40 \cdot 10^{-3} = 300 \text{ohm}$$

A medium power transistor model 2T6551 can be used. It can be seen using output transistor's parameters that collector current would be 40mA, which corresponds to the base current 2mA. The emitter's current which is an input to the gate of triac is the sum of the collector and base current of transistor and it's less than the maximum of triac's current. The diagram of power unit is shown on Fig. 2.

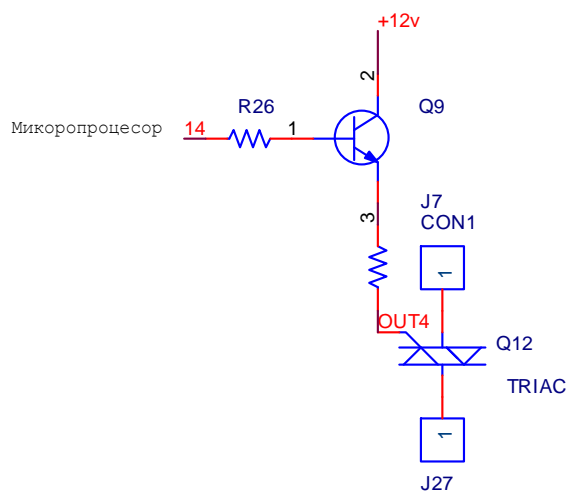


Fig. 2. The diagram of power unit

To achieve simultaneous amplitude manipulation of the output current and switching output, switching voltages of triacs are connected in series to the triacs switching outputs. In this case the output inductive load is to be connected in series between the two triacs. This is shown in the diagram on Fig. 3. The connectors (J7-J12) relate the findings of the secondary coils of different voltages of the transformer.

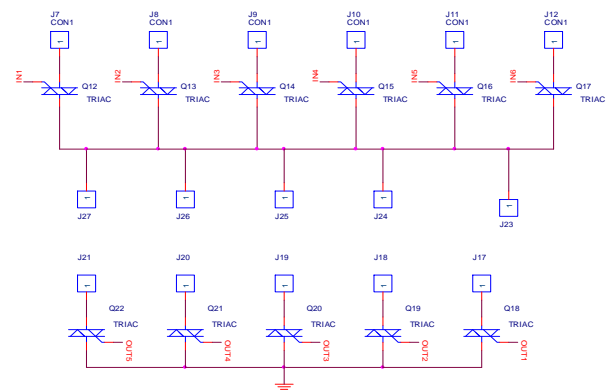


Fig. 3. The diagram of power system

As first step a load should be placed on the output of the generator. It's necessary to be provided signal to the gate of one of the triacs (Q12-Q17) which is chosen for what will be output amplitude signals. The circuit of the transformer secondary winding is closed only when given the signal to one and triacs (Q18-Q22) and a connection through the load during the triacs to the table. The used software provide that in every time only one triac from the group Q12-Q17 is open and only one triac from the group Q18-Q22 is open. The rest triacs are closed in the same time. For all solid steps are observed similar features so that all elements used in transistor stages are the same. Same are also all triacs used in the generator. Ensuring a stable constant tension, which determines the work mode for operation of the constituent elements of the generator is designed using classical stabilizer circuit. AC input voltage of the transformer first face of the scheme Greeks, smoothes then be submitted to the stabilizers IS 7812 and IS 7805 for precise stabilization.

3. DESIGN OF PHYSICAL COMMUNICATION BETWEEN MICROPROCESSOR AND IT'S MANAGED MODULES

The management of multifunctional pulse generator is fully implemented using a microcomputer. It has 25 input / Exit buffers organized as follows:

- Four inputs - for providing a possibility of external influence on the generated frequency;
- Five output provided for switching and control signals to the output device;
- Six exits down switching voltage secondary winding of the transforme;
- One output to generate a beep;
- Six concludes the realization of communication with liquid crystal display
- Three input/output for providing communication with an integrated I2C Clock IC PCF8583.

- Conclusion RA3 - switching voltage of 15V
- Conclusion RA4 - switching voltage of 18V
- Conclusion RD0 - switching voltage of 21V
- Conclusion RD1 - switching voltage of 24V

Management unit switching output is realized using five concludes the microprocessor configured as outputs:

- Conclusion RC1 - for switching output 1
- Conclusion RC2 - for switching output 2
- Conclusion RC5 - for switching output 3
- Conclusion RC6 - for switching output 4
- Conclusion RC7 - for switching output 5

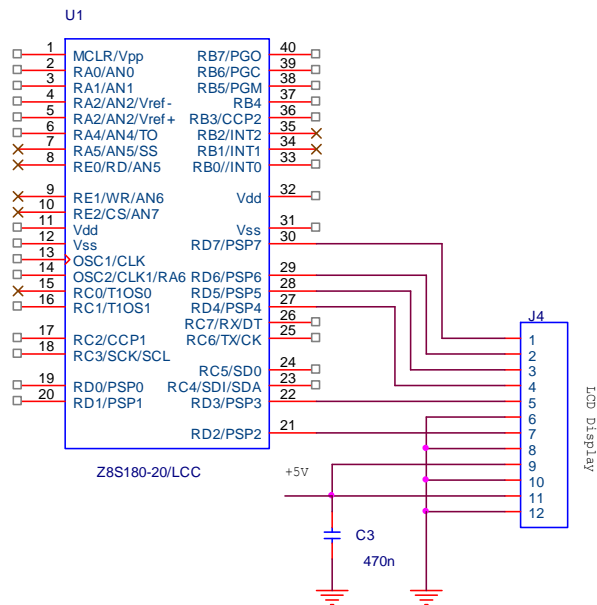


Fig. 4. The principal linked diagram to a microcomputer

The principal linked diagram to a microcomputer is shown on Fig. 4. Four bit interface is used for communication with the display. This facilitates the realization of the projected hardware enhancements. The disadvantage is you will be sent information on two cycles and shipment process is slower than when using an 8-bit interface. In the design process was identified from this will not affect the accuracy of the work unit. Use the findings of the microcomputer are:

- RD2 – to R / S switch between registry data and commands
- RD3 – as at R / W switch mode read or write mode
- RD4–RD7 – inputs for information exchange.

Management unit switching voltage is realized by using six concludes the microprocessor configured as outputs. These are:

- Conclusion RA1 - switching voltage of 9V
- Conclusion RA2 - switching voltage of 12V

Communication between the microprocessor PcF8583 and integrated circuit is implemented in I2C interface. He held the following conclusions of microprocessora:

- Conclusion RC3 - Seril clock-submission of a series of clock pulses to the circuit
- Conclusion RC4 - Seril DATA-submission of information by serial clock pulses to the circuit
- Conclusion RB0/INT0 – adopting external breaks. Receiving signals from integral circuit.

User intervention in the operation of a micro-computer is implemented with the help of four buttons. They are connected to the four outlets of the CPU and are configured as outputs. These are:

- RB7 – serving to stop / pause / procedure for generating a periodic pulse train and entry menu is setting the parameters of the generated signals
- RB6 – served to start / continue the procedure of generating a periodic pulse sequences / store the changes made by the user.
- RB5 – serves to increase the frequency / time / duty cycle of the pulse sequences / voltage output. Switching from automatic to manual mode to change the frequency of pulse outputs
- RB4 – serves to reduce the frequency / time / duty cycle of the pulse sequences / voltage output. Switching from automatic to manual mode to change the frequency of output pulses.

To make an audible alarm is used piezoelectric buzzer. It is connected to terminal RB0 na micro-processor in limiting resistor to ground

4. CONCLUSION

A new method for design of power unit of system for therapy using “running” low frequency magnetic field is done in the paper.

Acknowledgments

The paper will be included in the Proceedings of 7th INTERNATIONAL CONFERENCE on Communications, Electromagnetics and Medical Applications (CEMA'12) Athens, Greece, November 08th - 10th, 2012 on the base of financial support of contract 121нд0019-07, Sector for scientific research of Technical University – Sofia, Bulgaria

References

- [1] SIEMENS Medical Engineering Group, "Units for Physical Therapy And Diagnosis", p. 230, 2002.
- [2] W. Y. Riadh, "Electromagnetic Fields and Radiation (Human Bioeffects and Safety)", Marcel Dekker Inc. Canada, 2001, ISBN 0-8247-0877-3.
- [3] Д. Димитров, Медицински системи за въздействие на електромагнитно поле върху човека, учебник, издателство на ТУ-София, 2007
- [4] V. Mihaylov, Kalin L. Dimitrov, Dimitar C. Dimitrov, Research on the influence of permanent magnetic field during live tissue laser treatment, 3rd International Conference "Communication, Electromagnetism and Medical Application, Athens, Greece, November 6-8, 2008, p. 12-156

INVESTIGATION ON MOTION OF IONS IN ALIVE TISSUE UNDER INFLUENCE OF TOROIDAL LOW FREQUENCY MAGNETIC FIELD

Atanas Dimitrov*, Dimitar Dimitrov**, Sasho Guergov***, Anton Savov****

*Technical University of Sofia, Bulgaria, Faculty of Telecommunication, "Kl. Ohridsky" str. 8, 1000 Sofia, Bulgaria, T.+359(2)9652278; E-mail: atanasddimitrov@gmail.com.,

**Technical University of Sofia, Bulgaria, Faculty of Telecommunication, "Kl. Ohridsky" str. 8, 1000 Sofia, Bulgaria, T.+359(2)9652278; E-mail:dcd@tu-sofia.bg

*** Technical University of Sofia, Bulgaria, Faculty of Mechanical Technologies, TU-Sofia, "Kl. Ohridsky" str. 8, 1000 Sofia, Bulgaria, T.+359(2)9653246; E-mail:sguergov@tu-sofia.bg

****Specialised Hospital for Rehabilitation "St. Mina", Warshetc, T.+359 878492308

Abstract

The application of low frequency magnetic field can be meet in many procedures of physiotherapy. Often one pair of coils are enough for application of low frequency magnetic field. But in this case the number of "appropriate" pathologies is limited. Because of that usually more than one pair of coils are used for the procedures. The different coils can be situated at different part of the human body, according to the physician's recommendations. The procedure would be user friendly if some mechanical devices can be used for providing of space dispositions of coils.

One very useful disposition of coils is this one when the space configuration of magnetic field is like toroidal magnetic field.

1. INTRODUCTION

In the process of design of multifunctional flexible system for physiotherapy a bed for "running" low frequency magnetic field has been designed (Fig.1)

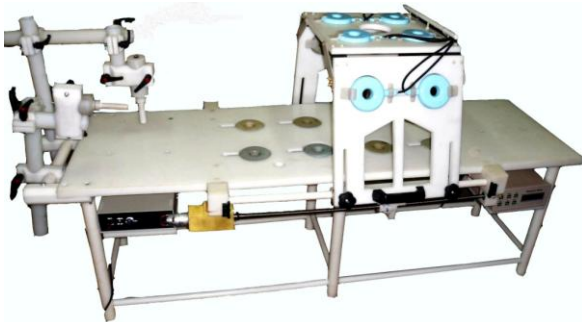


Fig. 1. Patient's bed

Two devices for acupuncture pressure are situated on the "magnetic". Therefore it's possible to be used acupuncture together with magnetotherapy as one new method for therapy, which can provide a good results of therapy for a short time. The coils are situated on the plane of bed and on special mechanical trapezium stand. Because of that the coils on the bed (under trapezium stand) together with the coils on the trapezium stand provide magnetic field which space configuration is approximately like toroidal magnetic field. It's clear that during the process of therapy the ions of human body are under influence of toroidal magnetic field.

2. MOTION OF IONS IN ALIVE TISSUE UNDER INFLUENCE OF TOROIDAL LOW FREQUENCY MAGNETIC FIELD

Let us consider a magnetic field which in cylindrical coordinates has only a component B_φ and which is uniform in the φ – and z – direction. In the absence of volume currents it follows from the 2nd Maxwell equation that

$$\frac{\partial B_\varphi}{\partial r} = -\frac{B_\varphi}{r}. \quad (1)$$

In this coordinate system the velocity of the particle can be represented as

$$\vec{v}_c = \vec{v}_r + \vec{v}_z, v_\varphi = v_\varphi.$$

Equation of drift velocity of the center of gyration of charged particle is

$$\vec{u}_c = -\vec{\varphi}_0 \times r_0 \frac{1}{r \frac{e}{mc} B_\varphi} \left(\frac{1}{2} v_c^2 + v_\varphi^2 \right) \quad (2a)$$

$$u_\varphi = v_\varphi. \quad (2b)$$

As equation (2a) involves the value of the charge e carried by the particle, it follows that the u_c

drift for negatively charged particles in a direction opposite to the drift of positively charged particles. It's interesting to note that the component of the drift associated with the speed v_c arises

From the radial non-uniformity of B_ϕ , whereas the component associated with v_ε derives from the centrifugal force mv_ϕ^2/r of the circulating particle. This latter component can be also calculated directly from a force-balance equation

$$\vec{r}_0 \frac{mv_\phi}{r} = \frac{e}{c} \vec{u} \times \vec{B} \quad (3)$$

which gives:

$$u = \frac{mc}{e} \frac{v_\phi^2}{rB_\phi} \quad (\text{cm/sec}) \quad (3a)$$

A beam of particles injected tangentially into the field B_ϕ will spiral around the axis whilst individual particles will also spiral on tube of flux. The trajectory of individual particles is, therefore, a double helix. The problem of how the injection speed $v_{\phi 0}$ is divided into v_c and v_ϕ of the spiral is outside the scope of this paper.

3. MOTION OF IONS IN THE FIELD OF A MAGNETIC LENS

The motion of charged particles in the field of a simple cylindrical magnetic lens can be considered from two extreme points of view. One is that of electron optics, in which it is usually assumed that the lens changes the momentum of the particles only by a small amount. The other view is found in plasma physics, where one usually assumes that the lens is so strong that the Larmor radius of particles is much smaller than the dimensions of the lens and that most of the particles to be studied have their velocities oriented at least in two dimensions. Somewhere between these extremes is the subject of cosmic ray interactions with the magnetic fields of cosmic clouds, of stars and of planets. In this section we shall deal with the motion for which

$$p \equiv \frac{mv}{c} \square d$$

where d is some characteristic dimension of lens. The description of the motion of such a particle can be based on the drift-velocity formulae. However, in

order to apply these equations, information is required on v_c and v_ϕ . This can be derived from the invariance of the total kinetic energy of the particle, which is

$$W = \frac{1}{2} m (v_c^2 + v_\phi^2) = \text{const.} \quad (4)$$

and from the adiabatic invariance of the magnetic moment μ of the particle defined as

$$\mu = \frac{\frac{1}{2} m v_c^2}{B} \quad (5)$$

The magnetic moment μ is only approximately invariant and its variation $\Delta\mu$ is critically dependent on ratio

$$\frac{v/L}{eB_0/2\pi mc} = \frac{\tau_c}{\tau_t}, \quad (6)$$

where τ_c is period of the cyclotron motion and τ_t is the transit time of the particle through a non-uniformity whose dimension is L . It can be shown that

$$\frac{\Delta\mu}{\mu} = \exp\left(a \frac{\tau_c}{\tau_t}\right) \quad (7)$$

and a is a factor depending on the relative amplitude $\Delta B/B_0$ of the non-uniformity.

The consequence of assuming that the magnetic moment is constant is that, apart from drift motion of center of gyration, a charged particle is bound to a surface of a tube of constant flux. Thus

$$\frac{\frac{1}{2} m^2 v_c^2}{B^2} \frac{B}{m} = \text{const. or } p^2 B = \text{const.}$$

and as $\pi p^2 = \phi$ where ϕ is the magnetic flux, it follows that the orbit of the particle links a constant amount of magnetic flux.

Let us consider the motion of a charged particle on a converging tube of flux of rotational symmetry. Here from

$$\vec{u}_c = \frac{\vec{B} \times \text{grad} B_z}{B^2 \omega_c} \left(\frac{1}{2} v_c^2 + v_\phi^2 \right)$$

gives

$$u_c = 0 \text{ owing to } \vec{B} \times \text{grad} B_z = 0.$$

The equation for u_ϕ does not contain any information as $u_\phi = v_\phi$. It is, therefore, necessary to find an equation for v_ϕ . This is

$$\frac{d}{dt} v_{\parallel} = \frac{F_{\parallel}}{m} \quad (8)$$

where F_{\parallel} is a force on the particle in the direction of the vector \vec{B} . This force is the component of the Lorentz force in this direction. Thus

$$F_{\parallel} = \left| \frac{e}{c} \vec{v} \times \vec{B} \right|_{\parallel} = \frac{e}{c} v_c B_r.$$

The component B_r is related to B_z through $\text{div} \vec{B} = 0$. Thus

$$\frac{\partial(rB_r)}{\partial r} = -r \frac{\partial B_z}{\partial z}. \quad (9)$$

Assuming that for $r \ll p$, $\partial B_z / \partial z$ is independent of r one obtains on integrating this equation with respect to r :

$$B_r = -\frac{1}{2} p \frac{\partial B_z}{\partial z}.$$

Substituting this into equation (9) yields

$$\begin{aligned} F_{\parallel} &= -\frac{1}{2} \frac{e}{c} v_c p \frac{\partial B_z}{\partial z} \\ F_{\parallel} &= -\frac{\frac{1}{2} m v_c^2}{B} \frac{\partial B_z}{\partial z} \end{aligned} \quad (10a)$$

or expressed in a vector form

$$F_{\parallel} = -\vec{\mu} \cdot \text{grad} B. \quad (10b)$$

The equation of motion in the B-direction becomes

$$\dot{v}_{\parallel} = \dot{u}_{\parallel} = -\frac{\vec{\mu}}{m} \cdot \text{grad} B_z \quad (11)$$

This equation shows that charged particles, incident on a region of strong magnetic field experience deceleration in the direction of \vec{B} and in some cases are reflected. However, as their total kinetic energy remains constant, it follows that as v_{\parallel} decreases v_c increases and vice versa. This can be expressed mathematically using eq. (4) as

$$v_c^2 = \frac{2W}{m} - v_{\parallel}^2 \quad (12)$$

The condition of reflection is that $v_{\parallel} = 0$. When this is so v_c reaches a maximum

$$v_{cM} = \sqrt{\frac{2W}{m}} \quad (13)$$

Assuming the magnetic moment to be invariant it follows that

$$\mu = \frac{\frac{1}{2} m v_{cM}^2}{B_M} = \frac{W}{B_M}. \quad (14)$$

It is clear that the smaller the magnetic moment, for a given total energy W , the further will the charged particle penetrate along the converging flux tube. A more general problem is represented by the motion of charged particle in a magnetostatic field whose flux tubes form a converging and bent bundle (fig. 4)

This is the configuration off axis of a cylindrical lens.

If B varies only slowly with respect to z one has $\vec{B} \times \text{grad} B_z \approx B \cdot \partial B_z / \partial r$ and equation (11) becomes

$$u_{\varphi} = \left[\left(\frac{\partial B_z}{\partial r} \right) / \left(\frac{eB^2}{mc} \right) \right] \left(\frac{1}{2} v_c^2 + v_{\parallel}^2 \right) \quad (15)$$

$$\dot{v}_{\parallel} = \frac{1}{2} v_c^2 B_z^{-1} \frac{\partial B_z}{\partial z} \quad (16)$$

The reflection condition remains approximately the same as formulated in equation (14).

However, the particle does not return after the reflection along the same tube of flux but precesses in the φ -direction during the reflection process.

Let us study this precession in the case of a magnetic mirror. This is a particular case of a lens geometry in which

$$B = B_0 \text{ for } z < a, \quad B = B_1 \text{ for } z > b$$

where $B_1 > B_0$ and $b > a$.

It follows from equation (14) that particles for which

$$\mu > \frac{W}{B_1}$$

will be reflected. Let us divide this inequality by $(v_{\parallel}^2)_0$ where $(v_{\parallel}^2)_0 = v_{\parallel}^2$ for $z < a$. Then

$$\frac{\left(\frac{v_c}{v_{\parallel}} \right)_a^2}{B_0} > \frac{\left(\frac{v_c}{v_{\parallel}} \right)^2 + 1}{B_1}.$$

Putting

$$\left(\frac{v_c}{v_{\square}} \right) = \tan \theta$$

where θ is the angle between the vector \vec{v}_0 and \vec{B}_0 , one can write the condition for reflection as

$$\sin^2 \theta > \frac{B_0}{B_1}. \quad (17)$$

We shall follow a typical particle which satisfies this inequality. The angle of precession φ of such a particle will be

$$\varphi = 2 \int_0^{\tau} \frac{u_{\varphi}}{r} dt = 2 \frac{c}{e} \int_0^{\tau} \frac{\partial B_r / \partial z}{rB} \left(\frac{2W}{B} - \mu \right) dz \quad (18)$$

This can be written as

$$\varphi = 2 \frac{c}{e} \int_a^{z-a} \frac{\partial B_r / \partial z}{rB} \left(\frac{2W}{B} - \mu \right) \frac{dz}{v_{\square}}.$$

From eq. (16) it follows that

$$v_{\square} \dot{v}_{\square} = \frac{\mu}{m} \frac{\partial B_z}{\partial t}$$

or

$$v_{\square} = \left[2 \frac{\mu}{m} (B_z - B_0) + v_{\square 0}^2 \right]^{\frac{1}{2}}. \quad (19)$$

Also near the z-axis (i.e. for $r < b - a$) one can expand B_z as

$$B_z(r_1, z) \cong B_A - \frac{1}{4} r^2 B_A^{\square}$$

where

$$B_A = B_A(0_1, z), B_A^{\square} = \frac{\partial^2}{\partial z^2} B_A. \quad (20)$$

Using this expression and equation (20) one obtains

$$\varphi \cong - \frac{c}{e} \int_a^{z-a} \frac{B_A^{\square} \left(\frac{2W}{B_z} - \mu \right) dz}{B_z \left[2 \frac{\mu}{m} (B_z - B_0) + v_{\square 0}^2 \right]^{\frac{1}{2}}} \quad (21)$$

which can be easily evaluated for a specific field geometry. It can be appreciated that owing to B_A^{\square} changing sign in the interval (a, b) the sign of φ may be either positive or negative.

The field of a magnetic dipole can be also regarded as a magnetic lens of the type discussed in this section. However, as the field strength of a dipole depends on the distance r from the center of the dipole as $1/r^3$, the motion of a charged particle in this field cannot be always correctly represented by the drift motion of its center of gyration. In particular, the theorem of conservation of the magnetic moment μ of the particle breaks down when the radius of gyration ρ becomes larger than the distance r .

CONCLUSION

A mathematical description of motion of ions under influence of toroidal low frequency magnetic field is done in the paper, The space configuration of approximately toroidal magnetic field depends to the currents in the coils, which consists "toroid". These currents can be managed using appropriate software. Therefore the space configuration of toroidal magnetic field can be managed also.

Acknowledgments

The paper will be included in the Proceedings of 7th INTERNATIONAL CONFERENCE on Communications, Electromagnetics and Medical Applications (CEMA'12) Athens, Greece, November 08th - 10th, 2012 on the base of financial support of contract 121пд0019-07,

Sector for scientific research of Technical University-Sofia, Bulgaria

References

- [1] SIEMENS Medical Engineering Group, "Units for Physical Therapy and Diagnosis". p.230, 2002
- [2] W. Y. Riadh, "Electromagnetic Fields and Radiation (Human Bioeffects and Safety)", Marcel Dekker Inc. Canada, 2001, ISBN 0-8247-0877-3.
- [3] Д. Димитров, Медицински системи за въздействие на електромагнитно поле върху човека, учебник, издателство на ТУ-София, 2007
- [4] V. Mihaylov, Kalin L. Dimitrov, Dimitar C. Dimitrov, Research on the influence of permanent magnetic field during live tissue laser treatment, 3rd International Conference "Communication, Electromagnetism and Medical Application, Athens, Greece, November 6-8, 2008, p.12-156
- [5] А. Попов, Д. Манова, Цифрова електроника, ТУ-филиал Пловдив, 1997
- [6] Д. Димитров, Комуникационни системи в медицината, учебник, издателство на ТУ-София, 2005.

MEDICAL INFORMATION SYSTEM FOR SELF MONITORING AND DISTANCE CONSULTATION

„Patient's Diary“
/Article/

Simona Lincheva

FKSY, TU-Sofia 1000 Sofia, BULGARIA

Phone / Fax: 0898551952, E-mail: simona_lincheva@yahoo.com

Abstract

Medical information system for self monitoring and distance consultation is an application built as a mobile diary for remote connection of patient and doctor. As anyone who uses the system can both lead their own diary and have constant information about how they felt, and send these data to a doctor for consultation. Another option offered by the system for self monitoring is an Internet connection, allowing instant information about a symptom or whatever it was.

1. INTRODUCTION

The system - "Patient's Diary" was written for the mobile operating system Android (maintained and developed by the Open Handset Alliance consortium, led by Google Inc), using different applications specially designed for this operating system.

2. SYSTEM INTRODUCTION

The main menu of the application, from where the user chooses sub-menus.



Fig. 1. Main interface of the system

The next step is to choose the appropriate sub-menu (each person chooses which menu to fill, according to the disease). As each sub-menu is different from the rest, it depends on the underlying data to be tracked as a disease.

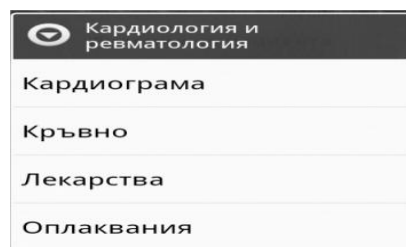


Fig. 2. Example: menu „Cardiology“

Table 1. Functionality of the system

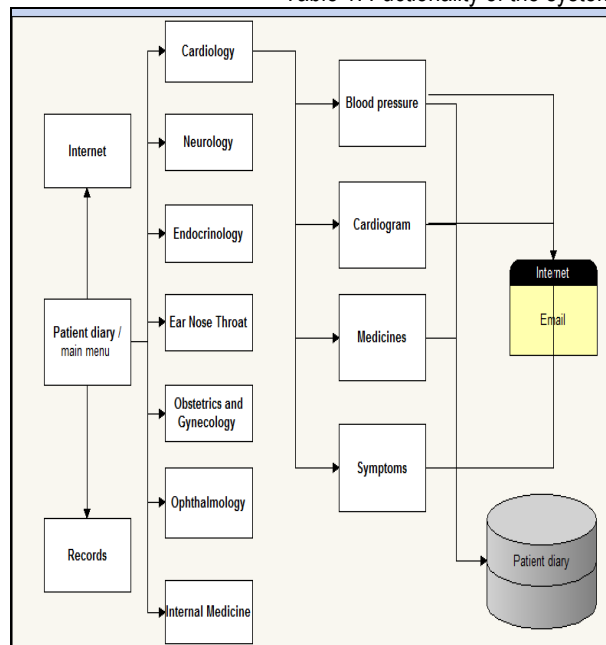


Fig. 3 presents the main menu of the application. From the main menu we go to the next menu as each menu meets the relevant field of medicine. The latest "Internet" gives possibilities for searching diseases and symptoms on the internet.

Each of the submenus has the functionality of recording in the database and an Internet connection, but the nature of the structure as input data varies according to the individual diseases.

For example I gave the menu "Cardiology", which in turn has four submenus (this is individual for each menu). The above figure shows the functionality of the submenus. Every one of them has the option to record in the database (similar to private patient card). And a part of the submenus have the option to send the data to email the doctor.



Fig. 4.1. Interface of the submenus



Fig. 4.2. Interface of the submenus

4. BUILDING THE REMOTE CONSULTATION



Remote consultation

The aim of the application is embedded in the idea that anyone who has any health problems can lead personal "diary" and sends the data to the doctor without having it go to a hospital or doctor's office.

„Patient's Diary” to some extent realized above idea, it allows sending of symptoms, blood pressure, cardiogram, etc. to the Internet. As enshrined algorithm send all or just a cardboard parts of it, according to the wishes of the patient or the doctor. The algorithm is not limited to connection patient - doctor, but in the future will allow doctor - patient and preservation of the recommendations of the doctor to be kept as a separate record in the application, and patients always have access to them.

Another important feature of the application is direct connection to the internet and possibility for a person immediately to check their symptoms online. As completely separate menu that offers list of options with different diseases and issues that can search the Web.

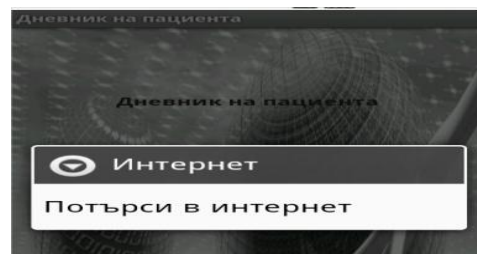


Fig. 5. "Internet" submenu

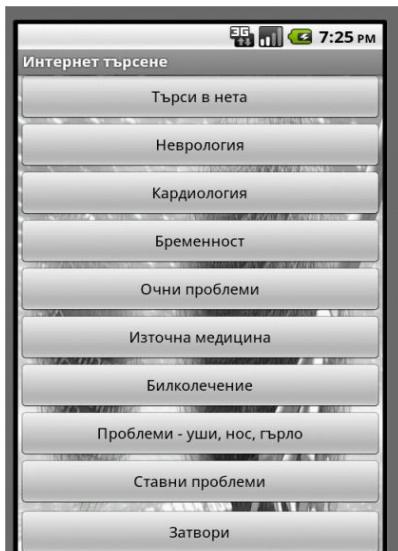


Fig. 6.1. Separate menu with list of possible choices

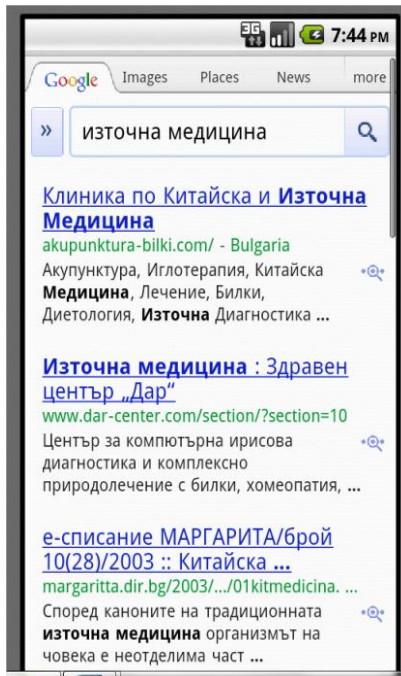


Fig. 6.2. Separate menu with list of possible choices



Fig. 7. Sub-menu "View diary"

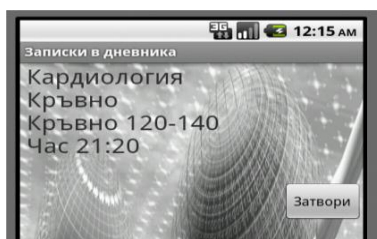


Fig. 8. The layout that displays the available records in the application

5. CONCLUSION

1. As a comparison between the „Patient's Diary” and existing medical systems, „Patient's Diary” is targeting the patients, the application is built to be used by the patient, to help both sides patient-doctor.

2. From the research that I've done, for similar to "Patient's Diary" applications from the ranking of the top 15 medical programs for mobile phones, the first five of these are directed to work with the medical staff and like my application was not elaborated

3. The system is friendly and flexible, used for distance monitoring if the patient by himself, using GSM.

4. The number of different parameters that are been monitoring depends in the patient illness and can be increased.

References

- [1] R.Meier, "Professional Android Application Development", Wrox, London, 10-08.
- [2] R.Rogers, J.Lombardo and Z.Mednieks, "Programming with the Google SDK", Shroff Publishers & Distributors Pvt Ltd, 01-10

EXPERIMENTAL INVESTIGATION ON COMPUTER RESTORATION OF FREQUENCY SPECTRUM OF ECG – SIGNALS IN THE CASE OF INFLUENCE OF NOISE

Tzveta Dimitrova, Lidia Jordanova

Technical University of Sofia
 Faculty of Telecommunication, Technical University of Sofia,
 8, Kl.Ohridski, str.1000 Sofia, Bulgaria
 Email: Tz.Dimitrova@tu-sofia.bg, jordanova@tu-sofia.bg

Abstract

Electrocardiographic signals are essential in medical diagnostic a wide range of pathologies in medicine. Therefore, there are stringent requirements for reliability in the transmission of these signals in any communications system. In this context, methods for improving the quality of transmitted medical information are up to date in the construction of modern communication system environments. Experimental studies on possibility for restoration of frequency spectrum of ECG signals using mathematical method of Eisenberg are described in the paper.

1. INTRODUCTION

As a result of the research was proposed theoretical expression (1), which serves as the basis for the construction of algorithms for computer restoration of frequency spectrum of ECG signals in the case of influence of noise using interpolation.

$$\dot{S}(\omega) = \lim_{m \rightarrow \infty} \sum_{k=1}^m \dot{S}(\omega_k) \frac{2i\sigma}{\omega - \omega_k + 2i\sigma} \times \prod_{j=1 \wedge j \neq k}^m \frac{(\omega - \omega_j)(\omega_k - \omega_j + 2i\sigma)}{(\omega - \omega_j + 2i\sigma)(\omega_k - \omega_j)}, \quad (1)$$

where:

$\{\omega_k\}$ is limited number of frequencies that are known spectral components of the signal; ω is an ongoing, random frequency value for which the calculated value of the spectral function $\dot{S}(\omega)$ inside the interval of recovery of the signal spectrum;

$\sigma > 0$ is a parameter which depends on the accuracy in the process of restoration of spectrum of the ECG signal;

m is the number of preliminary known spectral components of the signal;

j and k are integers (counters).

2. ALGORITHM FOR COMPUTER RECOVERY OF SPECTRUM OF ECG-SIGNALS IN THE CASE OF INFLUENCE OF NOISE BY INTERPOLATION

Figure 1 shows the proposed algorithm for computer recovery of spectrum of ECG-signals in the

case of influence of noise by interpolation on the basis of equation (1). Compared to extrapolation, interpolation is more accurate and faster method of recovering signals. In this case, the optimal ratio between the number m of known components $\dot{S}(\omega_k)$ and coefficient σ , determining the accuracy of the calculations according to the equation (1) is not as important and time-consuming, since above certain values results differ after the fourth decimal place. The explanation for this stems from the fact that in mathematics task of interpolation is considered correct. In the case of interpolation interval Passed ECG signal has no major delays because the value of the coefficient σ is calculated once, then its value is used for all frequency components undergoing restoration.

3. EXPERIMENTAL INVESTIGATIONS

Experiments were conducted with real ECG signal representing the normal sinus rhythm of 40-year-old man without any apparent arrhythmia. Signal duration is about 18 hours, but for the purposes of this experiment, we used only small parts of this time interval. Was conducted utilizing a series of experiments using the algorithm (Fig.1) for t interpolation of the spectrum.

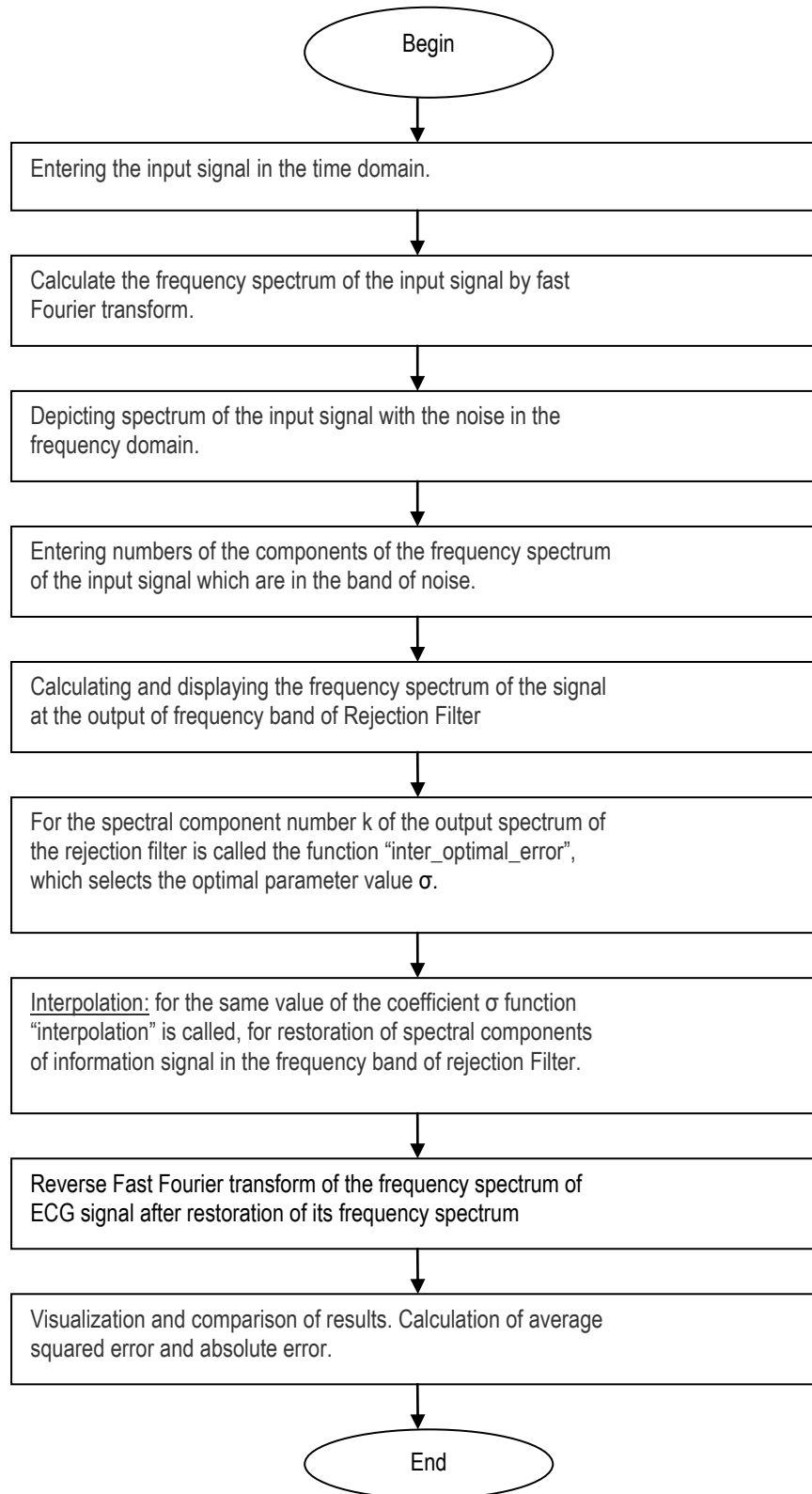


Fig. 1. Algorithm for restoration

Experiment 1. In Fig. 2 and Fig. 3 are shown the experimental results of fragment ECG signal with duration 1s (a total of 128 points, the discrete frequency is 128 Hz) and 10 components for recov-

ery (from 20Hz to 29 Hz). The resulting average squared error is 0.0053 and the maximum absolute error is 1.6623. The coefficient σ was taken with a value 0.0144.

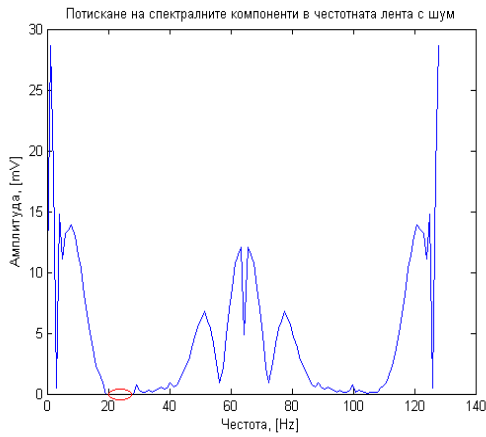


Fig. 2. Frequency spectrum $\hat{S}_R(\omega)$ of output signal of rejection filter

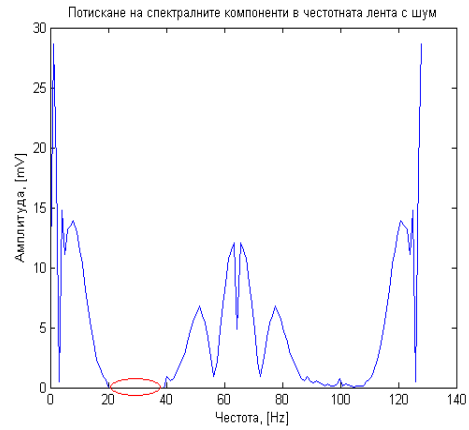


Fig. 4. Frequency spectrum $\hat{S}_R(\omega)$ of output signal of rejection filter

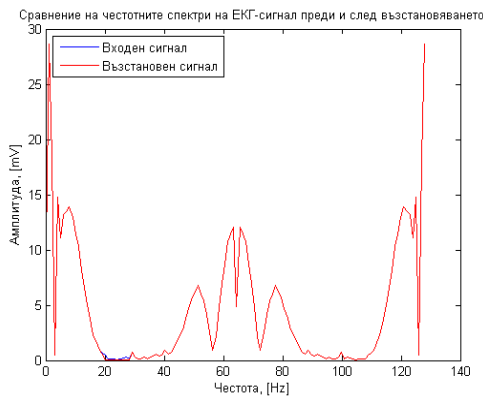


Fig. 3a. Spectral functions of input signal $\hat{S}_{in}(\omega)$ and output signal $\hat{S}_a(\omega)$

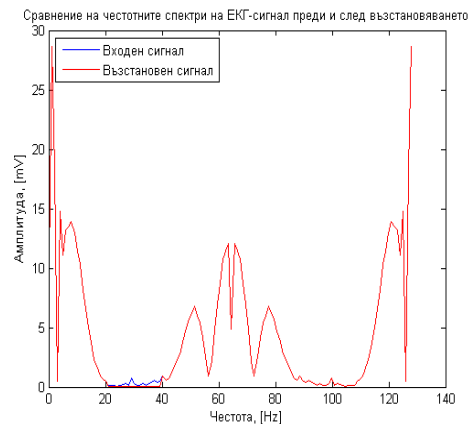


Fig. 5a. Spectral functions of input signal $\hat{S}_{in}(\omega)$ and output signal $\hat{S}_a(\omega)$

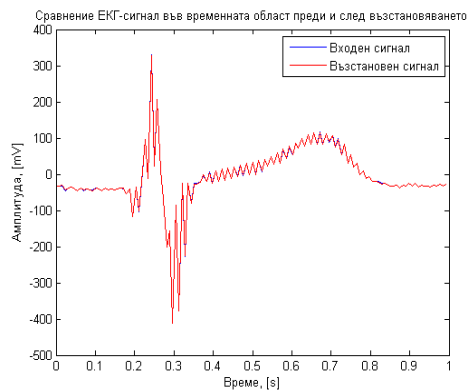


Fig. 3b Function of input signal $s_{in}(t)$ and output signal $s_a(t)$ in time

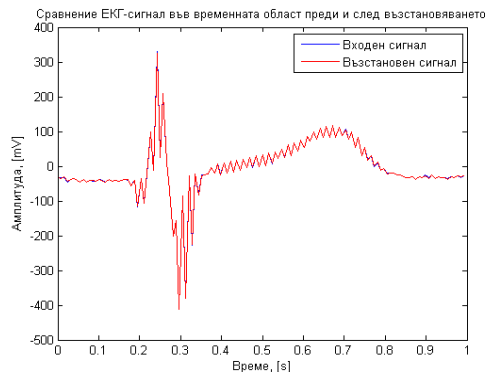


Fig. 5b. Function of input signal $s_{in}(t)$ and output signal $s_a(t)$ in time

Experiment 2. In Fig. 4 and Fig. 5 are shown the results for the same length of EKG-signal (1s), but with an increased number of spectral component for recovery (from 21 Hz to 40 Hz). It is clear that average square error increases to 0.0138, expanding the frequency band of noise even other conditions would be the same. The maximum absolute error is also increased to 4.1949, but the results continue to be relatively good. Coefficient σ has a value of 0.0134.

Experiment 3. In this case, the length of the interval of the ECG signal is taken 10s, a noise band width is narrow (75 to 80 Hz). The results show that the computation time increases due to the increased number m of known frequency components, which is understandable given the expression (1). In this case, the amplitudes of the spectral components in the band of the Restoration are small and therefore the average squared error is small. It's 0.0767. For maximum absolute error should I obtain 29.2536. The calculations are made for parameter σ value 0.002.

Experimental results on amplitude-frequency spectrum of the ECG signal are shown in Fig. 6 and Fig.7.

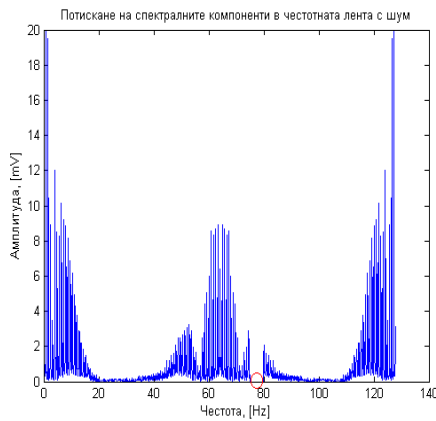


Fig. 6. Frequency spectrum $\hat{S}_R(\omega)$ of output signal of rejection filter

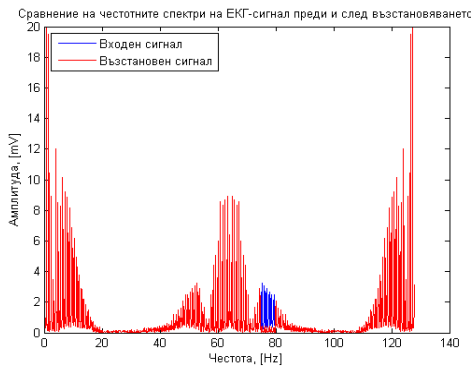


Fig. 7a. Spectral functions of input signal $\hat{S}_m(\omega)$ and output signal $\hat{S}_a(\omega)$

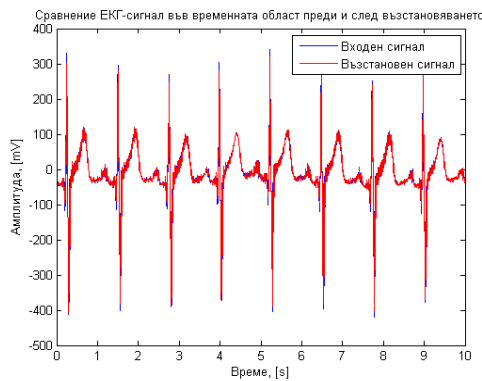


Fig. 7b. Function of input signal $s_{in}(t)$ and output signal $s_a(t)$ in time

4. CONCLUSIONS

1. Interpolation gives relatively good results on the recovered amplitude-frequency spectrum, even if not calculated the optimal value of the coefficient σ . This reduces the computation time according to the algorithm in Fig. 2, and increasing of the error is small. This is a very great potential to improve the performance of the digital filter, which works on the basis of the equation (1) and algorithm on fig. 2. For

example, in the recovery of 10 spectral components of the finite ECG signal with duration of 1s and frequency band (from 100 Hz to 110 Hz), $\sigma = 0.0001$, the average square error is 0.0009 and the maximum absolute error is 4.2787.

2. In many cases, because of difference between amplitudes of the various components of the amplitude-frequency spectrum of the ECG-signal, a precise and accurate results can be obtained by pre-determining the optimal parameter σ value.

3. Theoretically the optimal parameter value σ should be calculated in advance for calculating each spectral component in the band interpolation according to the equation (1). Then the results would be very accurate and this would enhance significantly the quality of transmitted information at the output of digital filter, but the price for this would drastically reduce the performance of the said digital filter, especially when processing signals have a wide frequency band noise. Of course this is a typical problem of the digital filters. This problem did not stop digitization of communication systems through the use of ever faster microprocessors.

4. Theoretically, this estimation of the parameters is necessary. However, as seen from the above experiments, sometimes it's permissible to avoid pre-optimization of parameter σ in the process of interpolation. This is due to the fact that the task of interpolation is mathematically correct.

5. APPENDIX AND ACKNOWLEDGMENTS

The research described in this paper is supported by the Bulgarian National Science Fund under the contract No ДДВУ 02/74/2010.

References

- [1] Айзенберг Л. А., Экстраполяция функций, голоморфных в произведение полуплоскостей или полос. Аналитическое продолжение спектра, Докл. АН СССР, 1986, т.290, N 2, с.265-268.
- [2] Айзенберг Л. А., Б. А. Кравцов, Вчислительный эксперимент по аналитическому продолжению спектра Фурье одномерных финитных сигналов, АН СССР, Инст. физики им. Л. В. Киренского, 1987.
- [3] Айзенберг Л. А., Экстраполяция функций, голоморфных в произведение полуплоскостей или полос. Аналитическое продолжение спектра, Сиб. мат журнал, июль - август 1988.
- [4] Айзенберг Л. А., Кравцов Б. А., Шаймкулов Б. А., Оценка устойчивости для интерполяции сигналов с финитным спектром Фурье и виислительным эксперимент., "Автометрия", бр.4 1989.
- [5] Айзенберг Л. А., Димиев С. Г., Маринов М. С., Комплексен анализ и някои негови приложения, ТУ-София, 1992

A REGION GROWING SEGMENTATION ALGORITHM BASED ON CLAHE AND WAVELET TRANSFORMATION FOR ULTRASOUND IMAGES

Veska M. Georgieva

Faculty of Telecommunications, Technical University of Sofia, Bulgaria
1000 Sofia, "Kl. Ohridsky" str. 8
T. (+359 2) 965-3293; E-mail: vesg@tu-sofia.bg

Abstract

Segmentation of medical images using region growing technique is a popular method because of its ability to involve high-level knowledge of anatomical structures in seed selection process. Due to its non-invasive nature and easily portable devices, ultrasound imaging is nowadays used for the diagnostic and clinical studies of many diseases. The quality of ultrasound (US) images is very important by detection of some pathological modifications in a body structures and tissues. This paper presents an approach for US image segmentation of internal organs. As element of stage for pre-processing is used enhancement, based on contrast limited adaptive histogram equalization (CLAHE), following by noise reduction, based on the Wavelet Packet Decomposition (WPD).

Implementation results are given to demonstrate the visual quality in the perspective of clinical diagnosis.

1. INTRODUCTION

Among all other imaging techniques like Computer Tomography (CT), Magnetic Resonance imaging (MRI), US imaging is cheap, non-invasive and does not emit any radiation. But CT and MRI images are taken in well defined planes and the organs in the images are more homogeneous and so are much easy to segment as compared to US image. US images contain speckle noise, attenuation artifacts and organs don't appear homogeneous so it is difficult to be segmented. Many challenging methods have been adopted for proper segmentation of US images [1],[2].

In the paper is presented one approach based on CLAHE for contrast enhancement and noise reduction on the base of wavelet packet decomposition as stages of preprocessing.

To improve the diagnostic quality of the medical objects some parameters of the wavelet transforms are optimized such as: determination of best shrinkage decomposition, threshold of the wavelet coefficients and value of the penalized parameter of the threshold. This can be made adaptively for which image on the base of calculation and estimation of some objective parameters. For US image segmentation is used a region growing technique because of its ability to involve high-level knowledge of anatomical structures in seed selection process.

2. CLAHE FOR CONTRAST ENHANCEMENT

Contrast limited adaptive histogram is a technique utilized for improving the local contrast of images. CLAHE does not operate on the whole image works like ordinary Histogram Equalization (HE), but it works on small areas in images, named tiles. Each tile's contrast is enhanced, so that the histogram of the output area roughly matches the histogram determined by the 'Distribution' parameter. This parameter can be selected depending on the type of the input image. The adjacent tiles are then combined using bilinear interpolation to eliminate artificially induced boundaries. The contrast, particularly in homogeneous regions, can be limited to avoid amplifying any unwanted information like noise which could be existed in images. The algorithm CLAHE limits the slope associated with the gray level assignment scheme to prevent saturation. The CLAHE method can be divided into steps to achieve as following [3]:

- The US image is divided into contextual regions which are continuous and non-overlapping. Each contextual region size is $M \times N$ pixels;
- The histograms of each contextual regions are calculated;
- The histograms of each contextual region are clipped.

For limiting the maximum slope is to use a clip limit β to clip all histograms. This clip limit can be

related to what is referred to as clip factor, α in percent, as follows (1), [4]:

$$\beta = \frac{MN}{L} \left[1 + \frac{\alpha}{100} (S_{\max} - 1) \right] \quad (1)$$

where α is a clip factor, $M \times N$ are numbers of pixels of each region and L are the number of gray-scales;

Finally, cumulative distribution functions (CDF) of the resultant contrast limited histograms are determined for grayscale mapping. The result mapping at any pixel is interpolated from the sample mappings at the four surrounding sample grid pixels. The procedure of CLAHE can be applied to Y component of the selected image that is processing in YUV system as more effectiveness.

3. NOISE REDUCTION

3.1. Noise model in US images

In an US image contained additive Gaussian white noise the basic model for each pixel is as follows (2) [5]:

$$s(x, y) = f(x, y) + n(x, y) \quad (2)$$

where $f(x, y)$ is the desired image, without noise, $n(x, y)$ is $N(0,1)$ noise.

As speckle noise is proportional to the desired signal it is generally modeled as multiplicative noise (3):

$$s(x, y) = f(x, y).n(x, y) \quad (3)$$

where $f(x, y)$ is the desired image, without noise, $n(x, y)$ is the noise.

Logarithmic transformation of a US image converts the multiplicative noise model to an additive noise model (4):

$$\log(s) = \log(f) + \log(n) \quad (4)$$

Our goal is to extract f and reduce the noise n .

3.2. Noise reduction based on WPD

The next stage of the algorithm is noise reduction. It is based on the wavelet packet transform [6]. Based on the organization of the wavelet packet

library, it can be determinate the decomposition issued from a given orthogonal wavelets. The classical entropy-based criterion is a common concept for finding on optimal decomposition. It's looking for minimum of the criterion from three different entropy criteria: the energy of the transformed in wavelet domain image, entropy by Shannon and the logarithm of the entropy by Shannon. By looking for best shrinkage decomposition to noise reduction two important conditions must be realized together. They are the conditions (4) and (5):

$$E_K(S) = \min, \quad \text{for } K = 1, 2, 3 \dots n \quad (4)$$

where E_K is the entropy in the level K for the best tree decomposition of the image s

$$s_{ij} \geq T \quad (5)$$

where s_{ij} are the wavelet coefficients of s in an orthonormal basis, T is the threshold of the coefficients.

By determination of the threshold it is used the strategy of Birge-Massart. This strategy is flexibility and used spatial adapted threshold that allows to determinate the threshold in three directions: horizontal, vertical and diagonally. Choosing the threshold too high may lead to visible loss of image structures, but if the threshold is too low the effect of noise reduction may be insufficient. The procedure for noise reduction can be determined on the base of some calculated estimation parameters [6].

4. SEGMENTATION

Region growing is one of the simplest approaches to image segmentation; neighboring pixels of similar amplitude are grouped together to form a segmented region. However, in practice, constraints, some of which are reasonably complex, must be placed on the growth pattern to achieve acceptable results [7].

5. EXPERIMENTAL PART

The formulated stages of processing are realized by computer simulation in MATLAB 7.12 environment by using IMAGE PROCESSING TOOLBOX and WAVELET TOOLBOX. In analysis are used 20 grayscale US images from abdominal organs with size 640x480 pixels. Some results from

simulation, which illustrate the working of proposed algorithm, are presented in the next figures below. In Fig. 1 is shown the original US image of size 640x480 pixels with stone of GB Neck. In Fig. 2 is presented the result of CLAHE preprocessing. In Fig. 3 is shown the US image after CLAHE and noise reduction based on WPT. In Fig. 4 is illustrated the result of segmentation by proposed approach. It presented better the located stone of GB Neck and its boundaries.



Figure 1. Original US image



Figure 2. US image after CLAHE



Figure 3. US image after CLAHE and noise reduction



Figure 4. US image after segmentation

6. CONCLUSION

In the paper is presented a new approach to US image segmentation on the base of wavelet packet decomposition. The proposed approach combines CLAHE with noise reduction to achieve better results for segmentation of different objects in the ultrasound images. The implemented studying and obtained results by using of real images attempt to make diagnostic more precise.

The proposed approach can be demonstrated by studying of medical image processing in engineering and medical education.

Acknowledgments

This paper was supported by the Joint Research Project Bulgaria-Romania (2010-2012): "Electronic Health Records for the Next Generation Medical Decision Support in Romanian and Bulgarian National Healthcare Systems", DNTS 02/19.

References

- [1] A. Khana, M. Sood, S. Devi, "US Segmentation based on Expectation Maximalization and Gabor Filter", *International Journal of Modeling and Optimization*, Vol.2, №3, 2012, pp.230-233.
- [2] J.A. Noble, "US Image Segmentation: A Survey", *IEEE Transactions on Medical Imaging*, Vol.25, №8, 2006, pp.175-180.
- [3] Z. Xu, X. Lin, X. Chen, "For removal from video sequences using contrast limited histogram equalization", *Proceedings of the International Conference on Computational Intelligence and Software Engineering*, IEEE Xplore Press, Wuhan, 2009, pp.1-4.
- [4] Ali M. Reza, "Realization of CLAHE for Real-time Image Enhancement", *Journal of VLSI Signal Processing*, Vol. 38, Kluwer, 2004, pp.35-44,
- [5] V. Georgieva, "Edge Detection in US Medical Images using Wavelet Decomposition", *Proceedings of CEMA'10*, Athen, Greece, 2010, pp.108-111.
- [6] V.Georgieva, R. Kountchev, "An influence of the wavelet packet decomposition on noise reduction in ultrasound images", *Proceedings of ICES'06*, Sofia, Bulgaria, 2006, pp.185-188.
- [7] Sheng-Chih-Yang, Chuin-Mu Wang, Yi-Nung Chung, Giu-Cheng Hsu, San-Kan Lee, Pau-Choo Chung and Chein-1 Chang "A Computer Aided System for Mass Detection and Classification in Digitized Mammograms", *Biomedical Engineering-Applications, Basis and Communications*, 2005, vol. 17, No.5, pp. 215-228.

GUI FOR SEGMENTATION OF MEDICAL IMAGES

Veska M. Georgieva

Faculty of Telecommunications, Technical University of Sofia, Bulgaria
1000 Sofia, "Kl. Ohridsky" str.8
T. (+359 2) 965-3293; E-mail: vesg@tu-sofia.bg

Antonia D. Nankova

Faculty of German Engineering Education and Industrial Management, Technical University of Sofia, Bulgaria
1000 Sofia, "Kl. Ohridsky" str.8
E-mail: antonianankova@gmail.com

Abstract

In the paper is presented software for segmentation of medical images and its graphic user interface (GUI). It works in the MATLAB environment and uses IMAGE TOOLBOXES defined functions. Two basic methods for image segmentation such as region-growing and split & merge algorithms are used, regarding to process different medical modalities of the images. The GUI proposes also an interactive option to choose region of interest (ROI) in the processed image and some parameters of the applied methods.

The proposed GUI can be applied to real medical images attempt to make diagnostic more precise. The presented GUI is suitable also to engineering education for studying of this processing.

1. INTRODUCTION

The medical images provide important anatomical information to physicians and specialist upon which can be made diagnoses [1]. Segmentation is a classical problem in image processing; it can be described as the process of partitioning an image into a set of non-overlapping homogeneous regions. The goal of segmentation is to simplify and to change the representation of an image into something that is more easier to analyze. Image segmentation is typically used to locate objects as organs and tumors and their boundaries (lines, curves, etc.) in medical images. This is a process of assigning a label to every pixel in an image such that pixels with the same label share certain visual characteristics. Region growing is one of the simplest approaches to image segmentation; neighboring pixels of similar amplitude are grouped together to form a segmented region. However, in practice, constraints, some of which are reasonably complex, must be placed on the growth pattern to achieve acceptable results [2]. Split and merge segmentation techniques are based on a quad tree data representation whereby a square image segment is broken (split) into four quadrants if the original image segment is no uniform in attribute. If four neighboring squares are found to be uniform, they are replaced (merge) by a single square composed

of the four adjacent squares [3]. This approach tends to be computationally intensive.

The software is created in MATLAB 7.12 environment by using IMAGE PROCESSING TOOLBOX.

The graphic user interface consists of checkboxes, buttons, edit boxes, pop-up controls, which make it easy to use. Users enter or choose input data in a single form, because input information changes and visualizations are easier and faster in this way. The processed image can be saved on the disk and so can be used to another processing or its visualization.

2. THE GUI FOR SEGMENTATION OF MEDICAL IMAGES

The GUI for region segmentation of medical images is shown on Fig. 1. It is divided in several areas, where the user applies different settings, concerning image segmentation techniques and theirs parameters and areas for universal application.

The area "Input Image Path" is for entering an image file name with an image file extension. The user can navigate among the folders in the work folder and choose image by using "Browse" button and view the image by using "View Image" button. The segmentation technique can be selected in area "Image segmentation", shown in Fig. 2.

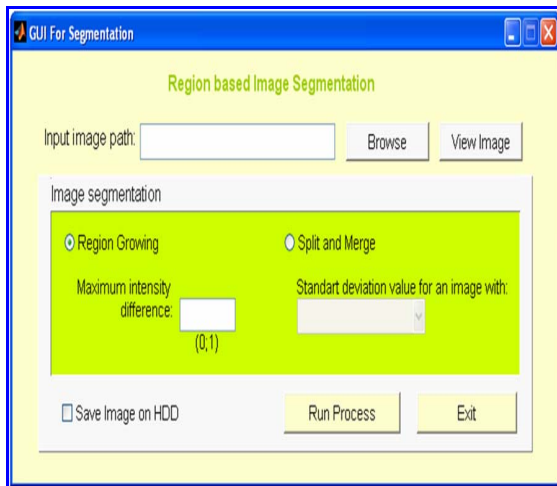


Figure 1. GUI for segmentation of medical images

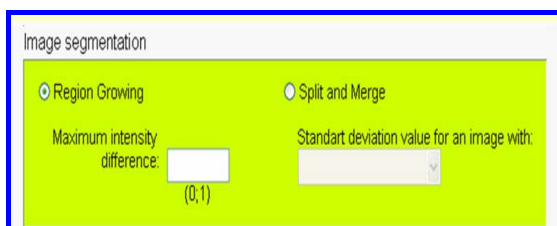


Figure 2. Area "Image segmentation"

The user can select two different segmentation techniques: region-growing and split and merge algorithms. The important parameters of these methods are maximum intensity difference (threshold) with values between 0 and 1. It can be input manually. Another parameter is a standard deviation. It is specific for the split and merge algorithm.

"Save Image on HDD" is checked to save results in image files in 'jpg' format. After choosing all input information the procedure of processing begins, when the user clicks on button "Run Process". Then the final result is shown – original image, and processed images. When button "Exit" is pressed the program can be closed.

3. TASKS CARRIED OUT FROM THE MAIN PROGRAM

The basic algorithm that works behind is shown in Fig. 3.

By acting of component from GUI can be implemented a callback-function from the main program. Every graphic component can be treated to object. Every object can be referred to handle. The objects referred a complex of attributes, which can be manipulated from the software. The multifarious attributes can be leaved for using in MATLAB environment, such as "Enabled", "Value", "Visible", "On", "Off" etc. [4]. Every attribute can be enabling in the

presence of corresponding handle or reference to the object. Every graphic component can be reiterated to a cycle of events for the MATLAB environment by initialization of the graphic application. It submits addresses of the callback-functions, associated to a given event, which are important. By its identification can be called out a corresponding callback-function. One of the important tasks that the main program has is input data validation. The execution is canceled if an error concerned with wrong information occurs. Another essential purpose of the main program is presenting the input information in appropriate data structures. It is necessary for the next steps in the processing strategy, in this step the processing is made with appropriate input data. Wrong information prevents segmentation from carrying out or may lead to wrong output.

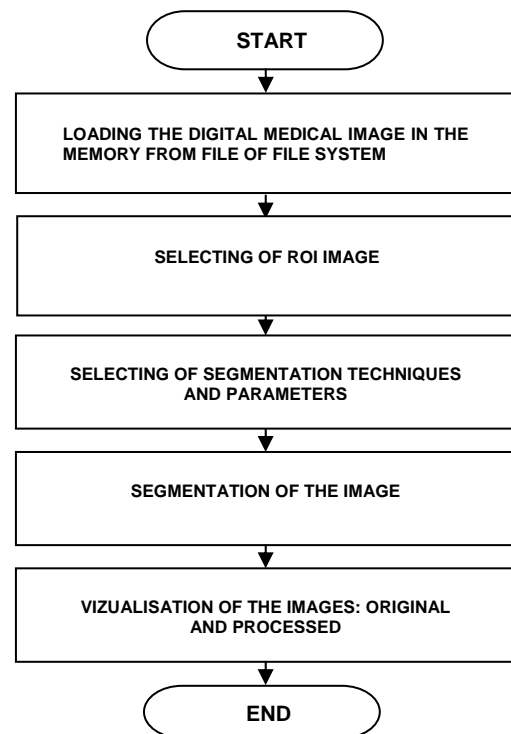


Figure 3. Block diagram of the algorithm

Some results from simulation, which illustrate the working of the program, are presented in the next figures below. In Fig.4 is shown the original CT image of size 650x650 pixels from abdominal organes.

In Fig.5 are presented the selected CT ROI image of size 460x375 pixels from spleen and its modifications, obtained by region growing and split & merge region segmentation algorithms. The best result is obtained for the value 0.2 of the parameter threshold by region growing algorithm. The value of standard deviation by split and merge algorithm is defined in the case of better contrast.



Figure 4. Original CT image

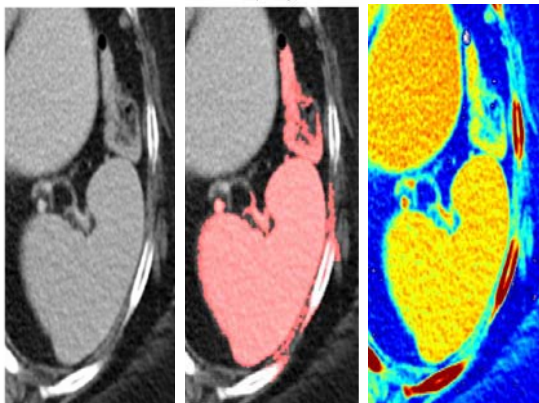


Figure 5. CT ROI image and its modifications obtained by region growing and split & merge algorithms

In Fig. 6 is presented only the segmented spleen extracted from whole CT image of abdominal organs, obtained by region growing algorithm.



Figure 6. Segmented CT image with extracted spleen

4. CONCLUSION

In the paper is presented a GUI for region segmentation of medical images. It uses MATLAB defined function and works in MATLAB 7.12 environment. The processing can be used to locate objects as organs and tumors and their boundaries by using of region growing and split and merge algorithms. The GUI can be used in engineering education for studying this process. It can be used also in real time to provide important anatomical information in medical images to physicians and specialist upon which can be made diagnoses of different diseases. The results by segmentation of sequences of CT images can be used for future application in 3D visualization.

Acknowledgments

This paper was supported by the Joint Research Project Bulgaria-Romania (2010-2012): "Electronic Health Records for the Next Generation Medical Decision Support in Romanian and Bulgarian National Healthcare Systems", DNTS 02/19.

References

- [1] M. Smith, A. Docef, "Transforms in telemedicine applications", Kluwer Academic Publishers, 1999.
- [2] Sheng-Chih-Yang, Chuin-Mu Wang, Yi-Nung Chung, Giu-Cheng Hsu, San-Kan Lee, Pau-Choo Chung and Chein-1 Chang "A Computer Aided System for Mass Detection and Classification in Digitized Mammograms", Biomedical Engineering-Applications, Basis and Communications, vol. 17, No.5, pp. 215-228, 2005.
- [3] W. Pratt, "Digital Image Processing", John Wiley & Sons Inc., 2001.
- [4] MATLAB User's Guide. Accessed at: www.mathwork.com

PROCESSING AND TRANSMISSION OF EEG SIGNALS

Dejan Milev

Faculty of Telecommunications, Technical University of Sofia, Bulgaria
1000 Sofia, "Kliment Ohridski" str.8
E-mail: dmilev@tu-sofia.bg

Abstract

Relations between spatial attention and motor intention were investigated by means of an EEG potential elicited by shifting attention to a location in space as well as by the selection of a hand for responding. High-density recordings traced this potential to a common front parietal network activated by attention orienting and by response selection. Within this network, parietal and frontal cortex were activated sequentially, followed by an anterior-to-posterior migration of activity culminating in the lateral occipital cortex. Based on temporal and polarity information provided by EEG, we hypothesize that the front parietal activation, evoked by directional information, updates a task-defined preparatory state by deselecting or inhibiting the behavioural option competing with the cued response side or the cued direction of attention. These results from human EEG demonstrate a direct EEG manifestation of the front parietal attention network previously identified in functional imaging.

1. INTRODUCTION

The methods in examining brain diseases are improving continuously in recent years. Due to the advantages of non-invasive measurement and the capability of long term monitoring of the EEG signal, the electroencephalograph machine plays an important role in brain examination and study, question system would be enhanced significantly.

The one of purposes of this study is to improve the conventional architecture of electroencephalograph. In this work, a multi-channel EEG recording system is proposed. The Bluetooth module is adopted as transmission interface such that the wire lines between the EEG acquisition circuit and computer interface are removed. This also avoids serious signal distortion and provides better quality

EEG signals. Owing to the features of energy-saving and easy development, the TI-MSP 430 chip is utilized for serving as core processor in the digital circuit.

Therefore, the digital filter can be implemented in the digital circuit to filter out the noise from the EEG signal and make the electroencephalogram reproduce with low distortion. Using the system, the non-successive brain activities such as epilepsy, sleeping disorder and abnormal behaviour can be measured. To provide an effective EEG reading program on PC or

PDA, a simple but effective classification process of the EEG signal is conducted. Under the condition of long-term recording of EEG signal, the activities of penitent always cause disturbance dur-

ing observation. To achieve correct reading for EEG signals it is necessary to develop a specific algorithm to perform signal processing tasks. Therefore, this work divides the processing task for recorded EEG signal into subtask including segmentation, characteristics extracting, and clustering. A modified bisecting means algorithm is also proposed to classify the EEG signals into simple and understandable groups of waveforms. For doctors or researchers, this algorithm is applicable to syndrome diagnosis from the acquired specific EEG signal of sleeping and can facilitate the follow-up study of brain diseases.

Once the EEG signals had been acquired, they were converted by ADC circuit into digital form and then pre-filtered by the digital filter built-in MSP 430 chip. These pre-processed data remove the outliers and make subsequent signal clustering task easier and better. The processed signals are transmitted to the back-end via the Bluetooth module. The proposed classification algorithm is applied to the recorded signals to execute off-line analysis, which is described in detailed as follows.

2. MAIN TEXT

Electroencephalography (EEG) has long been used as a standard tool to localize the sources of brain electric activity.

Nevertheless, this technique shows limitations in the spatial resolution with which these sources can be localized as well as difficulties related to non-

existence of a unique solution to the EEG Inverse Problem (IP). ([1]–[2]).

Once the EEG signals had been acquired, they were converted by ADC circuit into digital form and then pre-filtered by the digital filter built-in MSP 430 chip. These pre-processed data remove the outliers and make subsequent signal clustering task easier and better. The processed signals are transmitted to the back-end via the Bluetooth module. The proposed classification algorithm is applied to the recorded signals to execute off-line analysis, which is described in detailed as follows. The characteristic matrices of the whole EEG signals consist of frequencies and amplitudes features in each small EEG segment. Finally, the characteristic matrices were treated as input to the modified bisecting k-means algorithm, which can classify EEG segments that possess similar features to the same group. For easier identification, the grouped segments are highlighted in a fashion of color-marked presentation.

The segmentation, feature extraction, and classification of pre-processed EEG data complete the signal clustering task. The flow chart of EEG signal classification is illustrated in right hand side of Fig. 1.

The EEG signals in various time points possess different statistic feature. This means that the EEG signal is a

A detailed introduction of segmentation, characteristic extraction, and sequence of classification are described in the following

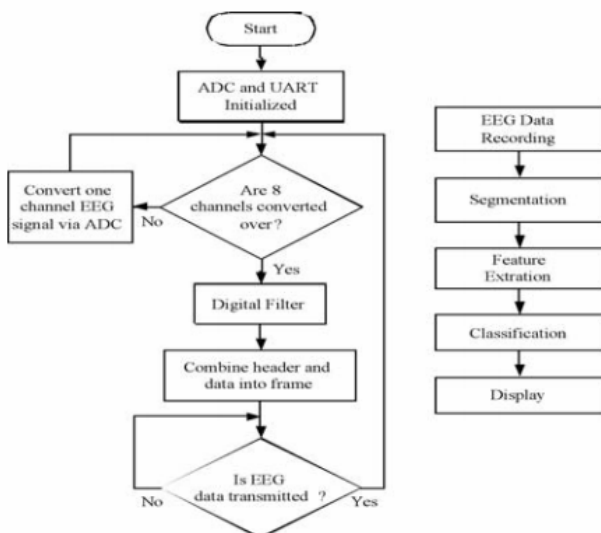


Fig. 1. Flowchart for EEG signals processing from data acquisition to classification

Signal segmentation is usually based on the energy and frequency of signal [7-8], and the difficulty mainly comes from that the energy and frequency

may vary simultaneously. In general, the EEG signal changes due to different physiological and psychological status, and is called a time varying signal. Therefore, for analysis of the EEG, the signal has to be divided according to its characteristics.

3. ILLUSTRATIONS

An EEG signal is usually acquired through silver-chloride covered electrodes, though sometimes other materials like pure silver, tin, steel or gold are used. The signal amplitude is only a few microvolt and needs to be amplified several thousand times before it can be captured. Because it is faint, the signal can very easily drown in noise, particularly 50/60Hz hum from the mains which is transmitted capacitive (i.e. by an electric field) from the wiring in your house.

To handle this, the signal is first amplified by a high quality instrumentation amplifier, which measures the voltage difference between two locations on the scalp. In the example in the previous section, we used C3 and P3. This ensures that a large percentage of the mains hum never enters the system, because the level of the mains hum on those two locations is essentially the same. Afterwards the signal strength is increased further by normal amplifiers, and passed through a low-pass filter which minimizes distortion caused by so-called aliasing that may occur when the signal is converted to digital samples. Below is the block diagram of one EEG amplifier channel, and the Right-leg driver (DRL-circuit).

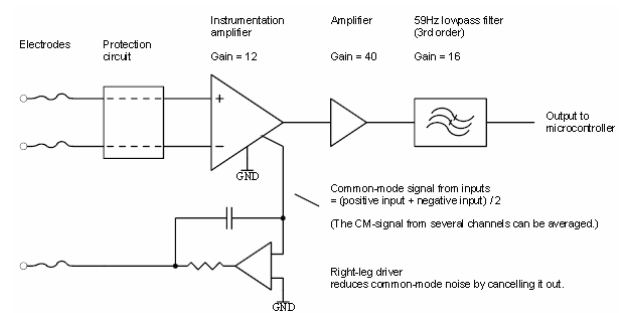


Fig. 2. Simplified block diagram of the ...

Some parts are not included here. The schematic gives you all the details if you are interested.

The EEG signal is picked up by the two topmost electrodes and passed through the protection circuit. It serves two purposes: First, it protects the circuitry from electrostatic discharge (ESD) and second it protects the user from failing circuitry. Leaving the protection circuit, the signal enters the

instrumentation amplifier where it is amplified 12 times. After that, the signal is amplified about 40 times in a second amplifier stage. You can't see it in the diagram, but there is a reason for splitting the amplification into two steps like this. Between the two stages there is a high-pass filter which removes DC-voltage offsets. Some electrode materials, such as gold or steel, are polarization. This means that electric charge can accumulate on the surface of the electrode, building up a relatively large DC-voltage, sometimes several hundred mill volts if you are unlucky. In theory, you would amplify a 200mV signal 480 and get a 96 volt output. In reality, the circuitry can handle about 2.5V so the output signal would be stuck at a maximally high or low level, usually +/- 2.5V and not contain any EEG. The high pass filter tries to solve this problem. Finally, the signal is amplified 16 times more and low pass filtered. The filtering is done to prevent aliasing effects later on, when the signal is digitized. Below the signal amplifiers, and the filter, sits a third amplifier pointing the other way, seemingly sending a signal to the user. This is the right-leg driver. It is named like this for historical reasons. The driver is, and was, previously only used by ECG meters, which measures the electrical activity in the heart. During ECG sessions, the driver (also abbreviated DRL, for Driven Right Leg) is attached to the right leg, as far away from the heart as possible. The purpose of the DRL is to reduce common-mode signals such as 50/60Hz mains hum, by cancelling them out. It replaces a ground electrode which older EEG designs use, and can attenuate mains hum up to 100 times more than the instrumentation amplifier can do by itself. After the filtering, the signal is ready for acquisition by the analog-to-digital converter which in our case is located inside a microcontroller. The microcontroller sends the digitized EEG to a PC via a standard serial cable. To protect the user from electrical faults, the EEG device is electrically isolated from the PC and external power sources. The block diagram below shows this.

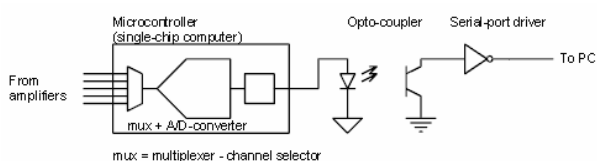


Fig. 3. Simplified block diagram of the Modular EEG microcontroller, opt coupler and RS232 interface.

4. CONCLUSION

The architecture of Bluetooth wireless multi-channel EEG recording system is studied in this paper. The wireless transmission mechanism eliminates wire-line connections. Also, the signal filtering and digitization in the system reduce the possible noise interference. In contrast with the current EEG recording systems, such improvements make this multi-channel EEG signal measuring system more applicable to studying on non-consecutive brain diseases. To verify the practicality of the proposed system, a sinusoidal testing signal is transmitted via the Bluetooth module.

References

- [1] Analog Devices "AD7716", Rev A, 1995 Available: http://analog.com/UploadedFiles/Data_Sheets/9287474ad7716.pdf
- [2] Jun Li, Sharp. Interfacing a MultiMediaCard to the LH79520 System-On-Chip, <http://sharpsma.com/pub/productfocus/publications/>
- [3] micro/mcu/tec_appnote_LH79520_multimediacar.pdf
- [4] Texas Instruments. MSP430x1xx Family User's Guide, <http://focus.ti.com/lit/slau049.pdf>
- [5] SD Card Association. <http://sdcard.org/>.
- [6] D. A. Peredina and A. Allen, "Telemedicine Technology and Clinical Applications," *JAMA*, vol. 273, 1995, pp. 483-88.
- [7] D. F. Leotta and Y. Kim, "Requirements for Picture Archiving and Communications Systems (PACS)," *IEEE EMB Mag.*, vol. 12, Mar. 1993, pp.62-69.
- [8] F. Goeringer, "Medical Diagnostic Imaging Support System for Military Medicine," *SPIE Medical Diagnostic Imaging IV: Image Capture, Formatting, and Display*, vol. 1444, 1991, pp. 340-50.
- [9] American College of Radiology, National Electrical Manufacturers Association, "Digital Imaging and Communications in Medicine (DICOM): Version 3.0," Draft Standard, ACR-NEMA Committee, Working Group V], Washington, DC, 1993.
- [10] P. A. West, Private communication, Department of Family Medicine, University of Washington, Seattle, Aug. 1995.
- [11] M. A. Cawthon et al., "Preliminary Assessment of Computed Tomography and Satellite Teleradiology from Operation Desert Storm," *Invest. Radiol.*, vol. 26, 1991, pp. 854-57

METHOD AND SYSTEM FOR REMOTE MONITORING MULTIPLE MEDICAL PARAMETERS

Dejan Milev

Faculty of Telecommunications, Technical University of Sofia, Bulgaria
1000 Sofia, "Kliment Ohridski" str.8
E-mail: dmilev@tu-sofia.bg

Abstract

An integrated medical monitoring system comprising at least one patient monitor, at least one central monitor, and at least one remote access device which are tied together through an integrated communications link is disclosed. The communications between various components of the system are bi-directional, thereby affording the opportunity to establish monitoring parameters from remote locations, provide interactive alarms and monitoring capabilities, and provide data exchange between components of the system.

Remote monitoring activity based on Doppler shifts in radio signals shows promise in medical and security applications, however the problems of motion artifacts and presence of multiple subjects limit the usefulness of this technique. By applying MIMO signal processing, it is possible to overcome limitations of current systems and isolate signals from multiple sources.

1. INTRODUCTION

The performance of enterprise wireless LANs over the past few years, and especially since the introduction of 802.11n, has evolved to the point where industry analysts now expect Wi-Fi to replace wired Ethernet as the network connection of choice[1]. In this I will discuss the capabilities required to transform an 802.11n network into an Multi-purpose Medical Mobility (MMM) network. These capabilities fall into several different categories: reliability, security, versatility, scalability, upgradeability, manageability, interoperability [5].

Some systems depend on a hardwired system which requires that patients be disconnected from a monitor, connected to a mobile monitor in transit, and then reconnected to the system at new location. Furthermore, an additional monitor and often different sensor devices must be attached to the patient when the patient is in transit. These systems, therefore, are inefficient for use in clinical settings where patients are frequently transferred between various facilities [6].

Furthermore, when an emergency situation occurs, prior art systems generally require a relatively long time period to determine that an emergency has occurred and to broadcast the signal to a remote caregiver. This delay is extremely important in critical care monitoring, where a matter of seconds

can make a significant difference in the outcome of a patient experiencing a life-threatening condition [7].

Other problems associated with prior art medical alert systems include difficulties associated with controlling the broadcast of a message and difficulties associated with determining whether an emergency message has been received.

2. MAIN TEXT

The latest development in WLANs for medical applications is the 802.11n standard. Finalized include new options for even better performance, 802.11n uses Multiple Input, Multiple Output (MIMO) and other techniques to significantly increase the achieved bit rate over distance (rate-range) performance of a Wi-Fi connection [8-9].

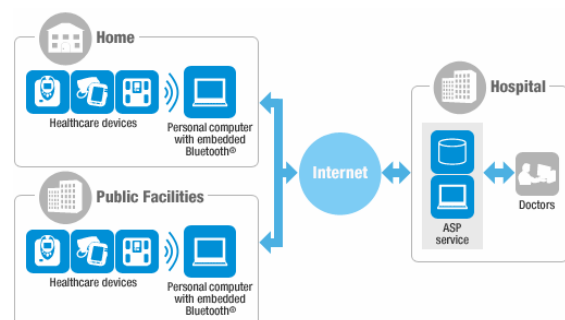


Fig. 1. Telemedicine System Service

The most significant performance improvements are due to a doubling of the channel bandwidth, from 20 to 40 Mbps, and dividing the video stream into two or more spatial streams, capable of finding separate paths from transmitter to receiver.

For healthcare organization, 802.11n increases the bandwidth available to medical applications by a factor of 5x to 7x over earlier Wi-Fi, performance surpassing a wired 100 Mbps Ethernet connection. Higher network capacity means the WLAN is more than ever suited to multi-use, multi-media traffic: new applications such as video streaming, and high-speed transmission of large files such X-ray images become much easier implement [10].

Remote sensing of heart and respiration activity by measuring Doppler shift in radio signals is a promising technique for unobtrusive health monitoring and life sensing, with proof of concept demonstrated for various applications [2-4]. When more than one target is in view, multiple transmitters and receivers providing multiple signal copies could be used to distinguish between the different sources of Doppler motion, isolate the desired signal, and determine a number of targets [11].

3. ILLUSTRATIONS

The system MIMO consisting of n_{rx} receive antennas, forming two proper linear antenna arrays. The arrays are spatially separated, for example, occupying two opposite walls in a room while facing each other (Fig. 2).

The MIMO receiver has knowledge of the pilot signals, and it applies channel estimation to learn the channel response between each transmit and receive antenna. Consequently, an estimate of the channel

$$\hat{h}_{ij} = h_{ij} + n_{ij},$$

where n_{ij} is the additive white Gaussian noise corresponding to the thermal noise. The noise has a zero-mean complex Gaussian distribution with the variance N_e given as

$$N_e |_{dBm} = 10 \log_{10}(KTB) - G_e + 30 [dBm]$$

where K is Boltzmann's constant, T is the environment temperature, B is the signal bandwidth and G_e is a gain introduced by the estimation procedure.

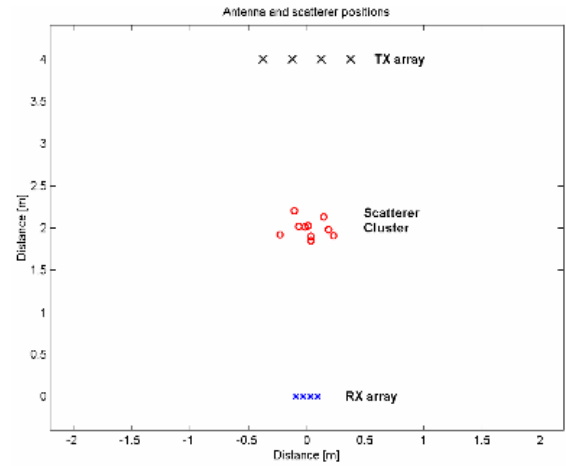


Fig. 2. A typical arrangement of Tx and Rx antennas, and cluster of scatterers that models a human body

Simulations were done for MIMO system with 4 transmit and 4 receive antennas, with the carrier frequency of 2.4 GHz, and 2λ and $\lambda/2$ separation between transmit and receive antenna elements. The two arrays are 4 meters apart. The scatterer cluster of 10 scatterers is randomly positioned, with the diameter $D=0.5m$. Based on the above assumptions, the channel response between the i th receive and j th transmit antenna ($i=1, \dots, n_{rx}$ and $j=1, \dots, n_{tx}$) is

$$h_{ij} = \sqrt{P_j} \frac{\lambda}{4\pi} \left(\frac{1}{d_{ji}} e^{i\left(\frac{2\pi}{\lambda}d_{ji}\right)} + \sum_{k=1}^{N_s} \frac{\sqrt{S_s}}{\sqrt{4\pi d_{jk}}} e^{i\left(\frac{2\pi}{\lambda}d_{jk} + \varphi_{jk}\right)} \frac{1}{d_{ki}} e^{i\left(\frac{2\pi}{\lambda}d_{ki}\right)} \right)$$

where d_{jk} the distance between transmit antenna j and scatter k , d_{ki} is the distance between scatter k and receive antenna i , d_{ji} is the distance between transmit antenna j and receive i , and finally, φ_{jk} is a random phase shift.

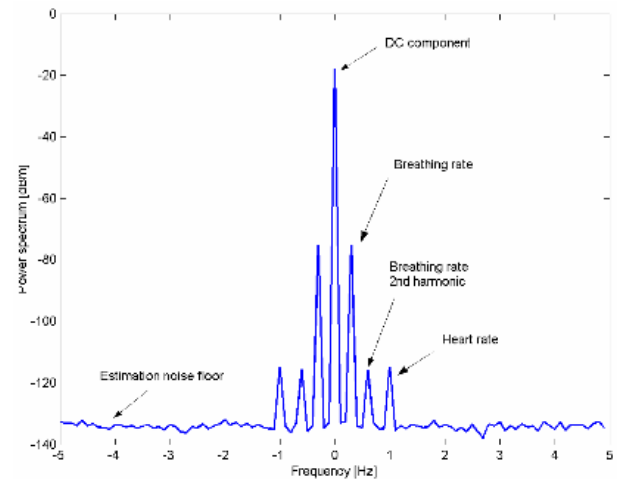


Fig. 3. The power spectrum of the channel state estimate sequence

Figure 3 shows the power spectrum of the channel state estimate sequence averaged over all transmitter-receiver pairs. The accumulative Tx power from all Tx antennas is 20 dB. The MIMO channel state sampling frequency is 10 Hz and the total of 100 samples/Rx-Tx pair is collected.

4. CONCLUSION

This paper demonstrated that Multi-purpose Medical Mobility networks can provide comprehensive network-edge connectivity with full communication reliability and end-to-end Quality of Service.

The application of MIMO systems to detection of cardiopulmonary signals resulting from Doppler shifts in radio signals. In future work the effect of different number of antennas and antenna arrangements on system performance will be investigated.

Mobility network can now reliably and securely meet the connectivity needs of all data, voice, and video applications in

Healthcare organization of virtually any size.

References

- [1] J. Pan and W.J. Tompkins, "A real-time QRS detection algorithm," *IEEE Trans. Biomed. Eng.*, vol. BME-32, pp. 230-236, 1985.
- [2] J. C. Lin, "Microwave sensing of physiological movement and volume change: a review," *Bioelectromagnetics*, vol. 13, pp. 557-565, 1992.
- [3] K. M. Chen, D. Mirsa, H. Wang, H. R. Chuang, E. Postow, "An X-band microwave life detection system," *IEEE Transaction of Biomedical Eng.*, vol. 33, pp. 697-70, 1986.
- [4] V.M. Lubecke, O. Boric-Lubecke, G. Awater, P.-W. Ong, P. Gammel, R.-H. Yan, J.C. Lin, "Remote sensing of vital signal with telecommunications signals," *World Congress on Medical Physics and Biomedical Engineering (WC2000)*, Chicago IL, July 2000.
- [5] BlueRadios, "BR-C30 Class1, Class2, and Class 3 Bluetooth ver1.2", 2005. Available: <http://www.blueradios.com/BR-C30.pdf>
- [6] Welch Allyn OEM Technologies, "ECG/Respiration ASIC: ECG 3-lead, 5 lead, 12-lead and RESP Signal Processing", (11/09/2003).
- [7] S.Yu, J Cheng, "A Wireless Physiological Signal Monitoring System with Integrated Bluetooth and WiFi Technologies", *Proceedings of the 2005 IEEE Engineering in Medicine and Biology 27th Annual Conference Shanghai, China, September 1-4, 2005.*
- [8] C. S. Patichis, E. Kyriacous, S. Voskarides, M. S. Patichis, R. Istepanian, and C. N. Schizas, "Wireless telemedicine systems: an overview," *IEEE Antennas Propag. Mag.*, vol. 44, Apr. 2002, pp.143-153.
- [9] A. Hernandez, F. Mora, G. Villegas, G. Passariello, and G. Garrault, "Real-Time ECG Transmission Via Internet for Nonclinical Applications", *IEEE Trans. Inform. Technol. Biomed.*, Sept. 2001, pp. 253-257.
- [10] Moody, G.B., Mark, R.G., "Development and evaluation of a 2-lead ECG analysis program," *Computers in Cardiology*. 1982; 39-44.
- [11] J. L. Urrusti and W. J. Tompkins, "Performance evaluation of an ECG QRS complex detection algorithm," *Proc. Annual International Conference of the IEEE Engineering in Medicine and Biology Society*, pp. 800-801, 1993.

CREATING A WEB SITE FOR MEDICAL EQUIPMENT

Silvia Bankova

Technical University – Sofia
14“Gevgeli” street, Pleven 5800, Bulgaria
Tel.: +359889759748
E-mail: sbankova@abv.bg

Abstract

There are billions of people around the world – each and every single one of them with all their needs, dreams and beliefs. Today, however, we are all bound by one of the greatest communication sources of the world – the Internet. An enormous part of our planet's population uses it in order to receive information. One of the most efficient ways is by visiting web sites including those for medical equipment.

1. INTRODUCTION

Specialised “St. Mina” hospital for rehabilitation in the town of Varshets is a proud owner of a web site which introduces visitors to institution's work in the field of medicine. The aim of the staff their patients to gain more accurate idea of the medical equipment of “St. Mina” inspired the creation of a graduation work under the guise of a web site called “Specialised Medical Equipment used in “St. Mina” hospital – town of Varshets”.

2. PREPARING FOR BUILDING THE WEB SITE

Before starting creating even a single page of the web site. I needed some specific information about instition's medical equipment. In order to do that I visited the hospital's inmates. The staff was kind to show me all premises and told me about each and every piece of equipment. I was allowed to take pictures in order to present my future web site visitors not only with text information but also with a variety of photos. My diploma work was suggested to be attached to hospital's general site.

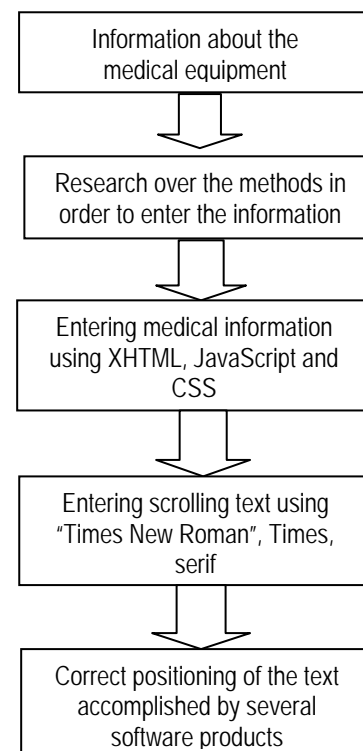
No sooner had I visited “St. Mina” in Varshets than I proceeded to the next step of the plan – my own preparation. It included reading plenty of books and magazines on the topic, surfing through different articles on the Internet and observing codes of popular and interesting web sites.

All things considered, I made my decision to use XHTML, JavaScript and CSS as web building tools.

3. BUILDING ENTERING MEDICAL INFORMATION ALGORITHMS

Apart from gathering the information that was needed, I followed step- by- step instructions which

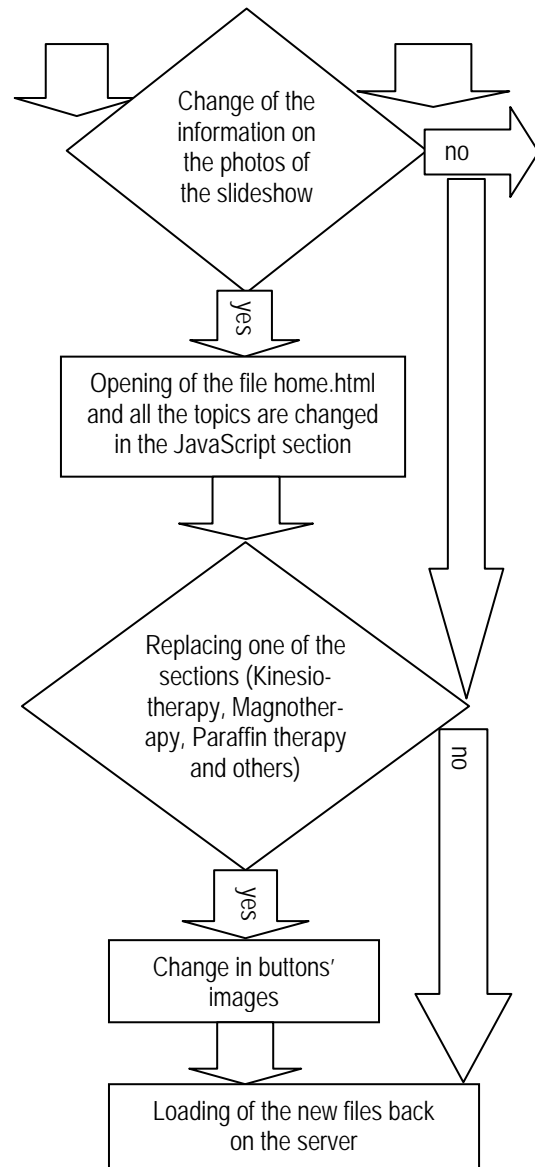
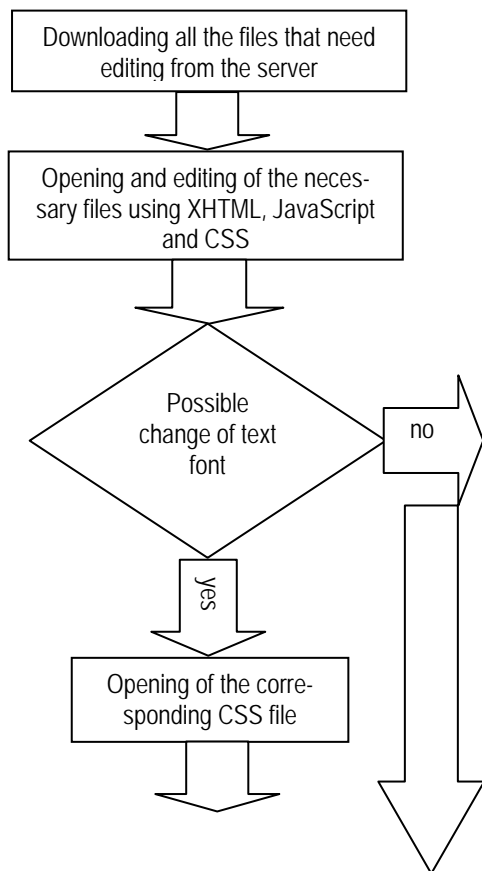
I structured myself in order to enter text. First of all, the whole medical information received was divided into sections such as Magnotherapy, Physical therapy, Kinesiotherapy and others. Thanks to the Internet and all literary sources written in “References” section I did a research about the various ways to enter the information. XHTML, JavaScript and CSS helped me to include the texts into the right sections. By means of “Times New Roman”, Times, serif the whole information about the medical equipment was added to the scroll field of content area. Correct positioning of the text was accomplished by several software products. The whole process is illustrated below:



4. BUILDING EDITING MEDICAL INFORMATION ALGORITHMS

If one or several pages of the web site need to be edited, a special procedure is followed. A web resource is fully functional when it is placed on a server. If information is to be edited, all elements that need to be changed have to be downloaded to a local folder created especially for the aim. The necessary file is to be found while opening the folder and with the help of a text editor or a professional software program the information is going to be edited. It is possible to change the font of the text by opening the correspondent CSS file. All the information on the photos of the slideshow could be changed as well. In this case the home page called home.html is opened and all of the topics in the JavaScript part are replaced by new ones.

Correction of one of the sections (Kinesiotherapy, Magnotherapy, Paraffin therapy and others) leads to inserting new images of the buttons in the menu. Finally, the edited files are loaded back on the server. Illustration of the algorithm is shown below:

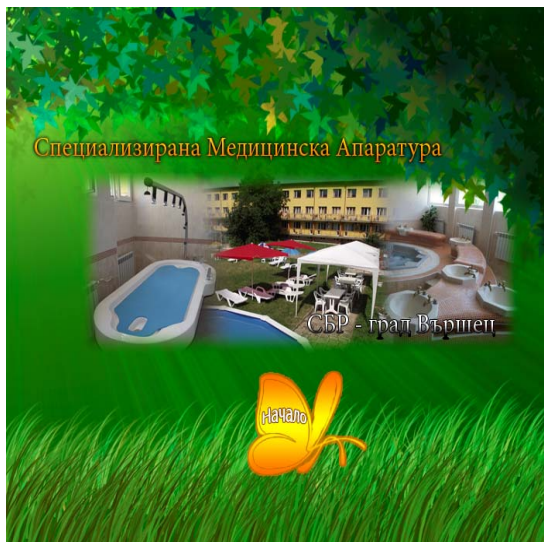


5. BUILDING THE WEB SITE "SPECIALISED MEDICAL EQUIPMENT USED IN "ST. MINA" HOSPITAL – TOWN OF VARSHETS"

There are two main principles used by web developers to create their sites. The first one is to consider the design of each web page. The best way of all is to have choices or to create more than one version of a page. Following this idea I succeeded in designing two types of the main page. The decision which one to work on was made by taking into account several major problems. It is of great importance visitors of the web site to navigate easily through the pages and to evaluate the functionality in a proper way. Under no circumstances is to be underestimated the design of the general web site of the hospital – the look of both sites should be approximately equivalent.

Another important fact of web building is the colour scheme of each page. On the one hand, it is visitors who will not accept the look of the site if it is based on the principle of using many colours as possible. It is not recommended to use a lot of colour nuances as well. On the other hand, it is of vital importance for a site to be built based on a web colour scheme. Moreover, different types of monitors require appropriate representation of some non web – based colours. If monitors do not act for the highest quality of picture as far as web – based colours are concerned, this leads to some lack of the site design.

Considering all mentioned, it was my second version that I continued building. Both of the designs are shown below:



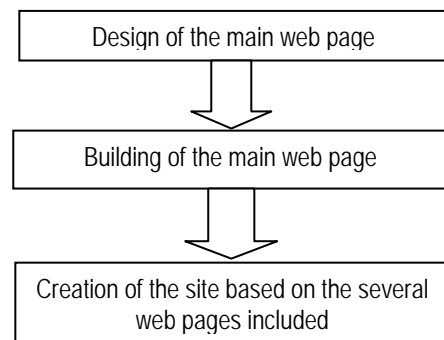
First version of the main web page



Second version of the main web page chosen the most suitable for building the site

Building the whole web site needed one step further to be paced. Usage of web – based languages helps completing the creation and adds functionality and dynamics to our work. Reviewing all options on the theme, I chose XHTML, JavaScript and CSS as my partners in the finishing part of the process.

Assuming all said, my work as a whole, could be divided into three periods – design of the main web page, building it and creation of the site based on the several web pages included. A scheme of the whole process could be seen below:



6. CONCLUSION

Building the web site “Specialised Medical Equipment used in “St. Mina” hospital – town of Varshets” is a result of ideas accomplished thanks to the medical staff of the institution and the abilities of the contemporary technologies. The road of site development has not been finished yet. The layers of improvement will proceed increasing their numbers but two of them will be realized in the near future. The tendencies to use smartphones and tablets to connect to the Internet, to talk to relatives and friends and other kinds of use, opened the doors to ideas for recreation of the site for medical equipment into mobile. Thus all patients, medical staff as well as many other people will have access to the information wherever they are. A printable version of the site is also taken into account. If such is used, the necessary information will be easily materialized into paper version. On the other hand, the text will be shown as a whole and reading through it will be faster.

Technologies tend to develop every single day, web sites increase their numbers and change the way they are built and the way they look – this is the future, the time of change of human beings and its global network of information.

7. APPENDIX AND ACKNOWLEDGMENTS

Final version of "Specialised Medical Equipment used in "St. Mina" hospital- town of Varshets" web site is shown below:



References

- [1] MacDonald M., "Creating a Web Site: The Missing Manual", Second edition, ZeST Press, Sofia, 2009
- [2] Adobe Creative Team, Adobe Dreamweaver CS3, Official educational course, Softpress, 2008
- [3] .NET Team, The Website, Interminds Publishing, Sofia, 2011
- [4] .NET Team, Full guide about Landscape Photography, How to take unique photos, Interminds Publishing, Sofia, 2010
- [5] Internet sources
<http://www.uoci.net>
<http://www.wikipedia.org>
<http://www.creativepro.com/article/combine-image-creatively-photoshop>
<http://www.dynamicdrive.com/dynamicindex14/fadeinshow.htm>
<http://www.youtube.com/watch?v=DVfxe4pqvo8&feature=relmfu>

EUROPEAN CENTRE FOR PROJECT/INTERNSHIP EXCELLENCE

Nuno Escudeiro¹, Paula Escudeiro²

^{1,2}Instituto Superior de Engenharia do Porto
Rua Dr António Bernardino de Almeida, 431, 4200-072 Porto
²GILT

Rua Dr António Bernardino de Almeida, 431, 4200-072 Porto
T. +351 228 340 500; F. +351 228 321 159; E. ¹nfe@isep.ipp.pt; ²pmo@isep.ipp.pt.

Abstract

Project/Internship course units are particularly valuable to undergraduate degrees. It is through this type of courses that students have the chance to practice their technical skills in a real-world-like setting and experience soft skills that are a key factor for employability. There are many distinct flavors of Project/Internship courses throughout Europe. Nevertheless, there is a lack of foundation supporting innovation, development and dissemination of the field. The purpose of PRAXIS is to fill this gap and set a European dimension to this instructional paradigm. In this paper we describe the PRAXIS concept, its development plan and the foreseen outcomes.

1. INTRODUCTION

Project/Internship (PI) course units create an environment that is a unique cradle to forge students' soft skills and attitudes, such as, team work, leadership, communication, initiative, focus. Addressing and improving these skills in students efficiently and efficaciously is seldom done by any other type of instruction. A PI is probably the most efficient way to improve these skills in students since even a very short PI course unit has significant impact in students' competences. It is the appropriate setting to improve students' affective domain, an important domain in today's society, in any study area.

This type of instruction is very suited to the Bologna paradigm raising the interest of European Higher Education Area (EHEA) players into it.

Despite the relevance and added value of this type of instruction, despite the high interest that it raises in higher education institutions (HEI), there is no European cluster specifically addressing the field and there is no planned effort to improve and innovate in the field. The purpose of the PRAXIS network is to set a European dimension to PI instruction type.

PRAXIS' mission is to become recognized as the leading authority worldwide in the field of the PI instruction type by creating and maintaining an environment that promotes and supports innovation in the field aimed at improving students' employability, soft skills and attitudes.

Our goals are: (a) to promote a European Center for Excellence in the field of PI initiatives by leveraging common interests and promoting cooperation among stakeholders, bringing all of them together, creating an environment to discuss and to promote innovation in the field, joining efforts and exploiting synergies and results from each other; (b) set a European marketplace of PI maximizing students' chances to find a project course matching their needs and, at the same time, setting a place to deploy innovative project course units by making them visible and available to students.

The perception of this opportunity to contribute to the EHEA by providing foundation to support innovation in the PI field together with our strong convictions on these assumptions arose from our previous experience in PI related issues, from all the contacts and discussion around these subjects that we have been promoting in the last few years and from our former work on multinational project teams, mainly at the MUTW – Multinational Undergraduate Team Work, an Erasmus Multilateral Project, co-funded by the EU from October 2009 till December 2011[1].

In the rest of the paper we will briefly describe the motivations moving PRAXIS towards its goals, the work plan we are applying to deploy PRAXIS and some final considerations.

2. RELATED WORK

There are many distinct flavors of PI courses throughout the EHEA, such as:

- multinational teams of students working at their home institutions and communicating virtually (MUTW)

- multinational teams working at a host institution (European Project Semester from Copenhagen University College of Engineering)

- multidisciplinary teams (project course at the University of Minho in Portugal and the International Integrated Project from the Fontys University in Netherlands)

- capstone project courses developed in a company or at a research lab (most engineer universities)

- small project course units running at the end of the semester (LAPR course unit at Instituto Superior de Engenharia do Porto in Portugal)

Some European projects and other initiatives focused on students' skills show the interest motivated by the field:

- FS-Biotech - Future Skills for Biotechnology "Skills to transform the future"; an Erasmus project, coordinated by Universidade Católica do Porto, that fosters cooperation between companies and Universities and the adaptation of curricula to companies needs in terms of valued skills

- EUROPLACEMENT is another LLP project that focuses on the development of graduates' transferable skills, and provides them with procedures for quality work experience, adapted to improve their own existing competence sets

Although we have not found any direct competitor for PRAXIS – someone who is worried with a comprehensive study of the field and focused on innovation and on promoting students' employability – there are many institutions that offering internship to students.

The interest in PI and students' employability field is notorious. The issue is that there is no declared centralized hub to join all players together and to promote innovation and exchange of experiences in the field. PRAXIS will set such a facility with the aim of joining efforts, promoting awareness, taking advantage of synergies and encouraging innovation and dissemination of best practices.

3. MOTIVATIONS AND OBJECTIVES

The lack of foundation to support innovation in the field of PI is the main motivation for PRAXIS. There is an opportunity to fill in this gap and to bring a European dimension to the field, empowering students, HEI, companies and the EHEA in general

with an extended set of opportunities to grow and profit from this instructional paradigm.

Establishing a center of excellence and a virtual marketplace for PI clearly marks a position and openly exposes this kind of instruction to all players assuring the European dimension that is required to empower the field. This European dimension will reach both students, who will have the chance to select the offer that is most suited to their needs, and teachers, who will have available the resources to discuss and bring to light their ideas in the field, a clear contribution to the development of EHEA.

There are already several distinct flavors of PI courses, with huge added value to the players, offered regularly in European HEI. However, these opportunities are not available neither known to all the students that might be interested in enrolling. Dissemination is a hard enterprise to take on one's own for several reasons, such as lack of resources and motivation. The benefits of these initiatives are not exploited given their local scope. Having the means to expose them worldwide will certainly generate economies of scale and encourage innovation in the field contributing to the exploitation of best practices in the field.

Student's employability is improved by PI courses to an extent that is not easily achievable by other instruction types. PI courses force students to develop soft skills and attitudes while training technical competence. This mix produces good results fast. Nevertheless, there is no cluster developing the field. There is a window of opportunity to set the agenda and to promote innovation in the field in Europe that PRAXIS intends to take, thus, incorporating new qualifications into the EHEA.

The frontend of both the European Center for PI Excellence and the PI market will be freely available online achieving a worldwide coverage. These facilities set a meeting point for players in the field. Operating them will enforce multilateral cooperation to discuss relevant issues and to organize mobility for students selecting PI courses abroad. This cooperation is of high quality since it has a concrete goal in mind: improving student's value-to-labor-market.

Both the PI marketplace and the European Center for PI Excellence, two innovative outputs of PRAXIS, will be deployed through the internet and supported by ICT technologies. The comprehensive resource on PI materials, to be gathered and maintained by PRAXIS, including content and teaching materials, mainly directed to students, and technical

materials, mainly directed to staff from the higher education institutions, to employers and to other stakeholders, will also be supported by ICT.

The PI instructional type, the focus of PRAXIS, is highly efficient; even a short PI course has high impact in students' competences. The conditions under which students do their assignment in PI courses is unique, significantly contributing to improve students' soft skills and attitudes and, as a consequence, their employability.

From the productivity point of view, PRAXIS promotes the reuse of the best practices in the field by making the most effective PI courses widely available thus contributing to the Europe 2020 Strategy.

3.1. Mission

Our mission is to become recognized as the leading authority worldwide in the field of Project/ Internship instruction type aiming to improve students' employability and soft skills. Our activity, focused on achieving a widespread reputation and reach, will be based on the European Centre for Project/Internship Excellence and on the Project/ Internship Virtual Market.

3.2. Goals

Our strategic goals are:

1. To promote a European Center for Excellence in the field of Project/Internship initiatives by leveraging common interests and promoting cooperation among stakeholders, bringing all of them together, creating an environment to discuss and to promote innovation in the field, joining efforts and exploiting synergies and results from each other.
2. To set a European market of Project/Internships maximizing students' chances to find a project course matching their needs and, at the same time, setting a place to deploy innovative project course units by making them visible and available to students.

3.3. Added value

PRAXIS acts on a field closely related to the EU2020 flagships. The main outputs of PRAXIS, the PI market and the European Center for PI Excellence, provide means for students to take advantages of the global Europe wide offer by selecting

the most appropriate PI course given their interests. This makes easier for them to get the right skills and competences.

The main issues of Bologna 2.0 are also addressed. PRAXIS provides a widening access to state of the art initiatives, it brings a global dimension to the field and deploys transparency tools.

Creating a cluster and the required framework to promote the PI instruction type and related issues will contribute to the EHEA in an area that can bring important benefits to all players at low cost. The PRAXIS vision is supported on the exposure of what already exists in the expectation that this exposure, in an appropriate scenario, will promote discussion and innovation. The PI market promotes reusing best practices. Reusing, in this sense, means saving, getting the benefits at low cost.

European cooperation is a sine qua non condition for PRAXIS. PRAXIS goals are not achievable without a representative group that has the power to influence opinion and generate the mood. The bigger the consortium, the better chances we have to succeed.

4. WORK PLAN

PRAXIS is a three years project co-funded by the EU, running between October 2011 and September 2014.

The focus of the project during the first year will be on the analysis of the field and design of the models and tools to describe and operate on it. During this first year we will map and model the target field of PRAXIS. When referring to the field we mean the broad area of project/internship and similar instruction types along with any initiatives related to them and to improving student employability. A detailed map of the field, clearly showing where we stand and what the market needs are, will allow us to identify opportunities for innovation and for improvement. The PRAXIS buzzwords for the first year of the project are exploring, mapping.

The second year will be focused on setting up and deploying the center for excellence in the field and the virtual PI market (PI stands for Project/Internship). Designing the market and the center for excellence as well as setting them up targeted for the opportunities previously identified, while assuring the required critical mass, will be the main achievements of the second year of the project. Our second year will be guided by headings acting, innovating.

The third and last year will be focused on exploitation and sustainability to assure the continuity of PRAXIS beyond funding. We will be focused on identifying opportunities for enlarging the consortium and on making PRAXIS a renowned brand in the EHEA and abroad. The third year of PRAXIS will be focused on exploitation, sustainability.

5. CONCLUDING REMARKS

At the PRAXIS consortium, we are deeply convinced that it is possible to improve the quality of most current curricula of undergraduate degrees without demanding for structural changes that force institutions to apply huge resources and that are very costly and time consuming. We refer to improvements in students' employability, in developing students' soft skills and attitudes which are rather important in today's economy and labor market as recognized by the EU. These are transversal to the majority, not to say all, of the study areas, so PRAXIS will be valuable to most study areas.

The cost/benefit ratio of initiatives in PI course units is probably one of the lowest in curriculum development, requiring small changes to provide big improvements. Almost all undergraduate degrees contain a PI course unit in their curricula. All we need is to take advantage of these course units to make them provide to students, and also to their future employers and the society in general, all the benefits they can and which can be much more than those provided by today's common PI course units.

Offering valuable training to students, on one side, and being recognized by the society as a valuable higher education provider, on the other, are among the general objectives of any HEI. The PRAXIS network moves towards these objectives since it will create new conditions to improve students' skills at no additional cost and without requiring any structural changes in degrees' curricula. From this point of view, all that PRAXIS is doing is providing a distribution channel for the best practices in PI that will become available for use by any HEI without additional costs of any kind. With PRAXIS anyone will be able to benefit from best practices and contribute to innovation in the PI field.

Acknowledgments

The work and the outcomes described in this paper are due to the PRAXIS consortium and to the dedication of all partners involved in it (www.praxisnetwork.eu).

This work has been funded with support from the European Commission under grant 518811-LLP-1-2011-1-PT-ERASMUS-ENW. This publication reflects the views only of the author, and the Commission cannot be held responsible for any use which may be made of the information contained therein

References

- [1] Multinational Undergraduate Team Work – Excellence in International Capstone Projects, Escudeiro, N.F., Escudeiro, P.M. Eds, IOS Press BV, Netherlands, 2011.